PROCEEDINGS OF THE TWENTY-SEVENTH ANNUAL BIOCHEMICAL ENGINEERING SYMPOSIUM

September 13, 1997

Lory Student Center
Colorado State University
Fort Collins, Colorado

Sponsored by

Department of Chemical & BioResource Engineering
Colorado State University

and

Colorado Institute for Research in Biotechnology

Vincent G. Murphy
Editor

Proceedings of the Twenty-Seventh Annual Biochemical Engineering Symposium

September 13, 1997

Vincent G. Murphy
Editor

Department of Chemical & Bioresource Engineering
Colorado State University
Fort Collins, Colorado 80523

PREFACE

The Twenty-Seventh Annual Biochemical Engineering Symposium was held at Colorado State University on September 13, 1997. Approximately seventy students and faculty from six universities (Colorado State University, Iowa State University, Kansas State University, University of Colorado, University of Oklahoma, and University of Wyoming) attended the symposium. The program consisted of nine oral presentations and twenty posters. As has been the practice at previous symposia in this series, all presentations represented ongoing or completed projects conducted by graduate students from the participating universities.

Fifteen authors submitted full papers for this proceedings, and seven others contributed summary abstracts. Most describe work in progress that will be discussed more fully in subsequent articles appearing in refereed journals.

I wish to express my sincere thanks to all those who participated in the symposium and especially to those who presented papers and posters. I also wish to acknowledge my gratitude to the Department of Chemical & BioResource Engineering at Colorado State University and to the Colorado Institute for Research in Biotechnology for their financial support of the symposium.

Vincent G. Murphy
Editor

TABLE OF CONTENTS

Twenty-Seventh Annual Biochemical Engineering Symposium

Colorado State University
Fort Collins, Colorado
September 13, 1997

8:30-9:50 a.m. **Session I** (Lory Student Center, Room 230)

8:30 **Welcome**

8:35 **New Fusion Protein Systems Designed to Increase Soluble Cytoplasmic Expression of Heterologous Proteins in *Escherichia coli*.** Gregory Davis, Clause Elisee, Denton Newham, and Roger Harrison (University of Oklahoma).

9:00 **Mutations to Alter *Aspergillus awamori* Glucoamylase Selectivity.** Hsuan-Liang Liu, Pedro Coutinho, Clark Ford, and Peter Reilly (Iowa State University).

9:25 **The Effects of Physiological Intermittent Pressures on Cartilage Regeneration.** Scott Carver and Carole Heath (Iowa State University).

9:50-10:15 a.m. **Break**

10:15-11:30 a.m. **Session II** (Lory Student Center, Room 230)

10:15 **A Model of the Effects of Acclimation on the Cardiorespiratory and Thermoregulatory Systems.** Dawn Downey and Richard Seagrave (Iowa State University).

10:40 **Development of a Biosensor for 1,2-Dichloroethane.** Derek Campbell, Cord Mueller, and Kenneth Reardon (Colorado State University).

11:05 **Lyophilization-Induced Phase Separation: Effects on Hemoglobin Structure.** Martin Heller and Theodore Randolph (University of Colorado at Boulder); John Carpenter (University of Colorado Health Sciences Center).

11:30-1:00 p.m. **Lunch**

1:00-2:15 p.m. **Poster Presentations** (Lory Student Center, East Ballroom)

2:15-3:35 p.m. **Session III** (Lory Student Center, Room 230)

2:15 **Long-Term Solution Stability of Recombinant γ-Interferon: The Link Between Solution Thermodynamics and Degradation Kinetics.** Brent Kendrick and John Carpenter (Univesity of Colorado Health Sciences Center); Theodore Randolph (University of Colorado at Boulder).

2:40 **Primary Recovery Improvements Using Polymeric Flocculants.** Hugh Graham, Naz Karim, and Brian Batt (Colorado State University); A.S. Cibulskas (Cytec Industries).

3:05 **The Effect of Secondary Membranes on Protein Transmission in a Multicomponent System.** Vinod Kuberkar and Robert Davis (University of Colorado at Boulder).

3:30 **Invitation to Attend 1998 Symposium**

LIST OF POSTER PRESENTATIONS

1. **HL-60 Cell-Cell Interactions under Flow Mediated by Platelet Microparticles.** Brad Forlow and Matthias Nollert (University of Oklahoma).

2. **Intracellular Calcium Changes in Endothelial Cells Exposed to Flow and Agonist Stimulation.** Laura Worthen and Matthias Nollert (University of Oklahoma).

3. **Design of a Bioartificial Nerve Graft for Regeneration in the Periphery.** Gregory Rutkowski and Carole Heath (Iowa State University).

4. **Maximizing Protein Synthesis in High Cell Density Perfusion Bioreactors.** Frank Lee, Paul Todd, and Dhinakar Kompala (University of Colorado at Boulder).

5. **Strategy for Improving Large-Scale *In Vitro* RNA Transcription.** Naiomi Breckenridge and Robert Davis (University of Colorado at Boulder).

6. **Identification of Different Phases in a Fermentation Using a Neural Network.** Laurent Simon, Naz Karim, and Amanda Schreiweis (Colorado State University).

7. **Cascade Concentration of *Spirulina platensis* Based on Inertial Migration.** Steven Dahl, Allen Rakow, and Kevin Ryan (Colorado State University).

8. **Recovery of Fusion Proteins from Canola Protein Extracts by Adsorption Chromatography.** Chenming Zhang and Charles Glatz (Iowa State University).

9. **Isoelectric and Polyelectrolyte Precipitation of Recombinant Proteins in Canola Extract.** Ferhana Zaman, Jocelyn Pollack, and Charles Glatz (Iowa State University).

10. **Effect of High Pressure on Crystallization of Subtilisin Mutants.** Rutta Waghmare, Marika Joona, Maurice Larson, and Charles Glatz (Iowa State University); Jonathan Webb and Theodore Randolph (University of Colorado at Boulder).

11. **Effect of a Closely Related Contaminant on the Crystallization of an Oligonucleotide.** Stephen Cape and Paul Todd (University of Colorado at Boulder).

12. **The Effects of Solution Additives on the Stability of Recombinant Human Interferon-Gamma during Freeze Drying and Reconstitution.** Serena Webb, S. Rule, and Theodore Randolph (University of Colorado at Boulder); John Carpenter (University of Colorado Health Sciences Center).

13. **The Effect of Non-Ionic Surfactants on the Stability of Lyophilized CNTF.** LaToya Jones and Theodore Randolph (University of Colorado at Boulder); B.S. Chang (Amgen); John Carpenter (University of Colorado Health Sciences Center).

14. **Preparation of Controlled Drug Release Microspheres and Application to Osteomyelitis and Ocular Angiogenesis.** Rick Falk and Theodore Randolph (University of Colorado at Boulder); Robert Beauvais, Jeffrey Meyer, and Mark Manning (University of Colorado Health Sciences Center); Mark Reynolds (Ribozyme Pharmaceuticals).

15. ***Ex Vivo* Studies of Controlled-Release Drug Preparations in Bovine Vitreous Humour.** Jing Xu, Theodore Randolph, and Victor Barocas (University of Colorado at Boulder).

16. **Plant Uptake and Transport of Trichloroethylene in the Rhizosphere.** Jiang Hu, Muralidharan Narayanan, L.C. Davis, and Larry Erickson (Kansas State University).

17. **Toluene Contamination Enhances Populations of Toluene Degraders in the Rhizosphere.** Xiaowei Wu and L.C. Davis (Kansas State University).

18. **An Experimental Study of Trichloroethylene Fluxes into the Atmosphere.** Qizhi Zhang, L.C. Davis, and Larry Erickson (Kansas State University).

19. **Microbial Transport in a Pilot-Scale Biological Treatment Zone.** Daniel Adams, Michael Malusis, Kenneth Reardon, and Charles Shackelford (Colorado State University); Al Bourquin and Douglas Mosteller (Camp Dresser & McKee)

20. **Bioreactor Development for Removal of Can Manufacturing Emissions.** Julio Zimbron, Adeyma Arroyo, and Kenneth Reardon (Colorado State University).

LIST OF PARTICIPANTS

Colorado State University: Dan Adams, Dale Brown, Derek Campbell, Steve Dahl, Zoila Flores-Bustamante, Hugh Graham, Linda Henk, Ellen Johnson, Naz Karim, Jin-Sung Kim, Jin-Woo Kim, Wei-chuang Lin, Jim Linden, Melissa Miller, Vince Murphy, Jeremy Porter, Allen Rakow, Ken Reardon, Kevin Ryan, Sigrid Schreiber, Laurent Simon, Andy Spasoff, Amy Weber, and Julio Zimbron.

Iowa State University: Scott Carver, Dawn Downey, Zhiliang Fan, Ruth Fink-Winter, Justin Glenn, Marika Joona, Hsuan-Liang Liu, Mark Mowry, Luke McConeghey, Kaz Omori, Peter Reilly, Greg Rutkowski, Vibhu Sharma, Ruta Waghmare, David Wendt, Ferhana Zaman, and Chenming Zhang.

Kansas State University: Larry Erickson, Jiang Hu, and Xiaowei Wu.

University of Colorado: Naiomi Breckenridge, Stephanie Bryant, Steve Cape, Rick Falk, Martin Heller, LaToya Jones, Dhinakar Kompala, Vinod Kuberkar, Frank Lee, Ted Randolph, Jennifer Shull, Paul Todd, Yanqzu Wang, Serena Webb, and Jing Xu.

University of Oklahoma: Greg Davis, Brad Forlow, Roger Harrison, and Laura Worthen.

University of Wyoming: Jason Burdick, Pat Gilcrease, Collin Greenwell, Jolene Ignowski, Mikki Martin, and Travis Rybicki.

Mutations to Alter *Aspergillus awamori* Glucoamylase Selectivity

Hsuan-Liang Liu, Pedro M. Coutinho, Clark Ford[1], and Peter J. Reilly
Departments of Chemical Engineering and [1]Food Science and Human Nutrition
Iowa State University
Ames, IA 50011

ABSTRACT

Mutations Asn20→Cys/Ala27→Cys (SS), Ala27→Pro, Ser30→Pro, Lys108→Arg, Gly137→Ala, Tyr312→Trp and Ser436→Pro in *Aspergillus awamori* glucoamylase, along with a mutation inserting a seven-residue loop between Tyr311 and Gly314 (311-314 Loop), were kinetically characterized. No active Lys108→Met glucoamylase was found in the supernatant after being expressed from yeast. Lys108→Arg, 311-314 Loop and Trp312→Tyr glucoamylases have lower activities than wild-type glucoamylase; other GAs have the same or higher activities. SS and 311-314 Loop glucoamylases give dramatically decreased formation rates of isomaltose, the main byproduct, in 30% (w/v) glucose solutions at 35, 45, and 55°C, correlating with higher peak glucose yields from 30% (w/v) maltodextrin hydrolysis. Conversely, Lys108→Arg glucoamylase has isomaltose formation rates significantly higher and glucose yields much lower than wild-type glucoamylase. Gly137→Ala and Tyr312→Trp glucoamylases also give high glucose yields at higher temperatures. Mutated glucoamylases that catalyze high rates of isomaltose formation give higher glucose yields from lower-DP than from higher-DP maltodextrins, opposite normal experience with more efficient glucoamylases.

INTRODUCTION

Glucoamylase (1,4-α-D-glucan glucohydrolase, EC 3.2.1.3, GA) catalyzes -D-glucose release from the nonreducing ends of starch and related oligo- and polysaccharide chains by α-1,4-glucosidic bond hydrolysis. *Aspergillus awamori* and *Aspergillus niger* GAs, which have identical amino acid sequences (Svensson *et al.*, 1983; Nunberg *et al.*, 1984), are widely used in industry to produce high-glucose syrups, to be converted primarily to fructose and ethanol. GA can also hydrolyze α,β-1,1-, α-1,2-, α-1,3-, and α-1,6-glucosidic bonds at much lower rates (Hiromi *et al.*, 1966a,b; Meagher and Reilly, 1989). GA also synthesizes various α-linked di-, tri-, and tetrasaccharides in high D-glucose concentrations by reforming all the above bonds (Pazur and Okada, 1967; Hehre *et al.*, 1969; Pazur *et al.*, 1977; Nikolov *et al.*, 1989), as the law of microscopic reversibility mandates. This limits D-glucose yield from starch hydrolysis to about 95% of theoretical. In these condensation reactions, isomaltose [α-D-glucopyranosyl-(1→6)-D-glucose, iG_2] is the thermodynamically favored product.

In the present work, we constructed three single mutations, Lys108→Arg, Lys108→Met, and Tyr312→Trp, and one insertional mutant, Tyr311-Tyr312-Asn313-Gly314→Tyr311-Asn-Gly-Asn-Gly-Asn-Ser-Gln-Gly314 (311-314 Loop) by site-directed mutagenesis to study substrate specificity and to increase glucose yield. Both Lys108 and Tyr 312 are located in the

$(\alpha/\alpha)_6$-fold of the catalytic domain in segments that connect α-helices 3 and 4 and 9 and 10, respectively (Aleshin *et al.*, 1992).

Lys108 is totally conserved in all GAs except *Clostridium* GA, where it is missing (Coutinho and Reilly, 1997). The *Clostridium* GA has relatively high α-1,6 activity (Ohnishi *et al.*, 1992). Lys108 is proposed to form a hydrogen bond with the 6-OH of the reducing glucosyl residue of G_2 at subsite 2 through a surface water molecule (Coutinho and Reilly, 1994a). However, this surface water does not form a hydrogen bond with either 1-deoxynojirimycin (Harris *et al.*, 1993) or acarbose (Aleshin *et al.*, 1994) due to their shifted positions in the active site. There is no hydrogen bond in the GA-iG_2 complex through this group, since it is now part of the glucosidic bond. We replaced Lys108 with Arg and Met residues to study the influence of side-chain surface charges on enzyme-substrate stabilization in a well defined void formed by the aromatic residues Tyr50, Trp52, Tyr116, and Trp120.

Two individual loop replacements and one double loop replacement have been constructed in *A. awamori* GA to mimic part of the *H. resinae* GA sequence (Fierobe *et al.*, 1996). The double mutation had approximately twofold higher relative catalytic efficiencies for hydrolysis of α-1,6- over α-1,4-linked substrates. Although loop replacement based on sequence homology is a powerful tool for altering substrate specificity (Fierobe *et al.*, 1996), loop insertion or deletion has not been attempted in the GA catalytic domain. GAs from *Rhizopus* and some other subfamilies have longer amino acid sequences than do *A. niger* or *A. awamori* GAs (Coutinho and Reilly, 1994a) and therefore may have different active-site conformations. *Rhizopus niveus* GA has a catalytic efficiency about 20-50% that of *A. niger* GA for iG_2 hydrolysis (Tanaka and Takeda, 1994) with about the same catalytic efficiency for G_2 hydrolysis (Ohnishi, 1990). Therefore we designed the 311-314 Loop mutation to mimic the *Rhizopus* GA sequence.

Tyr311 participates in a hydrogen-bond network with the general catalytic base Glu400 (Harris *et al.*, 1993) through the invariant Tyr48. The large loss in substrate affinity of Glu400→Gln GA is because of destabilization due to disruption of the hydrogen-bond network involving the Glu400 γ-carboxyl group, the Tyr48 hydroxyl group and the Tyr311 hydroxyl group (Aleshin *et al.*, 1994). Tyr311 is also totally conserved (Coutinho and Reilly, 1997). Based on the above evidence, we chose Tyr312, located right behind Tyr311 in the enzyme-substrate complex, to be mutated to Trp. This introduced a bigger side chain to supply stronger support to Tyr311 in forming the tight hydrogen-bond network described above.

Some previously constructed thermostable mutant GAs, Asn20→Cys/Ala27→Cys (SS) (Li and Ford, 1997), Ser30→Pro (Allen *et al.*, 1997), Gly137→Ala (Chen *et al.*, 1996), and Ser436→Pro (Li *et al.*, 1997), along with one thermosensitive mutant GA, Ala27→Pro (Li *et al.*, 1997), were tested to investigate a potential relationship between enzyme thermostability and specificity. The SS mutation was designed to create a disulfide bond on the catalytic domain surface and to stabilize GA against unfolding. The Ser30→Pro, Gly137→Ala, and Ser436→Pro mutations were meant to stabilize GA by reducing the conformational entropy of unfolding, and are the most stable mutant GAs in a series of previously made X→Pro and Gly→Ala substitutions (Chen *et al.*, 1996; Li *et al.*, 1997; Allen *et al.*, 1997). Only Ala27 and Ser30 among these residues are located in conserved regions, and neither of them is totally conserved (Coutinho and Reilly, 1994a,b).

Previous studies have attempted to improve GA substrate specificity by single-residue substitutions: Ser119→Tyr, Gly183→Lys, and Ser184→His GAs all had 2.3- to 3.5-fold enhancement of the ratio of catalytic efficiencies of G_2 hydrolysis to iG_2 hydrolysis (Sierks and Svensson, 1994; Svensson *et al.*, 1995). Eleven mutations at positions not totally conserved around the GA active site were constructed by Fang *et al.* (1997a,b) to alter selectivity of *A. awamori* GA. Tyr116→Trp, Ser119→Gly, Ser119→Trp, Gly121→Ala, Arg241→Lys, Ser411→Ala, Ser411→Gly, and Gly121→Ala/ Ser411→Gly GAs all gave significantly increased glucose yields at 55°C compared to wild-type GA. In general there was an inverse correlation between peak glucose yield and the ratio of initial rate of iG_2 formation to that of glucose formation.

MATERIALS AND METHODS

Methods for enzyme production and purification, protein concentration measurement, enzyme kinetic assays, maltooligosaccharide hydrolysis and glucose condensation reactions were described by Fang *et al.* (1997a). Specific activities were determined as in Fang *et al.* (1997b).

Materials

Glucose, maltose, maltotriose (G_3), maltotetraose (G_4), maltopentaose (G_5), maltohexaose (G_6), maltoheptaose (G_7), glucose oxidase, peroxidase, and α-naphthol were from Sigma. Isomaltose was purchased from TCI America. Maltrin® M100, M180, and M250 maltodextrins, of Dextrose Equivalents (DE) 10, 18 and 25, respectively, and with average degrees of polymerization (DP) of 10, 6, and 4, were donated by Grain Processing Corporation. Other materials were as in Fang *et al.* (1997a).

Site-Directed Mutagenesis

Site-directed mutagenesis was performed with the Muta-Gene phagemid *in vitro* mutagenesis kit from Bio-Rad (Kunkel *et al.*, 1987) on an *Bam*HI-*Xho*I fragment of the wild-type GA cDNA inserted into the phagemid vector pGEM7Z(+). The vector was then transformed into *E. coli* CJ236 (*dut*$^-$, *ung*$^-$) to produce uracil-containing single-stranded DNA to be used as the template in site-directed mutagenesis. The following mutagenic oligonucleotide primers were synthesized at the Iowa State University Nucleic Acid Facility: 5'-GGT CTC GGT GAG CCC AGG TTC AAT GTC GAT-3' (Lys108→Arg), 5'-GGT CTC GGT GAG CCC ATG TTC AAT GTC GAT-3' (Lys108 →Met), 5'-TAC CCT GAG GAC ACG TAC **AAC GGC AAC GGC AAC TCG CAG** GGC AAC CCG TGG TTC CTG TGC-3' (311-314 Loop), and 5'-GAG GAC ACG TAC **TGG** AAC GGC AAC CCG-3' (Tyr312→Trp), the bold letters indicating the changed or added nucleotides. All mutations were verified by DNA sequencing. The mutated GA cDNAs were subcloned into YEpPM18 and then transformed into *S. cerevisiae* C468 as previously described (Chen *et al.*, 1994a). Construction of the Gly137→Ala (Chen *et al.*, 1996), SS, Ala27→Pro, Ser436→Pro (Li *et al.*, 1997), and Ser30→Pro (Allen *et al.*, 1997) GAs is described separately.

Protein Electrophoresis

Soluble extracellular fractions of 5-d yeast cultures from 5-L fermentations of wild-type and Lys108→Met GAs were concentrated 500-fold by ultrafiltration, added to 2X SDS-PAGE buffer, and heated at 95°C for 5 min. The samples were subjected to SDS-PAGE on a 1-mm thick 10% gel at 60 V for 5 h along with high molecular weight markers, followed by staining with Coomassie Brilliant Blue R for 20 min and by destaining with distilled water for 24 h. The resulting gels were transferred onto a 0.2-mm nitrocellulose membrane with a Bio-Rad Trans-Blot SD semi-dry transfer cell.

Irreversible Thermoinactivation

GAs (0.475 μM) were incubated in 0.05 M NaOAc buffer, pH 4.4, at 70°C for 12 min. Samples were taken at 2-min intervals, quickly chilled on ice, and then stored at 4°C for 24 h before being subjected to residual activity assay at 35°C. Enzyme activity was determined with 0.117 M maltose in the same buffer. Seven samples were taken at 7-min intervals and added to 0.4 volume of 4 M Tris-HCl buffer, pH 7.0, to stop the reaction. The resulting glucose was measured by the glucose oxidase method (Rabbo and Terkildsen, 1960).

RESULTS

Thermoinactivation

Wild-type, Lys108→Arg, 311-314 Loop, and Tyr312→Trp GAs followed first-order decay kinetics, as have all previous mutant GAs tested for thermostability (Chen *et al.*, 1994a,b, 1995, 1996; Li *et al.*, 1997; Allen *et al.*, 1997), with rate coefficients at 70°C of 0.036, 0.073, 0.075, and 0.053 min^{-1}, respectively. Except for Ala27→Pro, other mutant GAs studied here were more thermostable than wild-type GA (Chen *et al.*, 1996; Li *et al.*, 1997; Allen *et al.*, 1997).

Enzyme Kinetics

After expression from yeast colonies, Lys108→Met GA produced no starch-clearing halo on an SD + His + 1% soluble starch plate. It yielded no detectable activity in the supernatant of a yeast fermentation broth after specific activity assay with 4% maltose. Lys108→Met GA gave a band with 1/3 the intensity of wild-type GA after submitting the concentrated supernatants to 10% SDS-PAGE. The mutated GA did not bind to an acarbose-Sepharose affinity column, since no detectable peak was observed by ultraviolet adsorption at 280 nm at the retention time characteristic of GA after elution by 1.7 M Tris-HCl at pH 8.0. Therefore this mutated GA was not studied further.

Specific activities of wild-type, Lys108→Arg, 311-314 Loop, and Tyr312→Trp GAs were 15.5, 11.5, 9.07 and 11.9 IU/mg, respectively, determined by 4% (w/v) maltose in 0.05 M NaOAc buffer at 45°C, pH 4.4. All other mutant GAs studied here except Ala27→Pro had

about the same or greater specific activities than wild-type GA (Chen *et al.*, 1996; Allen *et al.*, 1997; Li *et al.*, 1997).

Maltodextrin Hydrolysis

Figures 1-3 show the results of 30% (w/v) DE 10 maltodextrin hydrolyses at 35, 45, and 55°C, respectively, with 1.98 μM GA. Panel a) here and in later figures has data for wild-type GA and those mutant GAs constructed first in this work; panel b) here and later has data for wild-type GA and those mutant GAs meant to increase GA thermostability. Data (not shown) for DE 18 and DE 25 maltodextrins are similar. SS and 311-314 Loop GAs had the highest peak glucose yields, while Lys108→Arg GA had the lowest yields. Glucose concentrations decreased after reaching maximal values because of conversion to oligosaccharides, especially at higher temperatures. Initial glucose formation rates appear in Table I. They were generally lowest for 311-314 Loop GA because its specific activity with 4% (w/v) maltose substrate was only 60% that of wild-type GA. Thermostable mutant GAs generally had higher initial glucose formation rates than wild-type GA, while thermosensitive GAs had lower rates. Initial glucose formation rates often slightly increased with increasing substrate DE.

Glucose Condensation Reactions

Formation of iG_2 from condensation of 30% (w/v) glucose at 35, 45, and 55°C with 1.98 μM GA is shown in Figures 4-6, respectively, with initial rates appearing in Table I. SS and 311-314 Loop GAs had the lowest initial rates at all three reaction temperatures, while Lys108→Arg and Ala27→Pro GAs had the highest initial rates.

Specificity for α-1,6-Linked Product Synthesis Versus α-1,4-Linked Substrate Hydrolysis

The ratio of the initial rate of iG_2 formation by condensation of 30% glucose to that of glucose formation from 30% DE 10, 18 and 25 maltodextrin hydrolysis was taken to estimate the selectivity for α-1,6-linked product synthesis over α-1,4-linked substrate hydrolysis (Table I). Lys108→Arg and SS GAs had the highest and lowest ratios, respectively, among wild-type and mutant GAs at all reaction temperatures. The 311-314 Loop GA also had low ratios, as did than those for G_2 hydrolysis. These results can be compared to the ratios of catalytic efficiencies of G_2 to those of iG_2, where 311-314 Loop GA had the highest value, Lys108→Arg GA had the lowest, and SS and Tyr312→Trp GAs had values similar to wild-type GA.

DISCUSSION

SS GA had initial rates of iG_2 formation 25-50% those of wild-type GA, even though initial glucose formation rates increased. Among the GAs tested here, SS GA is the only one whose mutat-ion introduced a covalent bond. This may have made the enzyme even more rigid and restricted its natural flexing action, favoring the α-1,4 over α-1,6 substrate binding conformation.

Introduction of unfavorable contacts between the Pro pyrrolidine ring and neighboring groups by the Ala27→Pro mutation resulted in decreased GA thermostability (Li *et al.*, 1997). The mutation yields incompatible ϕ and ψ angles, and this may have favored formation and hydrolysis of α-1,6-linked substrates, reducing glucose yield.

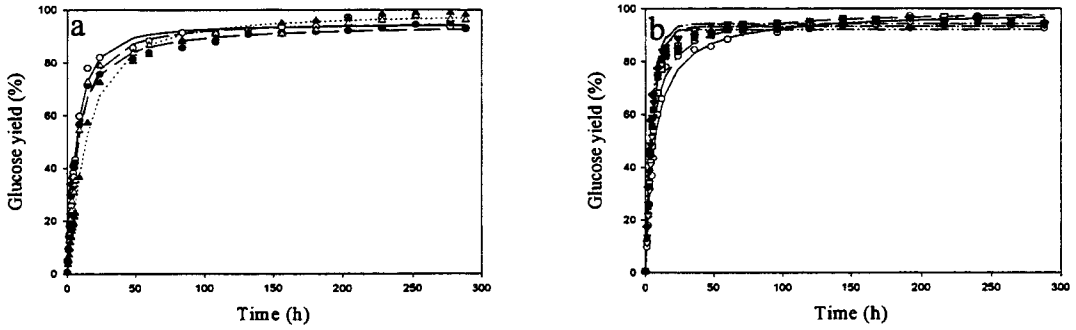

Figure 1. Glucose formation during the incubation at 35°C of 30% (w/v) DE 10 maltodextrin with 1.98 μM GA in 0.05 M NaOAc buffer, pH 4.4 for (a) wild-type (○, ——), Lys108→Arg (●, —— ——), 311-314 Loop (△, ·····), Tyr312→Trp (▲, — —) (b) wild-type (○, ——), SS (□, —— ——), Ala27→Pro (■, —— ——), Ser30→Pro (▽, ·····), Gly137→Ala (▼, · —— · ——), and Ser436→Pro (◆, ·· —— ·· ——) GAs.

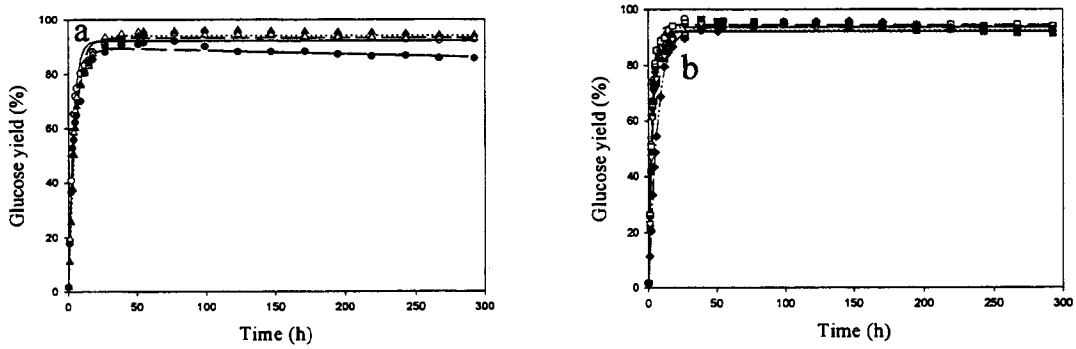

Figure 2. Glucose formation during the incubation at 45°C. Conditions and captions are the same as in Figure 1.

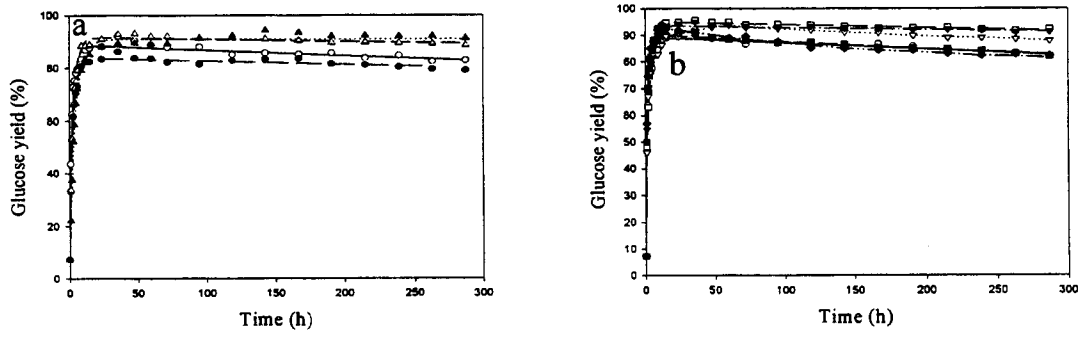

Figure 3. Glucose formation during the incubation at 55°C. Conditions and captions are the same as in Figure 1.

Table I. Initial rates of glucose and isomaltose formation in the hydrolysis of 30% (w/v) maltodextrins and condensation of 30% (w/v) glucose, respectively, and their relative ratios for wild-type and mutant GAs at 35, 45, and 55°C.

	Initial rates (mol/mol GA·s)						
	Glucose			$iG_2 \times 10^3$	Initial rate $iG_2 \times 10^3$ / Initial rate glucose)		
GA form	DE 10	DE 18	DE 25		DE 10	DE 18	DE 25
35°C							
Wild-type	32.8 ± 1.4[a]	36.3 ± 1.6	38.6 ± 2.1	15.2 ± 0.5	0.46	0.42	0.39
SS	48.1 ± 2.2	47.9 ± 2.4	46.8 ± 2.9	7.07 ± 0.33	0.15	0.15	0.15
Ala27→Pro	41.4 ± 1.9	45.4 ± 2.3	46.4 ± 3.5	43.7 ± 1.9	1.06	0.96	0.94
Ser30→Pro	39.7 ± 1.8	46.1 ± 2.6	46.3 ± 3.4	22.9 ± 0.8	0.58	0.50	0.49
Lys108→Arg	32.6 ± 1.6	34.5 ± 2.0	34.1 ± 1.9	50.9 ± 1.9	1.56	1.48	1.49
Gly137→Ala	44.9 ± 2.3	48.6 ± 2.7	49.2 ± 3.3	19.1 ± 0.7	0.43	0.39	0.39
311-314 Loop	20.9 ± 1.1	23.9 ± 1.3	24.6 ± 1.7	6.71 ± 0.24	0.32	0.28	0.27
Tyr312→Trp	26.9 ± 1.4	31.2 ± 1.9	33.1 ± 2.0	15.5 ± 0.6	0.58	0.50	0.47
Ser436→Pro	45.1 ± 2.6	53.3 ± 3.3	55.5 ± 4.2	47.5 ± 1.8	1.05	0.89	0.86
45°C							
Wild-type	101 ± 5	102 ± 5	98.7 ± 5.3	39.6 ± 2.9	0.39	0.39	0.40
SS	129 ± 6	125 ± 5	110 ± 6	16.4 ± 1.0	0.13	0.13	0.15
Ala27→Pro	99.5 ± 5.3	95.8 ± 4.8	93.2 ± 5.8	79.2 ± 4.2	0.80	0.83	0.85
Ser30→Pro	98.8 ± 5.4	107 ± 5	119 ± 6	51.0 ± 2.2	0.52	0.48	0.43
Lys108→Arg	77.1 ± 4.3	77.3 ± 4.2	76.7 ± 5.3	85.5 ± 4.7	1.11	1.11	1.11
Gly137→Ala	102 ± 6	110 ± 5	112 ± 7	30.7 ± 1.8	0.30	0.28	0.27
311-314 Loop	61.2 ± 3.8	68.4 ± 3.4	70.3 ± 5.1	14.6 ± 1.1	0.24	0.21	0.21
Tyr312→Trp	78.4 ± 4.5	80.3 ± 4.7	81.6 ± 5.5	34.3 ± 1.8	0.44	0.43	0.42
Ser436→Pro	87.9 ± 5.3	125 ± 7	113 ± 7	68.3 ± 3.6	0.78	0.55	0.60
55°C							
Wild-type	240 ± 15	258 ± 17	313 ± 23	129 ± 7	0.54	0.50	0.41
SS	268 ± 17	311 ± 20	322 ± 22	32.4± 2.7	0.13	0.11	0.11
Ala27→Pro	258 ± 18	302 ± 21	295 ± 19	163 ± 9	0.63	0.54	0.55
Ser30→Pro	284 ± 20	334 ± 23	346 ± 24	119 ± 6	0.42	0.36	0.34
Lys108→Arg	152 ± 11	166 ± 12	170 ± 10	216 ± 14	1.42	1.30	1.27
Gly137→Ala	288 ± 21	333 ± 23	325 ± 23	83.4 ± 5.4	0.29	0.25	0.26
311-314 Loop	191 ± 14	205 ± 16	221 ± 15	49.5 ± 2.7	0.26	0.24	0.22
Tyr312→Trp	169 ± 13	211 ± 15	217 ± 16	117 ± 7	0.69	0.55	0.54
Ser436→Pro	301 ± 22	322 ± 25	330 ± 23	124 ± 8	0.41	0.39	0.38

[a] Standard error

Ser30→Pro GA produced comparatively fewer α-1,6 bonds at increased temperatures, suggesting that introduction of a Pro residue at the second position of a type II β-turn in this region causes an entropy change not only to reduce conformational unfolding, but also to favor the α-1,4 binding mode at the active site.

The Lys108→Arg mutation increased binding affinity of the α-1,6-linked iG_2 compared to wild-type GA. The 4-OH group of iG_2 appears to be involved in a conformational adjustment to optimize binding energy in the GA-iG_2 complex (Frandsen *et al.*, 1996) and Lys108 can form a hydrogen bond to either the 2- or 3-OH of the nonreducing glucosyl residue (Aleshin and Honzatko, 1995), so tighter hydrogen binding due to increased surface charge in Lys108→Arg GA would stabilize this complex in the transition state. Lys108 is involved in

the enzyme-substrate complex in the S2 region along with three invariant residues, Trp120, Gln124, and Asp126 (Coutinho and Reilly, 1994a). The Trp120 loop region plays an important role in directing conformational changes controlling the postulated rate-limiting product release step from maltooligosaccharide hydrolysis (Natarajan and Sierks, 1996). The Lys108→Arg mutation may push the Trp120 loop to the catalytic center, restricting glucose release and causing it to become competitive substrate. This would lead to iG_2 synthesis instead of maltooligodextrin hydrolysis.

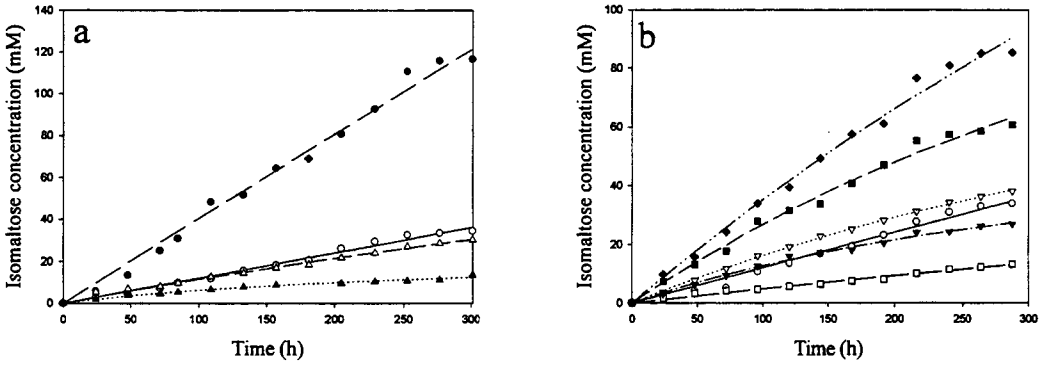

Figure 4 Formation of iG_2 during incubation at 35°C of 30% (w/v) glucose. Captions are the same as in Figure 1.

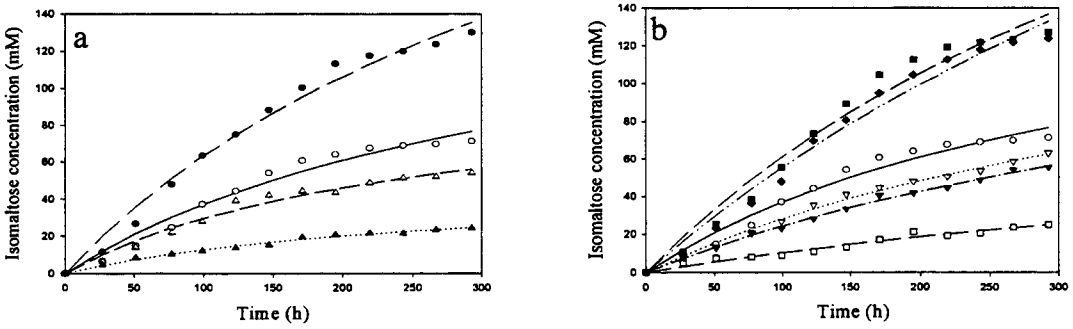

Figure 5 Formation of iG_2 during incubation at 45°C of 30% (w/v) glucose. Captions are the same as in Figure 1.

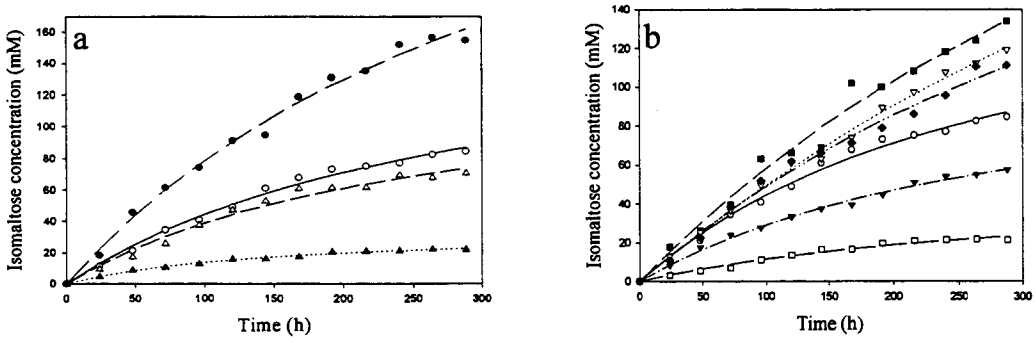

Figure 6 Formation of iG_2 during incubation at 55°C of 30% (w/v) glucose. Captions are the same as in Figure 1.

The observations that Lys108→Met GA 1) formed no halos on starch plates after expression from yeast colonies, 2) had no detectable activity in concentrated fermentation culture supernatants, 3) formed a GA band with 1/3 the intensity of wild-type GA on 10% SDS-PAGE gel, and 4) could not be purified by acarbose-Sepharose affinity chromatography suggest that this mutated GA is expressed in an inactive form due to the loss of substrate-binding ability. The long Met side chain is nonpolar, relatively unreactive, and cannot be protonated, so Met108 has no side-chain surface charge nor any ability to form hydrogen bonds with substrates.

These two mutations demonstrate that changing Lys108 strongly affects GA. Removing its surface charge yields a GA that does not bind substrates and therefore totally loses activity, while increasing its surface charge favors α-1,6 bond synthesis over α-1,4 bond hydrolysis. We suggest that Lys108 is more important for helping to retain active-site conformation for substrate binding.

The Gly137→Ala mutation increased GA thermostability by strengthening the fourth α-helix and preventing catalytic domain from unfolding (Chen *et al.*, 1996). Even though Gly137 is not directly involved in catalysis or substrate binding, the strong stabilization of this helix by Ala residue substitution has made the conformational adjustment around the catalytic cavity disfavor α-1,6-linked substrate formation, especially at higher temperatures. This results in higher glucose yields for this mutant GA than for wild-type GA.

Introducing a long sequence into the active-site environment by 311-314 Loop GA increases the binding affinity for both α-1,4- and α-1,6-linked substrates because the conformational change may reduce the binding energies required to form the enzyme-substrate complex. This allows the substrate to progress into subsite 1 more easily while undergoing a slow unimolecular enzyme-substrate complex migration step. A "dead-end pocket" model of the GA active site was proposed based on X-ray structural studies, suggesting that water displacement from subsite 1, where a cluster of seven water molecules exists in the absence of substrate, is a crucial step in the GA catalytic mechanism (Aleshin *et al.*, 1994). The conformational change by the 311-314 Loop mutation may also help to accommodate the simultaneous transport of water molecules as the substrate enters in orproduct diffuses from subsite 1. Glucose release after hydrolysis, the proposed rate-limiting step for maltooligosaccharide hydrolysis (Kitahata *et al.*, 1981; Sierks and Svensson, 1996; Natarajan and Sierks, 1996), may be relatively easier and faster than from wild-type GA because of the bigger loop introduced around the active site, which may make iG_2 synthesis less likely.

Tyr312 was replaced by Trp to study the importance of the hydrogen-bond network in which it participates on the substrate affinity without destroying the network. The indole side chain of Trp is much bigger and stiffer than the Tyr side chain while both side chains are aromatic, so a Tyr312→Trp mutation is a good choice to make this hydrogen-bond network narrower and to form a stronger affinity with substrates. Tyr312→Trp GA had slightly higher ratios of initial rates of iG_2 formation to that of glucose formation (Table I), with peak glucose

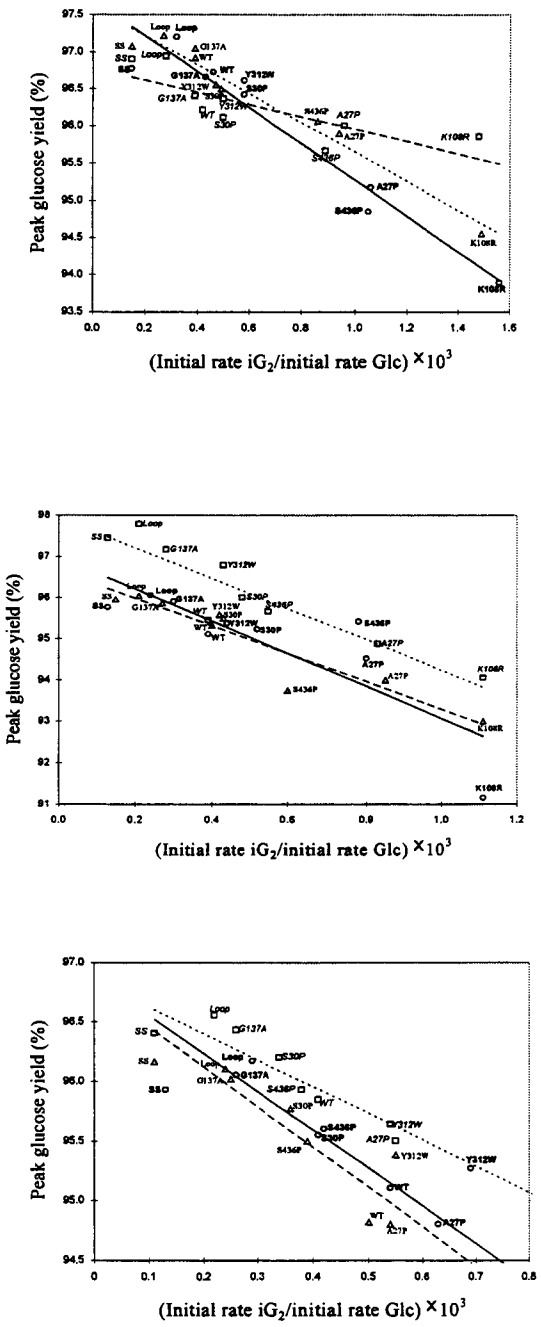

Figure 7. Peak glucose yield vs. (initial rate of iG_2 formation/initial rate of glucose formation) at 35°C (left), 45°C (middle), and 55°C (right) with 1.98 μM GA in 0.05 M NaOAc buffer , pH 4.4. DE 10 (○, ——), DE 18 (△, – –), and DE 25 (□, —— ——) maltodextrins.

yields about 0.5% lower, 0.4% higher, and 2% higher than wild-type GA at35, 45, and 55°C, respectively.

Ser436→Pro had a lower initial rate ratio for iG_2 formation over glucose formation than wild-type GA and had an increased glucose yield only at 55°C. The space-filling effect engendered by inserting the Pro rigid backbone into a random coil in a packing void of unknown function causes more hydrophobic interaction at higher tempera-tures, thus reducing the confor-mational en-tropy of unfolding. This entropy decrease helps GA to make a conformational adjust-ment favoring α-1,4-linked substrate.

The hypothesis that decreasing the ability of GA to synthesize iG_2 would increase the glucose yield was proved by Fang *et al.* (1997a,b). In this study, we have also proved this hypothesis at 35, 45 and 55°C with a different group of mutated GAs. Figure 7 demonstrates an inverse relationship between peak glucose yields and relative initial rate ratios for iG_2 formation over glucose formation.

In summary, we have successfully changed the substrate specificity to reduce iG_2 formation by the SS and 311-314 Loop mutations. We also have proved that conserved residue Lys108 is important in both catalytic mechanism and substrate specificity through the hydrogen-bond network with the substrate. The goal to form a narrower H-bond network through Tyr312→Trp GA has also been achieved here. SS GA is the best mutant GA so far constructed for both thermostability and substrate specificity.

ACKNOWLEDGEMENTS

This project was supported by the U. S. Department of Energy through the Consortium for Plant Biotechnology Research, Inc., by the U. S. Department of Agriculture through the Midwest Advanced Food Manufacturing Alliance, and by Genencor International, Inc.

REFERENCES

Aleshin, A. E. and Honzatko, R. B. (1995) Personal communication.
Aleshin, A., Golubev, A., Firsov, L. M. and Honzatko, R. B. (1992) *J. Biol. Chem.*, **267**, 19291-19298.
Aleshin, A. E., Firsov, L. M. and Honzatko, R. B. (1994) *J. Biol. Chem.*, **269**, 15631-15639.
Allen, M., Coutinho, P. M. and Ford, C. F. (1997) In preparation.
Chen, H.-M., Bakir, U., Ford, C. and Reilly, P. J. (1994a) *Biotechnol. Bioeng.*, **43**, 101-105.
Chen, H.-M., Ford, C. and Reilly, P. J. (1994b) *Biochem. J.*, **301**, 275-281.
Chen, H.-M., Ford, C. and Reilly, P. J. (1995) *Protein Eng.*, **8**, 575-582.
Chen, H.-M., Li, Y., Panda, T., Buehler, F. U., Ford, C. and Reilly, P. J. (1996) *Protein Eng.*, **9**, 499-505.
Coutinho, P. M. and Reilly, P. J. (1994a) *Protein Eng.*, 7, 393-400.
Coutinho, P. M. and Reilly, P. J. (1994b) *Protein Eng.*, 7, 749-760.
Coutinho, P. M. and Reilly, P. J. (1997) *Proteins*, accepted for publication.
Fang, T.-Y., Coutinho, P. M., Reilly, P. J. and Ford, C. (1997a) *Protein Eng.*, submitted for publication.
Fang, T.-Y., Honzatko, R. B., Reilly, P. J. and Ford, C. (1997b) *Protein Eng.*, submitted for publication.
Fierobe, H.-P., Stoffer, B. B., Frandsen, T. P. and Svensson, B. (1996) *Biochemistry*, **35**, 8696-8704.
Frandsen, T. P., Stoffer, B., Palcic, M. M., Hof, S. and Svensson, B. (1996) *J. Mol. Biol.*, **263**, 79-89.
Harris, E. M. S., Aleshin, A. E., Firsov, L. M. and Honzatko, R. B. (1993) *Biochemistry*, **32**, 1618-1626.
Hehre, E. J., Okada, G. and Genghof, D. S. (1969) *Arch. Biochem. Biophys.*, **135**, 74-89.
Hiromi, K., Takahashi, K. Hamauzu, Z., and Ono, S. (1966a) *J. Biochem.*, **59**, 469-475.
Hiromi, K., Kawai, M. and Ono, S. (1966b) *J. Biochem.*, **59**, 476-480.
Kitahata, S., Brewer, C. F., Genghof, D. S., Sawai, T. and Hehre, E. J. (1981) *J. Biol. Chem.*, **256**, 6017-6026.
Kunkel, T. A., Roberts, J. D. and Zakour, R. A. (1987) *Meth. Enzymol.*, **154**, 367-382.
Lee, D. D., Lee, Y. Y., Reilly, P. J., Collins, E. V., Jr. and Tsao, G. T. (1976) *Biotechnol. Bioeng.*, **18**, 253-267.
Li, Y., and Ford, C. F. (1997) In preparation..
Li, Y., Coutinho, P. M. and Ford, C. F. (1997) *Protein Eng.*, accepted for publication.
Matsumura, M., Yasumura, S. and Aiba, S. (1986) *Nature*, **323**, 356-358.
Meagher, M. M. and Reilly, P. J. (1989) *Biotechnol. Bioeng.*, **34**, 689-693.
Natarajan, S. and Sierks, M. R. (1996) *Biochemistry*, **35**, 3050-3058.
Nikolov, Z. L., Meagher, M. M. and Reilly, P. J. (1989) *Biotechnol. Bioeng.*, **34**, 694-704.
Nunberg, J. H., Meade, J. E., Cole, G., Lawyer, E. C., McCabe, P., Schweickart, V., Tal, R., Wittman, V. P., Flatgaard, J. E. and Innis, M. A. (1984) *Molec. Cell. Biol.*, **4**, 2306-2315.
Ohnishi, M. (1990) *Starch/Stärke*, **42**, 311-313.
Olsen, K., Christensen, U., Sierks, M. R. and Svensson, B. (1993) *Biochemistry*, **32**, 9686-9693.
Pazur, J. H. and Okada, S. (1967) *Carbohydr. Res.*, **4**, 371-379.
Pazur, J. H., Cepure, A., Okada, S. and Forsberg, L. S. (1977) *Carbohydr. Res.*, **58**, 193-202.
Rabbo, E. and Terkildsen, T. C. (1960) *Scand. J. Lab. Investig.*, **12**, 402-407.
Sierks, M. R. and Svensson, B. (1994) *Protein Eng.*, 7, 1479-1484.
Sierks, M. R. and Svensson, B. (1996) *Biochemistry*, **35**, 1865-1871.
Svensson, B., Larsen, K., Svendsen, I. and Boel, E. (1983) *Carlsberg Res. Commun.*, **48**, 529-544.
Svensson, B., Frandsen, T. P., Matsui, I., Juge, N., Fierobe, H.-P., Stoffer, B. and Rodenburg, K. W. (1995) *Carbohydrate Bioengineering*, Petersen, S. B., Svensson, B., and Pedersen, S., eds., Elsevier Science, Amsterdam, pp. 125-145.
Tanaka, A., and Takeda, S. (1994) *Biosci. Biotechnol. Bioeng.*, **58**, 1809-1813.
Wells, J. A. (1990) *Biochemistry*, **29**, 8509-8517.

New Fusion Protein Systems Designed to Increase Soluble Cytoplasmic Expression of Heterologous Proteins in *Escherichia coli*

Gregory D. Davis, Claude Elisee, Denton M. Newham, and Roger G. Harrison
School of Chemical Engineering and Materials Science
University of Oklahoma
Norman, OK 73019

ABSTRACT

We have developed fusion protein systems which have significantly increased the soluble expression levels of an insoluble heterologous protein in *Escherichia coli* at 37°C relative to those of the thioredoxin fusion protein system. Using human interleukin-3 as a model heterologous insoluble protein, three gene fusions were constructed that code for a native *E. coli* protein at the N-terminus and the insoluble protein at the C-terminus. The three native *E. coli* proteins, NusA, GrpE, and bacterioferritin (BFR), were chosen based on their favorable cytoplasmic solubility characteristics as predicted by a statistical solubility model for recombinant proteins in *E. coli* [Wilkinson, D.L. and R.G. Harrison. *Bio/Technology,* **9**: 443-448 (1991)]. Modeling predicted the probability of soluble fusion protein expression in the following order: NusA (most soluble), GrpE, BFR, and thioredoxin (least soluble). Expression experiments showed that NusA fusion protein was expressed almost completely in the soluble fraction. GrpE and BFR fusion proteins were partially soluble and thioredoxin fusion protein was expressed almost completely in the insoluble fraction. These results have a broad significance to the biotechnology field since insoluble heterologous protein expression in *E. coli* continues to be a pervasive problem. Also, these results represent an example of how statistical modeling can be used to design novel protein expression systems.

INTRODUCTION

A major benefit resulting from the advent of recombinant DNA technology has been the large scale production of proteins of medical or industrial importance. While production of heterologous proteins in bacterial hosts (e.g. *Escherichia coli*) has been implemented successfully in the biotechnology industry, limitations of bacterial expression systems pervasively prevent new proteins from being brought to the market. When high expression levels are achieved, recombinant proteins are frequently expressed in *E. coli* as insoluble protein aggregates termed "inclusion bodies". Although initial purification of inclusion body material by cell lysis and centrifugation is relatively simple, the protein must be subsequently refolded into active form which is typically a cumbersome trial and error process resulting in large losses of protein activity (1). In addition, once an extraction and refolding procedure has been

developed, it is scarcely practical on an industrial scale (2). In a detailed economic analysis of the production of heparinase I (3) it was determined that the production costs of soluble and insoluble heparinase I production were equal even when soluble expression levels were 23% lower than insoluble expression levels. Thus, it is much more desirable to maximize soluble heterologous protein expression whenever possible.

A common strategy to avoid inclusion body formation is to fuse the protein of interest (a.k.a. the target protein) to a protein known to possess high expression levels in *E. coli* (a.k.a. the carrier protein). The success of such a method depends largely upon the ability to predict the combined chemical characteristics of the two proteins as a fusion. This raises a very common biochemical question which is central to this study: how can protein structure and function be accurately predicted based upon amino acid sequence alone? The particular "structure and function" focus of this project is simply recombinant protein solubility in the *E. coli* cytoplasm during high level expression. The general hypothesis of this work is that if a carrier protein is highly soluble in the *E. coli* cytoplasm, it will allow a normally insoluble protein to be expressed in soluble form when both proteins are expressed together as a fusion.

MATERIALS AND METHODS

Statistical Modeling

A two parameter version of a statistical recombinant protein solubility model (4) was used as the basis for the selection proteins for this study. A custom C computer program was written and used to search all *E. coli* proteins contained in the SWISS-PROT protein databank. This program used as input a single text file created by and downloaded from the SWISS-PROT World Wide Web server (http://expasy.hcuge.ch) which contained approximately 3700 *E. coli* protein sequences. The program calculated the solubility of all sequences and tabulated those having a favorable solubility probability. NusA, GrpE, and BFR proteins were chosen for study from this analysis.

Materials

The Expand™ High Fidelity PCR System and T4 DNA Ligase were purchased from Boehringer Mannheim (Indianapolis, IN). Restriction enzymes for constructing expression vectors were purchased from New England BioLabs (Beverly, MA) and Promega Corporation (Madison, WI). Gene fragments were agarose gel purified prior to ligation according to the GeneClean protocol (BIO101, Vista, CA). Antibodies and rhIL-3 standards were purchased from R&D Systems (Minneapolis, MN). Chemiluminescent Western blot reagents and secondary antibodies were purchased from BioRad (Hercules, CA).

The genes for the NusA, GrpE, BFR, and hIL-3 proteins were kind gifts from Michelle Hanna (University of Oklahoma), Debbie Ang (University of Geneva), Simon Andrews (University of Sheffield), and Lambert Dorssers (Dr. Daniel den Hoed Cancer Center, Netherlands), respectively. Plasmid pTrx-2 containing the thioredoxin gene was purchased from ATCC (Rockville, MD).

Primers for the PCR amplification of gene fragments were manufactured by the Molecular Biology Resource Facility at the University of Oklahoma Health Sciences Center (Oklahoma City, OK). The sequencing of gene fusions was performed by the Recombinant DNA/Protein Resource Facility at Oklahoma State University (Stillwater, OK).

Construction of Expression Vectors

All gene fusions were constructed and expressed in plasmid pKK223-3 (Pharmacia Biotech, Piscataway, NJ). Site directed mutagenesis using the polymerase chain reaction (PCR) was used to amplify the genes of interest from plasmid templates and also introduce the appropriate restriction sites. The gene constructs consisted of an *Eco*RI site at the 5' end followed by the ATG start codon and the open reading frame of the carrier gene. An *Age*I was placed at the 3' end of the carrier gene, followed by an site Factor Xa coding sequence. The open reading frame of the target gene (hIL-3) was placed immediately down stream of the Factor Xa sequence. A *Hin*dIII site was placed at the 3' end of the target gene following the stop codon. A three fragment ligation reaction was performed using the target gene, the carrier gene, and the *Eco*RI/*Hin*dIII linearized pKK223-3. The ligation reaction was then transformed into *E. coli* JM105 and the colonies were screened by SDS-PAGE for overexpression of the fusion protein by a growth limitation method method (5).

Fusion Protein Expression and Fractionation

E. coli JM105 harboring pKK223-3 containing the fusion gene of interest was grown to mid-log phase (OD_{600} = 0.4) at 37°C in shake flasks. The *tac* promoter was induced by adding isopropyl-1-thio-β-D-galactopyranoside (IPTG) to a final concentration of 1 mM, and the cells were grown for an additional 3 h. The cells were harvested by centrifugation and were resuspended in a solution containing 50 mM NaCl and 1 mM EDTA at pH 8.0. The cells were lysed by sonication at 4°C for 30 sec at 90 W and then allowed to cool for 30 sec on ice. This cycle was repeated 4 times for a total sonication time of 2 min. The inclusion body material was then removed from the cell lysate by centrifugation at 12,000 x *g* for 30 min at 4°C.

SDS-PAGE, Western Blotting, and Protein Assays

The supernatant of the cell lysate containing water soluble proteins was lyophilized and resuspended in a volume of gel loading buffer to give a final concentration equivalent to the inclusion body fraction so that relative soluble/insoluble

protein concentrations in SDS-PAGE gels represent those in the original culture. Cell proteins were separated on 12% (w/v) polyacrylamide gels (6) and detected with Coomassie brilliant blue. Quantitative protein determination was made using ImageQuant densitometry software (Molecular Dynamics, Sunnyvale, CA) to read band intensities of Coomassie stained gels which were scanned in at a grayscale pixel density of 300 dpi on a Vista S-12 scanner (UMAX Technologies, Inc., Fremont, CA). Pixel values were normalized by selecting a rectangular area corresponding to the shape of the lane, and averaging the pixel values over the width of the rectangle. The averaged pixel values were then plotted versus the length of the lane, and the resulting peaks were integrated to determine the percent of total cell protein. Western blotting was performed according to the protocol of the ImmunStar Chemiluminescent Detection Kit (BioRad, Hercules, CA). Total protein measurements were done according to the BCA protein assay (Pierce, Rockford, IL). The hIL-3 cell proliferation assay was performed by Robert House (IIT Research Institute, Chicago, IL) according to the method of Kitamura et al (7).

RESULTS AND DISCUSSION

Solubility of various human interleukin-3 fusion proteins

Figure 1 shows a 12% SDS-PAGE of hIL-3 fusions with BFR, GrpE, NusA, and thioredoxin. It can be seen in the SDS-PAGE gel that NusA is the carrier protein which is able to produce the highest level of soluble fusion protein, however, it is difficult to determine relative amounts of hIL-3 since Coomassie blue binds non-selectively. The GrpE and BFR fusion proteins demonstrated a partial solubility, while thioredoxin shows almost complete insolubility. A corresponding western blot is shown in Figure 2. This blot indicates only the presence of hIL-3 in the fusion protein and it shows that NusA is able to produce the highest levels of hIL-3 compared to any of the other fusion proteins.

The solubility results were quantified by densitometry analysis of the western blot and are compared with the predicted solubility in Table 1. The predicted solubility of the proteins corresponds to the experimental solubility results shown in Figures 1 and 2 and also correlates with the molecular weight of the carrier protein relative to the target protein. Thus, the solubility model was successful in predicting recombinant protein solubility. The activity assay of the fusion proteins is shown in Table 2 and was performed on soluble crude cell lysates prior to fusion protein cleavage with Factor Xa. First, the amount of hIL-3 present was estimated by SDS-PAGE, densitometry, and a BCA total protein assay. These estimates were then compared to a TF-1 cell proliferation assay to determine the percent native activity of each fusion protein. hIL-3 activity was found in all fusion proteins, with the highest level of native activity found in the NusA/hIL-3 fusion protein. Reductions in native activity maybe attributed to interferences of the carrier protein with the receptor binding domains of hIL-3, thus, the low activities of the BFR and GrpE fusions should

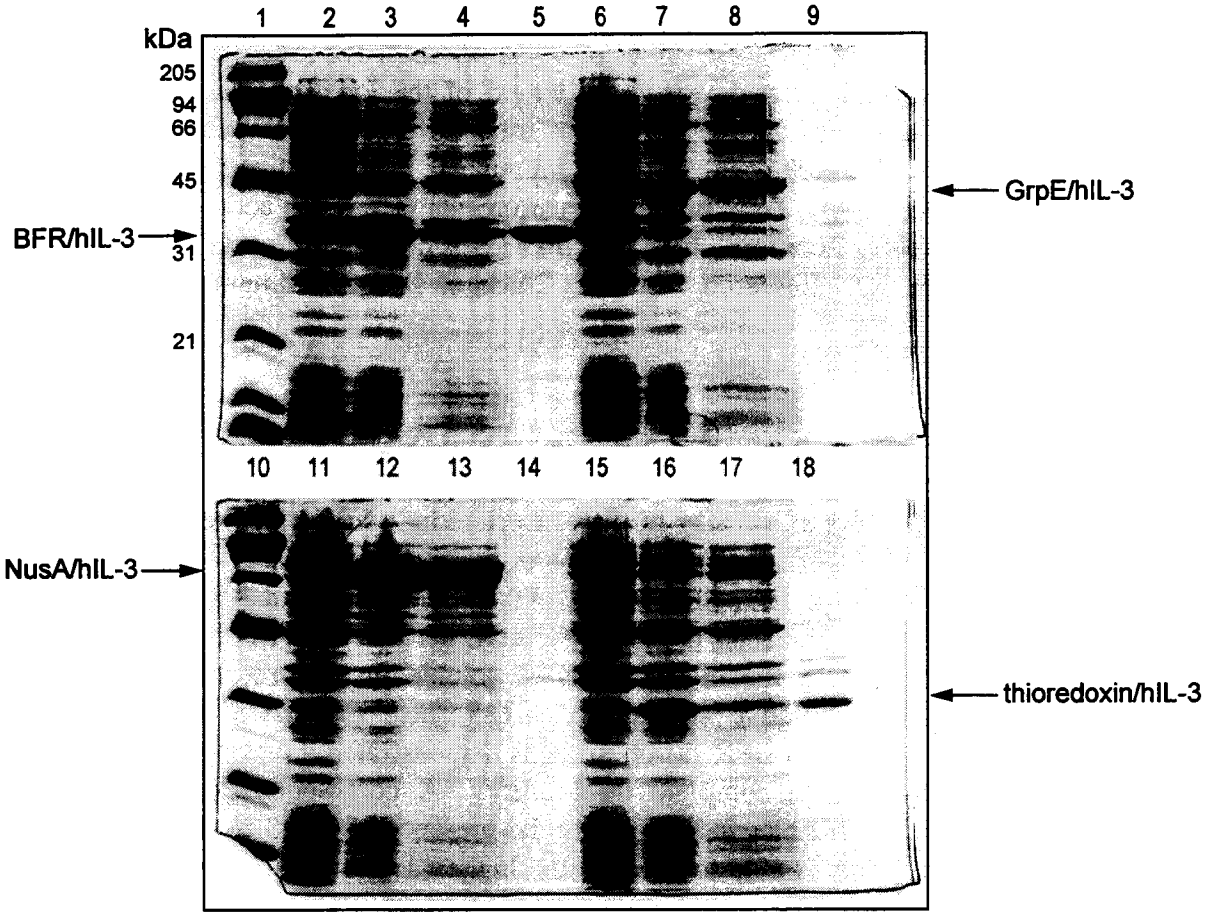

Figure 1. SDS-PAGE of Soluble and Insoluble Fusion Proteins. Lane 1, marker; Lane 2, BFR/hIL-3 uninduced; Lane 3, BFR/hIL-3 induced; Lane 4, BFR/hIL-3 soluble fraction; Lane 5, BFR/hIL-3 insoluble fraction; Lane 6, GrpE/hIL-3 uninduced; Lane 7, GrpE/hIL-3 induced; Lane 8, GrpE/hIL-3 soluble fraction; Lane 9, GrpE/hIL-3 insoluble fraction; Lane 10, marker; Lane 11, NusA/hIL-3 uninduced; Lane 12, NusA/hIL-3 induced; Lane 13 NusA/hIL-3 soluble fraction; Lane 14, NusA/hIL-3 insoluble fraction; Lane 15, thioredoxin/hIL-3 uninduced; Lane 16, thioredoxin/hIL-3 induced; Lane 17, thioredoxin/hIL-3 soluble fraction; Lane 18, thioredoxin/hIL-3 insoluble fraction. Fusion proteins were expressed from plasmid pKK223-3 under control of the *tac* promoter in *E. coli* JM105 at 37°C. Cells were induced with 1 mM IPTG.

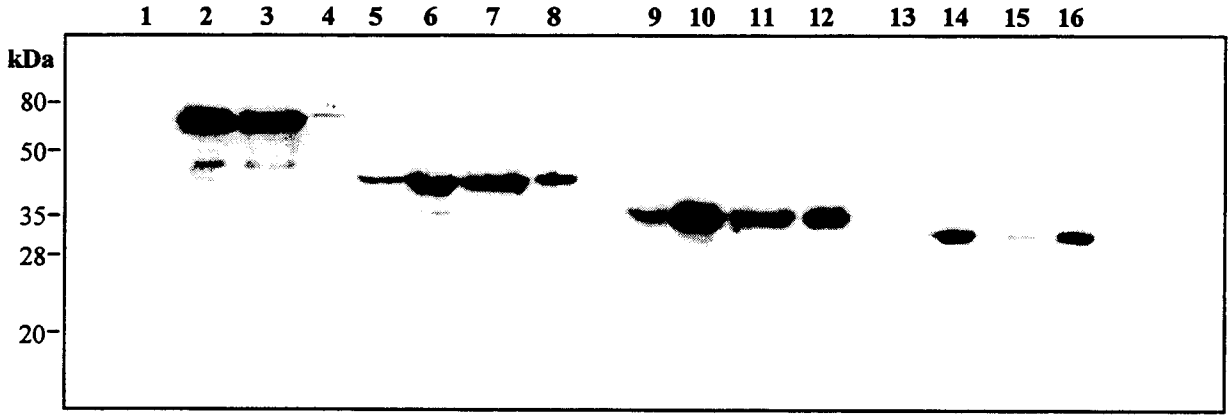

Figure 2. Western Blot of NusA, GrpE, BFR, and thioredoxin fusion proteins containing hIL-3. Lanes 1-4, NusA/hIL-3 uninduced, induced, soluble fraction, insoluble fraction respectively. Lanes 5-8, GrpE/hIL-3 uninduced, induced, soluble fraction, insoluble fraction respectively. Lanes 9-12, BFR/hIL-3 uninduced, induced, soluble fraction, insoluble fraction respectively. Lanes 13-16, thioredoxin/hIL-3 uninduced, induced, soluble fraction, insoluble fraction respectively. Fusion proteins were expressed from plasmid pKK223-3 under control of the *tac* promoter in *E. coli* JM105 at 37°C. Cells were induced with 1 mM IPTG and grown for 3 h post-induction. The blot was probed with mouse anti-hIL-3 monoclonal antibody and visualized using chemiluminescence.

Fusion Protein	MW (kDa)	% Soluble at 37°C	Predicted Solubility Probability (%)
NusA/hIL-3	71	97	84
GrpE/hIL-3	37	71	67
BFR/hIL-3	34	47	66
Thio/hIL-3	27	8	58

Table 1. Experimental and predicted solubility of various human interleukin-3 fusion proteins. The percent of soluble protein at 37°C was determined by densitometry analysis of the soluble and insoluble lanes of the western blot in Figure 2.

Fusion Protein	hIL-3 est. by SDS-PAGE/BCA (μg/ml)	hIL-3 Activity Assay (μg/ml)	Percent Native Activity
NusA/hIL-3	7.5	5.0	67
GrpE/hIL-3	5.2	0.3	6
BFR/hIL-3	8.7	1.0	12
thio/hIL-3	7.5	3.6	48

Table 2. Activity Assay of Human Interleukin-3. Fusion proteins from soluble crude cell lysates were assayed by SDS-PAGE, densitometry, and a BCA total protein assay to determine the total amount of hIL-3 present. The percent of hIL-3 which is active was determined by comparing the SDS-PAGE results to data from a TF-1 cell proliferation assay. NusA and GrpE fusion proteins were expressed at 37°C while the BFR and thioredoxin fusion proteins were expressed at 23°C to ensure ample protein for activity determination.

not rule out the possibility of their implementation as solubilizing proteins. One major advantage of the BFR protein is that it exhibits a characteristic red color due to its iron binding properties. The red color is most visible in the centrifuged pellet of cells overexpressing BFR and could serve as a useful marker during cloning procedures performed when constructing BFR fusion genes for soluble protein production.

CONCLUSIONS

It has been determined in this study that *E. coli* NusA has an exceptional potential for solubilizing heterologous proteins at 37°C. This could have a broad impact on the biotechnology industry since bacterial expression systems have many economic advantages over mammalian expression systems in terms of higher yields, lower process costs, and simplicity of culturing techniques. Using NusA as a fusion partner with hIL-3 and other target proteins may eliminate the need the reduce fermentation temperatures from 37°C during protein expression, thus eliminating a heat transfer step in protein production and ensuring a maximum growth rate for *E. coli*.

This study also demonstrates that recombinant protein solubility in *E. coli* can be reasonably predicted based on the statistical analysis of amino acid content. Each of the proteins chosen for study (NusA, GrpE, and BFR) were able to produce high levels of soluble protein when fused with hIL-3, a result consistent with modeling predictions. These results merit further investigation of *E. coli* proteins using the statistical protein solubility model in conjunction with other methods (catalysis of disulfide bonding, refolding by heat shock systems etc.) that increase levels of active heterologous protein production in *E. coli*. In addition, highly soluble proteins with novel purification properties should also be investigated.

ACKNOWLEDGMENTS

We would like to thank Daniel Riggs and David McCarthy at the University of Oklahoma Department of Botany and Microbiology for their helpful advice in developing cloning and screening procedures for vector constructions. The TF-1 Cell proliferation assay was graciously performed by Robert House at the IIT Research Institute in Chicago, Illinois. This work was funded by the National Science Foundation (Grant No. CTS-9502235)

REFERENCES

1. **Sharma, S.K.; Evans, D.B.; Tomich, C.C.; Cornette, J.C. and R.G. Ulrich.** 1987. Folding and Activation of Recombinant Human Prorenin. *Biotechnology and Applied Biochemistry.* **9**: 181-193.

2. **Datar R.V., Cartwright T., Rosen C.G.** 1993. Process economics of animal cell and bacterial fermentations: a case study analysis of tissue plasminogen activator. *Bio/Technology.* **11:** 349-357.

3. **Ernst, S. Garro, O.A., Winkler, S., Venkataraman, G., Langer, R., Cooney, C.L. and R. Sasisekharan.** 1997. Process simulation for recombinant protein production: cost estimation and sensitivity analysis for heparinase I expressed in *Escherichia coli. Biotechnology and Bioengineering.* **53**: 575-582.

4. **Wilkinson, D.L. and R.G. Harrison.** 1991. Predicting the solubility of recombinant proteins in *Escherichia coli. Bio/Technology.* **9**: 443-448.

5. **Davis, G.D. and R.G. Harrison.** 1998. Rapid screening of fusion protein recombinants by measuring effects of protein overexpression on cell growth. *BioTechniques.* In press for Feb. 1998 issue.

6. **Laemmli, U.K.** 1970. Cleavage of structural proteins during the assembly of the head of bacteriophage T4. *Nature.* **227:** 680-685.

7. **Kitamura, T., Tange, T., Terasawa, T., Chiba, S., Kuwaki, T., Miyagawa, K., Piao, Y., Miyazono, K., Urabe, A. and F. Takaku.** 1989. Establishment and characterization of a unique human cell line that proliferates dependently on GM-SCF, IL-3, and erythropoietin. *Journal of Cellular Physiology.* **140**: 323-334.

Maximizing Protein Synthesis in High Cell Density Perfusion Bioreactors

Frank W.F. Lee, Stephanie Bryant, Paul Todd, and Dhinakar Kompala
Department of Chemical Engineering
University of Colorado
Boulder, CO 80309-0424

ABSTRACT

A new recombinant Chinese hamster ovary (CHO) cell line (2GAR24) has been cloned by the stable transfection with a newly constructed expression vector (pAβGneoR) and under a selection pressure of 400 μg/ml G418 sulfate. Plasmid pAβGneoR contains the bacterial β-galactosidase gene (*lacZ*) which is controlled by the adenovirus major late promoter (AMLP), and a selection gene (*neo*^{r}), which can resist the neomycin analog G418 sulfate. The AMLP, which has been characterized as G1-phase specific, is expected to yield a non-growth-associated product formation pattern based on a cell-cycle model. This non-growth-associated product formation pattern is ideal for the high cell density bioreactor operation (e.g., fed-batch and perfusion cultures). In this study, most of intracellular protein production (β-galactosidase) in sequential batch cultures from this new CHO cell line occurred between the late lag phase and very early exponential phase. After the maximum production, the internal protein content dropped during the rest of exponential phase. This preliminary result has indirectly indicated the non-growth-associated product formation pattern.

INTRODUCTION

Protein synthesis in mammalian cells can be observed in two strikingly different patterns. (1) The production of monoclonal antibodies in murine hybridoma cultures is typically non-growth-associated, which shows an inverse relationship between the specific antibody production rate versus the specific cell growth rate (Miller *et al.* 1988, Batt *et al.* 1990, Suzuki and Ollis 1990). With this inverse relationship, the specific production rate of monoclonal antibodies has been easily maximized by culturing hybridoma cells at very low growth rates in high cell density fed-batch or perfusion bioreactors. (2) The production of most glycoproteins in recombinant mammalian cell cultures is found to be growth-associated, which a linear relationship between the specific antibody production rate versus the specific cell growth rate (Robinson and Memmert 1991). Applying the same bioreactor techniques to recombinant mammalian cell cultures results in drastically reduced production rates due to their growth-associated production. Optimization of such growth associated production requires high cell growth conditions, such as in repeated batch cultures or chemostat cultures. Unfortunately, the growth-associated production pattern requires maximization of cell mass production to accomplish our real goal of maximizing the product formation.

A cell-cycle model (Gu *et al.* 1994) predicts that the growth-associated pattern is obtained from S-phase specific production; the non-growth-associated pattern is obtained from the control of G1-phase specific production. There are some previous studies on cell-cycle-phase-dependent gene expression (Mariani et al. 1981, Kubbies and Stockinger 1990, Gu *et al.* 1993). After comparing the results among these published works, we hypothesized that the promoters might play the important role in the cell-cycle-phase-dependent gene expression. Our recent research has shown that this

growth-associated production in recombinant CHO cells is related to the S-phase specific production from the Simian virus (SV40) early promoter commonly used for driving the foreign gene expression (Banik *et al.* 1996, 1997). Using two stably transfected CHO cell lines, one producing a secreted glycoprotein, human β-interferon (Banik *et al.* 1997), and the other producing an intracellular reporter protein, β-galactosidase (Banik et al. 1996), under the control of the SV40 promoter, we have shown in continuous cultures that the product formation is strongly growth-associated. We have now replaced this S-phase promoter in newly constructed expression vectors with the adenovirus major late promoter (AMLP), which has been characterized to be G1-phase specific (Kubbies and Stockinger 1990) and expected to yield non-growth-associated product formation patterns based on the same cell-cycle model. Most of protein production in sequential batch cultures from this new CHO cell line occurred between the late lag phase and very early exponential phase. These preliminary results have indirectly indicated non-growth-associated product formation patterns.

MATERIALS AND METHODS

Plasmid Construction: Plasmid pADβ (obtained from Clontech, Palo Alto, CA) has the adenovirus major late promoter (AMLP) driving the synthesis of β-galactosidase from the recombinant bacterial *lacZ* gene. Plasmid pMAMneo (also from Clontech, Palo Alto, CA) contains the bacterial neomycin resistance gene, *neo*^{r}, driven by the simian virus (SV40) early promoter; this selection cassette was isolated by the restriction digestion with *Bam*HI and a 2.7 kb fragment was obtained in agarose electrophoresis gel. In order to simply select the CHO cells transfected with the expression vector, this 2.7 kb *neo*^{r} selection cassette was inserted at the unique *Sal*I site of plasmid pADβ after the modification of *Bam*HI ends to *Sal*I ends in the plasmid Sac-KISS-λ (Tsang *et al.* 1996). The transcription direction of the *neo* selection cassette is in reverse to that of the AMLP-driving *lacZ* gene to prevent the gene instability from the homologous recombination between two SV40 terminator sequences in the final construct. The final expression vector was designated as plasmid pAβGneoR. A schematic diagram of molecular cloning procedure is shown in Figure 1.

Cell Lines: Host cell line CHO-202 (obtained from Dr. W.E.C. Bradley, Institut du Cancer de Montreal) was stably transfected with plasmid pAβGneoR with lipofectin from Life Technologies (Grand Island, NY). The transfected cells were maintained under the selection pressure in neomycin analog, G418 sulfate at 400 μg/ml to prevent the growth of plasmid free cells. The transfected cells were then cloned and a high producing cell line (2GAR24) was isolated and used in all the experiments discussed below. Cell line 2GAR24 was cultivated for 10 weeks under the selection pressure to ensure stable transfection, before all the experiments reported here.

Medium and Supplements: The 2GAR24 cell line was cultured in serum-free IS-CHO medium from Irvine Scientific (Santa Ana, CA). The medium contains 8 g/l glucose and 8 mM glutamine. Antibiotics (penicillin G sodium and streptomycin sulfate both at 1000 units/ml) and antimycotic (amphotecirin B at 25 μg/ml) were added to the medium. Medium was also supplemented with G418 sulfate (Life Technologies, Grand Island, NY) at 400 μg/ml for selection pressure.

Cell Culture and Analytical Measurement: The recombinant 2GAR24 cells were adapted for growth in suspension culture, and all data shown below were obtained during cell growth in suspension culture. Batch suspension culture studies were conducted in 100 ml spinner flasks which were seeded with a cell density of 1-2 x 10^5 cells/ml. The spinner flasks were incubated at 36.5 °C in a water-jacketed incubator with CO_2 concentration maintained at 5%.

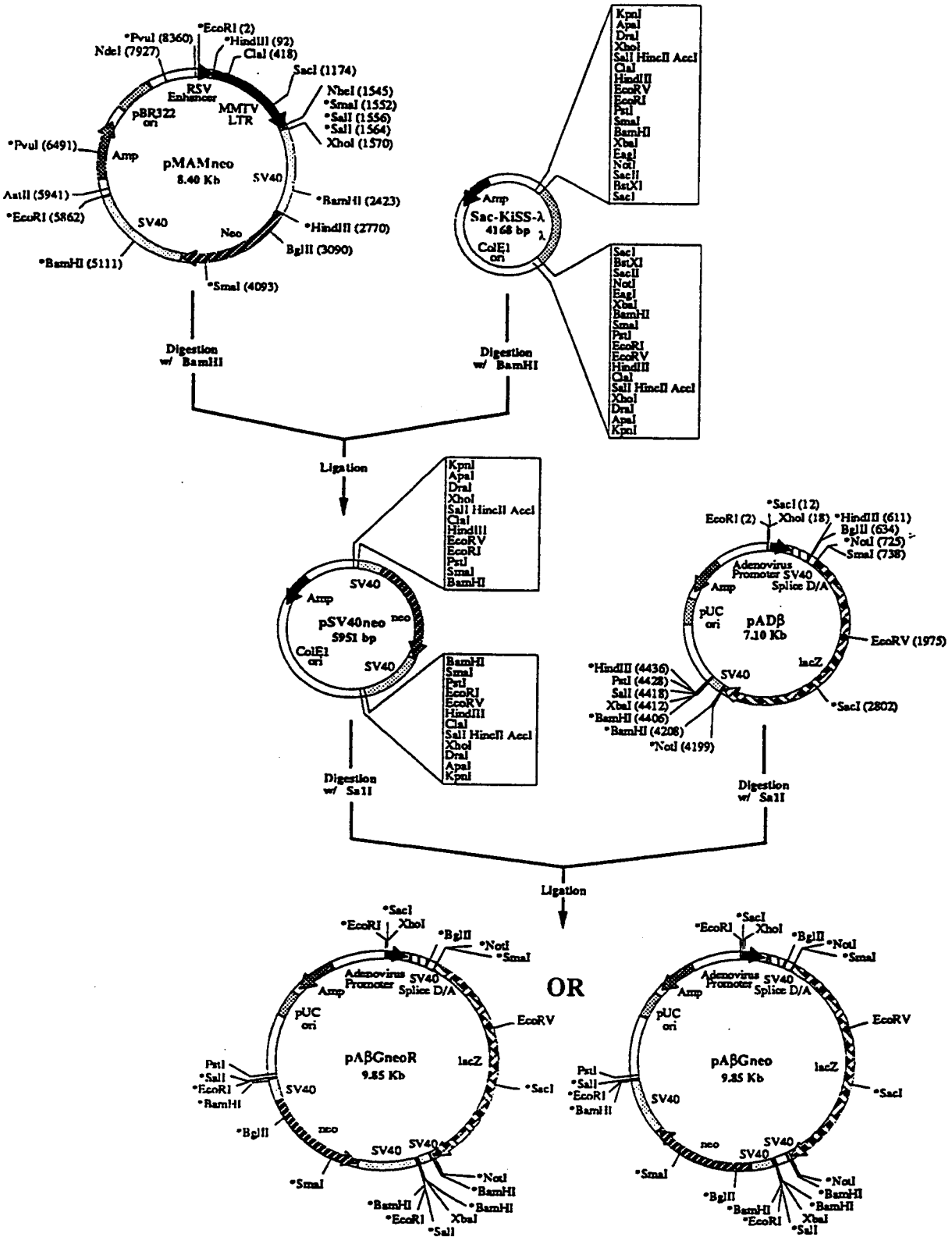

Figure 1. Schematic diagram of the molecular cloning work for the construction of plasmid pAβGneoR.

The viable cell density and the percentage of viable cells were determined by using a haemocytometer to count the cells after the cells were treated with 0.25% trypsin (Life Technologies, Grand Island, NY) for 15 minutes at 37 °C and then were stained with trypan blue (Life Technologies, Grand Island, NY). The incubation in trypsin before counting did not result in any decrease in cell viability.

The level of intracellular reporter protein (β-galactosidase) was measured using an assay with o-nitrophenyl-β-galactopyranoside (ONPG), which is hydrolyzed by β-galactosidase to yield a yellow colored product. At every sampling time, 1 ml of cell suspension culture was withdrawn from spinner flasks and centrifuged. The cell pellet was then re-suspended into 0.5 ml of phosphate buffered saline (PBS) and sonicated in an ice-water bath for 120 seconds at 50% duty cycle (Heat Systems-Ultrasonics, Inc., Model W-380). 1.3 ml freshly prepared Z buffer (0.06M Na_2HPO_4, 0.04M NaH_2PO_4, 0.01m KCl, 0.01M $MgSO_4$, 0.54% v/v β-mercaptoethanol, pH 7.0) and the cell lysate solution were added to 0.2 ml of 0.4% w/v ONPG solution. The absorbance of the reaction was measured as a function of time at 28 °C using a programmable spectrophotometer (Beckman, CA, Model DU50) at 420 nm. Because the reaction rate is zero order when ONPG is in excess, the activity of β-galactosidase is proportional to the slope of the product accumulation curve. In order to determine the concentration of β-galactosidase in the samples, a standard solution of β-galactosidase was also assayed in the procedure. The concentration of β-galactosidase in the sample was calculated by comparing the slope between the standard and the sample.

RESULTS AND DISCUSSION

Figure 2 shows the cell growth curve for the 2GAR24 cell line in two sequential batch suspension cultures seeded at a cell density of ca. 2×10^5 cells/ml. For most part of the batch culture, the percentage of viable cells is greater than 92%. The maximum specific growth rate of the cells occurs in the 24-48 hr period in each batch culture when the cells are in the mid-exponential growth phase (Figure 2a). The volumetric β-galactosidase concentration continues to increase when the live cell densities increase and reach the maximum when the cells enter the stationary growth phase (Figure 2b). However, the specific intracellular β-galactosidase content (Figure 2c) increases very significantly when the cells are in the lag phase (without the cell growth) and the early exponential phase (with the initiation of the cell growth) and is maximum at 24 hr when the cells enter the early exponential phase. After reaching the peak, the specific intracellular β-galactosidase content drops slightly, and is maintained relatively constant during the balanced growth phase, although the volumetric β-galactosidase concentration continues to increase due to the increase in cell number. In the late exponential phase, as the cell growth rate slows down, the synthesis of β-galactosidase (as seen in its volumetric concentration , Figure 2b) also slows down, resulting in a markedly decrease in the specific intracellular β-galactosidase content. These reproducible results(observed in at least 5 sequential batch cultures, two of which are shown in Figure 2) may be interpreted more quantitatively with a dynamic balance equation for the intarcellular reporter protein:

$$\frac{dP}{dt} = \alpha - \mu P - \beta P \qquad (1)$$

where P is the intracellular product content (mg/10^6 cells), α is the synthesis rate (mg/10^6 cells/day), μ is the specific growth rate (1/day), and β is the degradation rate (1/day).

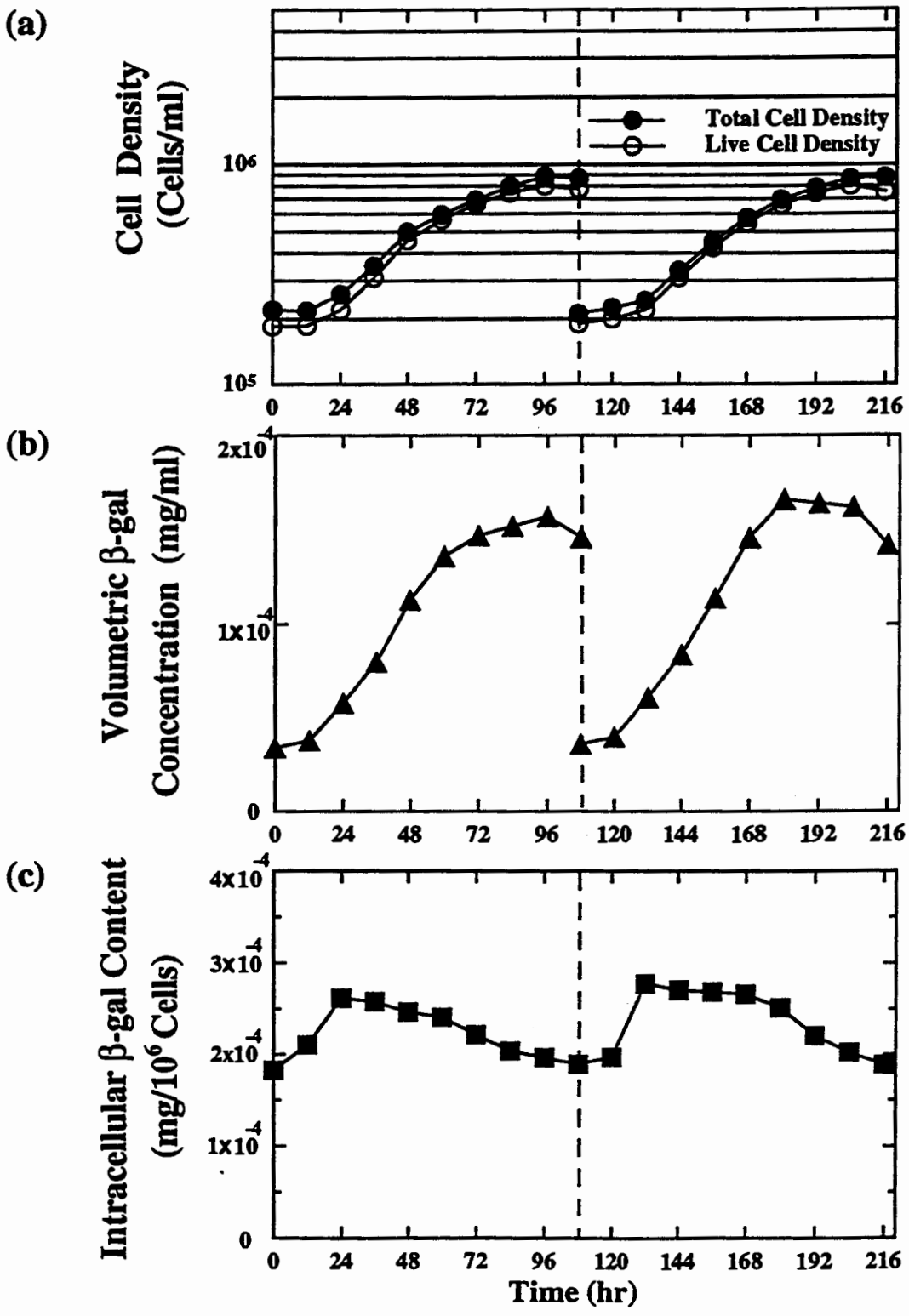

Figure 2. Time course of (a) total cell density (cells/ml) and viable cell density (cells/ml), (b) the volumetric β-galactosidase concentration (mg/ml), and (c) the specific intracellular β-galactosidase content (mg/10^6 cells) during two sequential suspension batch cultures.

There are three possible terms in the dynamic balance equation for the specific intracellular β-galactosidase content, P (mg/10^6 cells) (shown as Equation 1). The first term is the specific (per cell) synthesis rate, α (mg/10^6 cells/day), which changes systematically during the different phases of batch culture. The second term (μP) is the dilution of intracellular protein due to the cell growth. The last term (βP) represents a possible degradation rate inside the cells. The maximum increase in specific intracellular β-galactosidase content occurs in the cells with no or low growth (during the lag and early exponential phases). During these zero and low growth phases, the second and third terms representing the growth dilution and degradation terms are much smaller than the synthesis rate, causing the sharp increase in the intracellular β-galactosidase content. As the cells enter the exponential phase (24 - 60 hours, 132 - 168 hours), the intracellular protein content drops slightly and reaches a plateau as the growth dilution term becomes larger and the synthesis rate becomes smaller. The specific synthesis rate, α, of the intracellular β-galactosidase calculated from these data and equation, assuming negligible degradation rate till the late exponential phase, follows a reproducible pattern of high synthesis rate during the low growth rates in the initial lag and early exponential growth phases, and decreasing synthesis rates as the cells grow in the exponential growth phase. These results suggest that the synthesis of β-galactosidase under the influence of the G1 phase specific AML promoter in a single cell is non-growth-associated.

The previous results from our laboratory (Banik et al. 1996, 1997) showed that the synthesis of β-galactosidase under the influence of the S phase specific SV40 promoter in a single cell is strongly growth-associated; the specific intracellular β-galactosidase content increased very rapidly as the cells entered the exponential phase of growth (Banik *et al.* 1996). This growth-associated production is not the ideal for the high cell density bioreactors (e.g., perfusion and fed-batch cultures); it was verified for both intracellular protein (β-galactosidase, Banik *et al.* 1996) and secretory protein (human interferon, Banik *et al.* 1997). However, the non-growth-associated production under the control of the AML promoter is expected to be much more suitable for the high cell density bioreactors to optimize the protein production.

SUMMARY

The result from this study has the implication on foreign protein production from the G1 phase specific adenovirus major late (AML) promoter in high cell density bioreactor operation (such as fed-batch and perfusion culture) of recombinant Chinese hamster ovary (CHO) cells. We found the G1 phase specific AML promoter leads to the non-growth-associated production of proteins from the downstream structural genes (higher protein production at the reduced growth rates). Because the specific growth rates in high cell density fed-batch and perfusion cultures are very low, the non-growth-associated production will be preferred for the optimization of heterologous protein production in such systems.

ACKNOWLEDGEMENTS

This research was funded by NSF grant #BES-95048840. We thank Irvine Scientific, CA for the donation of serum-free IS-CHO medium. The CHO-202 cell line was a gift from Dr. W.E.C. Bradley, Institut du Cancer de Montreal. The plasmid Sac-KISS-λ was obtained from Dr. Tom C. Tsang at Arizona Cancer Center.

REFERENCES

Banik, G.G.; Todd, P. and Kompala, D.S. "Synthesis of a Secreted Glycoprotein (β-interferon) from SV40 Early Promoter in Continuous Cultures of Recombinant CHO Cells", Biotech. Bioeng. (1997), in press.

Banik, G.G.; Todd, P. and Kompala, D.S. "Foreign Gene Expression from S Phase Specific Promoters in Continuous Cultures of Recombinant CHO Cells", Cytotechnol. (1996) 22: 179-184.

Batt, B.C.; Davis, R.H. and Kompala, D.S. "Inclined Sedimentation for Selective Retention of Viable Hybridomas in A Continuous Suspension Bioreactor", Biotechnol. Prog. (1990) 6: 458-464.

Gu, M.B.; Todd, P. and Kompala, D.S. "Analysis of Foreign Protein Overproduction in Recombinant CHO Cells: Effect of Growth Kinetics and Cell Cycle Traverse", Ann. of New York Acad. Sci. (Recombinant DNA Technology II) (1994) 721: 194-207.

Gu, M.B.; Todd, P. and Kompala, D.S. "Foreign Gene Expression (β-galactosidase) during the Cell Cycle Phases in Recombinant CHO Cells", Biotech. Bioeng. (1993) 42: 1113-1123.

Kubbies, H. and Stockinger, H. "Cell Cycle Dependent DHFR and t-PA production in cotransfected, MTX Amplified CHO Cells Revealed by Dual Laser Flow Cytometer", Exptl. Cell Res. (1990) 188: 267-271

Mariani, B.D.; Slate, D.L. and Schimke, R.T. "S Phase-Specific Synthesis of Dihydrofolate Reductase in Chinese Hamster Ovary Cells", Proceeding of National Academy of Sciences, USA (1981) 78: 4985-4989.

Miller, W.M.; Blanch, H.W. and Wilke, C.R. "A Kinetic Analysis of Hybridoma Growth and Metabolism in Batch and Continuous Suspension Culture: Effect of Nutrient Concentration, Dilution Rate, and pH", Biotech. Bioeng. (1988) 32: 947-965.

Robinson, D.K. and Memmert, K.W. "Kinetics of Recombinant Immunoglobulin Production by Mammalian Cells in Continuous Culture.", Biotech. Bioeng (1991) 38: 972-976.

Suzuki, E. and Ollis, D.F. "Enhanced Antibody Production at Slowed Growth Rate: Experimental Determination and a Simple Structural Model ", Biotech. Bioeng. (1990) 6: 231-236.

Tsang, T.C.; Harris, D.T.; Akporiaye, E.T.; Schulter, S.F.; Bowden, G. T. and Hersh, E.M. "Simple Method for Adapting DNA Fragments and PCR Products to All of the Commonly Used Restriction Sites", Biotechniques (1996) 20: 51-52.

Identification of Different Phases in a Fermentation Using Neural Networks

Laurent Simon, M. Nazmul Karim, and Amanda Schreiweis
Department of Chemical & Bioresource Engineering
Colorado State University
Fort Collins, CO 80523

ABSTRACT

This research focuses on the development of a Neural Network to identify different phases in the growth cycle for a batch cultivation. The species used in the study was a recombinant strain of *Bacillus subtilis*.

The first part of this work illustrates how one can improve the performance of a Neural Network by increasing the input vector. The classification of the 4 phases of the growth cycle using multi-layer perceptrons (MPL) is presented. The age and optical density of the cell were initially fed into the Neural Network as input variables. The desired output was a 4-dimensional Boolean vector representative of the 4 major phases. The training set consisted of data generated by growing a strain *B. subtilis* DB486 for approximately 20 hours in 250 ml optimized media. Upon recall, a lag of about 2 1/2 hours was clearly established followed by an exponential, stationary, and six-hour death phase. Tested on 3 distinct growth cycles, the network classified about 78 % of the input patterns.

The network performance was greatly enhanced by the addition of the first and second derivatives of the optical density. The new architecture was then coupled to a Jordan network with locally recurrent processing elements (PE) in order to forecast the state of the fermentation based on data collected during the first 5 hours. Although the cell concentrations were slightly underestimated, this hybrid network was able to predict the cells' behavior for the next 6 hours.

INTRODUCTION

This case study deals with one of the major applications of Neural Network in biochemical engineering, phase classification in a fermentation process. A microorganism inoculated into a sterilized medium undergoes 4 major phases of growth. These include a lag or induction phase, an exponential or growth phase, a stationary and a death phase. In the lag phase, cell division does not occur. The length of the lag phase is mostly attributed to the type and age of the microorganism, the size of the inoculum, and culture parameters such as temperature and nutrient concentration (1). In the exponential phase, the cell number follows an exponential trend as division takes place. The growth rate increases with the cell number density. Lack of nutrients and overpopulation push the microorganism into a stationary phase where no further increase in cell density is to be expected. This stage is followed by a decrease in the number of viable cells as a result of toxic waste buildup and depletion of nutrients.

Growth-phase classification is very important in biochemical engineering for control or optimization purposes. Primary metabolites are usually produced in the exponential phase. They are growth-related products that can be modeled using material balances around the reactor. In order to write a control algorithm for the fermentation, a process engineer needs to distinguish among the different phases since they show different patterns. On the other hand, secondary metabolites are generated as the cells enter the stationary phase. Consequently, it becomes crucial to know the growth phase in case particular inducers have to be added to the media.

For scale-up purposes, the cells should be harvested while they are in the exponential phase. Failure to transfer while the cells are in the log phase can compromise growth. It is well documented that the physiological age of the inoculum has a great impact on the duration of the lag phase (2).

To classify the different phases of the growth cycle, a Neural Network was constructed. Neural Networks have become important computational tools in areas such as product design and formulation, process monitoring and diagnosis (3). They are also used in bioprocess state estimations (4). Their applications range from speech recognition to prediction of the stock market. They are widely used because of their ability to relate an array of phenomena and observations that can not be translated into equations. The user of Neural Networks aims at associating a set of input patterns to corresponding output patterns. Such a mapping can be accomplished once the network has learned previous patterns.

The Neural Network architecture is very similar to what is commonly perceived to take place in the brain. Input variables are initially fed to the network (Figure 1). They are then passed to layers that are made up of artificial neurons. These artificial neurons, also called processing elements, constitute the backbones of the Neural Network. They linearly combine

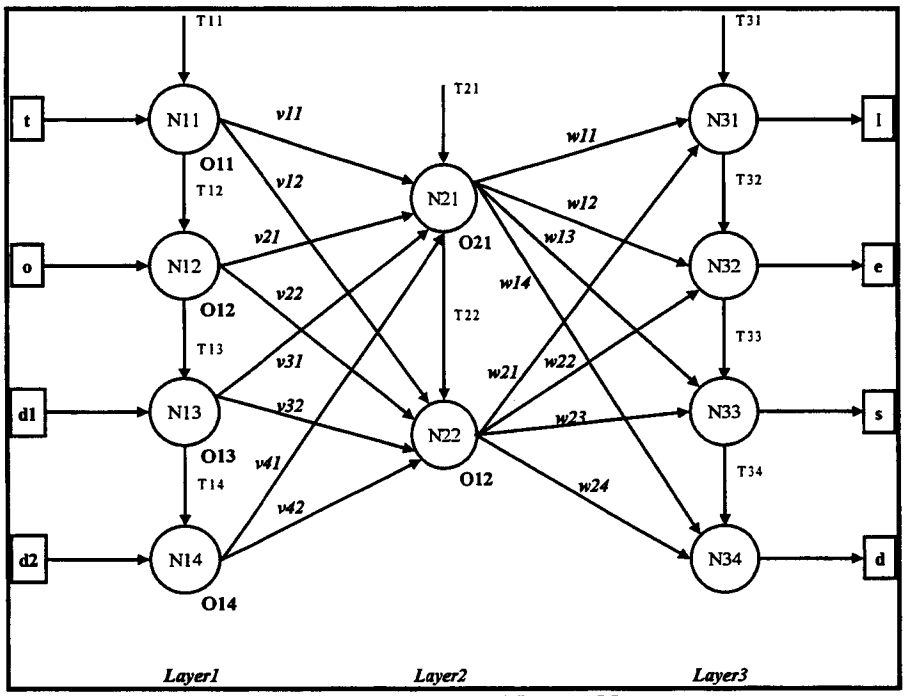

Figure 1. A three-layer Neural Network

the input patterns using weight factors such as w1i, and w2i and then compute the total activation by subtracting an internal threshold Ti. A transfer function is then used to relate the total activation to the output of the neuron. An output layer stores the results yi of the network, which are compared to target values and the errors are fed back into the network. The weights are updated according to a learning algorithm. The procedure is repeated until the desired values are reached.

The development of a Neural Network requires a training set made up of known input and output patterns. The network tries to learn the underlying relation based on the given examples. It is then exposed in the recall phase to inputs already seen. This stage is very important because one has a chance to improve the performance of the network and test different topologies. The final step is the crucial testing phase during which the network is fed new data.

In a recent study, growth-phase classification was done using Neural Networks and 2-dimensional input vectors whose components are the time and the cell density (3). Time was introduced as an input variable in order to distinguish between the induction and stationary phases. However, the death phase was not included in the training process. Misclassification was a major concern since the transition regions between phases are not well defined.

RESEARCH METHODOLOGY

To alleviate problems related to misclassifications and long training time, the following approach was followed. Inputs were added to the network that captured different trends in the growth cycle. In addition to the time and optical cell density, the first and second derivatives of the optical density were also used. The first derivative, which is the slope of the growth curve, sheds light on the lag and stationary phases. A zero slope is indicative of a stationary or induction phase. The second derivative represents changes in the slope of the curve. It underlines a change in cells' behavior as they approach the stationary phase.

The lag phase was calculated using the Monod method (5). For consistency, the instantaneous change in optical density at the end of the lag phase was used to estimate the length of the stationary phase. In other words, if the cells left the lag phase when the change in cell density was only 0.001, a slope of 0.001 was also used as an upper limit for the stationary phase. The 4 phases were then translated into Boolean vectors and served as outputs to the network in the training and testing stages. The induction, log, stationary and death phases were respectively replaced by the vectors [1,0,0,0], [0,1,0,0], [0,0,1,0], [0,0,0,1]. This design was then compared to networks trained with only the time and optical density as input variables.

Later, an MLP with locally recurrent context units was designed. Even though the learning rule is still a static backpropagation algorithm, the Jordan network is provided with a memory depth embedded in a time constant t. In the end, such a neural model can be used to solve temporal problems. The model was trained on four growth curves of the B. *subtilis* exhibiting different lag times. This array of data was necessary to guarantee appropriate predictions based on information collected during the first 5 hours.

Finally, a hybrid model was constructed to provide prediction and classification. The Jordan network predicts the cell concentration 6-step ahead while the standard MPL uses the resulting data to indicate the phase of the fermentation.

MATERIALS AND METHODS

The microorganism used was a strain of *B. subtilis* deficient in 4 extracellular proteases: neutral, alkaline, serine and bacillopeptidase F (6). The culture was initially grown on plates made from tryptose blood agar base with kanamycin. In the place of blood, we substituted yeast extract as a nitrogen source. Luria broth was used as the preculture media at a pH of 7.4. The cells grew in a 500 ml shake flask at 200 rpm and 37 °C. The active media took up a volume of 250 ml. Once in the exponential phase, 0.4 % of inoculum were then transferred to a 250 ml optimized cultivation medium (6) in a 500 ml shake flask. Samples were withdrawn every 2 hours and centrifuged for 3 minutes. The supernatants were saved for future analyses and the cells washed and resuspended in distilled water. The optical density of the washed cells was measured at 600 nm and multiple dilutions were done when necessary in order to maintain an optical density of about 0.3.

EXPERIMENTAL RESULTS

In order to train the network, optical density data were obtained by growing the strain of *B. subtilis* for about 18 hours. The data were filtered using polynomial approximations on different sections of the curve. Filtration of the data using polynomial fits, wavelets or fourier transforms is very important in Neural Network development, especially when one is working with a limited data set.

The lag phase was calculated by first plotting the logarithm to the base two of the optical density as a function of time. These data were taken in the exponential phase. A linear regression resulted in the following equation:

$$\log2(O.D.) = 0.28t - 1.18$$

By substituting the initial optical density in the above equation and solving for t, a lag of 2.7 hours was obtained. This method introduces less bias in estimating the length of the induction phase since it is not based on visual inspection of the growth cycle. The end of the lag phase corresponded to a slope of 0.09. This value was then used to evaluate the duration of the stationary phase. The death phase lasted 6 hours.

The fermentation provided only 8 input patterns. To facilitate training of the network, additional data were directly taken from the fitted line. A Feed-Forward Neural Network with 2 hidden layers was developed. The input and output patterns were made up of 4-dimensional vectors. An input vector **I** of the form [t, o, d1, d2] was constructed. The components represent the time, and the optical density along with its first and second derivatives. Each vector **I** is associated to an output vector **O**: [l, e , s, d]. Thirty neurons make up the first

layer. The second layer is composed of 10 neurons. Such a topology was required after the network failed to learn with 1 hidden layer and fewer neurons.

The data were divided into 2 sets so that training and testing could take place on the entire range. During the recall and testing phases, the training and testing sets were correctly classified.

The next step was to run the network with 3 different growth cycle data using the same microorganism. The same method was used to grow the cells. The results are shown in Figure 2 where the labels L, E, and D respectively represent the lag, exponential and death phases predicted by the network. To distinguish among the curves, no label was used for Cycle a. Cycles b and c were respectively marked with the star (*) and number (#) symbols.

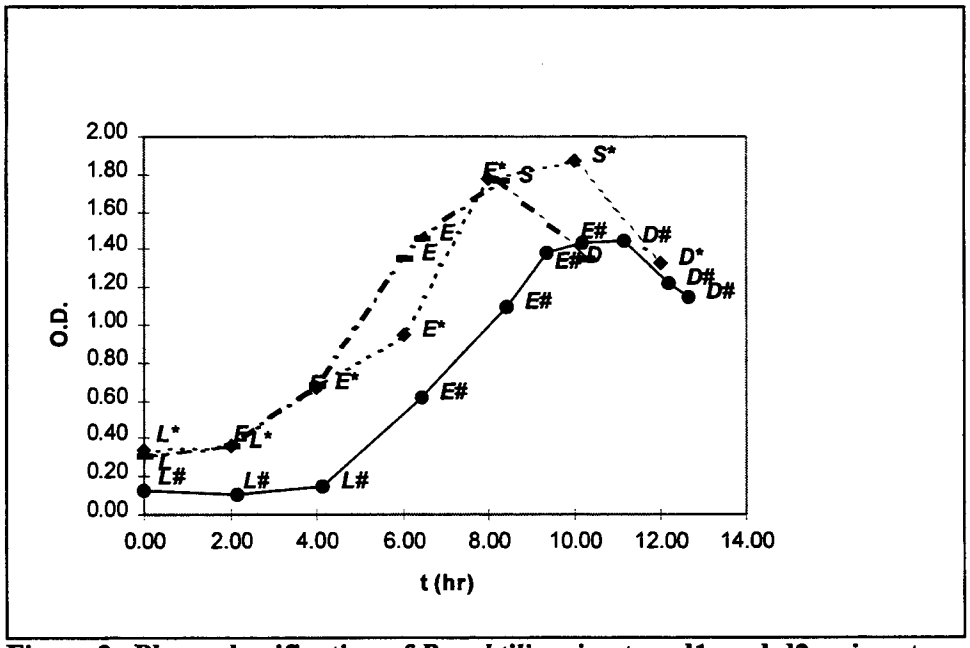

Figure 2. Phase classification of *B. subtilis* using t, o, d1, and d2 as input variables

The network was able to classify 96 % of the data. Misclassifications were determined based on limits established during the training stage. In order to test the performance of the network, two other networks were built, leaving out the second derivative in one case, and both derivatives in another. Using the same data as before, Figures 3 and 4 show the predictions. The network performance decreased from 83 % percent when the second derivative is discarded to63 % when one uses only the time and optical density as inputs to the network.

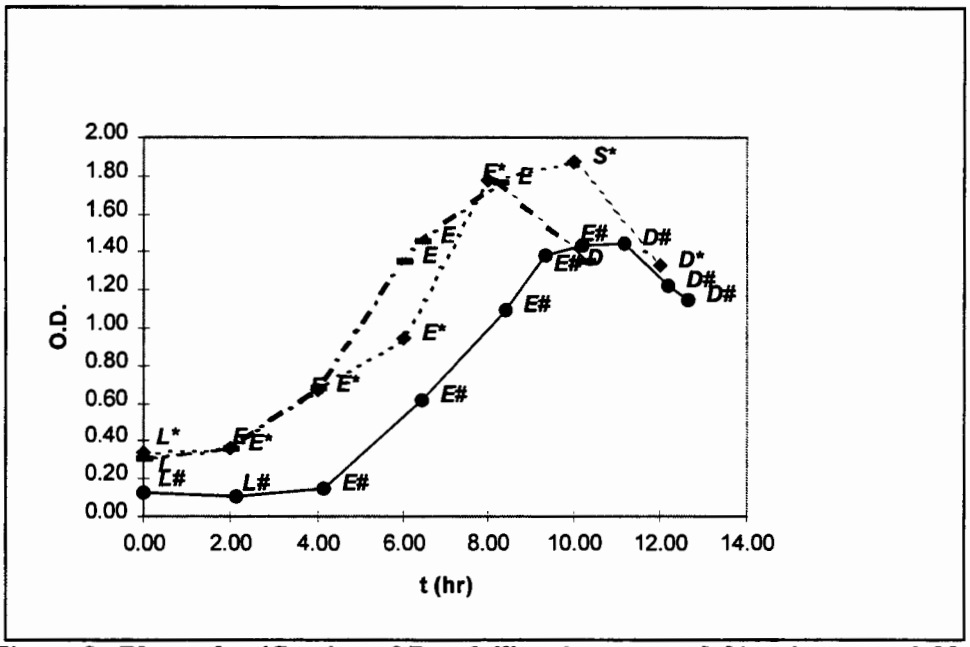

Figure 3. Phase classification of *B. subtilis* using t, o, and d1 as input variables

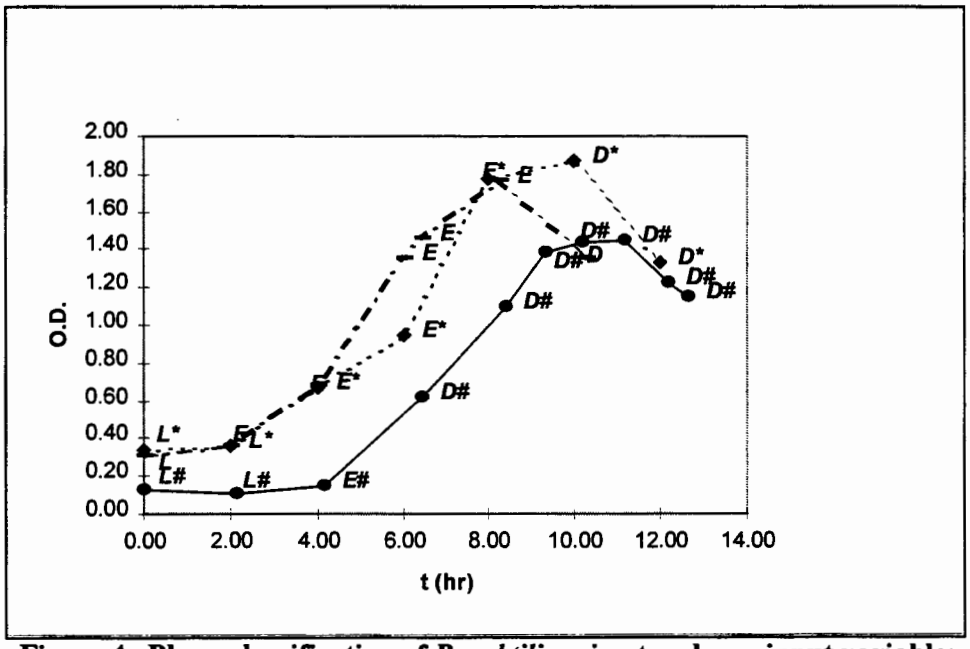

Figure 4. Phase classification of *B. subtilis* using t and o as input variables

It is very important to be able to classify the phases in a fermentation so the process can be fully automated. However, one of the challenges is to forecast future behaviors so appropriate actions can be taken at an early stage in the fermentation. The idea is to build a network that can make multi-step ahead predictions solely based on information provided during the first hours of the process. A similar approach can be found in the works of Linko et al. in their studies of lysine fermentation (7). This model would then be coupled to the

previous classic MLP configuration to form a hybrid network capable of approximating the time the cell would enter or leave a stage.

To accomplish this task, a Jordan model was built. It is a Recurrent Network that can remember past activities. The output values were fed into the input layer. These new data were shifted along the input vector in the form of context units. A time constant t determined the memory span of the network.

For training purposes, four different growth curves were used. They were distinct in the duration of their lag phases and slight variations in initial glucose concentration. It is important to cover a reasonable range of operation so that extrapolation does not become an issue.

The Jordan Network was applied to the three growth cycles previously used. Figure 5 shows the network approximation 7-step ahead. The vertical line shows the time when prediction starts. The curves prior to this line are not identical because the data were filtered in order to provide additional points for a sampling interval of an hour. The errors increase with the length of the prediction horizon. This trend is very typical and reflects the fact that actual values are gradually discarded and replaced by predicted values. Prediction of the 7th data point is not recommended since the model at that point only uses estimated values as basis for further forecasts. The next 2 cycles are plotted on Figures 6 and 7.

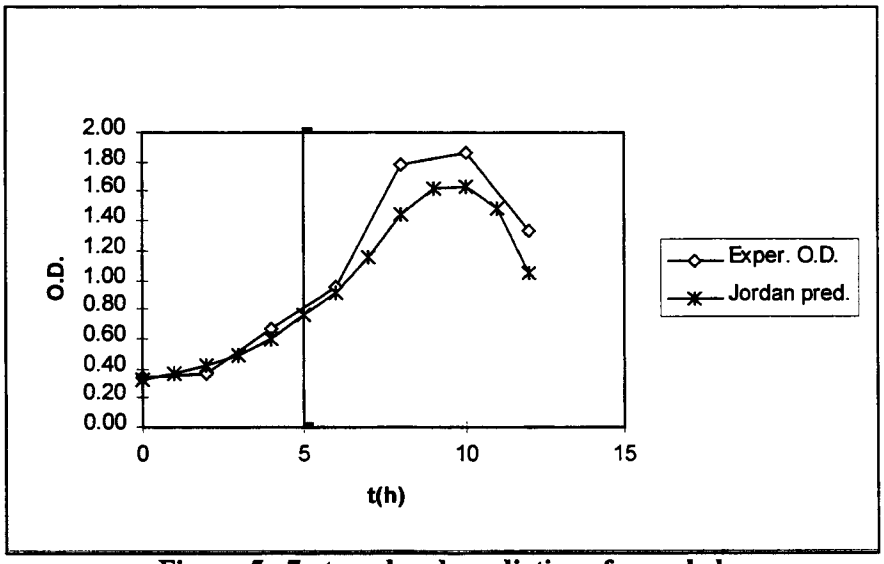

Figure 5. 7-step ahead predictions for cycle b

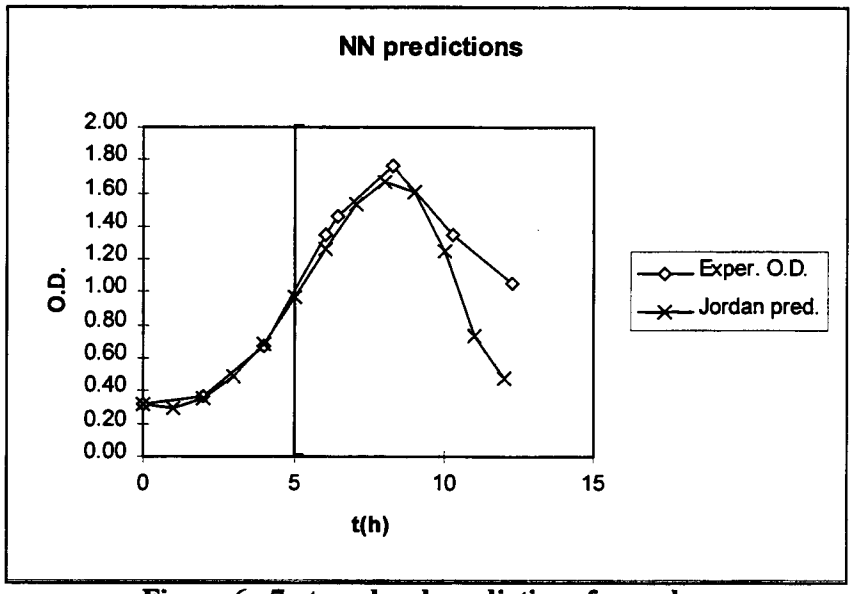

Figure 6. 7-step ahead predictions for cycle a

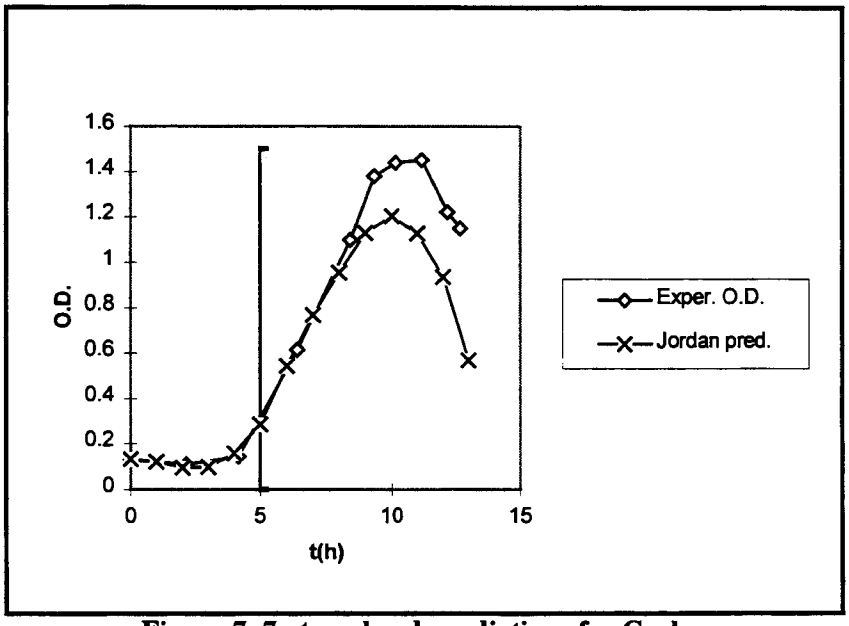

Figure 7. 7-step ahead predictions for Cycle c

The final task was to apply the predicted data to the standard MLP in order to approximate the time the cells would be in a particular phase. This is crucial in biotechnology when elicitors or inducers need to be added to the media in order to increase the production of metabolites. The results are plotted in Figure 8. The predicted data were correctly classified and show good agreement with the results plotted in Figure 2.

Based on data taken for the first 5 hours, this hybrid network accurately predicted the phases of the fermentation even though the cell concentrations were underestimated. Implemented on line, the Network would send this information to a controller that would prompt the addition of inducers to the cultivation media at the optimum time. The controller might even be instructed to terminate the fermentation if the network sensed a low productivity level.

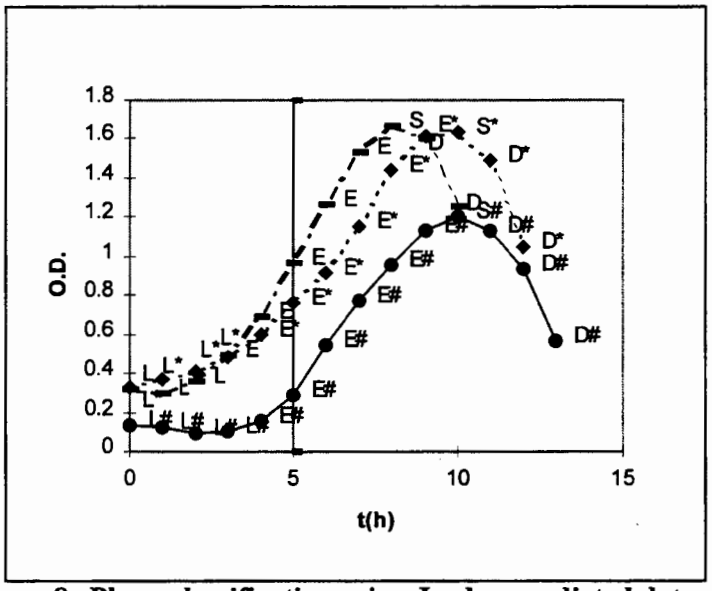

Figure 8. Phase classification using Jordan predicted data and the t-o-d1-d2 network

CONCLUSIONS

Using a feed-forward Neural Network, it was possible to identify the growth phases in a fermentation process. By taking full advantage of the growth curve, a 4-dimensional input vector was constructed. Its components were the time, the optical density, the instantaneous rate of change of the optical density along with its second derivative. The target output was a 4-dimensional Boolean vector made up of the 4 major phases. With two hidden layers, the Network was able to learn the patterns. The classification index increased from 67 to 87 % with the addition of the first derivatives (Figures 3 and 4). Ninety-eight percent of the data were classified when the second derivative of the optical density was added to the input pattern (Figure 2). This improved topology was then used in conjunction with a Jordan Network in order to predict the cells' behavior. Good agreement with the actual data was obtained for the first 4 hours (Figures 5, 6 and 7); however, the performance of the Jordan Network decreased as the prediction horizon became larger.

REFERENCES

1. Lee, J. M. (1992), *Biochemical Engineering*, Prentice Hall, Englewood Cliffs, NJ.

2. Dunkan, D. W. Jr., and J. T. R. Nickerson (1963), "Effect of Environmental and Physiological Conditions on the Phase of Adjustment of *Pseudomonas fragi*," *Appl. Microbiol.* **11**: 179-183.

3. Baughman, D.R. and Y. A. Liu (1995), *Neural Networks in Bioprocessing and Chemical Engineering*, Academic Press, Inc., San Diego, CA.

4. Karim, M. N. and S. L. Rivera (1992), "Use of Recurrent Neural Networks for Bioprocess Identification On-Line Optimization by Micro-genetic Algorithm," *Proceedings Amer. Control Conf.*, p. 1931, Chicago, IL.

5. Monod, J. (1949), "The Growth of Bacterial Cultures," *Ann. Rev. Microbiol.* **3**:371-394.

6. Park, K. (1993), "Environmental Effects on Cell Metabolism and Recombinant Protein Production by *Bacillus subtilis*," PhD Dissertation, Colorado State University, Fort Collins,CO.

7. Linko, S., Y.-H. Zhu and P. Linko (1995), "Neural Networks in Lysine Fermentation," *6th International Conference on Computer Applications in Biotechnology*, p. 336, Garmisch-Partenkirchen, Germany.

Cascade Concentration of *Spirulina platensis* Based on Inertial Migration

S.R. Dahl, A.L. Rakow, and K.C. Ryan
Department of Chemical and Bioresource Engineering
Colorado State University
Fort Collins, Colorado
80523-1370

ABSTRACT

Branched tube separators can be used to form a staged system for concentrating dilute suspensions of *Spirulina platensis*. Previous work yielded a fifty-fold increase in concentration where only one design parameter was altered in order to maximize the recovery of the microalgae (1). Branched tube separator configuration can be changed to achieve different flow characteristics, concentration factors, and rates of recovery. In this study, the side branch diameter was reduced by 50% in the later stages in order to decrease flow through the side branch. Overall, a dilute suspension (0.015% DM) was concentrated to approximately 1.0% DM in 10 stages with a recovery of 88%.

INTRODUCTION

Spirulina platensis is used as a nutritional supplement and contains 60-70% protein, along with other important vitamins and fatty acids. *Spirulina* is usually grown at dilute concentrations, e.g., less than 0.1%DM, and concentrated by techniques such as centrifugation and filtration.

A branched tube separator, however, has distinct advantages over conventional techniques (2). The method is dependent on particle size and shape and utilizes the fluid dynamic properties of flowing suspensions. *Spirulina*, which has a helical shape (Figure1) and lengths in the 10 to 1000+ micron range, undergoes lateral migration towards an equilibrium radial position in the upstream laminar flow (Figure 2). When pumped through a tube with appropriate diameter, a region of relatively particle-free suspension forms outside the region of concentrated particles. In a branched tube separator, the outer dilute region is directed through a branch, allowing the more concentrated portion in the center to continue along in the main tube. By matching the resistance of the branch to that of the flowing dilute region, efficient skimming of the suspension can be achieved (3).

In previous experiments, high recovery was achieved by reducing the product branch length as the concentration was increased along the cascade to .54% DM in seven stages (1). This modification creates a lower resistance in the product branch, thereby reducing Q1/Q2, which is the ratio of the side stream flow to the product flow. This is necessary because as the concentration increases along the train, the region of concentrated particles shifts toward the outer wall. The exit length reduction was limited to 2.5 cm due to end effects and/or gravity head changes, which altered the upstream particle profile.

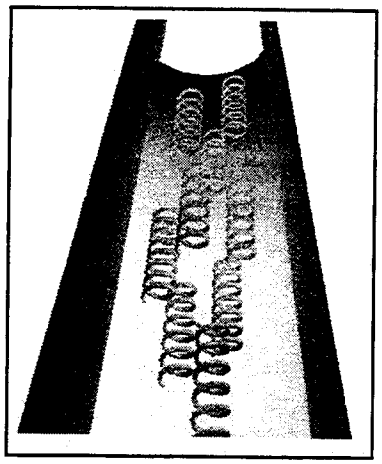

Figure 1. A computer generated diagram of the flowing suspension, illustrating the helical shape of *Spirulina Platensis*.

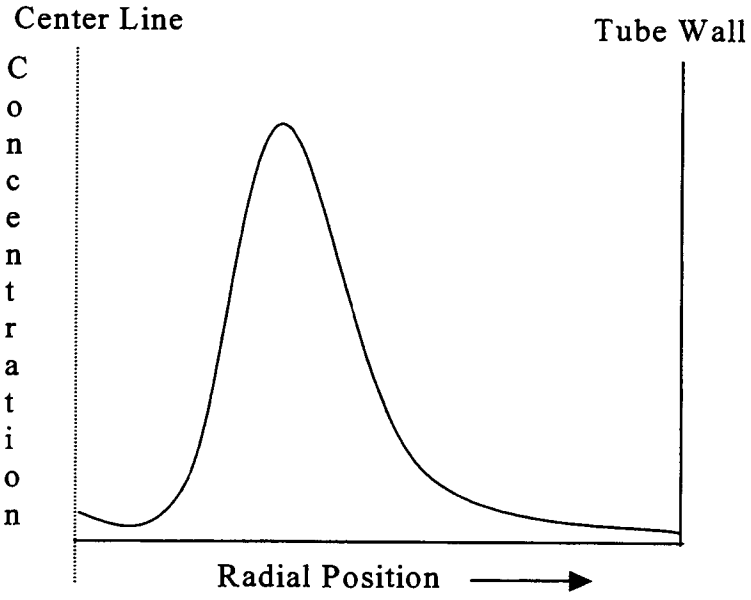

Figure 2

In order to complete the concentration train to achieve product concentration in the neighborhood of 1% DM, we utilized the results of auxiliary experiments, which showed that in a double-branched system, as γ (side/center diameter ratio) decreased, recovery increased. Therefore, in this study a branch system was constructed with a γ of approximately 0.5. This system was used in the later stages of the train (8-10) to concentrate a dilute suspension to approximately 1% DM while maintaining high recovery.

MATERIALS AND METHODS

A suspension of *Spirulina platensis* was grown in an air cooled, continuously stirred, 10 liter flask in standard Zerouk medium with $NaHCO_3$ as the main carbon source at an approximate pH of 9. Direct measurement of concentration was accomplished by a standard, dry mass determination technique and reported as percent dry mass.

A Cole-Palmer Masterflex peristaltic pump was used to flow a *Spirulina* suspension down through a vertically mounted separator system at a Reynolds number of approximately 1500 (Figures 3-4). The side and center streams were collected directly into graduated cylinders for measurement.

Branch System 1, which was constructed with Pyrex glass, is shown in Figure 3. System 2, shown in Figure 4, was similar to System 1; the major difference was the lower branch diameter ratio of $\gamma = 0.5$ instead of $\gamma = 1.0$.

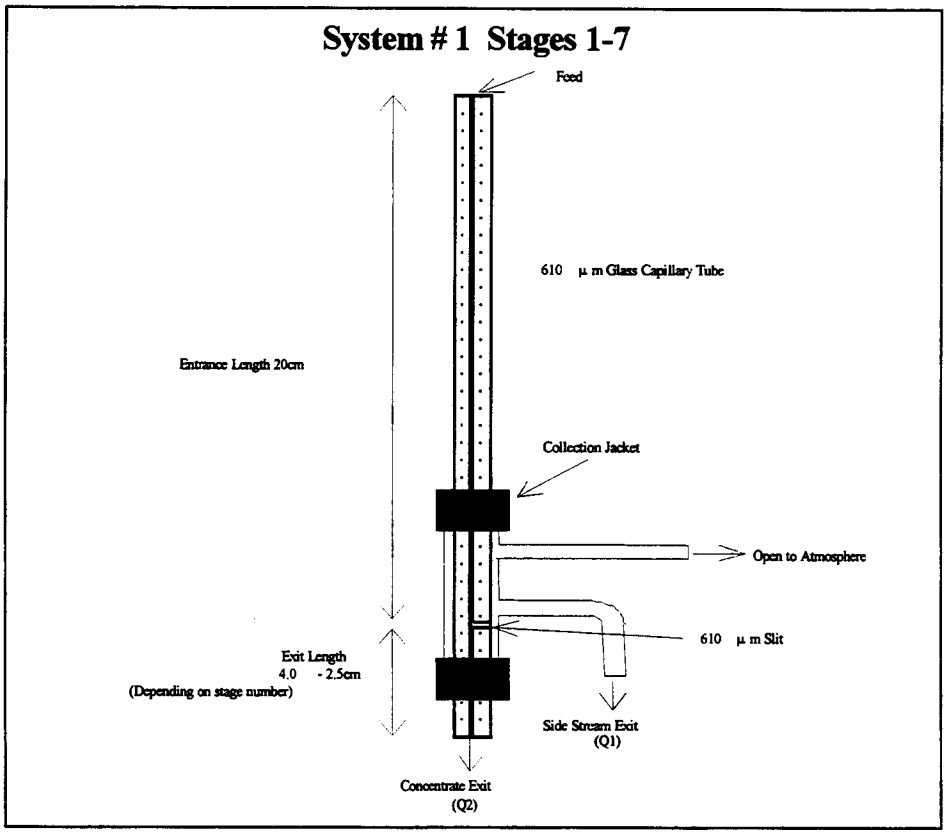

Figure 3

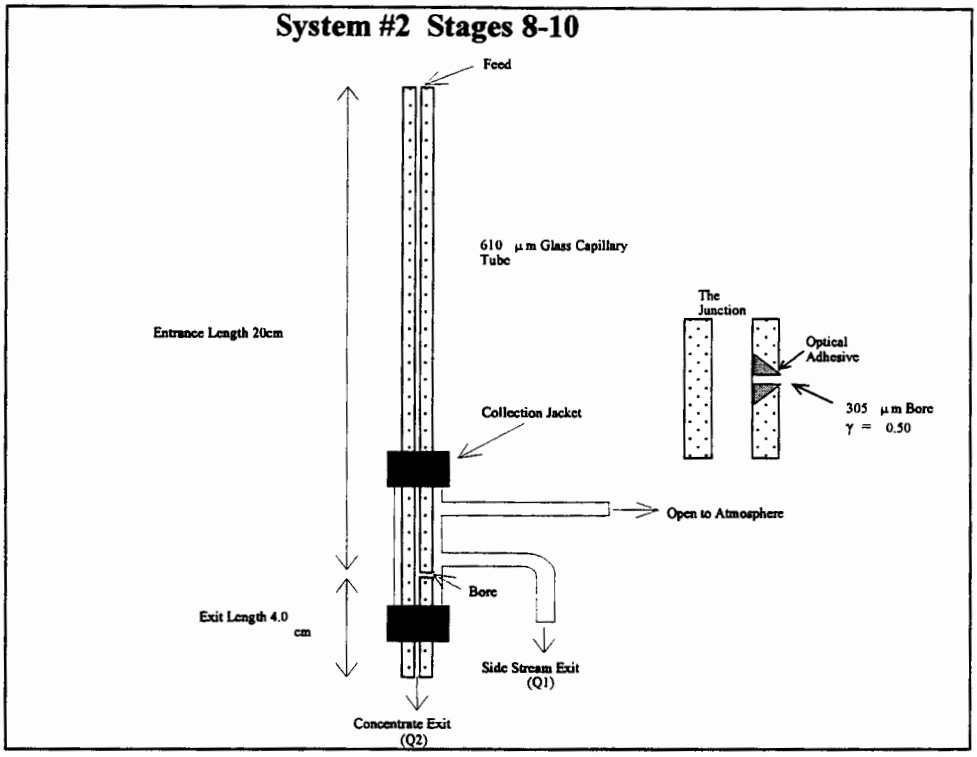

Figure 4

Both glass systems were constructed by cutting into the glass wall exactly 20 cm downstream from the entrance, without penetrating into the main branch, thus creating a very thin layer of glass between the inside and outside diameter. A diamond tipped bit was used to break through this thin layer, resulting in a hole of approximately the same diameter as the capillary bore. Collection of the side stream suspension was facilitated by a glass jacket encasing the region of the slit, with an upper port open to the atmosphere and another, curved port, for collection.

In order to create a side branch diameter smaller than the main tube diameter in System 2, a stainless steel wire of 610 microns was placed in the main capillary and another wire of 305 microns was placed perpendicular into the side hole until the two wires touched. Optical Adhesive was then used to fill the slit volume around the smaller wire. After allowing the adhesive to set with UV light, the wires were removed, leaving a smooth exit bore. The system was then placed in a convection oven at 50°C overnight to allow the adhesive to completely cure.

Due to concentration limitations in the bioreactor, the later stage product streams could not immediately be fed to their respective subsequent stages. Adequate volumes of high concentration feed had to be built up in order to conduct the later stage experiments. Therefore, there are slight differences in concentration between the product stream from the previous stage and the feed stream to the subsequent stage in stages 7-10 (Table 1).

RESULTS

Figure 5 below includes the major results of this study. In some instances the concentration exiting a particular stage differs slightly from the feed concentration entering the next stage. In these instances the average concentration is reported.

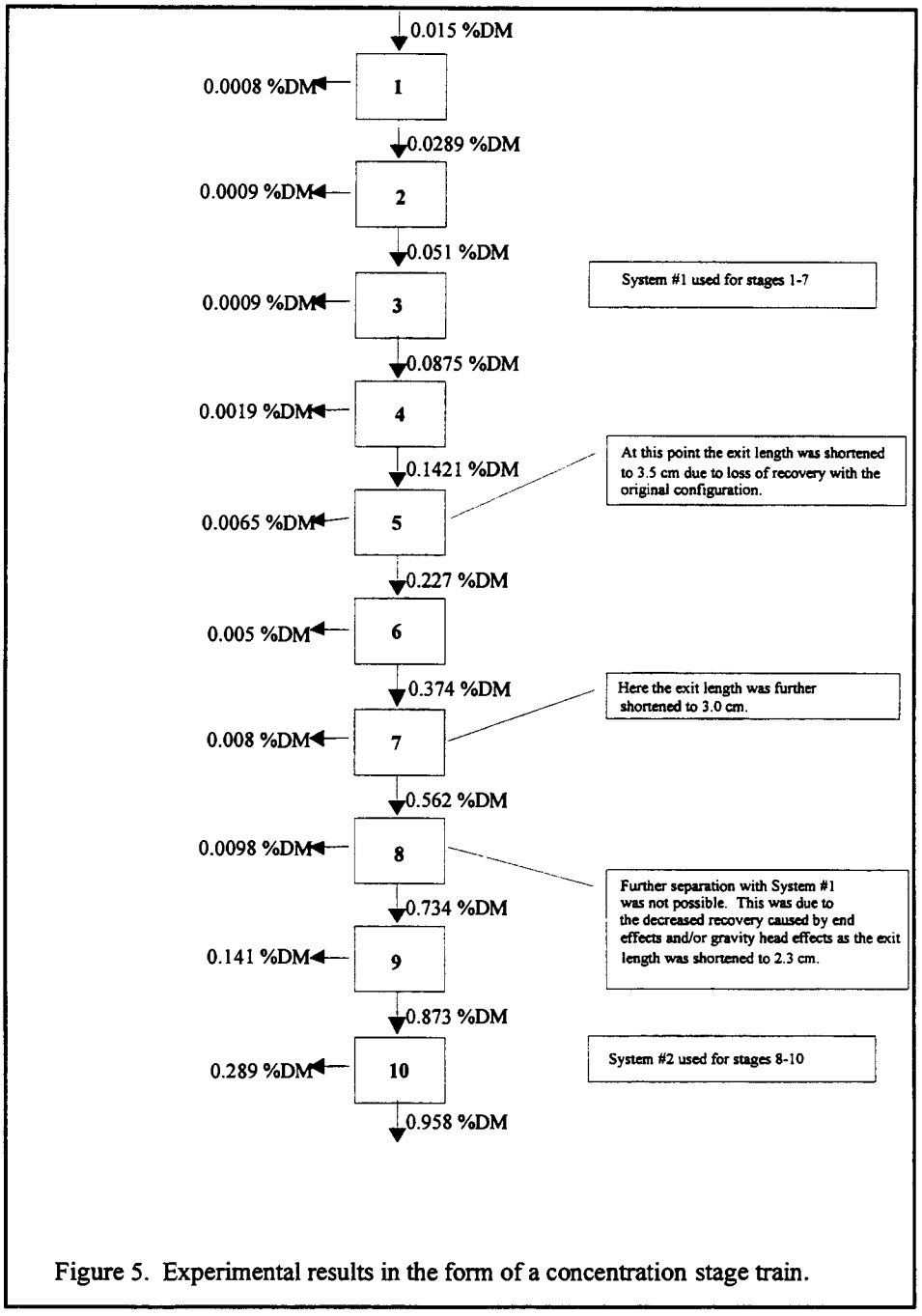

Figure 5. Experimental results in the form of a concentration stage train.

DISCUSSION

By reducing γ, the ratio of side to main channel branch diameter, as well as adjusting branch length ratio, a complete stage train was established for the concentration of *Spirulina platensis* with high recovery. These changes allowed for more efficient skimming of the dilute outer region of the flow (4). These results can be utilized to design a tubular cascade. For a feed concentration of 0.015 %DM at a rate of 1000 ml/s, the required number of tubes for each stage is given in Table 1. Due to variations in the Reynolds number in the later stages, the number of required tubes per stage does not consistently decrease with the flow rate.

Stage Number	Flow Rate (ml/s)	# of Tubes	Q_1/Q_2	%DMi	$\%DM_1$	$\%DM_2$	Concentration Factor	Stage % Recovery
1	1000	1471	0.86	0.015	0.0008	0.0289	1.93	100
2	537	758	0.79	0.0289	0.0009	0.051	1.76	97
3	300	410	0.77	0.051	0.0009	0.0875	1.72	100
4	170	213	0.71	0.0875	0.0019	0.142	1.62	96
5	99	136	0.695	0.147	0.0065	0.227	1.54	99
6	58	71	0.59	0.227	0.005	0.347	1.53	100
7	37	31	0.405	0.373	0.008	0.54	1.45	100
8	26	34	0.141	0.584	0.0998	0.701	1.2	98
9	23	23	0.135	0.767	0.141	0.887	1.16	100
10	20	26	0.148	0.859	0.289	0.958	1.12	97
Total # of Tubes		3173				Overall % Recovery		88

Table 1

Additional recovery can be achieved by concentrating some of the side streams (DM_1). Other side streams can be recycled to the bioreactor in a continuous process.

CONCLUSIONS

Alteration of parameters such as product branch length and side stream branch diameter proved effective in maximizing the recovery of *Spriulina platensis* in a cascade-like process.

ACKNOWLEDGEMENTS

This work was supported by an NSF REU supplemental grant to CTS-9404556. Mike Olsen was of great help in the construction of the branched tube system. Doug Whitt constructed the system for the auxiliary $\gamma \approx 0.5$ experiments.

REFERENCES

(1) Poflee N.M., Rakow A.L., Ryan K.C., Dahl S.R., and Dandy D.S. (1997) Maximization of recovery of *Spirulina platensis* in a staged process based on inertial migration. Accepted for publication in *Separation Science and Technology*.

(2)Rakow A.L., Chappell M.L., and Long R.L. (1989) Concentration of bioparticles by axial migration in laminar flow. *Biotechnology Progress* 5(3): 105-110.

(3) Rakow A.L.(1991) Fluid Particle Separator with Pressure Drop Resistance Matching. *US Patent No.* 5,076,943.

(4) Poflee N.M., Rakow A.L., Werntz M., and Pons M.N. (1994) Stagewise design for concentration of *Spirulina platensis* based on lateral migration with flow through vertical tees. *Bioseparation* **4**: 237-246.

Cross-Flow Filtration of Bacterial Lysate with Flocculation

Hugh Graham and M. N. Karim
Department of Chemical and Bioresource Engineering
Colorado State University, Fort Collins, CO 80523

A.S. Cibulskas
Cytec Industries
Stamford, CT 06904.

ABSTRACT

Cross-flow, or tangential flow, particle filtration is a high shear application in which the use of flocculant may have benefits if the problems associated with shear disruption of flocs can be overcome. Cross-flow filtration is commonly used in biotechnological separation processes and problems related to membrane fouling are often encountered. These could potentially be reduced if the fouling components are well flocculated. An increase in particle size associated with flocculation will also increase the filtrate flux according to models of particle cross-flow filtration. This research used polymeric flocculants to flocculate *E. coli* lysate suspensions, a heterogeneous biocolloid, and found conditions involving a small initial floc size which improved the cross-flow filtration flux by a factor of two to three under typical cross-flow filtration conditions. This novel approach is compared with conditions that give a larger floc size where filtrate flux is lower than the unflocculated case. The results are repeated at pilot scale and are compared with theory. The effects of particle size and shear are discussed.

INTRODUCTION

Cross-flow or tangential flow filtration has wide application in biopharmaceutical solid-liquid separation and in purification processes (1,2). Following a typical fermentation process for the production of a biologic product, a cross-flow microfiltration process can be used as the first biomass-broth separation step. For a separation process involving cell lysis, cross-flow microfiltration is also used to separate soluble products from insoluble cell debris or to separate insoluble products from soluble contaminants. Ultrafiltration using molecular weight cutoff membranes is commonly used to separate a peptide or nucleic acid product from contaminants of differing molecular weight, for example, buffer components, viral contaminants, and even macromolecules of significantly differing molecular weight. Diafiltration is also commonly used in combination with cross-flow microfiltration and ultrafiltration to exchange buffers or to recover additional soluble material from lysate. The biomass filter cake is typically highly compressible, deterring the use of traditional dead-end filtration in many processes. Cross-flow filtration avoids this problem by the use of high

membrane sweep velocities to eliminate the build up of a flow-inhibiting boundary layer or a deposition of solid material at the filtration membrane, thereby ensuring that filtrate flux rates are maintained at a high level (see Figure 1).

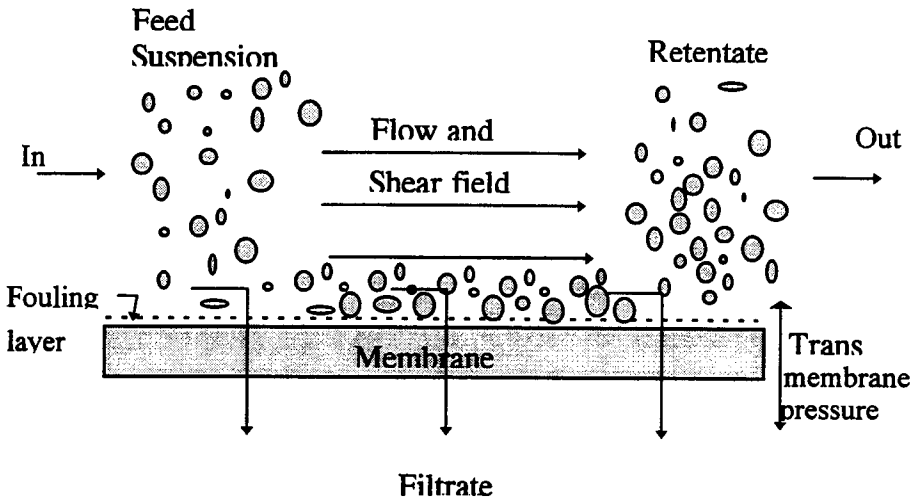

Figure 1: Cross-flow microfiltration performing solid-liquid separation. Membrane pore size is less than particle size.

Cross-flow filtration is often preferred over centrifugation for primary product separation in a biologic process, for example, the need for pellet resuspension that may be required with a centrifugation process is avoided and the process of diafiltration can be used to eliminate several process steps. Centrifugation of bacterial lysates (without the use of flocculants) is highly capital intensive. The small size of particles in lysate means that high centrifugation forces or residence times are required for good separation and cross-flow filtration using microfiltration membranes has been found to be more economical (2).

This study is the first to successfully examine the use of polymeric flocculants as an aid to the process of cross-flow microfiltration of bacterial lysate and identifies floc properties that can significantly enhance the efficiency of the process.

Filtration Theory

Several factors control the mass transfer process in dead-end and cross-flow filtration. The flow through the filter cake and the filter medium or membrane is driven by a transmembrane pressure difference. The bulk mass transport through a membrane filtration system can be described by the classical series resistance equation 1, which can be derived from Poiseuille's equation for streamline flow in porous media;

$$J_V = \frac{dV}{dt}\frac{1}{A_m} = \frac{\Delta P_{TM}}{\mu (R_M + R_C)} \qquad (1)$$

where J_v is the filtrate flux, ΔP_{TM} is the transmembrane pressure drop, μ is the filtrate viscosity and V is the filtrate volume passed in time t through a membrane of area A_m. R_m is the hydraulic resistance of the membrane layer and R_C is the resistance of the high solids content gel or cake layer adjacent to the membrane (3,4). The resistance terms in the denominator can be expanded to include resistances due to internal and external membrane fouling, R_{if} and R_{ef} (5). These additional resistances are caused by colloidal materials or macrosolutes that may bond to the pore walls or the membrane surface respectively and reduce the pore flow area. The two membrane surface resistances, R_C and R_{ef}, are affected by shear in cross-flow filtration and the resulting reduction of flow resistance at a high tangential shear rate is the chief advantage of this unit operation. Suspension particle size will directly influence the value of R_C, as with traditional dead end filtration, where the specific cake resistance is inversely proportional to the square of the characteristic particle dimension (6). R_C is given by equation 2,

$$R_C = \frac{\alpha \quad m_C}{A_M} \qquad (2)$$

where α is the specific resistance of the filter cake, m_C is the mass of filter cake deposited and A_m is the membrane area. The specific resistance is approximately related to particle properties by equation 3 (6),

$$\alpha = 45 \frac{\phi_w}{(\rho r_s^2 (1-\phi_w)^3)} \qquad (3)$$

where ϕ_W is the particle volume fraction at the wall (i.e., in the filter cake layer), ρ is the suspension density and r_S is the particle radius. Flocculation of the particulate suspension will increase the particle size and reduce the specific cake resistance, thereby theoretically increasing the filtrate flux. Additional effects may be attributed to flocculation process. Particle surface charge will be reduced and any electrostatic interaction with the membrane surface will be altered. In cross-flow particle filtration, particle size will also influence the stability of the filter cake layer. Larger particles will be affected to a different degree by the shear field, as reviewed in the following section.

Mass Transport in Particle Cross-flow Filtration

The literature suggests that flux rates are substantially higher for cross-flow particle microfiltration than those predicted by classical stagnant film models, due to the presence of one or more modes of particle transport away from the membrane and the filter cake layer (3,6,7). This particle motion away from the membrane reduces the filter cake thickness and hence lowers the cake resistance. The objective of this study is to investigate the effects of significantly enhancing the particle size in the suspension using polymeric flocculants. Several mass transport models for particle cross-flow filtration have been derived which can be used to predict the effect of particle size on the filtration process. With the stagnant film model, the only mode of particle transport assumed to occur is due to Brownian motion (2). As particle size increases, the amplitude of any Brownian motion decreases and thus disruption to the filter cake layer also decreases, leading to an increase (or rather, no dynamic reduction) in filter cake thickness and hence a decrease in filtrate flux. Particle motion may also be attributed to the "tubular pinch" or "inertial migration" effect that arises from interactions between

individual particles and the flow boundary (7). Particles in tubular flow tend to concentrate at a dimensionless radial position of about 0.6 from the tube center. A filter cake can only form on the membrane surface if the filtrate flux overcomes the inertial migration velocity, V_L, as given by equation 4,

$$V_L = \Psi \frac{\rho r_s^3 \gamma_w^2}{\mu} \qquad (4)$$

where, γ_w is the wall shear rate and μ is the fluid viscosity. The coefficient, Ψ, is a function of the flow characteristics (3). According to this model, filter cake will continue to deposit on the membrane surface, increasing R_C and decreasing the flux according to equation 1, until a steady state is reached where J_V is equivalent to V_L. A very strong dependence of flux on particle size is seen, as the expression for V_L given in equation 4 includes the third power of the particle size.

More recently, an alternative proposed mode of particle transport away from the membrane surface incorporating shear-induced particle diffusion has been modeled empirically. This type of particle movement is caused by collisions in a shear field and the model is based on a measured particle diffusion coefficient. This coefficient, D, has been found to be a function of r_s^2 and the first power of the shear rate, γ_w. It is also a function of the particle volume fraction, ϕ. Zydney and Colton (8) modeled the transport associated with this mode of particle movement and the model was improved by Davis and Sherwood (9). They give the result in equation 5,

$$J_V = 0.078 \left(\frac{r_s^4}{L} \right)^{\frac{1}{3}} \gamma_w \left(\frac{\phi_w}{\phi_b} \right)^{\frac{1}{3}} \qquad (5)$$

where ϕ_w and ϕ_b are the particle volume fractions at the wall (i.e., in the filter cake layer) and in the bulk respectively and L is the channel length. The variation of flux on particle size is not as high here as for the case modeled in equation 5 but a strong dependency (i.e., the 4/3 power) still exists. Models have also been developed to account for the potentially complex motion of particles along the surface of the membrane or the filter cake. These typically use a force balance on individual particles to determine whether a particle adheres to the filter cake or flow along the surface (3). In this model, flux is directly proportional to the particle radius. The mode of particle movement in cross-flow filtration may be due to a combination of all these model systems. A comparison has been made of data from a number of particle filtration systems including blood, bacteria and platelets as well as some inorganic systems. This shows that the measured diffusion coefficient based model, equation 5, gives a reasonable prediction of the filtrate flux (3,8).

Many other factors influence the transport process. The medium pH and ionic strength can affect the surface charge of the particulate matter as well as that of the membrane material. This can result in electrostatic repulsion (or attraction) forces between the particles and the membrane surface. These resistances to filtrate transport through the membrane can lead to a concentration polarization effect near the membrane surface. Concentration polarization is the term for a solute concentration gradient increasing from the bulk fluid level to a higher value at the membrane surface, where potentially filterable material is hindered from passage through

the membrane pores by surface or stagnant layer interaction effects. Membrane chemistry, pore size and geometry also alter the filtrate flow process. The feed rate to the membrane directly affects the sweep velocity and the shear rate adjacent to the membrane surface and this can also alter the transmembrane pressure profile through the membrane system. A membrane fouling layer may accumulate as the process proceeds, on the membrane surface or on the pore walls. Suspension components that are physiochemically attracted to the membrane surface bind to the membrane material, obstructing the pores and reducing the available area for filtrate flow. Fouling is particularly significant in a bacterial lysate separation process where many types of biological macromolecule are present in the suspension and any of these may be involved in the membrane fouling process (3).

The use of flocculants with cross-flow filtration has the potential advantage of increasing particle size and hence increasing the filtrate flux as predicted by equations 4 and 5. Additionally, in the case of a biological suspension, a flocculant may agglomerate membrane fouling components and effectively sequester these macrosolutes and colloidal materials in the larger solid particles. Particle surface charge will be reduced or neutralized by the agglomeration process, further reducing the chance of membrane fouling and concentration polarization effects. These benefits could all potentially increase the flux through the filter. The use of flocculants in a cross-flow filtration process involves several problems; most significant amongst these is deaggregation of the suspension. Even the strongest flocs are vulnerable to rupture in the relatively high shear fields used in cross-flow filtration (10) and, as floc rupture will tend to be irreversible, the above-mentioned benefits will quickly be lost, particularly in a typical batch filtration system with retentate recycle.

Flocculation in Cross-Flow Filtration

Previous studies of cross-flow filtration with flocculation have been limited, indeed the two topics are seldom mentioned in the same text. Stroh (in 11) discusses the advantages of cross-flow filtration processes and briefly discusses the application of agglomeration to the technique. He states that "at present, the formation of adequately rigid agglomerates for cross-flow filtration purposes by means of common physiochemical and mechanical agglomeration techniques is unfortunately not possible." Koglin (12) describes the use of polymeric flocculants with depth and dead-end filtration and notes that although techniques for the use of flocculation with cross-flow filtration do not currently exist, they will hopefully be developed in the future. A few studies have been published recently. Vigneswaran and Boonthanon (13) used in-line flocculation using poly-aluminum chloride ($Al_n(OH)_mCl_{(n-m)}$) to coagulate a bentonite suspension that was then passed through a cross-flow filtration system. They examined the effects of floc size and found that the filtrate flux rate could be improved by over 200 percent with the use of coagulants. They also reported encouraging results for small-scale cross-flow sewage treatment processes and for flocculation of bentonite suspensions with membrane back-flushing. A study of the use of poly-aluminum chloride as a process aid in the cross-flow microfiltration of synthetic raw water showed effects of residual floc surface charge and floc size on the type of membrane fouling observed (14). Mietton Peuchot and Ben Aim (10) also used poly-aluminum chloride to coagulate bentonite suspensions and measured filtrate flux in a stirred membrane filtration cell. They found that the optimum dose for filtration

matched that determined using a conventional jar test and that filtrate fluxes could be improved by a factor of up to 10 at this optimum dose. This work was scaled up to pilot scale (0.2 m^2 membrane area) using river water and again the filtrate flux rate was stated to be increased, this time by a factor of two. From this limited previous work, we can anticipate that polymeric flocculation may offer advantages when used with cross-flow filtration of bacterial lysate suspensions, but we can also predict that shear stress levels may be high enough to rupture the flocs. Therefore, the experimental design must revolve around the selection of shear resistant flocs and will use shear rate as a critical scaling factor.

Experimental Design

The separation of bacterial lysate was studied in this experiment. Bacterial lysate contains a profusion of soluble and insoluble biological macromolecules as well as various simpler ionic species. Many of these components can contribute to membrane fouling and the particular species that tend to bond to the membrane will vary depending on the membrane surface chemistry and the surface and particle charges at the filtration conditions. Variables such as suspension pH, flocculant chemistry and microporous membrane type were held constant in this study to ensure that the membrane and particle charge were consistent for all experiments performed. The flocculation condition sought for these experiments was required to give complete agglomeration of all material in the suspension. Small, dense flocs were desired as these were more likely to be resistant to shear forces. With the polymer series used in these experiments, a consequence of the smaller floc size selected was an increase in the width of the optimum dose band. The additional floc stability associated with the broad optimal dose range could allow shear-ruptured and de-aggregated flocs to remain relatively intact or possibly to re-aggregate.

Materials and Methods

E. coli K12 cells were grown using a fed-batch method on a minimal medium to a solids content of approximately 10% (15). Lysate was prepared by high pressure homogenization of the whole fermentation broth and was assayed to ensure consistent solids content, conductivity, pH and degree of lysis. A centrifuge tube test was used to establish a dose curve (15). Pellet volume was used as a measure of floc density and floc size was determined by visual microscopy. Microtubular filtration cartridges (A/G Technology Corporation, Needham, MA) were used at two different process scales with cartridges lumens of the same diameter (1 mm). These were used at the same shear rate for all of the experimental work. A shear rate of 8000 s^{-1} was used as the minimum suggested shear rate suitable for membrane fouling suspensions (16). The membranes were cleaned according to the manufacturer's instructions prior to each experimental run. The total volume of bacterial lysate suspension (or suspension plus flocculant) used for a filtration experiment at each scale was equal to the flow volume per minute required to achieve the desired shear rate. For small scale experiments, a lysate volume of 300 mL was used for a flow rate through the cartridge of 300 mL/min to give the shear rate mentioned above. Constant volume and solids content were

maintained by returning the collected filtrate to the suspension reservoir. Unflocculated suspensions were diluted to the same solids concentration as the flocculated suspensions with cell-free, depleted fermentation medium.

The equipment arrangement is shown in Figure 2. The peristaltic pump flow rate was calibrated at the flow conditions used in the experiment and the transmembrane pressure was monitored closely, particularly during the initial stages of the experiment. The throttle valve (a metal hose clamp) was adjusted to ensure consistent transmembrane pressure and a value of 10 psig was used for the majority of the experiments. All hoses were Masterflex silicone rubber or Norton PharMed polymer (Cole Parmer, Illinois). The filtrate pressure was kept at zero psig thus the transmembrane pressure was calculated as the average of the inlet and retentate pressures. The filtrate flow rate was measured by timed collection in a graduated cylinder. The magnetic stir plate was used for fluid mixing for suspension flocculation but during the experimental runs fluid mixing in the reservoir was largely induced by the high retentate recycle flow velocity.

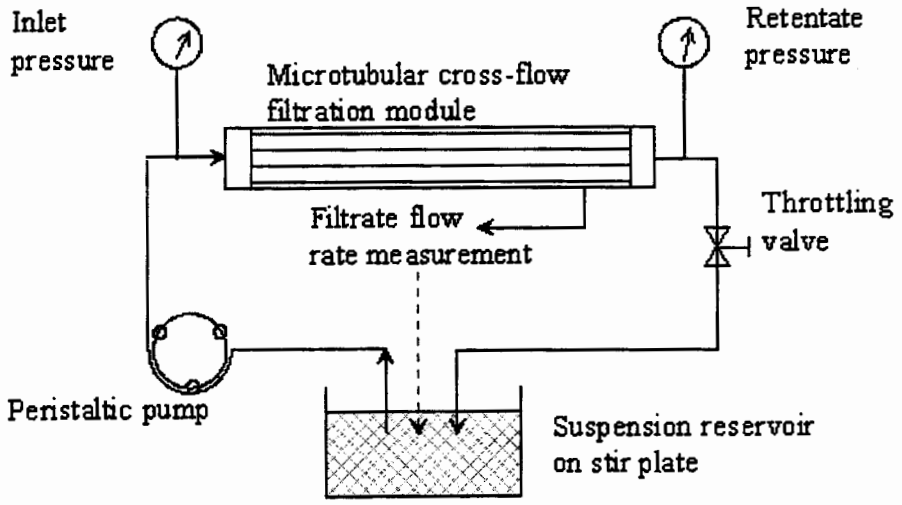

Figure 2: Cross-flow filtration experimental equipment schematic.

RESULTS AND DISCUSSION

Flux Improvement with Polymeric Flocculation

Flux was found to decrease rapidly during the cross-flow microfiltration of fresh, unflocculated *E. coli* lysate in accordance with expectations. The flux reduction is due to membrane fouling and cake formation. The polymer series examined in these studies contained a combination of tertiary and quaternary amine functionalities (Cytec Cysep 2833 through Cysep 2837, Cytec Industries, Stamford, CT). Successive polymers in the series contain different ratios of the two functionalities and produce flocculated suspensions and dose curves

with different properties. Flocculants in this series that produce larger flocs gave a narrower optimum dose. A dose curve for the first polymer used (Cysep 2836) is given in Figure 3. The flocs produced by this flocculant were barely visible to the naked eye and had an average characteristic dimension of 0.14 mm as determined by microscopic evaluation. In a centrifuge dose curve test, the flocculant produced a very clear supernatant over a broad optimum dose range. It also gave a pellet that was slightly less compact at the optimum dose than that produced by flocculants which produced a larger floc. This pellet was very stable and resistant to resuspension, implying good cohesive strength.

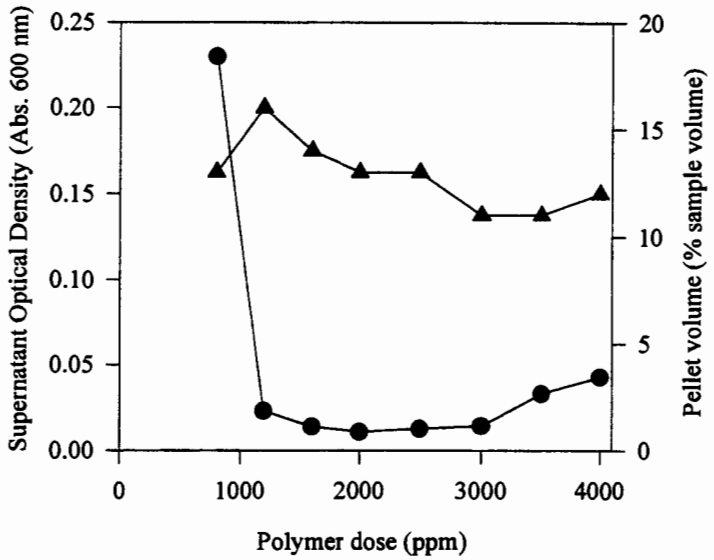

Figure 3: Flocculant dose curve for *E. coli* lysate using centrifuge tube test showing supernatant OD (•) and pellet volume (▲). Flocculant is Cytec Cysep 2836, 1% w/w polymer content. Sample comprises 5 mL lysate (~10% v/v solids content), with polymer dose and water to give 10 mL total volume.

Results of cross-flow microfiltration experiments comparing this flocculant at the optimal condition with an unflocculated suspension are given in Figure 4. Initial flux levels are much higher with the flocculated suspension and have been increased by a factor of 8.5 after 2.5 minutes. The flux level declines in both cases as the experiment proceeds but the stable plateau level reached after 20 minutes is still three times higher with the flocculated suspension than with the unflocculated suspension. Observation of samples from time points during the experimental run established that the floc size reduced rapidly (see Figure 5). Despite this floc size reduction, the suspension remained completely flocculated with no colloidal size particles being released into the surrounding medium (or if such particles were released during floc breakup, they re-aggregated prior to examination). Small scale settling tests (5 mL of retentate suspension in a test tube, allowed to settle for less than 5 minutes) also showed that the suspension was still fully flocculated. The solid material settled out completely and a crystal clear supernatant was rapidly produced ($OD_{600} < 0.2$).

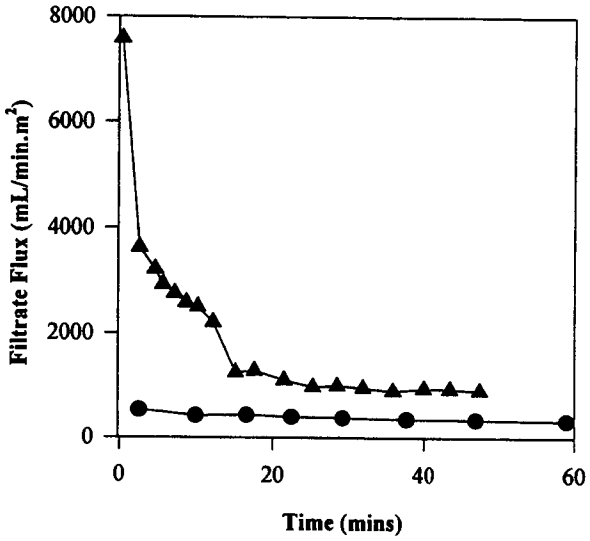

Figure 4: Microfiltration of *E. coli* lysate. Flux improvement with polymeric flocculation. Unflocculated (•) and flocculated (▲) flux. Membrane area 24 cm^2, nominal pore size 0.1 μm. Shear rate 8000s^{-1}. 10% lysate solids content. Flocculant Cytec Cysep 2836, 1% w/w. Dose: 2500 ppm.

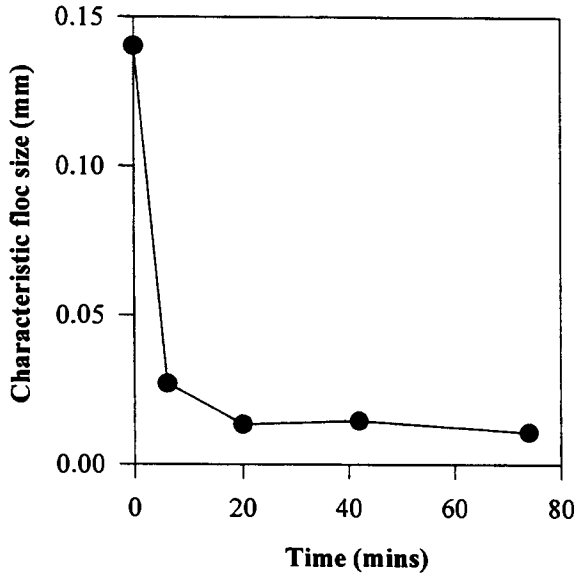

Figure 5: Floc size reduction during cross-flow filtration of *E. coli* lysate flocculated with Cytec Cysep 2836.

Effect of Initial Floc Size

The effect of initial floc size on the microfiltration of flocculated lysate was examined using another flocculant from the same series. This flocculant produces a much larger floc size but also has a narrower optimum dose range. The cross-flow microfiltration experiments described above were repeated and compared with results using the large floc size and the resulting flux rates are shown in Figure 6. The large flocs, which are much more typical of flocs that could be selected for centrifugation, dead end filtration or settling tank separation processes, are disadvantageous in this cross-flow filtration application. Although the initial flux level is slightly higher than the unflocculated flux, this advantage quickly disappears and is replaced by an overall decrease in the flux. As in the previous experiment, the small flocs, produced by the flocculant with a broad optimum dose range, gave a significant increase in the flux rate. The final plateau flux level was increased by a factor of over two. The large flocs break up to form colloidal size debris, such that a settling test or brief centrifugation leaves a cloudy supernatant. A sample taken prior to the start of the experimental run confirmed that the suspension was well flocculated with no unflocculated material in the supernatant. Micron-sized particulate matter could be microscopically observed between the floc fragments as the experiment progressed.

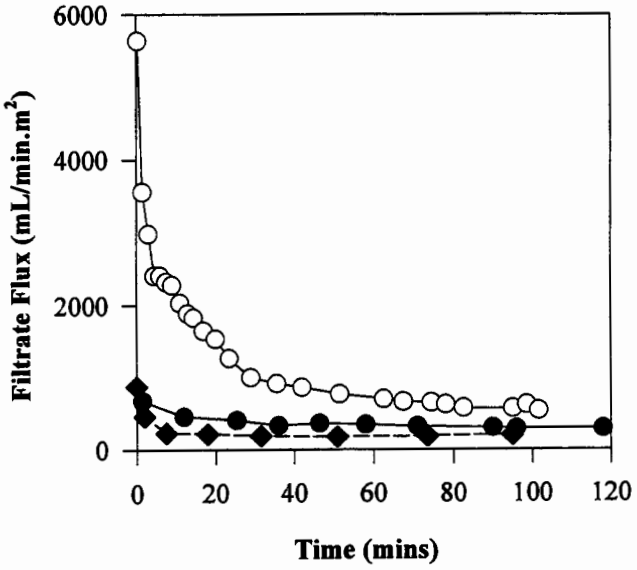

Figure 6: Microfiltration of *E. coli* lysate; effect of initial floc size. Conditions as Figure 4. Doses: Cysep 2836: 2500 ppm(○), small initial floc size; Cysep 2834: 1500 ppm(◆), large initial floc size, and unflocculated (•).

Larger Scale Experiments

A larger membrane area microfiltration module with similar micro-tubule materials and geometry was used to examine scale up effects. The membrane area was scaled up from 24 to

1400 cm^2. The experiment was scaled to maintain a constant transmembrane pressure and shear rate in the membrane tubules (8000 s^{-1}). This necessitated a higher suspension flow rate (8 liters/min) and the use of a larger pump and reservoir vessel to maintain the one minute average recirculation time used in previous runs. Of the three scaled-up runs performed, two showed a significant increase in filtrate flux with Cysep 2836 (smaller initial floc size) and one showed virtually no increase in filtrate flux over the unflocculated suspension. This last run used relatively stale bacterial lysate suspension which had been kept on ice overnight and may therefore have degraded. Seemingly, membrane fouling components were released into solution from the lysate during the storage period as it turned stale. These macromolecules were not subsequently flocculated, despite the clarity of the supernatant that was achieved during the flocculation tests, and as a result, excessive membrane fouling occurred. Results from one of the successful runs using fresh lysate are shown in Figure 7. An increase in the final plateau flux level by a factor of almost two was observed.

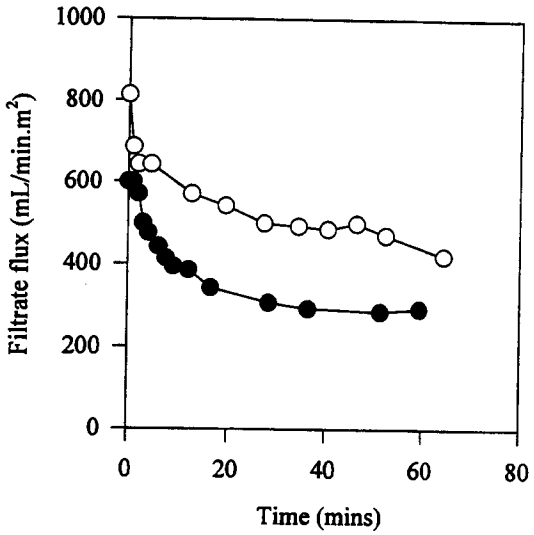

Figure 7: Cross-flow filtration of *E. coli* lysate - larger scale experiment. Flux improvement with polymeric flocculation. Membrane area 1400 cm^2, nominal pore size 0.1 μm. Shear rate 8000 s^{-1}. 10 % lysate solids content. Flocculant Cytec Cysep 2836, 1% w/w. Dose: 2500 ppm.

Several factors could not be maintained constant during the scale up process. The mixing in the reservoir during the run was visibly more intense in the scaled-up runs due to the high recirculation rate. The suspension temperature increased faster (due to energy input from the system friction losses) in the large scale runs. The pressure drop through the filtration module was slightly higher due to an increased micro-tubule length. Shear rate in the pump and associated tubing was also higher due to the increased flow rate (tubing size was increased over the smaller scale experiments but valves and fitting used were similar). Note that the initial peak flux observed with the flocculated suspension in this experiment is lower than that

seen in the small scale experiments. This may also be due to the higher overall shear in the experimental equipment.

The characteristic turbulent shear rate used in flocculation studies is the spatially averaged velocity gradient G (17),

$$G = \left(\frac{\varepsilon}{\nu}\right)^{\frac{1}{2}} \qquad (6)$$

where ε is the average turbulent energy dissipation rate and ν is the kinematic viscosity of the suspending medium. The observed increase in energy dissipation will increase the shear rate and may result in a different or more catastrophic form of floc break up. Models and studies of deaggregation processes predict that an increased shear rate will increase the rate of deaggregation of a coagulated suspension giving a change in the resulting particle size distribution (18). Two forms of aggregate disruption are commonly modeled, erosion of particles from the floc surface, and floc splitting or "bulgy deformation" (19). The former is associated with fluid eddies of a scale comparable to the floc size. The latter occurs where fluid forces are high enough to produce a pressure differential across the floc that can produce shear fragmentation. The shear fragmentation mode of deaggregation is more likely to predominate with larger, weaker flocs at higher shear levels. Shear fragmentation can take several forms; the primary floc can split into two similar smaller particles or, more catastrophically, into a spectrum of smaller floc sizes. More catastrophic floc breakup, whether due to higher shear or weaker floc structure, will release a higher proportion of colloidal and fouling material into suspension.

The effect of particle size on filtrate flux was discussed above. The release of small particles into the suspension can have the effect of reducing the mobility of the filter cake away from the membrane surface, hence reducing the filtrate flux. It should be further noted that *E. coli* lysate forms a highly compressible filter cake and this is true of many other biological suspensions. Thus any build up of filter cake on the filter membrane may cause a dramatic reduction in the filtrate flow rate.

Comparison of Figures 4 and 5 shows that there is a correlation between particle size and filtrate flux (Figure 8). Note that this correlation is not causal. Membrane fouling, filter cake compression and non-steady state effects are not taken into account. The decrease in particle size does coincide with a decrease in flux in general accordance with theory.

Initial studies of lower transmembrane pressures and lower shear rates within the membrane module have shown little effect on the observed improvement in flux described above. The implication is that much of the floc deaggregation occurs in the pump and throttle valve and that the shear rate within the module does little to disrupt the flocs. A shear rate of 8000 s^{-1}, as used in these studies, corresponds to a Kolmogoroff microscale of turbulence (a measure of the smallest eddy size in turbulent flow) of only 11 μm. This is much smaller than the floc size used in these experiments, implying that bulgy deformation, rather than surface erosion, is the predominant form of deaggregation in these experiments.

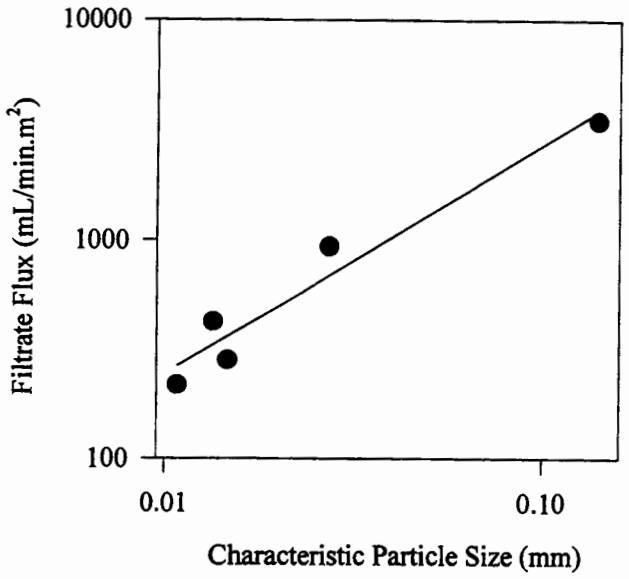

Figure 8: Decrease in non-steady state flux with particle size. Regression fit: Flux = 3.10^5 ($r_s^{1.04}$).

Flocculation theory states that stronger particle-particle bond strengths may produce less dense flocs as intra-floc particle movement is inhibited more rigid adhesion forces. Thus, during floc formation, a particle will adhere strongly to its initial point of contact and will not reposition itself into more intimate contact with neighboring particles. Denser flocs may be produced by weaker bond forces, but these will have more particle-particle contacts and more bonds. The actual floc strength is a function of the individual bond strengths and the number of bonds formed or the total particle adhesion area. Turbulence during floc formation and later will affect the degree of repacking of the floc structure and flocs that are initially more diffuse may become more dense with exposure to non-destructive turbulence forces. This experiment did not examine this concept and exposed all flocs to potentially destructive forces at an early stage in their existence.

CONCLUSIONS

This study is the first in which polymeric flocculants have successfully been used in cross-flow particle filtration, in this case in the cross-flow microfiltration of bacterial lysate. Stable flux improvement was observed when a flocculant was used which produced small, dense flocs and which showed a broad optimum dose band in a dose curve experiment. These small flocs reduced in size during cross-flow experiments but did not release colloidal material into the suspending medium. A flocculant with a narrower optimum dose range and which gave a larger initial floc size did not increase the filtrate flux in cross-flow filtration. The flocs were catastrophically disrupted by the shear field and colloidal size material was released. The use of small, dense flocs is therefore a viable strategy for flux improvement in cross-flow filtration processes. There is an observed relationship between decreased particle size and decreased flux, in line with trends predicted by theoretical models.

ACKNOWLEDGEMENTS

This work was funded by Cytec Industries, Inc., Stamford, CT and by the Colorado Bioprocessing Center (CBC). Assistance is gratefully acknowledged from CBC Director Dr. Brian Batt, CBC staff members Bill Lauderdale and Steve White, and former CBC Director Dr. E. Dunlop.

REFERENCES

(1) Dickenson, C. *Filters and filtration handbook. (3rd ed.).* Elsevier, Oxford, 1992.

(2) Z.-G. Su and C.K. Colton. Crossflow Membrane Filtration. In *Protein Purification Process Engineering,* R.G. Harrison, editor. Marcel Dekker, New York, 1993.

(3) L.J. Zeman and A.L. Zydney. *Microfiltration and Ultrafiltration, Principles and Applications.* Marcel Dekker, New York, 1996.

(4) R.H. Perry, D.W. Green, and J.O. Maloney, *Perry's Chemical Engineers' Handbook. (6th ed.).* McGraw Hill, New York, 1984.

(5) C. Visvanathan and R. Ben Aim. Studies on Colloidal Membrane Fouling Mechanisms in Crossflow Microfiltration. *J. Membrane Sci.*, 45:3-15, 1989.

(6) A.G. Fane. Ultrafiltration of Suspensions. *J. Membrane Sci.*, 20:249-259, 1984.

(7) M.R. Doshi and D.R. Trettin. Ultrafiltration of Colloidal Suspensions and Macromolecular Solutions in an Unstirred Batch Cell. *Ind. Eng. Chem. Fundam.*, 20:221-229, 1981.

(8) A.L. Zydney and C.K. Colton. A Concentration Polarization Model for the Filtrate Flux in Crossflow Microfiltration of Particulate Suspensions. *Chem. Eng. Commun.* 47:1-21, 1986.

(9) R.H. Davis and J.D. Sherwood. A Similarity Solution for Steady-State Crossflow Microfiltration. *Chem. Eng. Sci.*, 45:3204-3209, 1990.

(10) M. Mietton Peuchot and R. Ben Aim. Improvement of Crossflow Microfiltration Performance with Flocculation. *J. Membrane Sci.*, 68:241-248, 1992.

(11) *Coagulation and Flocculation, Theory and Applications.* B. Dobiáš, editor. Marcel Dekker, New York, 1993.

(12) B. Koglin. Influence of Agglomeration on the Filtering Properties of Suspensions. *Chem.-Ing.-Tech.* 56:111-117, 1984.

(13) S. Vigneswaran and S. Boonthanon. Cross-flow Microfiltration with In-line Flocculation. *Water*, 29-31, 1992.

(14) V. Lahoussine-Turcaud, M. Wiesner, J.Y. Bottero, and J. Mallevialle. Coagulation-Flocculation with Aluminium Salts: Influence on the Filtration Efficacy with Microporous Membranes. *Water Research*, 26:695-702, 1992.

(15) H. Graham. Colloidal Properties of *Escherichia coli*. *Ph.D. thesis*. Colorado State University. In preparation.

(16) A/G Technology Corporation. *Operating guide*. A/G Technology Corporation Needham, MA, 1995.

(17) T.R. Camp and P.C. Stein. Velocity Gradients and Internal Work in Fluid Motion. *J. Boston Soc. Civ. Eng.*, 30:219-237, 1943.

(18) P.T. Spicer and S.E. Pratsinis. Coagulation and Fragmentation: Universal Steady-State Particle-Size Distribution. *AIChE Journal*, 42:1612-1620, 1996.

(19) R.J. Akers, A.G. Rushton, and J.I.T. Stenhouse. Floc Breakage: The Dynamic Response of the Particle Size Distribution in a Flocculated Suspension to a Step Change in Turbulent Energy Dissipation. *Chem. Eng. Sci.*, 42:787-798, 1987.

The Effect of Secondary Membranes on Protein Transmission in a Multicomponent System

Vinod Kuberkar and Robert H. Davis
Department of Chemical Engineering
University of Colorado
Boulder, CO 80309-0424

ABSTRACT

Crossflow microfiltration of yeast-protien mixtures was performed using 0.07 μm cellulose acetate membranes. Three distinct stages of protein transmission can be detected for the filtration of protein-only solutions. High transmission occurs when the membrane is being fouled internally. The transmission decreases sharply when cake formation occurs. After the cake is formed, and tangential shear prevents further deposition, the transmission gradually decreases. However, the yeast-protein suspensions behave differently. While the yeast decreases the overall flux through the membrane, it acts as a secondary membrane allowing only the protein molecules through the membrane, while preventing protein aggregates from fouling the membrane. This results in higher protein transmission for the filtration of yeast-protein suspensions compared to that of protein-only solutions.

The results indicate that an optimum yeast concentration exists which maximizes the long-term flux for yeast-protein mixtures. No trend was observed for long-term flux for yeast-protein mixtures with change in yeast concentration. The long-term transmission for yeast-protein mixture was always higher than that for protein-only solution.

INTRODUCTION

Crossflow membrane microfiltration is the process of separation of microparticles (particles with maximum dimensions between 0.02 μm and 10 μm) from their suspensions by forcing the fluid through narrow channels having microporous walls. The separation process is becoming popular in the petrochemical and especially in biotechnology industries.

As opposed to deadend filtration, where the suspension is forced normal to the membrane, in crossflow filtration, the suspension is forced tangential to the membrane. As the clear fluid is collected through the membrane, the rejected particles or solutes build up on the membrane. This constricts the channel and reduces the permeate flow through the membrane. This build-up stops after the tangential shear is large enough to prevent further deposition.

A high steady flux and complete protein transmission characterize an ideal membrane process for recovering proteins from a suspension containing cell or cell debris. A large amount of literature regarding protein filtration has been developed in recent years. Tracy and Davis (1994) studied fouling mechanisms for protein filtration. They observed the fouling to be both internal and external. Arora and Davis (1994) studied protein filtration through a yeast cake layer deposited on the membrane. The authors observed higher fluxes due to the presence of a yeast cake, as the yeast cake acts as a filter aid to remove protein foulants from the protein solution. Mueller and Davis (1996) studied filtration of protein solution through various membranes. The authors observed the transmission to be highest for cellulose acetate membranes, moderate for polysulfone, and least for polyvinylidene fluoride membranes. All these studies were done using a deadend filtration apparatus.

This work focuses on study of behavior of protein transmission and flux for crossflow filtration of yeast-protein mixtures. Changes in protein transmission with time for filtration of bovine serum albumin (BSA) solutions were studied. These changes were compared with those observed for filtration of yeast-BSA mixtures. The long-term flux and protein transmission were measured for all experiments. The variation of the long-term flux and the protein transmission with the change in yeast concentration for filtration of yeast-BSA mixtures were studied.

MATERIALS AND METHODS

Crossflow microfiltration experiments were done with 0.07 μm cellulose acetate membranes (Sartorious). The membranes were discarded after use. The clean membrane buffer flux was 0.06 cm/sec at 10 psi transmembrane pressure.

The schematic of experimental apparatus is given in Figure 1. The nitrogen pressure cylinder (US Welding, Industrial Grade) is used to pressurize feed and regeneration vessels (Alloy Products Corporation, one gallon). The feed reservoir is set on top of a magnetic stirrer (Thermolyne, Cimarec 3) so that the yeast-BSA mixture remains well mixed. The feed pump (Millipore, XX 80 000 00) pumps the feed through the membrane module (Millipore, Minitan-S). The retentate is recycled back to the feed reservoir. The permeate is collected in the permeate reservoir (4L flask). The permeate reservoir is on the balance (Mettler Instrument Corporation, PG 5002). The balance is connected to the computer (Gateway 2000, 4DX2-66V) through a serial port. To account for loss of permeate, the regeneration pump (Watson-Marlow, 101U) adds solution from the regeneration reservoir to the feed reservoir. The regeneration pump is controlled by the computer through the AD card (Data Translation, DT 2801). The solenoid valve (Burkhert Contromatic Corporation, 1053-S001-031-00) opens and allows permeate to flow when the experiment is started.

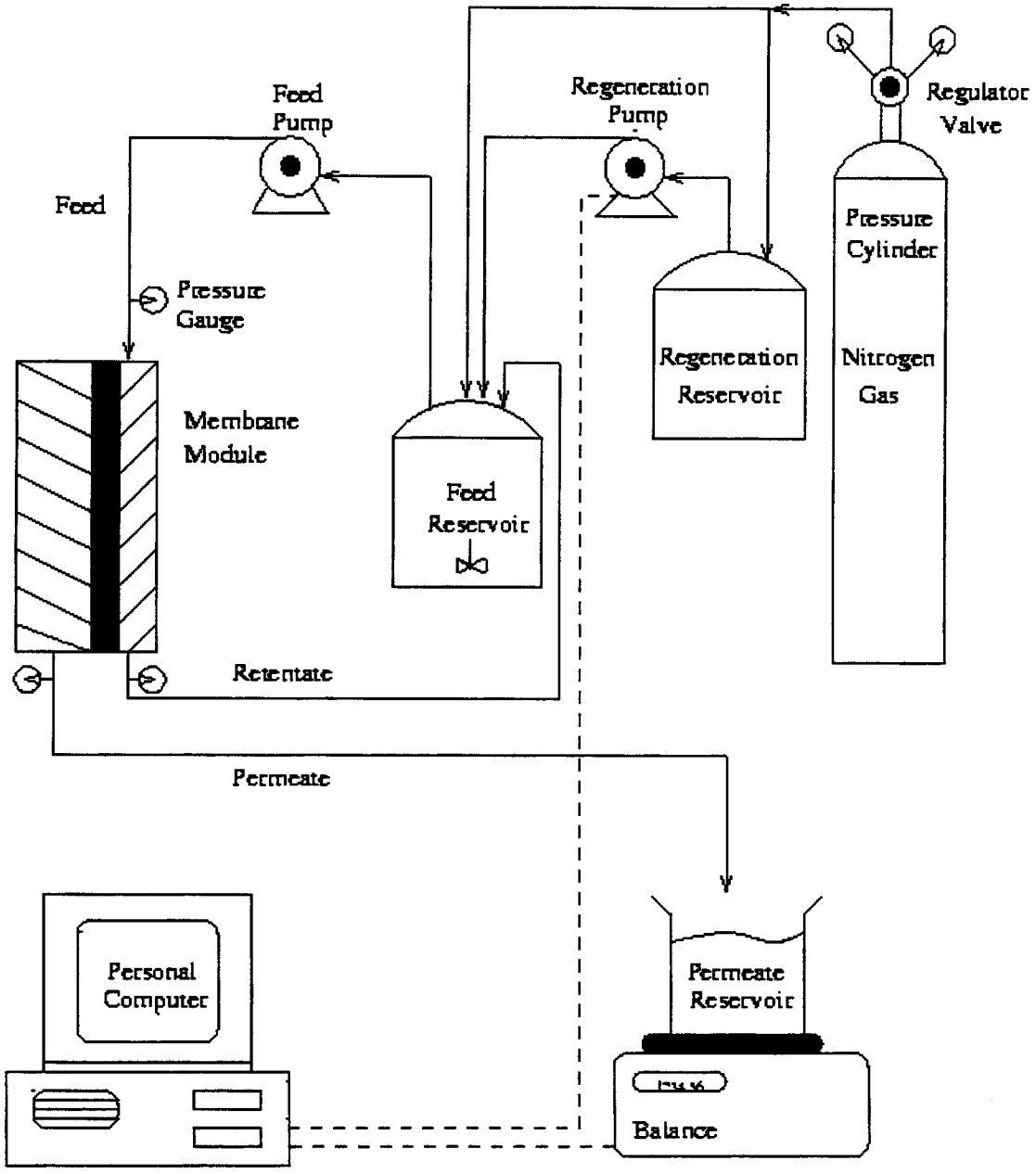

Figure 1: Schematic of the experimental setup

Yeast-BSA mixtures were prepared by mixing washed yeast (*Sacchromyces cerevisae*, commercially available Fleischmann's Active Dry Yeast) and BSA (Sigma, heat shocked fractionate, fraction V powder, catalog # A7906) of appropriate concentrations. Phosphate Buffer Saline (PBS) buffer was used as the suspending solution. The buffer was prepared by adding 80 g of NaCl (Fisher), 2 g of KCl

(Fisher), 14.4 g Na_2HPO_4 (Fisher), and 2.4 g KH_2PO_4 (Fisher) to 10 liters of deionized water. The yeast suspension was washed by centrifuging (Beckman GPR centrifuge) it for 10 minutes at 2500 RPM, discarding the supernatant, and resuspending the pellet. This procedure was repeated twice so as to wash the suspension three times.

The average forward transmembrane pressure drop was 10 psi. The recirculation flow rate of 6 ml/sec was used (which corresponds to the average velocity of 0.24 m/sec and the shear rate of 3600 1/sec at the membrane surface). The duration of all experiments was 4 hours (14,400 sec). The long-term flux was calculated by taking the average of the last 1000 seconds. The long-term transmission calculation was usually the average of the transmission of the last four samples taken.

Permeate samples were taken regularly (every 10 or 15 minutes). The protein concentration in the sample was determined using Protein Assay Kit (Sigma, catalog # P5656). In this test, an alkaline cupric tartarate reagent complexes with the peptide bonds of the protein and forms a purple color when the phenol reagent is added. The intensity of the color is read at 750 nm with a diode array spectrophotometer (HP 8452A). The concentration of BSA in sample is proportional to the optical density of the sample via a calibration curve.

Dry cell weight was determined after centrifuging the yeast suspension twice, washing in PBS buffer, and drying at 80 C over 24 hours. The weights were taken again after 48 hours to make sure they had not changed. The commercially available yeast is only 72 % in whole cells. The remaining 28 % is cell debris, salts, etc., which get thrown with the supernatant during washing. In this report, all yeast weights refer to nominal weights and not to the true dry cell weight (nominal weight is the amount of yeast (whole and broken) taken from the bottle).

RESULTS AND DISCUSSION

Figure 2 is a plot of Flux vs. Time of a BSA (2 g/L) run using a cellulose acetate membrane with a pore size of 0.07 μm. This plot reveals how quickly the flux decreases over time. The flux decreased rapidly until leveling off after 4000 sec. The fouled membrane flux at 14,400 sec was 0.00142 cm/sec. Over a time period of four hours, the flux through the membrane decreased more than 40-fold.

Figure 3 depicts the same experiment in a different way. Using the left ordinate axis, it is a plot of 1/Flux vs. Time. The curvature of an Inverse Flux vs. Time graph reveals whether the fouling is external or internal (Tracy and Davis, 1994). A concave curve indicates that the fouling is within the interior of the membrane. A convex plot reveals that the formation of a cake layer has occurred and the fouling is external. In Figure 3, notice that until about 2000 seconds, the fouling is internal. After 2000 seconds, the 1/Flux plot turns convex, indicating that the fouling is now external.

These results show that initially the proteins pass through the membrane. As time passes, however, the proteins bind to the pore walls, thereby constricting the pore. Once all possible internal fouling has occurred, the protein begins to form a cake layer on the external membrane surface. Since tangential shear prevents the formation of the cake layer past a certain thickness, the plot begins to level off after approximately 6000 seconds.

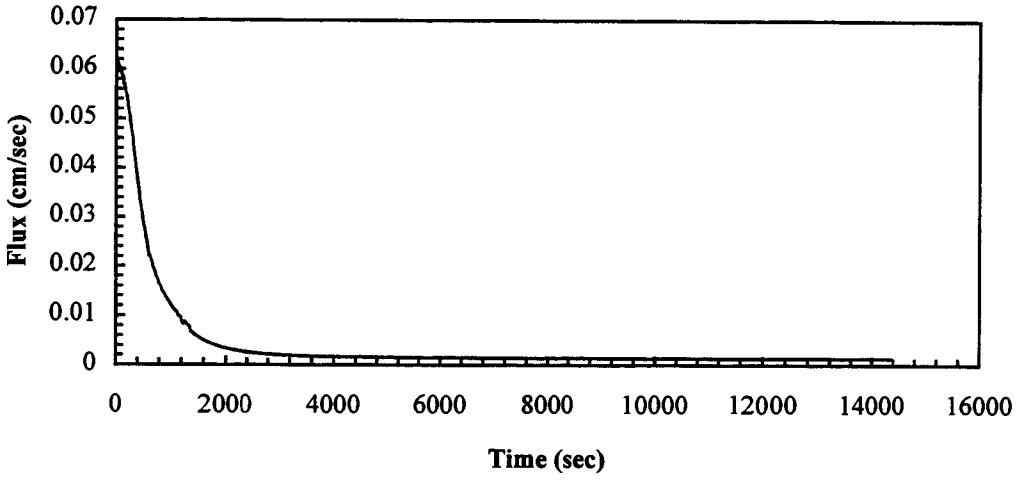

Figure 2: This plot of Flux vs. Time shows the quick decrease in flux (from 0.060 cm/sec to 0.0014 cm/sec) when a solution containing BSA (2 g/L) was filtered.

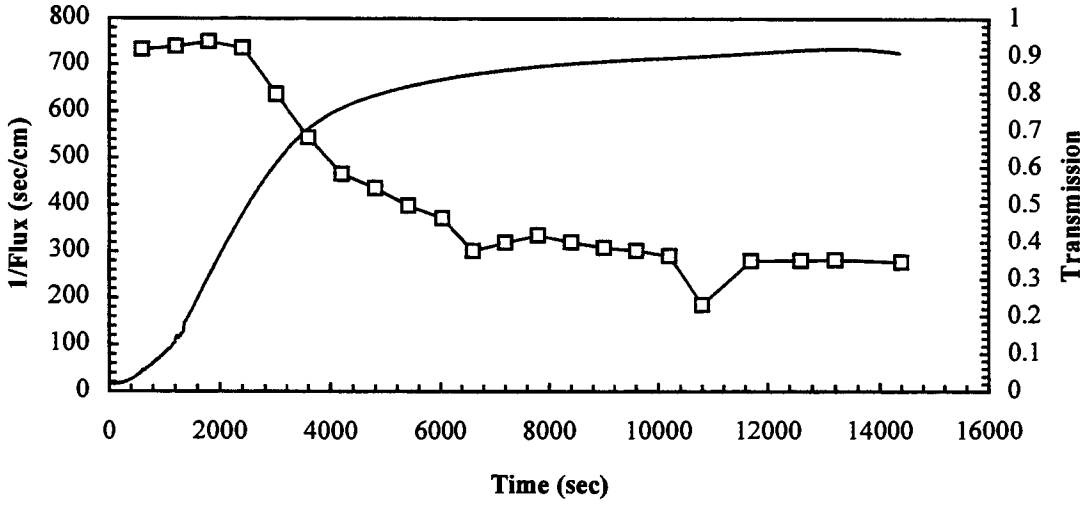

Figure 3: By plotting 1/Flux vs. Time, the curvature of the data reveals that internal fouling occurs first followed by external fouling. The Transmission vs. Time plot provides evidence that the largest decrease in protein transmission occurs when the external cake layer is forming.

On the right ordinate axis of Figure 3, a graph of Transmission vs. Time is plotted. During the internal fouling portion of the experiment (0-2000 seconds), the transmission remains high at approximately 90%. During the external fouling of the membrane (2000-6000 seconds), the transmission plummets to 45%. Throughout the rest of the experiment the transmission gradually decreases to a final average of 35%.

It has been proposed (Chandavarkar (1990), Arora and Davis (1994), and Guell and Davis (1996)) that the membrane fouling is primarily caused by BSA aggregates. BSA monomers have 17 disulfide bonds and one free thiol (-SH) group. The intermolecular disulfide bond formation results in formation of BSA dimers, which may form aggregates. The aggregates deposit near and/or inside membrane pores, and then act as nuclei for further deposition.

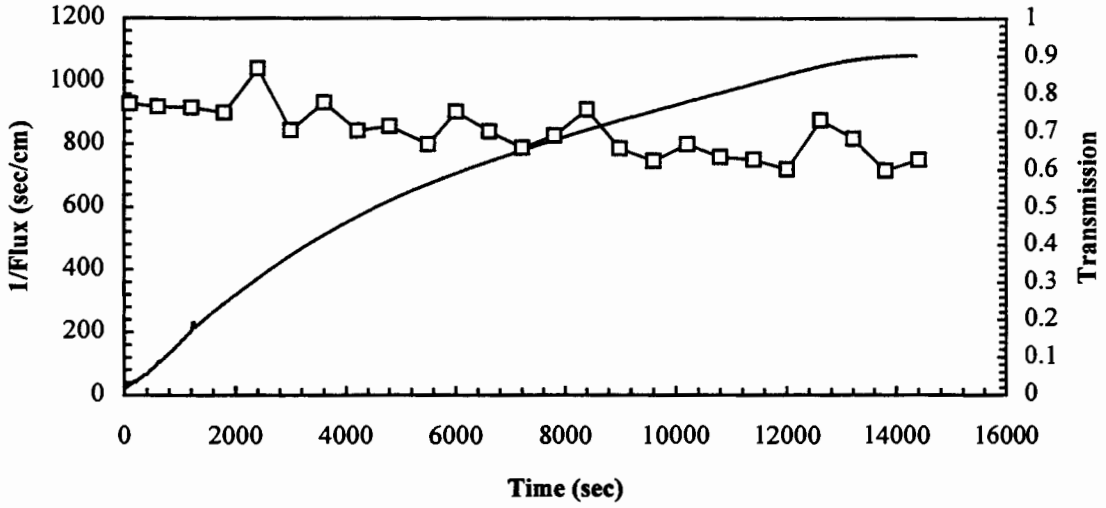

Figure 4: The 1/Flux vs. Time demonstrates the type of membrane fouling (initially internal, later external). Notice the absence of any sharp decrease in Transmission vs. Time plot.

Figure 4 is formatted exactly like Figure 3. It describes a system of yeast (10 g/L), BSA (3 g/L), and a 0.07 μm cellulose acetate membrane. The 1/Flux curve is entirely convex, except at small initial duration of experiment. The transmission is much different than that for the BSA only experiment. The transmission of protein across the membrane decreased gradually over the four hours from 90% to 75%. The phenomenon can be explained by proposing that the yeast forms a secondary membrane on top of the original membrane (Figure 5). The yeast layer prevents the protein aggregates from fouling the membrane. Instead, the protein molecules are allowed to pass through the membrane. So, the secondary membrane of yeast cake results in a low overall flux with relatively higher transmission throughout the experiment.

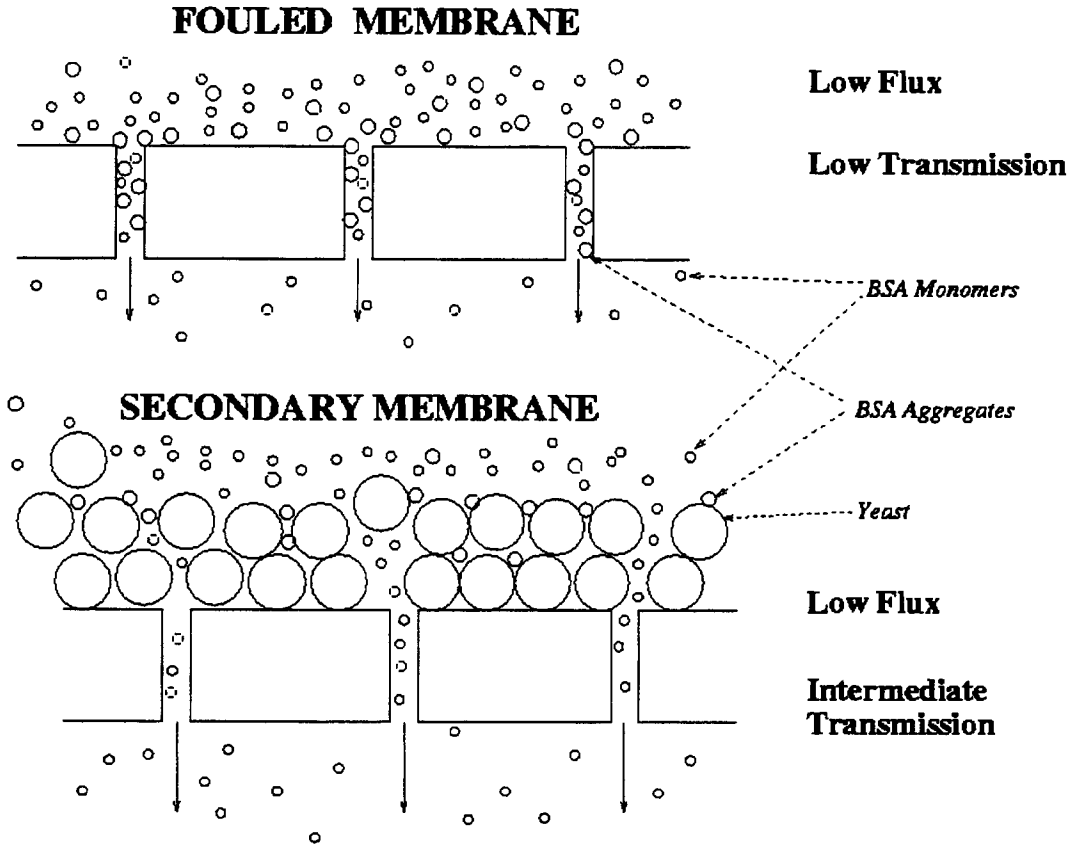

Figure 5: Schematic of yeast cake (secondary membrane) preventing protein aggregates from fouling the membrane (not to scale).

Figure 6 shows the variation of long-term flux with yeast concentration for filtration of yeast-BSA mixtures done using 0.07 μm cellulose acetate membrane, with BSA concentration at 2 g/L. The long-term flux for yeast-BSA mixtures is always lower than that for BSA-only solution. This is understandable as fouling due to BSA as well as yeast is present for yeast-BSA mixtures. At lower yeast concentrations, fouling due to BSA is significant. This happens as the yeast cake formation is slower for lower yeast concentrations. So the yeast cake does not provide significant protection against membrane fouling by BSA. This results in lower long-term flux. At very high yeast concentrations, the cake formation is quick and thus provides significant protection against membrane fouling by BSA. But the yeast cake itself provides high hydraulic resistance to the permeate flow. This causes lower long-term flux. Between these two extremes, an optimum yeast concentration exists (in this case, 5 g/L) which maximizes the long-term flux. At this concentration, the yeast cake provides significant protection against the BSA fouling by forming the yeast cake quickly, but does not provide very high hydraulic resistance to the permeate flow.

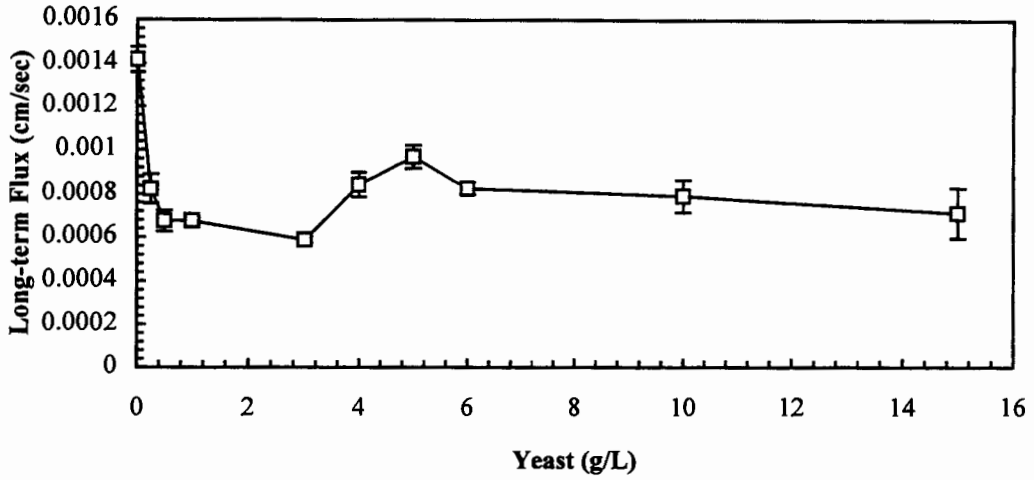

Figure 6: Plot of Long-term Flux vs. Yeast Concentration for yeast-BSA mixtures with BSA (2 g/L). Notice the maxima at yeast concentration of 4 g/L.

Figure 7 shows plot of long-term transmission vs. yeast concentration for filtration of yeast-BSA mixtures done using 0.07 μm cellulose acetate membrane, with BSA concentration at 2 g/L. The long-term transmission for yeast-BSA mixture is always higher than that for BSA-only solution. This is expected, as in the absence of yeast cake, BSA cake forms on the membrane. This results in lower protein transmission. In the presence of the yeast cake, BSA aggregates get trapped in the yeast cake. This prevents the BSA cake formation. So BSA monomers can approach the membrane pores through the relatively more permeable yeast cake. The relative variation of long-term transmission with yeast concentration for yeast-BSA mixture is not significant. The range of long-term protein transmission with yeast concentration for yeast-BSA mixture is between 60%-80%.

Figure 8 shows a plot of total permeate collected during the experimental duration (4 hours) vs. yeast concentration for filtration of yeast-BSA mixtures done using 0.07 μm cellulose acetate membrane, with BSA concentration at 2 g/L. Figure 8 shares some features of Figure 6, due to the same reasons (in fact, if the experimental duration is infinite, the total permeate plot will exactly resemble the long-term flux graph). The permeate plot exhibits very different behavior for very low yeast concentrations. The total permeate obtained for yeast-BSA mixture is comparable to (or higher than) that obtained for BSA-only solution. This behavior is total contrast with the long-term flux plot. This is because the fouling for yeast-BSA mixture is slower at lower yeast concentrations as compared to that for BSA solution. So even though the low yeast concentration is ineffective in long-term to prevent BSA fouling, it does slow it down for some period of time.

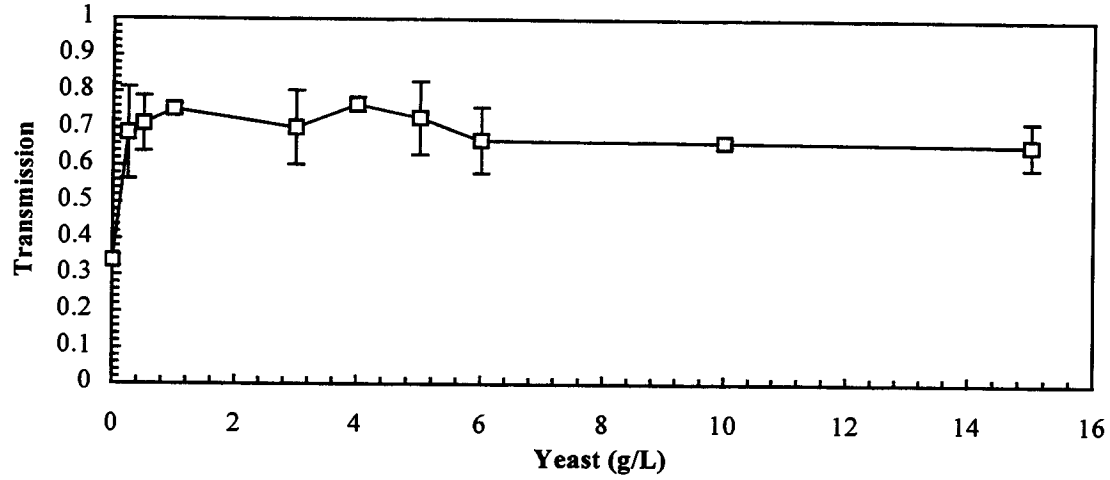

Figure 7: Plot of Transmission vs. Yeast Concentration with BSA (2 g/L). Notice that the transmission in absence of yeast (35%) is always lower than that in presence of yeast.

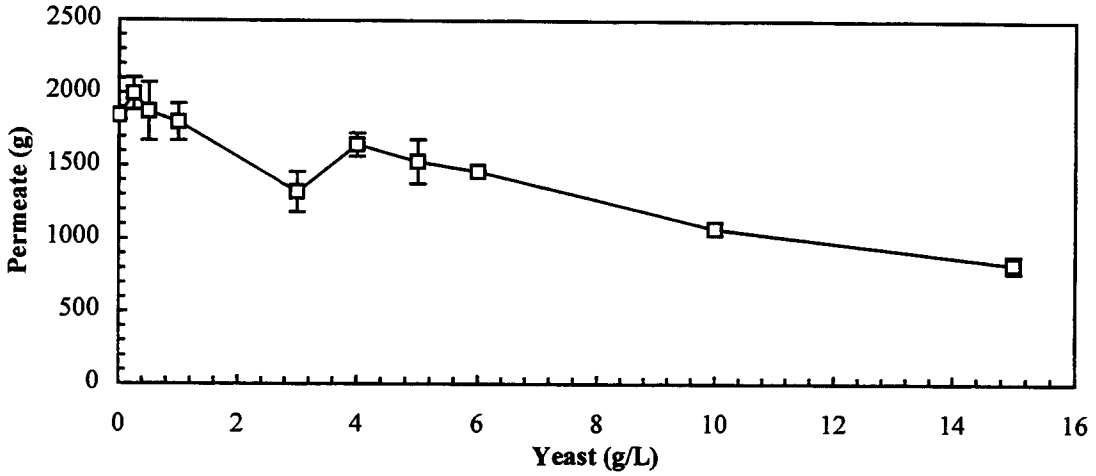

Figure 8: Plot of Permeate vs. Yeast Concentration for yeast-BSA mixtures with BSA (2 g/L). Notice that the total permeate for very low yeast concentration is comparable to (or higher than) that without yeast.

CONCLUSIONS

This study indicates importance of secondary membrane. For protein-only solutions, three stages of protein transmission are observed. The transmission is very high when the fouling is only internal. A sharp decrease in transmission occurs when external cake formation begins. The transmission begins gradual decrease as cake formation stops and cake consolidation begins. During filtration of yeast-BSA

mixtures, yeast cake forms secondary membrane which screens off protein aggregates, thus preventing protein cake formation. This results in higher protein transmission for yeast-BSA mixtures.

An optimum yeast concentration exists which maximizes flux for yeast-BSA mixtures. At lower yeast concentrations, significant internal fouling occurs as yeast cake formation is slower. This reduces the flux. At higher yeast concentrations, yeast cake provides significant hydraulic resistance for permeate flow, thus reducing the flux. At very low yeast concentrations, the rate of membrane fouling by protein aggregates is reduced significantly. This results in total collected permeate comparable to (or higher than) that collected for protein only solutions.

ACKNOWLEDGEMENTS

This work was supported by Colorado Institute for Research in Biotechnology and by the U.S. Bureau of Reclamation. The authors thank Fawad Ghafoori, Rory Moore, and Kristin Hendrickson for help with experiments. Rory Moore was supported by the National Science Foundation's Research Experiences for Undergraduate program.

REFERENCES

Arora, N., and Davis, R.H. (1994). Yeast cake layers as secondary membranes in dead-end microfiltration of bovine serum albumin. *J. Membr. Sci.* **92:** 247-256.

Chandavarkar, A.S. (1990). Dynamics of fouling of microporous membranes by proteins. Ph. D. Thesis, MIT, Cambridge, MA.

Mueller, J., and Davis, R.H. (1996). Protein fouling of surface modified polymeric microfiltration membranes. *J. Membr. Sci.* **116:** 47-60.

Parnham, C.S., and Davis, R.H. (1996). Protein recovery from bacterial cell debris using crossflow microfiltration with backpulsing. *J. Membr. Sci.* **118:** 259-268.

Romero, C.A., and Davis, R.H. (1991). Experimental verification of the shear-induced hydrodynamic diffusion model of crossflow microfiltration. *J. Membr. Sci.* **62:** 249-273.

Tracy, E.M., and Davis, R.H. (1994). Protein fouling of track-etched polycarbonate microfiltration membranes. *J. Colloid Interface Sci.* **167:** 104-116.

Lyophilization Induced Phase-Separation: Effects on Hemoglobin Structure

Martin C. Heller and Theodore W. Randolph
Department of Chemical Engineering
University of Colorado at Boulder
Boulder, CO 80309-0424

John F. Carpenter
Department of Pharmaceutical Sciences
University of Colorado Health Sciences Center
Denver, CO 80262.

ABSTRACT

Lyophilization, or freeze drying, of pharmaceutical proteins is often the only processing method that provides requisite long term product stability. Freezing and drying, however, can cause acute damage to proteins. To alleviate damage, formulations frequently include protein stabilizers (often polymers and / or sugars), as well as buffering salts and "inert" bulking agents. While great efforts are placed on developing a formulation and suitable lyophilization cycle, incompatibilities amongst components through freezing and drying have been almost completely ignored. We demonstrate that solutions of polyethylene glycol (PEG) and dextran, initially below critical concentrations for phase separation, do indeed experience a liquid-liquid phase separation induced by freeze concentration during the lyophilization cycle. The separation is shown to evolve with annealing at -7°C, and can be effectively inhibited simply by replacing NaCl with KCl in the formulation buffer. In addition, we show that phase separation causes unfolding of a model protein, recombinant hemoglobin, when freeze dried in the PEG / dextran system. When the phase separation is averted by switching to KCl, the protein structural damage is also avoided. Measurements of pH in the frozen solutions show that the structural damage is not a result of pH changes. We suggest that KCl forms a glass with rapid cooling which kinetically prevents the phase separation, and thus the protein structural damage.

INTRODUCTION

Lyophilization is often required in the processing of protein pharmaceuticals to provide a marketable product. With proper freeze drying, proteinaceous drugs are generally much more stable than in liquid formulations, easing transport and storage needs and improving shelf lives (Pikal, 1992). However, the processes of freezing and drying can cause irreversible damage to labile proteins, manifested as structural denaturation and loss of biological efficacy (Arakawa et al., 1993). To lessen the stresses of freeze drying, formulations commonly include excipients added as protein stabilizers, such as sugars, polyols, amino acids and a number of polymers (Arakawa et al., 1993). There is evidence that the stresses of freezing and drying need to be

addressed separately, sometimes requiring multiple stabilizers in a single formulation (Carpenter et al., 1993; Prestrelski et al., 1993). In addition, "inert" bulking agents are likely to be included to assure an aesthetically pleasing final product (Pikal, 1992). The resulting formulation can be a complicated mixture of macromolecular excipients, buffering salts, and protein. An effective freeze drying process involves the delicate, and highly empirical, balancing of formulation development with process conditions. While the various components employed may demonstrate single phase behavior in liquid solution, their compatibility through freezing and drying is not guaranteed, and to date, has generally been ignored.

An inevitable consequence of lyophilization is the concentration of solutes by the bulk formation of pure ice crystals. Solutes in the non-ice phase can reach concentrations as high as 20-50 times their initial concentration (Franks, 1992; Hatley et al., 1993), greatly increasing molecular interactions that were negligible in the dilute solution and, concomitantly, the propensity for phase separation between components. Recently, the existence of multiple glass transitions of maximally concentrated frozen solutions containing polyvinylpyrrolidone (PVP) and phosphate salts (Her et al., 1995) as well as PVP and dextran (Izutsu et al., 1996) have been reported. Multiple glass transitions were attributed in both studies to multiple amorphous phases in the freeze-concentrate arising from a phase separation between formulation components. Numerous systems relevant to protein formulation have demonstrated limited thermodynamic compatibility, leading to liquid-liquid phase separation in aqueous solutions. These include polymer-polymer (e.g., polyethylene glycol (PEG) - dextran, PVP - dextran, ficoll - dextran) and polymer - salt (e.g., PEG - potassium phosphate, PEG - sodium carbonate) systems commonly used in two-phase partitioning (Albertsson, 1986; Zaslavsky, 1995), as well as protein - protein (Broide et al., 1991; Tolstoguzov, 1988), protein - polysaccaride (Tolstoguzov, 1988), and protein - surfactant (Guo et al., 1990) systems. A common feature of these systems is the requirement of critical concentrations of components for phase separation. Thus, it is plausible that solute systems in a single phase prior to freezing would readily phase separate due to freezing-induced concentration. Such a phase separation occurring in a freeze drying formulation further complicates an already complex system, potentially providing additional avenues for protein damage. In addition to the above mentioned systems, the covalent attachment of PEG to protein surfaces for the purpose of increasing sera half-lives or reducing antigenicity (Kinstler et al., 1996) raises added questions of component compatibilities. Difficulty encountered in the freeze drying of such PEGylated proteins may in fact be related to a phase separation event since the attachment of the sterically excluded PEG is certain to alter the protein's compatibility with other formulation components.

We (Heller et al., 1996) have previously demonstrated that phase separation occurring during the lyophilization cycle results in an unfolded protein in the dried solid. In the current study, we demonstrate the kinetically limited nature of freezing-induced phase separation by manipulation of a PEG / dextran system through annealing and minor component changes. In addition, we provide data showing loss of native structure of a model protein, recombinant hemoglobin, in the dried solid as a direct result of the phase separation. Substituting KCl for NaCl in the studied system inhibits the liquid-liquid phase separation. This substitution in turn prevents the protein damage resulting from the phase separation, offering practical suggestions for avoiding the detriments of phase separation.

MATERIALS AND METHODS

Materials. Recombinant hemoglobin (rHb1.1) was provided by Somatogen, Inc. (Boulder, CO) in a solution of 5 mM potassium phosphate, 150 mM NaCl buffered at pH 7.4 (buffer A) with a protein concentration of 50 mg/ml. rHb1.1 is a recombinant human hemoglobin mutant that contains a glycine linkage of the α-globin subunits which prevents dissociation into $\alpha\beta$ dimers. An additional Asn-108$\beta \rightarrow$ Lys mutation reduces oxygen affinity (Looker et al., 1992). For KCl containing experiments, rHb1.1 was thoroughly dialyzed against 5 mM potassium phosphate, 150 mM KCl (pH 7.4) (buffer B). Polyethylene glycol 3350 (PEG) (average molecular weight of 3350 Da) was obtained from Sigma Chemical Co. and used as received. Dextran T500 (average molecular weight of 500,000 Da) was obtained from Pharmacia Biotech, free of heavy metal contaminations, and used as received. Stock solutions of PEG or dextran were made at 20% (w/w) in buffer A (or buffer B, where appropriate). Samples for lyophilization were prepared by combining stock solutions to obtain concentrations of 4% (w/w) PEG, 4% (w/w) dextran and 10 mg/ml hemoglobin. Salt concentrations were maintained at 5 mM potassium phosphate and 150 mM NaCl (or KCl) throughout.

Lyophilization. Aliquots of 1 mL were lyophilized in 5 mL serum vials (West Co.) using a FTS Systems microprocessor controlled tray dryer. For annealing experiments, samples were quench frozen by dipping vials in a dry ice / acetone bath (temperature ca. -82°C) for 1 minute. Vials were then immediately placed on the dryer shelf which was pre-cooled to -7°C. This was repeated at regular intervals to provide samples that had annealed at -7°C for various times (i.e., the first vials frozen and added to the shelf were the longest annealed samples, while the last vials added represent the "time zero" samples). After the time zero samples were added, the shelf set-point was reduced to -50°C, and sample temperatures were held below -30°C for 120 minutes before initiating drying. Primary drying proceeded at 60 mT vacuum with the shelf temperature set at -20°C, for 1000 minutes. Samples typically maintained temperatures below -30°C due to evaporative cooling, but arrived at shelf temperature prior to initiation of secondary drying steps. Secondary drying consisted of three steps, each of 120 minutes to 0°C, 10°C and 25°C, during which a vacuum of 60 mT was maintained.

Infrared Spectroscopy. Protein secondary structure was monitored using Fourier transform infrared spectroscopy (FTIR). Spectral collection and processing was as previously described (Heller et al., 1996). Briefly, lyophilized samples were compressed into a KBr pellet and placed immediately in the IR sample chamber. Spectra were collected with a Nicolet Magna Model 750 spectrometer, averaging 256 scans with a 4 cm^{-1} resolution. Second derivative analysis was used as the band-narrowing technique. Water vapor contributions were subtracted following established criteria (Dong et al., 1994), a seven-point smoothing was performed to remove possible white noise, and a baseline correction was performed over the amide I region (1700 cm^{-1} - 1600 cm^{-1}) following the criteria of Dong (Dong et al., 1995). Spectra were finally normalized by their total area over the amide I region to allow for direct comparison between spectra. Reported α-helix band depths are the greatest negative displacement of second derivative spectra at ~1656 cm^{-1}. IR spectra analyzed in this fashion demonstrated a high level of repeatability: spectra from 3 separate lyophilization annealing experiments (samples were: 4% PEG, 4% dextran, 5 mM PO_4, 150 mM NaCl, 10 mg/ml Hb, 4 hours of annealing at -7°C) gave a mean α-helix band depth of -0.0286 with a standard deviation of 0.000669 and a 95% confidence interval of 0.00166.

pH Measurements of Frozen Samples. pH measurements of frozen solutions were conducted according to previously described methods (Anchordoquy et al., 1996; Gomez, 1995) using a Friscolyte "B"electrode (LoT 401-60-S7/120, Mettler-Toledo). Sample temperatures were monitored using a K-type wire thermocouple attached directly to the pH electrode. Since this electrode cannot be operated below ~ -30°C, the dry ice / acetone quench freezing had to be substituted with freezing the sample by submersing in a circulating water / ethylene glycol bath precooled to -20°C. After the samples were completely frozen, the bath was warmed to -7°C and pH changes were monitored while annealing at this temperature.

Scanning Electron Microscopy. Lyophilized cake structures were examined using an ISI-SX-30 scanning electron microscope (SEM) operating at an acceleration voltage of 30 kV. Samples were adhered with a graphite adhesive to SEM stubs and gold sputter coated. This preparation was compared with samples prepared using a low temperature plasma coater to assure that the observed morphology was not an artifact of local melting of the cake structure. The low temperature preparation method gave identical cake morphology. Mean diameters of the dispersed phase were acquired by measuring a statistically significant number of droplets on the SEM images.

Thermal Analysis. Differential scanning calorimetry was performed on a Perkin-Elmer DSC-7. Aliquots of 20 µl were sealed in aluminum pans and cooled from 25 °C to -50 °C at 25 °C/minute, held at -50 °C for 5 minutes, then scanned till 0 °C at 5 °C/minute.

Powder X-Ray Diffraction. Powder X-ray diffraction studies of freeze-dried samples were carried out using a Sintag system with Ni-filtered Cu-Kα radiation. Samples were scanned from 25 to 55° (2θ) at a rate of 2° /minute.

RESULTS

Liquid-liquid aqueous phase separation occurs when enthalpically unfavorable interactions between unlike solutes overcome the entropic energy gain associated with complete mixing (Gustafsson et al., 1986). The result is two (or more) distinct equilibrium phases, each rich in one solute, which greatly reduces the interaction of incompatible solutes. The phase separation event, then, requires critical concentrations of solutes for the enthalpic contribution to become dominant. The phase behavior of aqueous solutions of PEG and dextran is well established (Albertsson, 1986). The critical concentrations for the formation of a two-phase system at 0°C are approximately 5 % w/w PEG 3350 and 5 % w/w dextran T500. Thus, the system of 4% PEG and 4% dextran studied here is well below the two phase region at 0°C and remains single phase up until the point of ice formation (usually around -10°C). It is expected, however, that freeze concentration will force the system into the two phase region, making the formation of a new phase thermodynamically favorable.

Evidence of Freeze-Concentration Induced Phase Separation. The appearance of the freeze-dried cake for samples containing 10 mg/ml recombinant hemoglobin (rHb1.1), 4% PEG and 4% dextran is shown in figure 1. Images a, b and c are of samples formulated with buffer A. The emergence of a second phase of spherical domains dispersed in a continuous phase is clearly evident. This closely resembles the dispersed droplet phase one would expect during the early stages of an aqueous liquid-liquid phase separation. Further, it is clear that the dispersed phase domain size evolves towards larger average drop sizes with annealing at -7°C (figure 2). While

the sample remains frozen at this temperature, there is still adequate macromolecular motion in the concentrated non-ice fraction to allow the development and ripening of two distinct phases, presumably one rich in PEG, the other rich in dextran. Images of KCl containing samples (figure 1 d, e & f), however, do not show the existence of a second discrete droplet phase. The dried solid is instead made up of a fine networking structure, typical of amorphous freeze-dried materials.

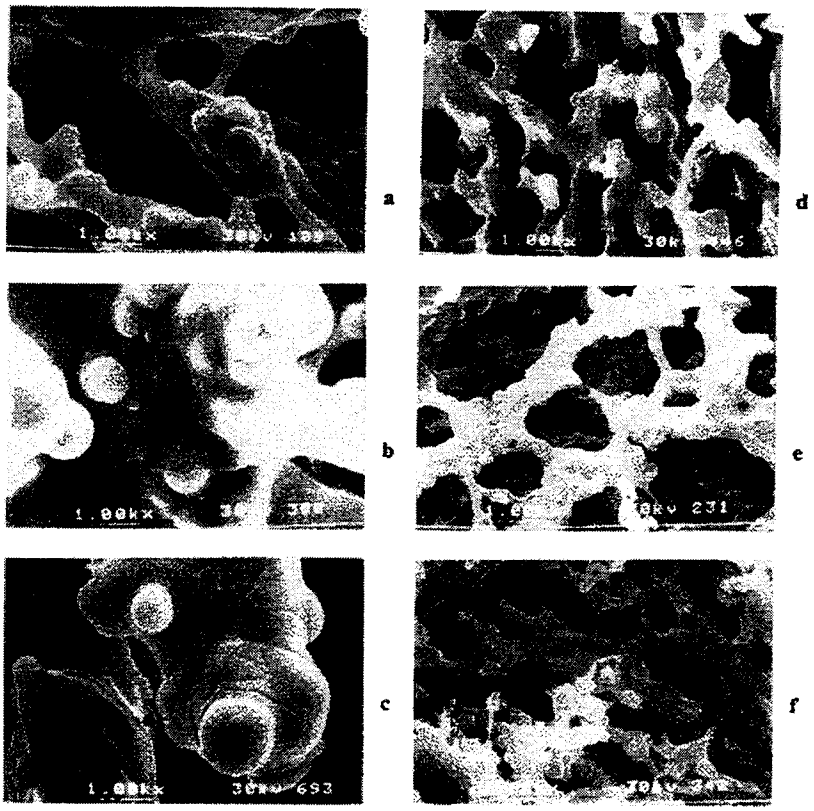

Figure 1. SEM photographs of the lyophilized cake showing the emergence of the PEG / dextran phase separation. Samples containing 10 mg/ml hemoglobin, 4% PEG, 4% dextran, in buffer A (5 mM phosphate, 150 mM NaCl) were allowed to anneal at -7°C prior to freezing for: a) 0 hours, b) 6 hours, and c) 12 hours. Images d, e, & f are from samples in buffer B (NaCl replaced by KCl), annealed for the same respective intervals as a, b, & c. Magnification is 1000x. The longer elevated bar directly below "1.00kx" is a 10μm marker.

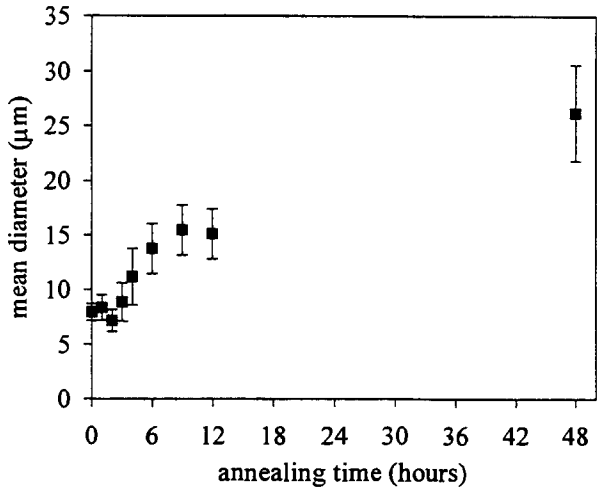

Figure 2. Growth of droplet-like dispersed phase as determined by SEM photographs of freeze dried samples containing 10 mg/ml hemoglobin, 4% PEG, 4% dextran, 5 mM phosphate, and 150 mM NaCl. Annealing time is at -7°C prior to drying. Error bars represent a 95% confidence interval.

Hemoglobin Structural Studies. We first examined the effect of freeze-drying recombinant hemoglobin in 4% PEG and 4% dextran on protein secondary structure in the dried solid. Figure 3 shows the conformationally-sensitive amide I region of the second derivative infrared spectrum of native hemoglobin in aqueous solution (solid trace). Native hemoglobin secondary structure is dominated by α-helices (87% by x-ray crystallography (Levitt et al., 1977)). The strong absorbance band at 1656 cm^{-1} in the FTIR spectrum is indicative of α-helical secondary structure. Also shown in figure 3 are the spectra of hemoglobin samples in the dried solid, lyophilized in buffer A (dotted trace) and in a solution containing 4% PEG and 4% dextran (dashed trace) which was processed without annealing. There is a clear decrease in the depth of the band at 1656 cm^{-1} (decrease in absorbance) for hemoglobin lyophilized in buffer alone relative to the solution state control. This decrease in the α-helix band is compensated by an increased absorbance at wavenumbers corresponding to other types of non-native secondary structure (beta sheet ca. 1610 - 1640 cm^{-1}, beta turn at 1670 - 1695 cm^{-1}, etc.), indicating that freeze-drying of hemoglobin in buffer alone causes significant denaturation of the protein. The partial retention of native α-helix band area for the polymer containing sample indicates that the 4% PEG/ 4% dextran system, when processed without annealing, offers some protection to the protein from the denaturing stresses of lyophilization.

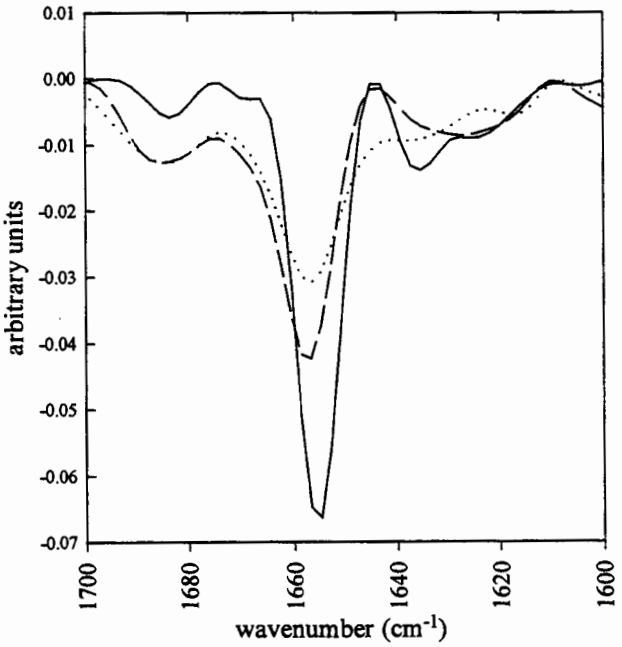

Figure 3. Amide I region of the second derivative infrared spectra of hemoglobin in solution (solid trace), and in the dried state, freeze dried in the presence of buffer A (dotted trace) and with the addition of 4% (w/w) PEG and 4% (w/w) dextran (dashed trace). The solution spectrum is considered native; deviations from this spectrum are indicative of secondary structural denaturation.

Annealing Experiments. While it is clear that the PEG / dextran system provides some protection during freezing and drying, the effect of a PEG / dextran phase separation on hemoglobin structure becomes evident with frozen samples allowed to anneal at -7°C prior to drying. As mentioned previously, samples at this temperature remain frozen, and thus freeze-concentrated, but there is adequate macromolecular motion to allow the relaxation of kinetically

hindered events such as phase separation. Figure 4 shows the depth of the α-helix band from second derivative IR spectra of hemoglobin in the dried state plotted versus sample annealing time at -7°C. The α-helix band is considered the primary indicator of native structure in these hemoglobin studies, and IR spectra have thus been reduced to this band depth for clarity. There is a definite decrease in α-helix content with annealing time for the samples formulated with buffer A, with an asymptotic value being reached after about 18 hours. The partial "protection" to the protein offered in this polymer system as seen in figure 4 is entirely overcome with annealing at -7°C, such that the degree of protein damage becomes greater than that seen in samples lyophilized from just buffer (fig. 3 & 4). The decrease in α-helix content with annealing does *not* occur, however, in samples formulated with buffer B, where NaCl in the formulation is simply replaced with KCl. In fact, there is virtually no change in the α-helix content for the KCl containing samples over the annealing times studied. In the absence of polymer (i.e., for hemoglobin freeze dried in phosphate buffer and salt), there is essentially no change in the protein structure in the dried state as determined by FTIR when switching from NaCl to KCl (data not shown).

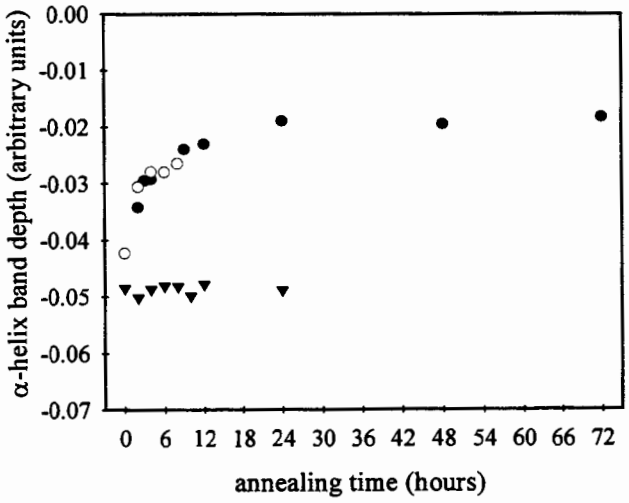

Figure 4. Depth of the α-helix band (ca. 1656 cm^{-1}) from second derivative infrared spectra of lyophilized hemoglobin as a function of sample annealing time at -7°C prior to drying for hemoglobin lyophilized with 4% PEG, 4% dextran in buffer A (NaCl) (●,○) and 4% PEG, 4% dextran in buffer B (KCl) (♦). Open circles represent a repeated experiment.

pH of Frozen Solutions. A well known potential danger of the use of phosphate buffers in freeze drying formulations is the preferential precipitation of sodium phosphate salts (Murase et al., 1989; van den Berg et al., 1959). The solubility of disodium phosphate is considerably lower than that of monosodium phosphate, and the disodium salt often will precipitate during the freezing step, causing pH reductions as great as 3 pH units in the remaining solution (van den Berg et al., 1959). Frozen pH results shown in figure 5 demonstrate, however, that while the buffer system used in this study does experience a significant pH decrease in the absence of polymer, the shift is almost completely damped in the presence of polymer. The prevention of acidification by high concentrations of polymers has been observed previously and attributed to

inhibition of disodium phosphate crystallization by the polymer (Anchordoquy et al., 1996). The protein denaturation seen in figure 4 is thus unlikely to be the result of a pH shift occurring during the annealing step.

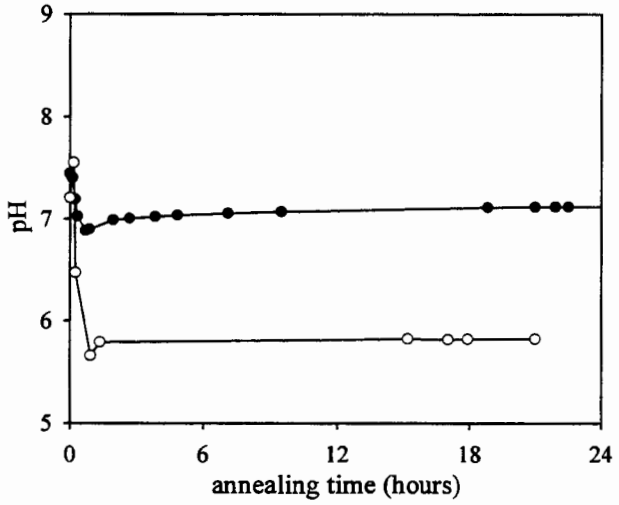

Figure 5. pH of frozen solutions of buffer A (5 mM potassium phosphate, 150 mM NaCl, pH 7.4) (O), and with 10 mg/ml recombinant hemoglobin, 4% PEG, and 4% dextran (●). Samples were initially frozen at -20°C and then allowed to anneal at -7°C.

DISCUSSION

It is apparent that the protein damage fostered during annealing as seen in figure 4 is related to a liquid-liquid phase split developing while samples are in a freeze-concentrated state. Supercooled samples of 4% PEG / 4% dextran remain homogeneous at temperatures below -7°C. As the solution freezes, however, the formation of pure ice concentrates the polymers (and other solutes), forcing them into a region of concentration where phase separation is thermodynamically favorable. The kinetics of this separation are dramatically slowed by elevated viscosities due to low temperatures and high concentrations, and eventually are halted altogether as the temperature is further decreased and the maximally concentrated solution goes through a glass transition (Franks, 1993). However, when the frozen system is allowed to anneal at -7°C, creating an ice phase in equilibrium with a freeze-concentrated liquid phase (or phases), the kinetically hindered phase separation occurs at a rate suggestive of diffusion limited growth (Shepilov, 1992) as seen in the growth of the dispersed phase shown in figure 2.

The increase in protein unfolding with annealing seen in figure 4 makes clear the counteracting effects of the protection provided by the polymers and the damage incurred by the phase separation event. The phase separation introduces a great excess of interfacial area, estimated by the appearance of the dried cake to be on the order of 550 cm^2/ml. This interface is between two solid phases in the dried cake, and not the solid/air surface area that is measurable

by techniques such as BET gas adsorption. The presented value was obtained by calculating the surface area of an average number of spheres of average diameter (10 μm) in a "volume" of dried solid seen in the SEM image. If the *anticipated* equilibrium volume were dispersed as 10 μm droplets (the experimental system likely does not reach complete equilibrium), the phase interfacial area would be about 1800 cm^2/ml. The surface area thus obtained is a rough estimate, but it is large compared to the initial vial-liquid and liquid-air surface areas (5.5 cm^2 and 2.5 cm^2, respectively). Proteins are known to concentrate, and even denature, at interfaces (Macritchie, 1978). The large excess of interface that a phase separation creates renders added stresses that can cause proteins to denature. Further, as the two phases dehydrate and shrink at different rates through drying, shear stresses will arise that might be detrimental to protein structure. The appearance of cracks along the interfaces in the dried cake (figure 1, especially image c) provides evidence for such differential shrinkage and the stresses it can impose. Finally, depending on the nature of the phase separating system, the protein will have a thermodynamic preference for one phase over the other and may partition into a phase with very low concentration of an intended stabilizer, reducing the protective effect. In room temperature phase separating systems of PEG and dextran (7% PEG 3350 / 7% dextran T500 in buffer A), hemoglobin partitions preferentially to the dextran phase with a partition coefficient (PEG phase/dextran phase) of 0.3-0.5 (Albertsson, 1986; Heller et al., 1996).

The system formulated in buffer B offers an important contrast to the freezing induced phase separation seen in the buffer A samples. We provide the first report that the detrimental effects of phase separation on protein structure can be inhibited by a simple alteration in solution components. Both KCl and NaCl have demonstrated only minor effects on the phase behavior of PEG / dextran systems at ambient temperatures (Albertsson, 1986; Zaslavsky, 1995), and to this end, the phase separation occurs at essentially the same concentrations at room temperature in both systems. We suggest that in our system, the propensity for KCl to form a stable glass when cooled rapidly is much greater than that for NaCl. Under the rapid dry ice / acetone quench freezing used in this study, it is likely that KCl forms a glassy solid which in turn inhibits the PEG / dextran phase separation. Differential scanning calorimetry performed on polymer containing frozen samples (in either buffer A or B) does not reveal the eutectic melting events seen in the absence of polymer (data not shown). Powder x-ray diffraction performed on the dried cake reveal faint crystal patterns in both NaCl and KCl samples (data not shown). Crystallization can occur at any point during the freezing *or* drying, however, so the appearance of small amounts of crystalline material in the dried solid does not reject the possibility of an amorphous structure in the frozen solution. The appearance of the dried cake in figure 1 (d, e & f) further suggest the formation of glassy KCl. The fine networking structure is indicative of a glass transition early in the freezing and cooling process, resulting in smaller ice domains (voids in the dried cake) that do not experience significant growth with annealing at -7°C. The glassy state of KCl also kinetically prevents the nucleation of the PEG / dextran phase separation by inhibiting the necessary molecular motions. It is expected that two distinct phases are still thermodynamically favorable, but the separation is simply prevented from occurring due to the high viscosities created by the glassy KCl. More importantly, whatever the mechanism of the KCl effect, preventing the phase separation in turn prevents the structural damage to hemoglobin.

CONCLUSIONS

The PEG / dextran system considered here demonstrates that component incompatibilities need to be considered when designing an effective formulation for protein lyophilization. A phase separation occurring between incompatible components creates yet another avenue for the destabilization and denaturation of already labile proteins. The creation of multiple non-ice phases, each presumably with unique glass transitions and drying characteristics, also further complicates the lyophilization process design. We have demonstrated that single-phase solutions of PEG and dextran are driven into a region of liquid-liquid phase separation by freeze concentration. The separation is kinetically hindered due to high viscosities and ice domains, leaving an excess of interfacial area in the dried solid. Recombinant hemoglobin freeze dried in this PEG / dextran system shows loss of native structure resulting from the phase separation. A simple replacement of NaCl with KCl in the formulation prevents the phase separation from occurring and concomitantly, prevents the structural denaturation of hemoglobin. While the phase separation tendencies of aqueous solutions of PEG and dextran are well known due to uses in purification processes, numerous other less obvious incompatibilities have been observed between components that are regularly included in protein formulations (Albertsson, 1986; Broide et al., 1991; Guo et al., 1990; Her et al., 1995; Izutsu et al., 1996; Tolstoguzov, 1988; Zaslavsky, 1995). Although *intentional* annealing may not be prevalent in industrial freeze drying, the heat duty of cooling large batches often makes achievable cooling rates quite slow. Thus, samples can spend considerable time in the freeze concentrated state, allowing phase separations to progress. Furthermore, we speculate that difficulties in formulating PEGylated proteins may arise from such phase separating components. PEG's relatively hydrophobic nature and large volume of exclusion increase its incompatibilities with a wide variety of other species, including salts, sugars, and other polymers. Clearly, there is a lack of knowledge of the behaviors of common formulation components at the low temperatures and high concentrations encountered in typical freeze drying applications, making predictions of phase separating tendencies difficult. It appears, however, that the damaging effects of a phase separation may be contained by straight forward kinetic orchestration that prevent the thermodynamic incompatibilities from being physically realized. Such manipulations may include altering process parameters to reduce time spent at temperatures above a glass transition, or by minor changes of solution components to enhance glass formation. A full understanding of these effects is needed if freeze-drying of protein drugs is to be reduced to a rational, predictable process.

REFERENCES

Albertsson, P.-Å. *Partition of Cell Particles and Macromolecules*; 3rd ed.; John Wiley & Sons: New York, 1986.

Anchordoquy, T. J.; Carpenter, J. F. Polymers Protect Lactate Dehydrogenase during Freeze-Drying by Inhibiting Dissociation in the Frozen State. *Arch. Biochem. Biophys.* **1996**, *332*, 231-238.

Arakawa, T.; Prestrelski, S. J.; Kenney, W. C.; Carpenter, J. F. Factors affecting short-term and long-term stabilities of proteins. *Adv. Drug Delivery Rev.* **1993**, *10*, 1-28.

Broide, M. L.; Berland, C. R.; Pande, J.; Ogun, O. O.; Benedek, G. B. Binary-liquid phase separation of lens protein solutions. *Proc. Natl. Acad. Sci. USA* **1991**, *88*, 5660-5664.

Carpenter, J. F.; Prestrelski, S. J.; Arakawa, T. Separation of Freezing- and Drying-Induced Denaturation of Lyophilized Proteins Using Stress-Specific Stabilization I. Enzyme Activity and Calorimetric Studies. *Arch. Biochem. Biophys.* **1993**, *303*, 456-464.

Dong, A.; Caughey, W. S. Infrared Methods for Study of Hemoglobin Reactions and Structures. *Methods Enz.* **1994**, *232*, 139-175.

Dong, A.; Prestrelski, S. J.; Allison, S. D.; Carpenter, J. F. Infrared Spectroscopic Studies of Lyophilization- and Temperature-Induced Protein Aggregation. *J. Pharm. Sci.* **1995**, *84*, 415-424.

Franks, F. Freeze-Drying: A Combination of Physics, Chemistry, Engineering and Economics. *Jpn. J. Freezing and Drying* **1992**, *38*, 5-16.

Franks, F. Solid aqueous solutions. *Pure & Appl. Chem.* **1993**, *65*, 2527-2537.

Gomez, G. Crystallization-related pH changes during freezing of sodium phosphate buffer solutions. PhD Thesis. University of Michigan, Ann Arbor, MI, 1995.

Guo, X.-H.; Chen, S.-H. Observation of Polymerlike Phase Separation of Protein-Surfactant Complexes in Solution. *Phys. Rev. Lett.* **1990**, *64*, 1979-1982.

Gustafsson, A.; Wennerstrom, H.; Tjerneld, F. The nature of phase separation in aqueous two-polymer systems. **1986**, *27*, 1768-1770.

Hatley, R. H. M.; Mant, A. Determination of the unfrozen water content of maximally freeze-concentrated carbohydrate solutions. *Int. J. Biol. Macromol.* **1993**, *15*, 227-232.

Heller, M. C.; Carpenter, J. F.; Randolph, T. W. Effects of Phase Separating Systems on Lyophilized Hemoglobin. *J. Pharm. Sci.* **1996**, *85*, 1358-1362.

Her, L.-M.; Deras, M.; Nail, S. L. Electrolyte-Induced Changes in Glass Transition Temperatures of Freeze-Concentrated Solutes. *Pharm. Res.* **1995**, *12*, 768-772.

Izutsu, K.-i.; Yoshioka, S.; Kojima, S.; Randolph, T. W.; Carpenter, J. F. Effects of Sugars and Polymers on Crystallization of Poly(ethylene glycol) in Frozen Solutions: Phase Separation Between Incompatible Polymers. *Pharm. Res.* **1996**, *13*, 1393-1400.

Kinstler, O. B.; Brems, D. N.; Lauren, S. L.; Paige, A. G.; Hamburger, J. B.; Treuheit, M. J. Characterizarion and Stability of N-terminally PEGylated rhG-CSF. *Pharm. Res.* **1996**, *13*, 996-1002.

Levitt, M.; Greer, J. Automatic identification of secondary structure in globular proteins. *J. Mol. Biol.* **1977**, *114*, 181-239.

Looker, D.; Abbott-Brown, D.; Cozart, P.; Durfee, S.; Hoffman, S.; Mathews, A. J.; Miller-Roehrich, J.; Shoemaker, S.; trimble, S.; Fermi, G.; Komiyama, N. H.; Nagai, K.; Stetler, G. L. A human recombinant haemoglobin designed for use as a blood substitute. **1992**, *356*, 258-260.

Macritchie, F. In *Advances in Protein Chemistry*; Anfinsen, C. B., Edsall, J. T. and Richards, F. M., Ed.; Academic Press: New York, 1978; Vol. 32, pp 283-326.

Murase, N.; Franks, F. Salt precipitation during the freeze-concentration of phosphate buffer solutions. *Biophys. Chem.* **1989**, *34*, 293-300.

Pikal, M. J. In *Encyclopedia of Pharmaceutical Technology*; Swarbrick, J. and Boyan, J. C., Ed.; Marcel Dekker, Inc.: New York, 1992; Vol. 6, pp 275-303.

Prestrelski, S. J.; Arakawa, T.; Carpenter, J. F. Separation of Freezing- and Drying-Induced Denaturation of Lyophilized Proteins Using Stress-Specific Stabilization II. Structural Studies Using Infrared Spectroscopy. *Arch. Biochem. Biophys.* **1993**, *303*, 465-473.

Shepilov, M. P. Calculation of kinetics of metastable liquid-liquid phase separation for the model with simultaneous nucleation of particles. *J. Non-Cryst. Solids* **1992**, *146*, 1-25.

Tolstoguzov, V. B. Concentration and purification of proteins by means of two-phase systems: membraneless osmosis process. **1988**, *2*, 195-207.

van den Berg, L.; Rose, D. Effect of Freezing on the pH and Composition of Sodium and Potassium Phosphate Solutions: the Reciprocal System KH_2PO_4-Na_2HPO_4-H_2O. *Arch. Biochem. Biophys.* **1959**, *81*, 319-329.

Zaslavsky, B. Y. *Aqueous Two-Phase Partitioning: Physical Chemistry and Bioanalytical Applications*; Marcel Dekker, Inc.: New York, 1995.

The Effect of Nonionic Surfactants on the Stability of Lyophilized CNTF.

LaToya Jones and John Carpenter
Department of Pharmaceutical Sciences
University of Colorado Health Sciences Center
Denver, CO 80262

Theodore Randolph
Department of Chemical Engineering
University of Colorado
Boulder, CO 80309

B. S. Chang
Amgen, Inc.
Thousand Oaks, CA

PURPOSE. The purpose of this study was to investigate the role of a ionic surfactant, Tween 20, in the freeze-dried formulation of ciliary neurotrophic factor (CNTF). Secondary structural changes of CNTF, as well as microscopic and macroscopic cake morphology, as a function of freezing conditions and the presence of surfactant were examined. In addition, soluble protein recovered following freeze-thawing in the presence and absence of Tween 20 was studied.

METHODS. CNTF formulations with and without Tween 20 were frozen by immersing in liquid nitrogen and then placed on a pre-chilled lyophilizer shelf or allowed to freeze as the freeze-dryer shelf was chilled. Secondary structural perturbations in the dried state were identified by comparing near infrared (IR) spectra of the freeze-dried samples to that of a liquid control. Microscopic cake morphologies were determined using scanning electron microscopy (SEM). Additionally, nitrogen BET isotherms were used to calculate the surface area created by the ice. CNTF recovery following freeze-thawing in the presence and absence of Tween 20 was quantified using UV spectroscopy.

RESULTS. The addition of Tween 20 did not prevent loss of secondary structure in the dried solid following freeze-drying, regardless of the freezing method. While the morphology of the freeze-dried cakes were affected by the freezing method, the addition of surfactant did not alter the appearance. CNTF recovery following freeze-thawing was improved by the addition of Tween 20. There was a decrease in surface area of ice formed in the presence of Tween 20 but not to an extent which could explain the protection observed following freeze-thawing.

CONCLUSIONS. Tween 20 is an effective stabilizer for CNTF exposed to the stresses of freezing and thawing; however, Tween 20 does not protect against the additional stress of drying experienced during lyophilization. Protein damage can be correlated with increased ice surface area. The stabilization provided by Tween 20 cannot be explained by an effect on ice surface area or morphology.

Effect of High Pressure on Crystallization of Subtilisin Mutants

R. Waghmare, M. Joona, M. Larson, and C. Glatz
Department of Chemical Engineering
Iowa State University
Ames, IA 50011

J. Webb and T. Randolph
Department of Chemical Engineering
University of Colorado
Boulder, CO 80309

ABSTRACT

High pressure has been reported to increase the rate of crystallization for some proteins like Glucose isomerase (Visuri et al., 1990). Also, crystallization at high pressures can be used as a probe to understand the mechanism of crystallization better through the calculation of activation volumes.

The possibility of enhanced crystallization rates at high pressure was explored for two subtilisin mutants, Purafect and Properase, which were supplied by Genencor Inc. Purafect and Properase differ in four amino acid residues. Unlike some other proteins like Lysozyme (Saikumar et al., 1995), no increase in crystallization rates was found after exposures to high pressures followed by atmospheric crystallization for both the mutants. Both the mutants crystallized slower at high pressure as compared to atmospheric pressure. For both, Purafect and Properase, the nucleation as well as the growth rates were found to decrease at high pressure.

Comparison of crystallization behaviors of Purafect and Properase showed that Properase crystallized slower than Purafect. Also, Properase had different crystal structure from Purafect. The study of amino acid residues involved in intermolecular contacts influencing crystallization behavior could be used as a probe to understand the mechanism of crystallization better.

INTRODUCTION

Crystallization is one of the oldest known purification techniques. The use of high pressure for protein crystallization was first reported for glucose isomerase by Visuri et al. (1990). The results from this study showed that the rate of crystallization was much higher at enhanced pressures.

In this work, the effect of high pressure on the crystallization of two mutants of the protease *subtilisin* was studied to explore the possibility of any enhanced rate of crystallization at higher pressures. The two mutants of subtilisin studied were Purafect and Properase. They differed in four amino acid residues. Ser 87, 101 and Val 104 in Purafect were replaced by Asn, Gly and Asn, respectively. Properase had Gly at 195, which was absent in Purafect. The mutants were provided by Genencor Intl.

Experiments were conducted with exposures to high pressure followed by atmospheric crystallization as such experiments enhanced the rate of crystallization for lysozyme by 2-3 times (Saikumar et al., 1995). The crystallization behaviors of the two mutants were compared to see the effect of mutations on crystallization behavior.

EXPERIMENTAL PROCEDURE

The experimental procedure is shown below:

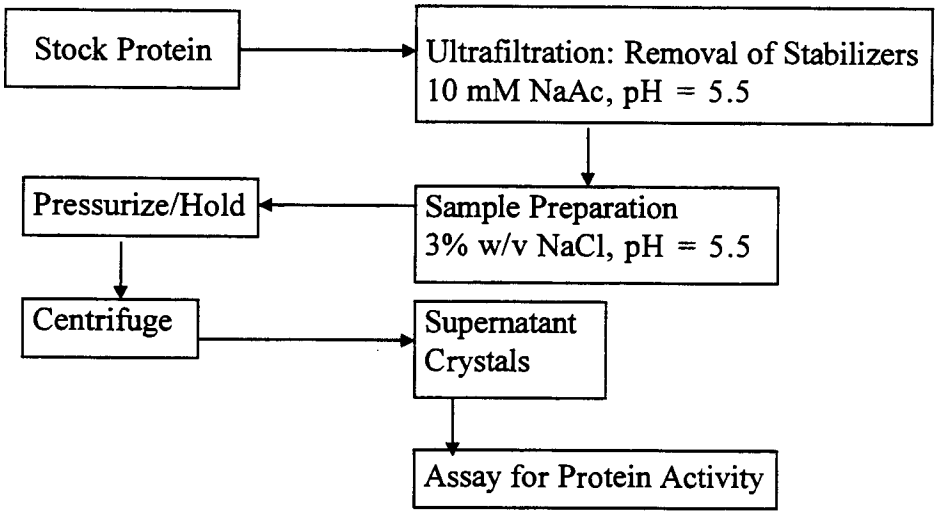

The cell used for high pressure crystallization was made up of stainless steel. A compressor was used to compress air. The compressed air was used to run a pneumatically actuated diaphragm pump. The pump pumped deionized water into the pressure cell, thus developing hydraulic pressure inside the cell. The pressure cell was isolated from the rest of the system once the desired pressure was reached by closing the deionized water inlet valve.

RESULTS

High Pressure Crystallization

• Figure 1 shows the concentration profiles of the mother liquor at atmospheric and high pressure for Purafect and Properase. Both crystallized more slowly at higher pressures.

•Figure 2 shows the crystalline yields of Purafect and Properase after various pressure treatments. A lower crystalline yield was obtained after a period of pressurization of 24/48 hours compared to the yield at 1 atm after 24/48 hours.

• Figures 3 (a) and (b) show the crystals of Purafect and Properase from atmospheric and high pressure crystallization. The crystals formed at atmospheric pressure were larger than those formed at high pressure. Properase crystals were different in shape than Purafect.

Atmospheric Crystallization

• Figure 4 shows the crystallization profiles with and without agitation (gentle tumbling) for Purafect and Properase at atmospheric pressure. Crystallization was faster for both with agitation. Properase crystallized more slowly than Purafect.

CONCLUSIONS

• For both, Purafect and Properase, high pressure decreased nucleation rate, growth rate, and overall crystallization rate.

• Agitation appears to result in secondary nucleation, which leads to higher rates of crystallization.

ACKNOWLEDGMENTS

• NSF grant number BES9510302 for funding of this project.

• Genencor, Intl. for providing Purafect and Properase.

Figure 1: Crystallization profiles [Supernatant conc. (mg/ml) vs time (hrs)]

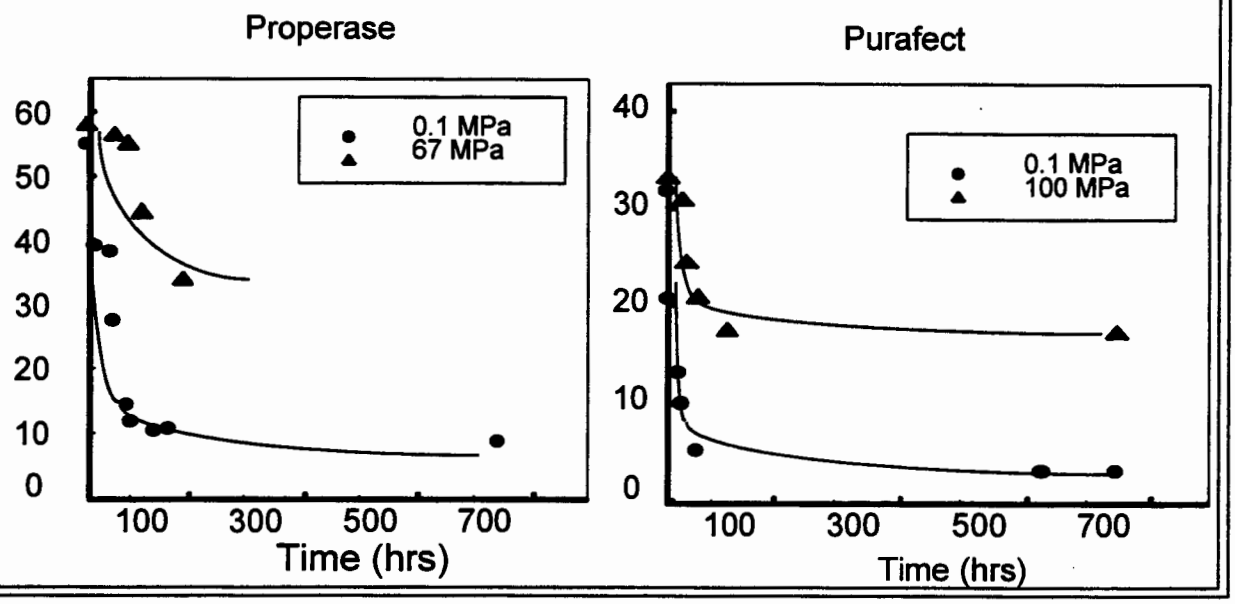

Figure 2: Crystalline yields (%) after pressure treatments

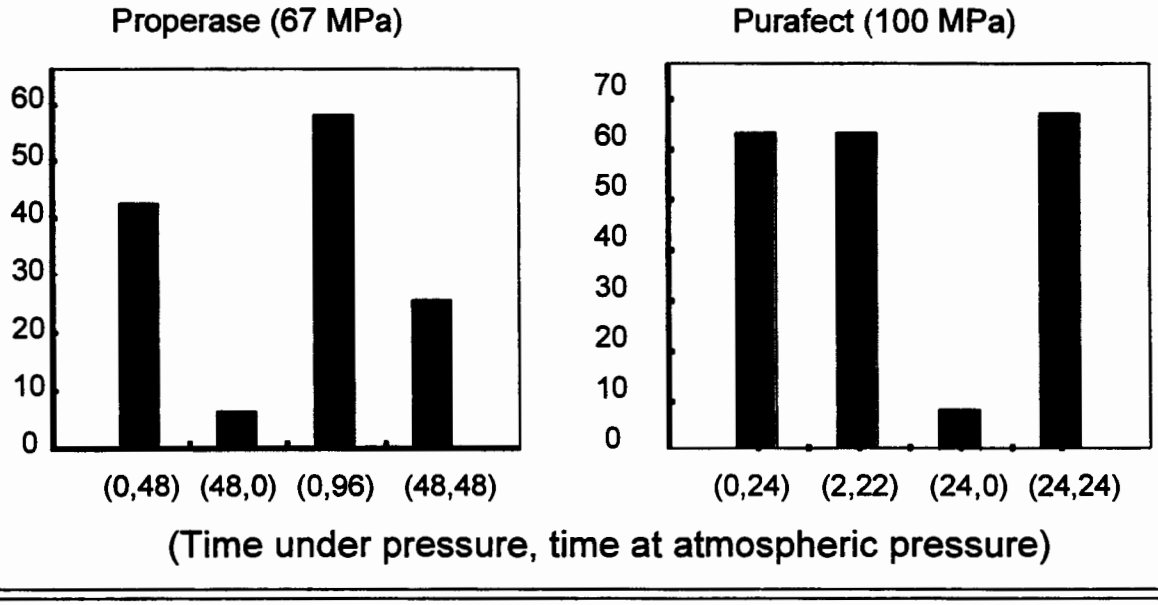

Figure 3a: Properase crystals after 48 hours (marker = 100 microns)

0.1 MPa

67 MPa

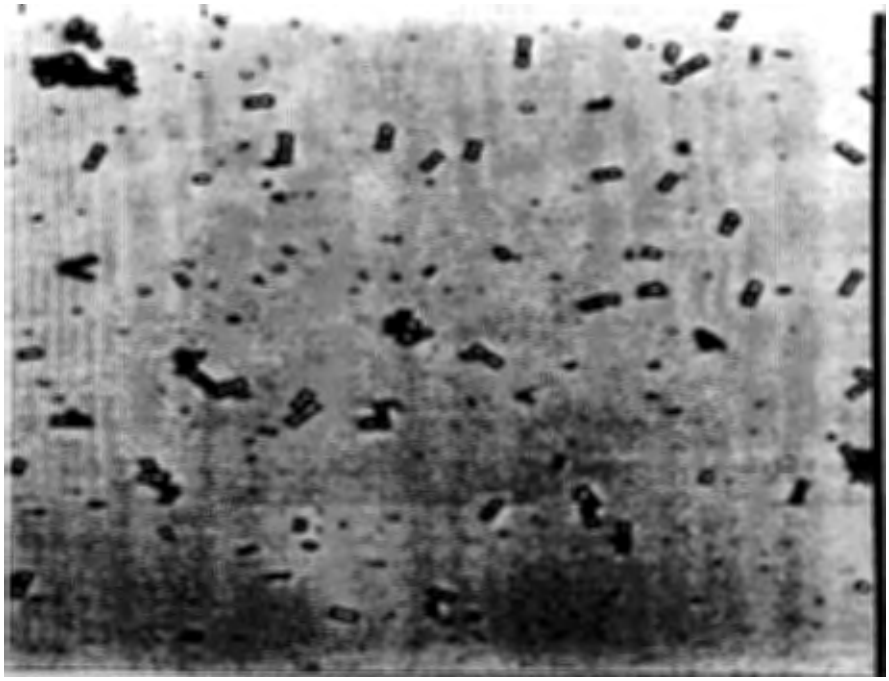

Figure 3b: Purafect crystals after 24 hours

0.1 MPa

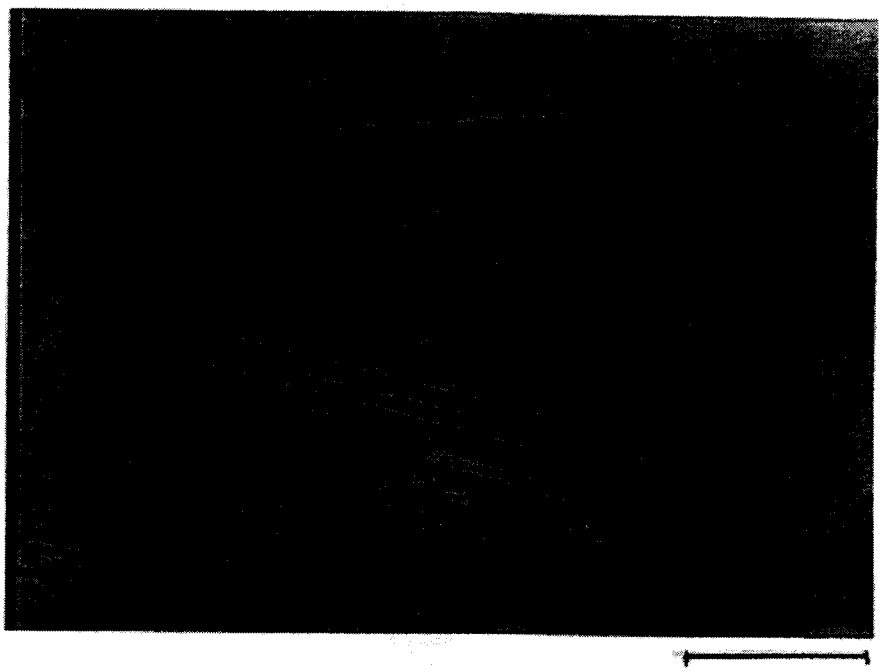

100 MPa

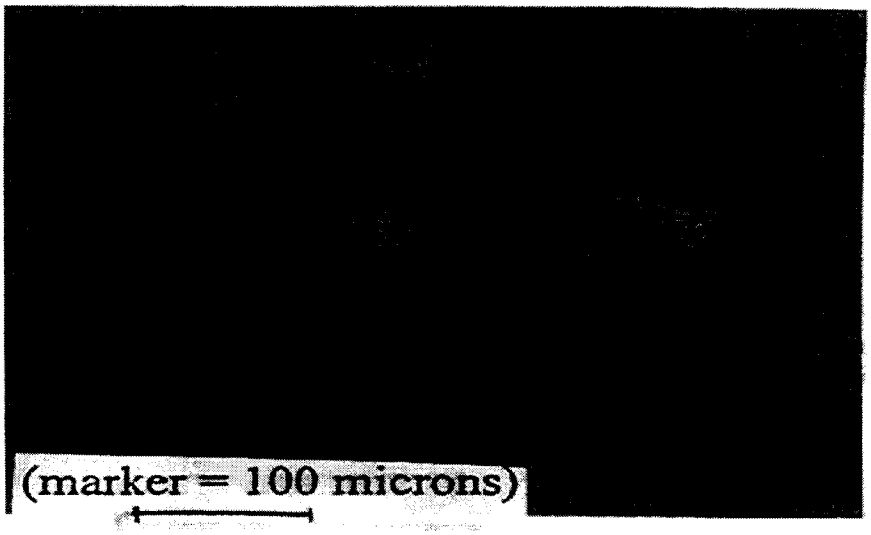

Figure 4: Atmospheric crystallization

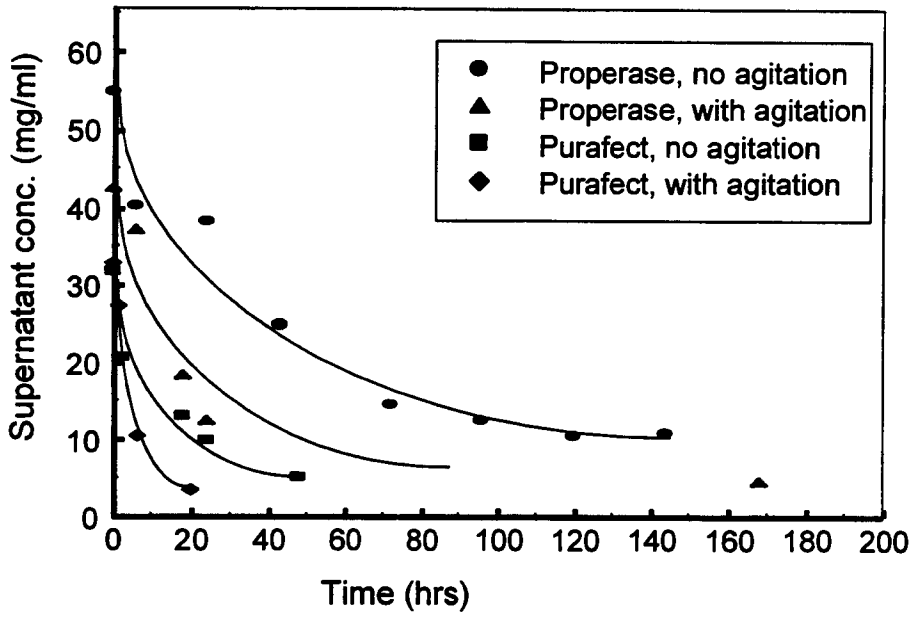

Isoelectric Precipitation of Recombinant Proteins from Canola Extracts

Ferhana Zaman, Jocelyn Pollack, and Charles E. Glatz
Department of Chemical Engineering
Iowa State University
Ames, IA-50011

ABSTRACT

Our goal is to develop an approach for protein recovery from canola that will be adaptable to a wide variety of recombinant proteins. In these experiments the model protein to be studied is T4-lysozyme which have been added to the canola extracts to simulate recovery of recombinant proteins while evaluating the merit of acid as a precipitating agent to enhance selectivity.

INTRODUCTION

Transgenic plants may provide us with a potentially inexpensive system for the large-scale production of proteins for industrial, pharmaceutical, and agricultural use.

Our goal is to develop an approach for protein recovery from canola that will be adaptable to a wide variety of recombinant proteins. For recombinant protein recovery the two downstream processes considered are :

- Extraction of target protein from host
- Purification of recombinant protein from host proteins and impurities

OBJECTIVE

In this work, the starting material for extraction is nontransgenic, defatted canola flakes. The canola proteins are extracted with alkali at room temperature. The effects of acid as a precipitating agent on selective precipitation of target proteins from native canola have been examined. In these experiments the model protein to be studied is T4- lysozyme which has been added to the extracts to simulate the presence of a recombinant protein.

BACKGROUND

Precipitation serves as a purification technique that is often used in the early stages of downstream processing for product stream concentration and fractionation. Some of the advantages of performing a precipitation operation include:

- easy adaptability to large scale
- uses simple equipment
- based on large number of alternative precipitants which are relatively inexpensive
- precipitants can be chosen which do not denature biological products.

Isoelectric Precipitation occurs when the pH is such that the protein attains an overall charge near zero. This condition is called the isoelectric point (pI) and is generally the point of minimum protein solubility. Lysozyme from phage T4 exhibits 9 positive net charges at neutral pH in its wild type form, its pI is higher than 9 and has a molecular weight of about 19,000.

EXPERIMENTAL STUDIES

Multiple-Staged Solvent Extraction of Oil from Dehulled Flaked Canola Meal

The objective of this study was to investigate the mass balance profile of the oil-content of canola in order to determine and optimize the number of extractions required to obtain defatted canola meal using multiple-staged solvent extraction of oil. Flaked dehulled canola meal was extracted with cold hexane (1 g meal/ 20 ml hexane) @room temperature in 4 simultaneous experimental runs. Each run was stopped after 1, 2, 3 or 4 extraction stages. Mixing time was 30 min during each extraction stage. After each stage, the slurry was filtered and fresh hexane solvent added. Samples from each run were analyzed for moisture-content and oil-content using the Gold-Fisch apparatus. Figure 1 shows the effect of number of stages on oil the oil content of the meal.

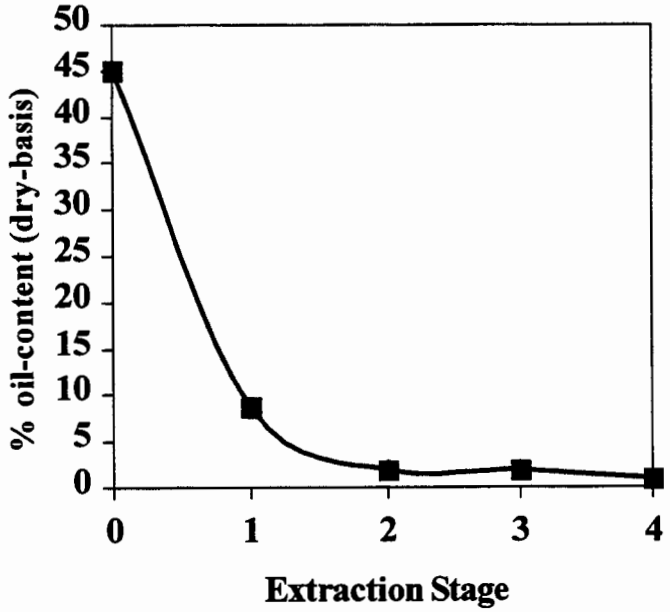

Figure 1: Mass Balance Profile of Oil-Content

pH Stability of T4 Lysozyme

0.10 mg/ml T4 lysozyme in phosphate storage buffer(pH ~ 7.3) was added to various buffer systems (see table below) to make final concentration of lysozyme @12.5 mg/ml.

Table 1. pH of various buffers made to 0.010 M concentration.

Buffer	pH
Acetate	4.0
Acetate	5.0
Phosphate	6.0
Phosphate	7.0
Tris	8.0
Glycine-NaOH	9.0

The active T4 lysozyme in each buffer system was then determined by the lysozyme activity assay (clearing of a *Micrococcus lysodeikticus* suspension). Results are shown in Figure 2.

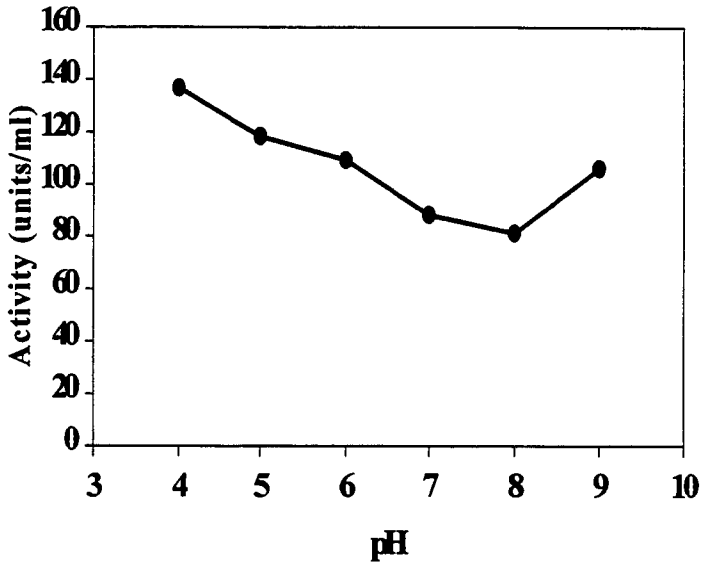

Figure 2: pH Stability of T4 Lysozyme

Isoelectric Precipitation of Unspiked Canola

Defatted flaked canola meal was suspended in aqueous NaOH (1 g meal/ 20 ml NaOH) @ room temperature and gently mixed for 2 hours with pH maintained @ 9.0. The slurry then was centrifuged at 15,000 rpm for 40 min @ 4^{o}C and the supernatant

filtered twice through 0.45 mm and 0.22 mm filters. The resulting protein concentration in the extract was 9.03 mg/ml.

Precipitation experiments were carried out in 14 ml Eppendorf tubes. 2.0 ml aliquots of canola extract @pH 9 were measured into 7 tubes, and each acidified with 0.2 M HCl and 0.01M HCl to attain pH's ranging from 3.0 to 9.0. Contents were mixed by gentle inversions of the tubes. Once precipitation was initiated, the slurry was allowed to sit for 10 min. Precipitate was removed by centrifugation at 15,000 rpm for 40 min @ 4°C, and supernatant volume and total protein content (the Bradford-Coomassie® dye-binding method) were measured. Results are shown in Figure 3.

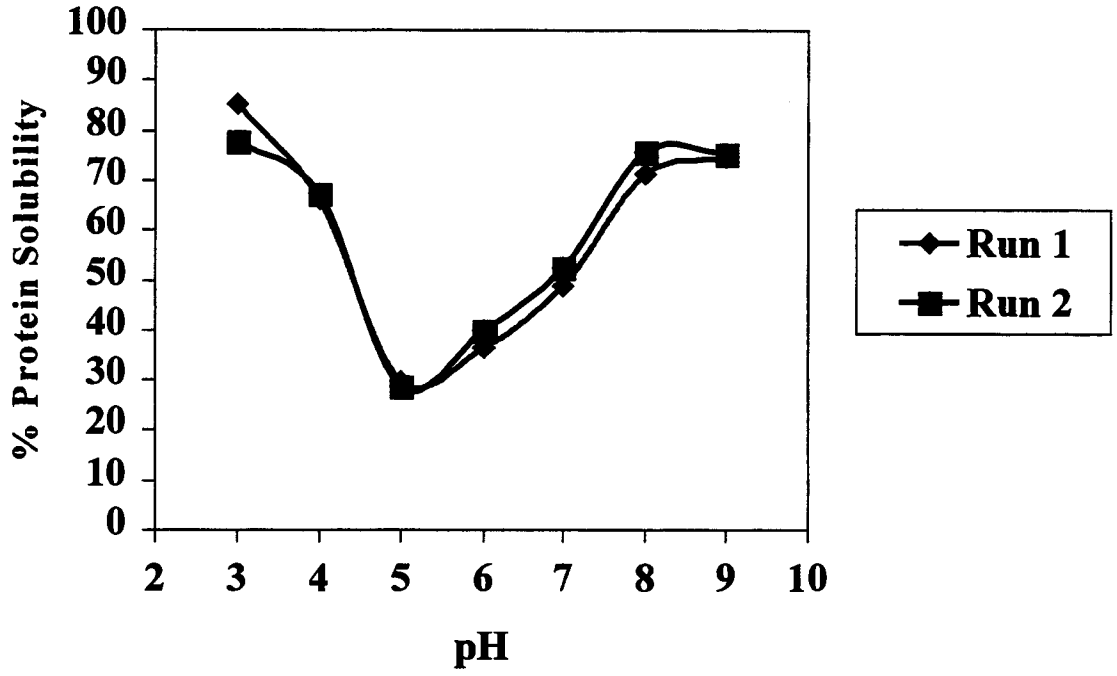

Figure 3: Native Canola Protein Solubility Profile

Isoelectric Precipitation of Canola Spiked with T4 Lysozyme

Canola protein extraction and precipitation experiments were carried out as outlined above but with a protein concentration of 9.23 mg/ml. 1.9 ml aliquots of canola extract @ pH 9 were measured into 7 tubes, and each acidified with 0.2 M HCl and 0.01M HCl to attain pH's ranging from 3.0 to 9.0. Each tube was then spiked with 0.1 ml of T4-lysozyme @ 13.64 mg/ml concentration and thoroughly mixed. After centrifuging as described above, supernatants were analyzed using T4 lysozyme activity assay and SDS-PAGE. Results are shown in Figures 4 and 5.

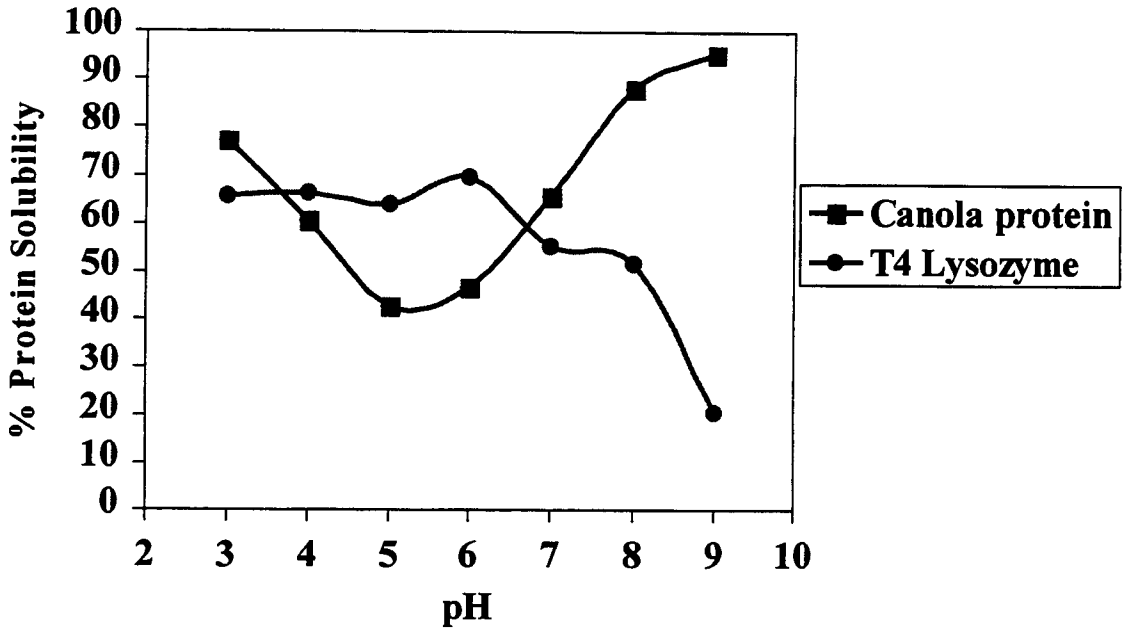

Figure 4: Canola Protein and T4 Lysozyme Solubility Profiles in Spiked Canola Extract

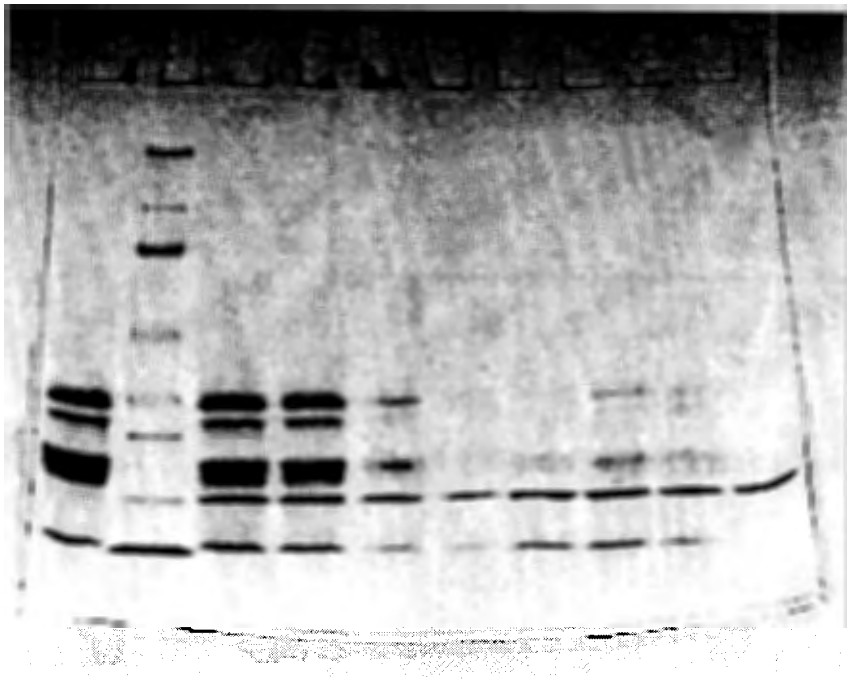

Canola Supernatants

A ⇨ Canola protein extract @pH 9
B ⇨ Broad MW Range Marker
C ⇨ pH 9
D ⇨ pH 8
E ⇨ pH 7
F ⇨ pH 6
G ⇨ pH 5
H ⇨ pH 4
I ⇨ pH 3
J ⇨ T4 lysozyme

Figure 5: Gel Electrophoresis of Spiked Canola Extract

RESULTS AND DISCUSSION

- Figure 1 shows that by extraction stage #2 the oil-content in the flakes is approximately 2% which is sufficient defatting.
- Figure 2 shows the acceptable stability of T4 lysozyme over a range which would encompass both protein extraction and precipitation.
- Figure 3 shows that the minimum solubility of protein in the supernatant occurs at about pH 5 with 70 % of the canola protein precipitated.
- Figure 4 shows a profile similar to that of Figure 2 with the minimum solubility of canola proteins occurring at pH 5. The plot also shows the solubility of T4 lysozyme in the extract as relatively constant at pH (3-6). However, there is approximately 80% insoluble lysozyme at pH 9.
- Figure 5 shows most of the native canola proteins are precipitated out (Column's F and G) at pH 6 and 5 leaving enriched T4 lysozyme.

CONCLUSIONS

Hence isoelectric precipitation has successfully produced a native canola protein concentrate and an enriched "recombinant" (i.e., T4 lysozyme) fraction.

ACKNOWLEDGEMENTS

This research was funded by NSF Grant BES# 9522644 and USDA NRICGP Grant # 95031130. The authors are grateful to Prof. Z. Nikolov and Dr. A. Kusnadi for their encouragement and assistance.

REFERENCES

Parry, R. M. Jr., Chandran, R.C., and Shahani, K. M. (1965). A Rapid and Sensitive Assay of Muramidase. *Proc. Soc. Exp. Biol. Med.*, **119**: 384-386.

Chen, M. and Rohani, S. (1991). Recovery of Canola Meal Proteins by Precipitation. *Biotechnology and Bioengineering*, **40**: 63-68.

Recovery of T4 Lysozymes from Canola Protein Extract by Adsorption Chromatography

Chenming Zhang and Charles E. Glatz
Department of Chemical Engineering
Iowa State University
Ames, IA 50011

ABSTRACT

As a host to produce recombinant proteins, canola has drawn more and more attention in industry due to the easy scale-up of production, developed harvesting and processing procedures, and easy storage and transportation. However, the lack of developed downstream processes to purify the recombinant proteins will delay the emergence of canola as a major source of recombinant proteins.

Native canola proteins are mainly composed of neutral 12S proteins and basic 2S proteins. In this work, different ion exchange chromatography methods are used to characterize the proteins, and an appropriate method is determined for the T4 lysozyme recovery experiments. T4 lysozyme and its mutants are chosen as target proteins because they have been well characterized and can be handily produced in our laboratory. The single and double mutant T4 lysozyme, with a charge of +7 and +5 in neutral solution respectively, are obtained by replacing the 16^{th} and $16/135^{th}$ lysine with glutamic acid of wild-type T4 lysozyme, which has 164 total amino acids and carries a charge of +9 at pH 7.0. The activity of T4 lysozyme is retained despite the replacement of lysine by glutamic acid. To mimic the protein extract of transgenic canola meal, T4 lysozymes are spiked into the non-transgenic canola protein extract, and the effect of protein charges in protein purification from canola protein extract are investigated. For single step purification of positively charged recombinant proteins from canola seed, general guidance is provided for appropriate protein genetic engineering.

Development of a Biosensor for 1,2-Dichloroethane

Derek W. Campbell, Cord Müller, and Kenneth F. Reardon
Department of Chemical and Bioresource Engineering
Colorado State University
Fort Collins, CO 80523

ABSTRACT

As concern about groundwater contamination grows, the need for non-extractive, continuous monitoring systems has become imperative. A fiber optic biosensor has been constructed to monitor, in-situ, 1,2-dichloroethane (1,2-DCA). 1,2-DCA is a common halogenated compound found in ground waters. The biologically active component was either whole cells or enzymes from *Xanthobacter autotrophicus* GJ10, a soil bacterium that hydrolytically dehalogenates 1,2-DCA. The biocomponent was coupled to a fiber optic pH optode using gel entrapment or chemical cross-linking techniques. At typical ground water conditions, the sensor could detect 1,2-DCA down to 11 ppm. Response was rapid with 90% of total signal change reached in 5-7 minutes which is very fast with respect to typical ground water migration rates. The sensor's small size and low cost-per-assay make this device extremely useful for implementation in a groundwater contaminant monitoring system.

INTRODUCTION

Background

More and more previously pristine drinking water sources are being found to be contaminated by organic pollutants. As groundwater resources serve as almost half of the West's drinking water and make up 97% of the world's potable water, it has become continually more important to protect and monitor these stores (McWhorter 1977; Freeze 1979). In response to efforts to characterize, control, and remediate these contaminated systems it is crucial to be able to accurately monitor pollutant levels. In-situ remediation and natural attenuation also require cost effective information on the efficacy of the remedial strategy. To this end a better monitoring system is needed for tracking the presence and migration of pollutants in ground water systems.

Quite a few technologies already exist or are in the final testing stages for groundwater monitoring. Traditionally, samples are extracted through ground water monitoring wells and sent to laboratories for analysis. This analysis is typically done by GC, MS, GC-MS, HPLC, or IC depending on the contaminants present. Field GC and spectrometry methods have been developed for the environmental industry and other non-traditional methods such as immunoassay kits and biosensors are becoming more excepted as measurement techniques. In deciding upon which technique to use for a particular situation one must decide upon the important characteristics of the monitoring process.

The cost to extract samples from the ground water and send them to a registered testing laboratory can be from $120-$200 per sample and this process can take weeks to return an answer. Often remedial actions require monitoring of major pollutants over very long time scales. If the number of samples being sent out for lab testing can be reduced substantial savings in monitoring costs can be made. These costs often make up a large part of the total remediation expense. The number of samples necessary to monitor a pollutant at a site can vary over time. At the beginning of a remediation process sampling may be required at very

short time intervals while less frequent monitoring can be carried out in the long term. In this situation it would be desirable to have a monitoring system that could operate continuously with the rate of sampling being chosen by the operator. In some situations, it is possible that by removing samples from the subsurface environment the chemistry of the sample could be changed resulting in inaccurate data. In-situ sampling techniques is desired in situations where this is a problem. Finally, the time and expense for extremely accurate laboratory data may not be necessary for every sample on a site where data is to be collected for long periods of time. A monitoring system that could give semi-qualitative or qualitative data (such as presence or absence of a pollutant) could be useful for further reducing the monitoring costs.

A biosensor consists of 2 main parts. The biologically active component, or biocomponent, is used as the recognition element. This element is capable of recognizing the analyte(s) of interest and causing some type of change in them. The biocomponent is in intimate contact with the physical transducer. This part of the biosensor detects the change caused by the recognition element and converts it to a measurable signal. This signal is then sent on to the data processing and output portion of the system.

There are quite a few options for both the biocomponent and the physical transducer. Main types of biocomponents include enzymes, whole microorganisms, antibodies, and plant cells. Physical transducers include electrochemical, optical, and acoustic systems. More detailed and specific lists can be found in (Marco 1996; Rogers 1996). There are quite a few current applications of biosensors available today such as sensors for urea, penicillin, organophosphate pesticides, BOD, and glucose with the later two being by far the most common. Again, more detailed lists can be found elsewhere (Gaisford 1989; Karube 1994; Dennison 1995; Rogers 1995; Marco 1996; Rogers 1996).

The use of biosensors to monitor groundwater contaminants can be applied to many of these situations. Through careful engineering biosensors can be made to give rapid, continuous, inexpensive analytical results, and they can designed to be very specific even in mixed organic wastes as well as working directly (without the addition of further reagents). The sensitivity of biosensors can also be very high as many biocomponents are catalytic in nature. As the basis for the sensors is on a cellular or sub-cellular level, they also can be made very small. Because of these advantages over traditional monitoring techniques in many situations biosensors can be much less expensive on a cost-per-assay basis. Perhaps the most beneficial usage of biosensors would be as a part of a integrated monitoring system including non-traditional in-situ techniques combined with traditional laboratory methods.

However, biosensors have disadvantages and challenges. Since the main component in the sensor is biological the working lifetime of the sensor and the method of storage can be an issue. Often a trade-off must be made in cost of refrigerated or frozen storage versus longer activity retention of the sensor. Activity loss can also occur through the immobilization and purification processes necessary for sensor construction. Response times can be longer than desired depending upon the immobilization technique as diffusion through gels and membranes will control the speed of the method. Whole cell biosensors have the added liability of not being as specific as enzyme-based sensors but are easier to construct and less expensive as costly purification techniques are often unnecessary.

EDB Sensor Principles

Once the desired characteristics for the sensing system have been outlined, the sensor components can be chosen. For this basic study, a fiber optic pH sensor (optode) was chosen as the physical transducer. Optical transducers are relatively simple, require no reference electrode, and don't have a signal that influences the biological response. The use of fiber optics for signal transduction allows one to have low signal losses over long distances. This

can be important as ground water sources can be up to 100 meters below the ground surface. A problem can be that extraneous light will influence the signal but this is not a problem in subsurface applications. Fiber optic pH optodes respond very rapidly to changes in pH and the signal doesn't depend on secondary reagents such as oxygen. One disadvantage is that the signal could be affected by changes in the ground water pH or buffer capacity. These effects must be characterized before the system is used in the field.

The biocomponent used in our experiments was either purified enzymes or whole cells from *Xanthobacter autotrophicus* GJ10. This soil bacterium is a gram negative, facultative methylotroph that constituitively produces two dehalogenases. In the first step of the enzymatic reaction with 1,2-dichloroethane (1,2-DCA), the haloalkane dehalogenase hydrolytically cleaves away a Cl^- ion, which generates a proton. This reaction takes place in the presence of water and causes a corresponding shift down in the pH of the surrounding region. In the early log phase of growth, the 1,2 dichloroethane (*dhlA*) dehalogenase is produced preferentially to the corresponding haloacid dehalogenase (*dhlB*). This bacterial strain and its enzymes are very well characterized (Janssen 1984; Janssen 1985; Keuning 1985; van den Wijngaard 1992; van den Wijngaard 1993) making it desirable for use in a proof-of-concept study.

1,2-Dichloroethane serves as a good model contaminant as it has a relatively simple structure, small size, and is aerobically degradable. It also is a very common groundwater pollutant that is used as an industrial solvent and seed fumigant.

Project Goals

The goals of this study were to first prove that the original concept worked and then to characterize the sensor as completely as possible. Next, experiments were performed on optimizing the system by working with enzyme based biosensors and freeze-drying as an improvement in storage techniques. The entire project was to serve as a proof-of-concept study for future work in creating biosensors for groundwater contaminants.

MATERIALS AND METHODS

Optical System

The biosensor was coupled to a long PMMA fiber optic cable (Laser Components) with a polished tip using a standard plastic ferrule. Light from a 5W halogen lamp was supplied and sent through a 480 nm bandpass filter. Fluorescent light from the pH optode passed through a 520 nm bandpass filter and was processed in a single channel photomultiplier (PMT R617 - from Hamamatsu) (Müller 1994; Müller 1994). The resulting potentiometric signal was then sent to a computer interface running a data collection program.

Physical Transducer

Plastic (PMMA), clad fiber optic cables from Laser Components with a core diameter of 1 mm were cut into lengths of 9-12 inches. Each cable was fit with a plastic ferrule lock and a gasket and cap to fit a 2 mL storage vial at the sensing end. The cladding was removed from 1-2 mm of the distal end and both ends of the optode were polished with very fine grit paper (LFG03P) to reduce signal losses through refraction of light. The pH optode was formed by using a modified immobilization procedure (Zhujun 1982) by affixing a pH-sensitive fluorophore to the distal end of the fiber optic cable. The dye, fluoresceinamine isomer 1 (Aldrich), was combined with polyvinyl alcohol and glutaraldehyde to form a

hydrogel that was applied to the tip using a pipette. After polymerization, the pH optode was stored in 0.1 M Na_2HPO_4 at room temperature. In this solution, the optode retains its activity for at least several months. Before use, each pH optode was tested in 4 mL of 1 mM Tris biochemical buffer with 0.5 wt% $CaCl_2$ at pH 7.3. After the sensor's output reached an equilibrium value (~5-15 minutes), a set amount of a pH 6 solution was added and the response recorded. Full response is usually reached in 5-10 minutes.

Cell Culture and Storage

Cultures of *X. autotrophicus* GJ10 on nutrient broth stabs were provided by Dr. Dick B. Janssen of the University of Groningen, The Netherlands. Cells of GJ10 were isolated on agar plates and then grown aerobically at 30° C in a rotary shaker. Cultivation was carried out in closed flasks filled to one-quarter capacity with growth medium. Growth medium was formulated as described elsewhere (Janssen 1984; Janssen 1985; Keuning 1985; van den Wijngaard 1993). Cells were harvested in the early log phase and concentrated by centrifugation to an optical density at 600 nm of about 0.5. They were then stored until use in a 20 mM PBS buffer solution at a pH of 7.4 at 4 °C.

Enzyme Purification and Lyophilization

Crude extract was harvested from resting cells by pulsed sonication for 5-15 minutes followed by centrifugation at 39100 g for 30-40 minutes. EDTA (1mM) was added to bind any remaining heavy metals in solution before sonication. The supernatant was decanted and protein concentration measured by BCA protein assay. Freeze-dried extracts and cells were produced by lyophilization in a freeze-drying unit. After appropriate processing and addition of the desired excipient, 5-10 mL of the solution was added to a 50 mL vessel. This vessel was frozen overnight at -80 °C and then placed in the lyophilizer operating at -55 °C and 15 mtorr for 24 hours. Cakes were examined for consistency and rehydrated for activity assays.

Activity Assays

Activity of whole cells and enzyme crude extracts were determined using a pH optode immersed in 4 mL of bulk solution of the biologically active component. The biocomponents were tested at pH 7.3 in a 1-10 mM Tris buffer with 0.5 wt% $CaCl_2$ at room temperature. 1,2-DCA was added by pipetting in the desired amount from the aqueous phase of a saturated solution (8690 mg/L at 20 °C) after the optode had reached an equilibrium value (5-30 minutes). All activity assays with crude extracts were carried out within 12 hours after purification. Whole cells were tested after transferring resting cells from PBS buffer to the measurement solution.

Biosensor Construction

Whole cell biosensors were created by entrapping a small amount of concentrated resting cells in a calcium alginate hydrogel at the end of a pH optode. Cells in PBS buffer were washed in measurement solution (see activity assays) and combined with 1% sodium alginate after almost all available supernatant was removed. Concentration of this mixture was about 0.2 mg wet cells / mL of gel solution. The solution was allowed to polymerize for 30 minutes at room temperature. After immersing the pH optode in 5.0 wt% $CaCl_2$ for 10 minutes, the sensing end was dipped into the alginate / cell gel and then back into the $CaCl_2$ solution. This was repeated and the biosensor was placed into the measurement solution and stored at 4 °C. Improved biosensors were fabricated using the same procedure with an added permeabilization step. After washing the cells in measurement solution, a 10 mM CHAPS

solution was added and the new solution was allowed to react overnight at 4 °C. The rest of the procedure was followed identically.

Enzyme-based biosensors were formed by combining 3 mg of freeze-dried crude extract stabilized in 2% bovine albumin with 7 mL of 5% glutaraldehyde and 20 mL dH_2O. This mixture was allowed to polymerize at room temperature and a bare pH optode was then dipped into the solution twice. The biosensor was then stored under the same conditions as the whole cell biosensor.

Testing of Biosensors

All biosensors and pH optodes were tested in a 4 mL sampling vessel that was shielded from extraneous light. Testing was performed at pH 7.3 in a 1-10 mM Tris buffer with 0.5 wt% $CaCl_2$ at room temperature. pH and buffer capacity are well within normal ranges for ground water. 1,2-DCA was added by pipetting in the desired amount from the aqueous phase of a saturated solution (8690 mg/L) after an equilibrium value was attained by the sensor (15-60 minutes). Complete mixing was ensured by continuous stirring at high speed in the sampling vessel. Measurement of change in potential was registered every 2 seconds for the duration of the experiment.

RESULT AND DISCUSSION

Proof of Concept

The initial experiment to show that the idea was feasible was carried out by testing a concentrated bulk cell solution for activity towards 1,2-DCA. A bare pH optode inserted in the solution registered a change in signal as Cl^- ions and protons were generated. Figure 1 shows the effect of an addition of 42 ppm (mg/L) of analyte to the bulk cell suspension in a 1 mM buffer solution at pH 7.3 after an equilibrium value for pH signal was reached (about 30 minutes).

A new equilibrium value was reached in about 40 minutes after the addition of the analyte. The decrease in signal mimics the effect of lowering the pH of the measurement solution validating the theoretical concept underlying this study. This assay provided a very simple way to check cellular activity towards the analyte of concern. No processing of cells except gentle centrifugation is necessary and the testing medium can be adjusted easily to whatever chemistry is desired. At this point, creation of a biosensor based on the original concept can be tested. The relatively high concentration of analyte necessary to produce a significant change in signal reflects heavily on the sensitivity of the biosensor created from the biocomponent. This will be discussed in detail in the next sections.

Immobilized Cell Biosensor Response

Once the initial concept was validated, a biosensor made by immobilizing whole *X. autotrophicus* GJ10 cells in Ca-alginate was created and tested. Calcium alginate hydrogels provide an extremely mild and versatile immobilization support for whole cells and enzymes (Hackel 1975; Kierstan 1977). 1,2-DCA (21 ppm) was added to a 1 mM Tris buffer solution after the biosensor signal equilibrium was reached in the measurement solution. The response is shown in Figure 2.

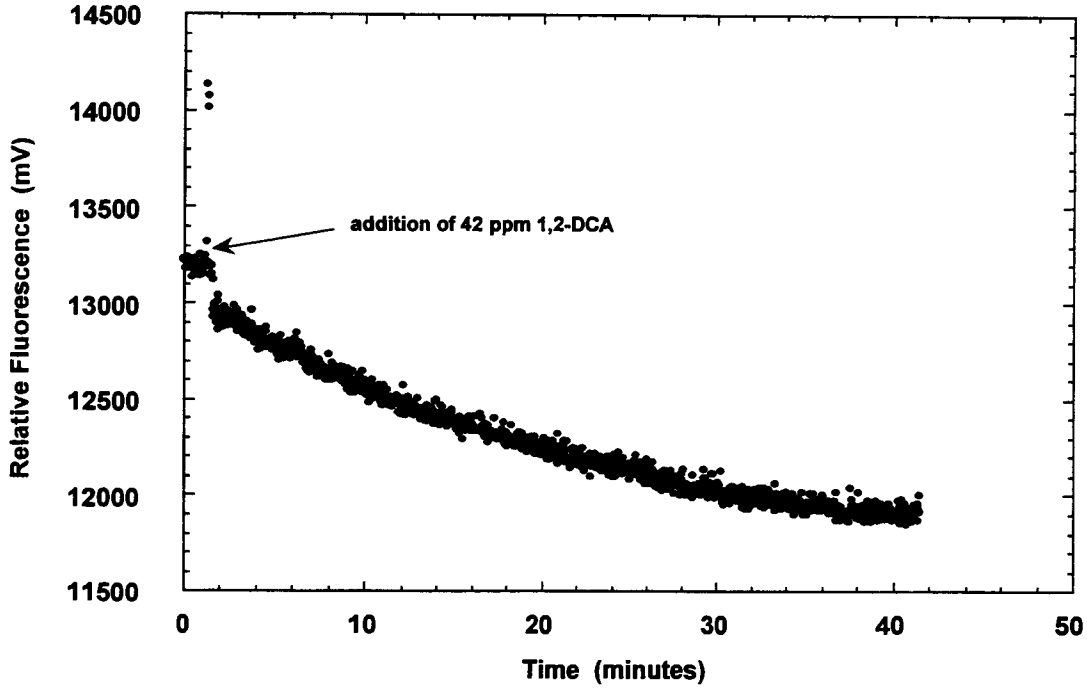

Figure 1. Whole cell suspension response

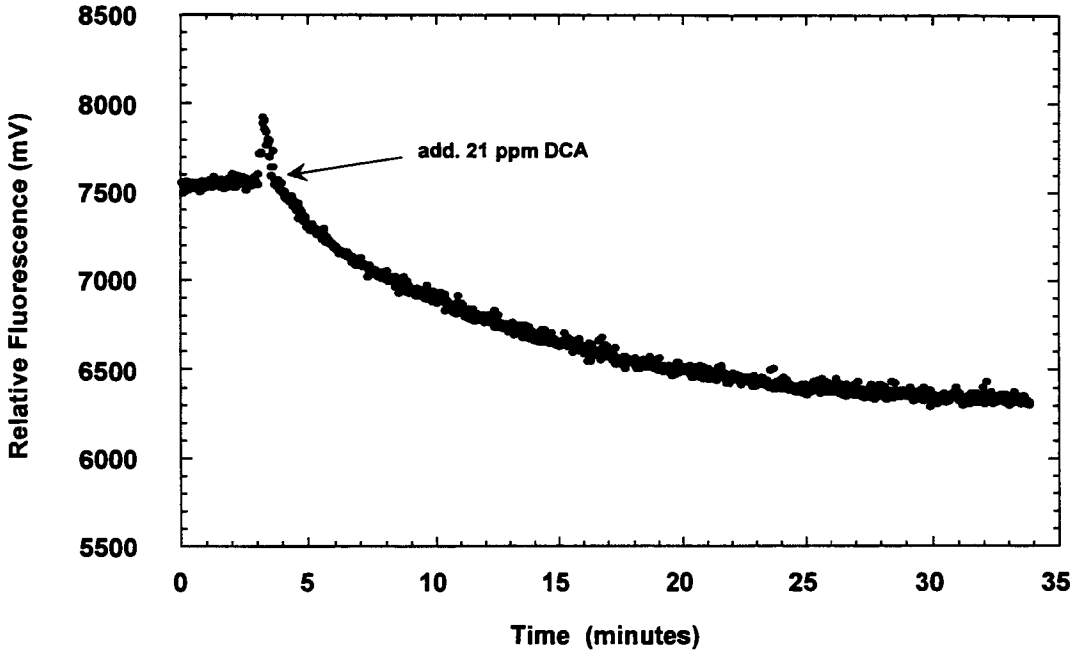

Figure 2. Immobilized whole cell biosensor response

The biosensor response to this addition of analyte was substantial and fairly rapid. The time to full signal can be difficult to determine so a more convenient measure of response speed is the length of time it takes to reach 90% of full signal. By this standard, the response time for the biosensor was about 15-20 minutes. This is a reasonable response time with respect to typical groundwater migration rates (typically on the order of cm/day). Although this experiment showed that a biological sensor for 1,2-DCA was possible to create, the concentrations that this sensor were tested at are much higher than environmentally relevant detection limits. The EPA mandated exposure limit (MCL) for 1,2-DCA is 5 ppb in drinking water.

Improved Immobilized Cell Biosensor Response

Transport across the cell membrane is important in determining the time in which an arbitrary response is reached. If this barrier were reduced or removed a corresponding decrease in response time could be achieved. This hypothesis was tested by permeabilizing the cell walls with a zwitterionic detergent, CHAPS. The improved biosensor was tested at a buffer strength of 10 mM with an addition of 21 ppm 1,2-DCA. Figure 3 shows that response time was improved to about 5-7 minutes for 90% of the total signal change even though the buffer capacity is higher. Differences in sensitivity are due to a corresponding improvement in pH optode manufacturing.

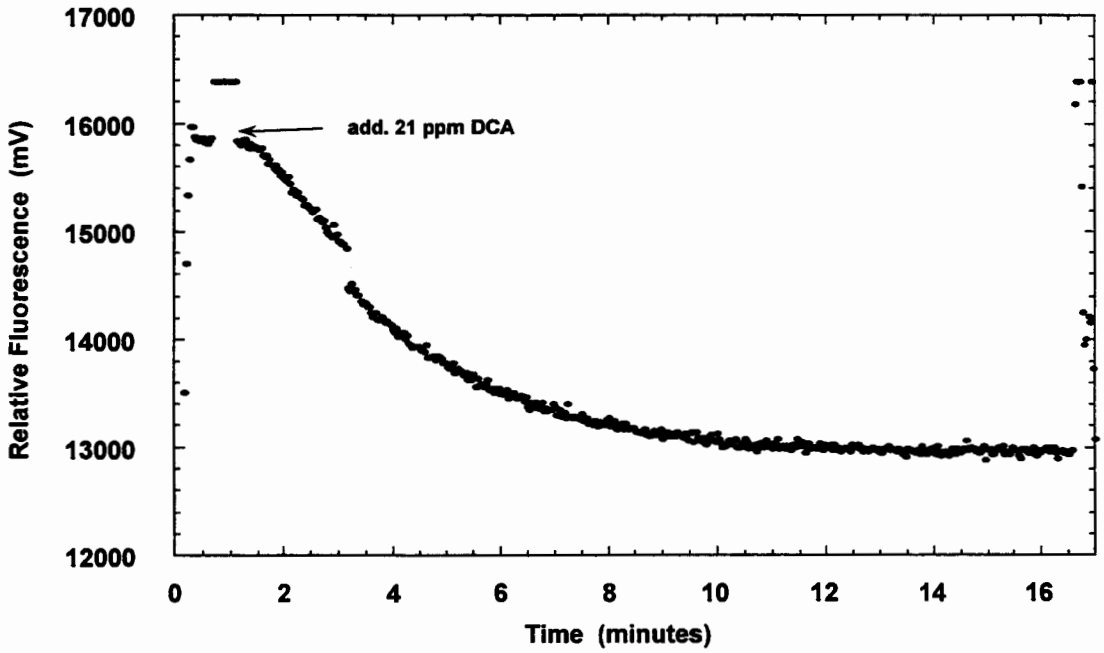

Figure 3. Improved immobilized whole cell biosensor

Calibration of Biosensor

Once the original concept of a 1,2-DCA biosensor was validated, the sensor was characterized to find information such as detection limits, usable lifetime, and response to changes in the sensing environment. Figure 4 shows the calibration curve for the whole cell biosensor over a range of 11-65 ppm. From the graph it can be seen that the calibration is fairly linear ($R^2 = 0.98$) in this range. Reproducibility of identical additions of analyte was also shown to be good (average standard error $< 9\%$).

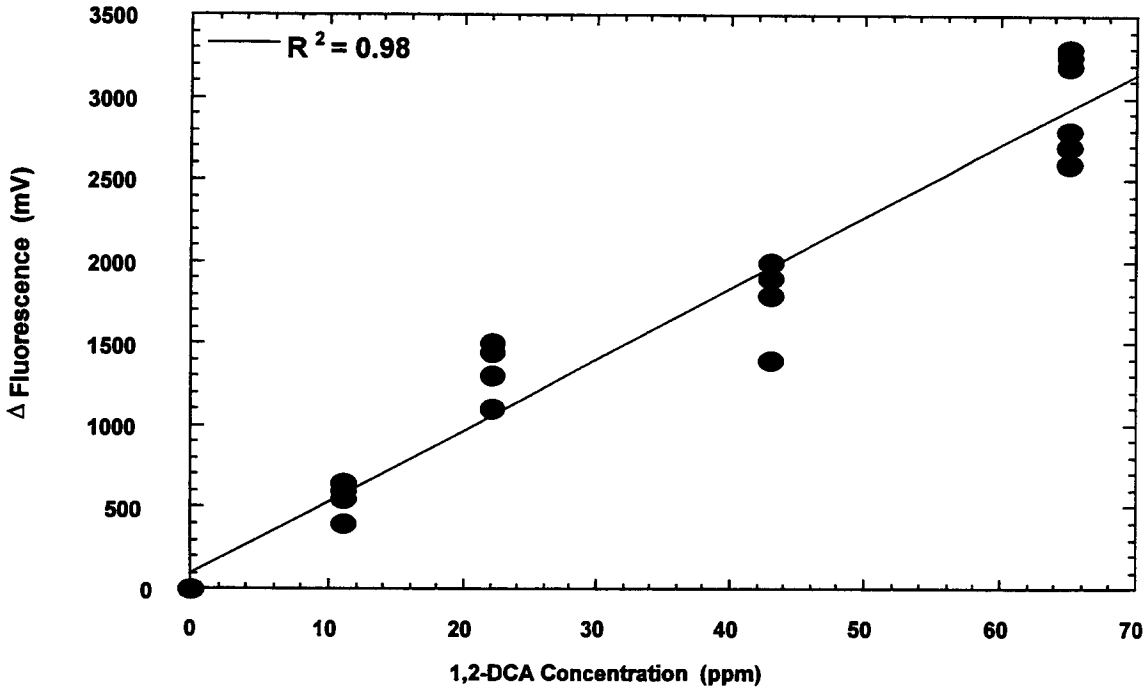

Figure 4. Biosensor calibration curve

Sensor Lifetime

An important liability for biosensors is that biological systems can show a decrease in activity over time. The whole cell biosensor was tested for a period with identical additions of 11 ppm 1,2-DCA in the 1 mM buffer measurement solution. Figure 5 shows that activity retention was maintained over at least 9 days.

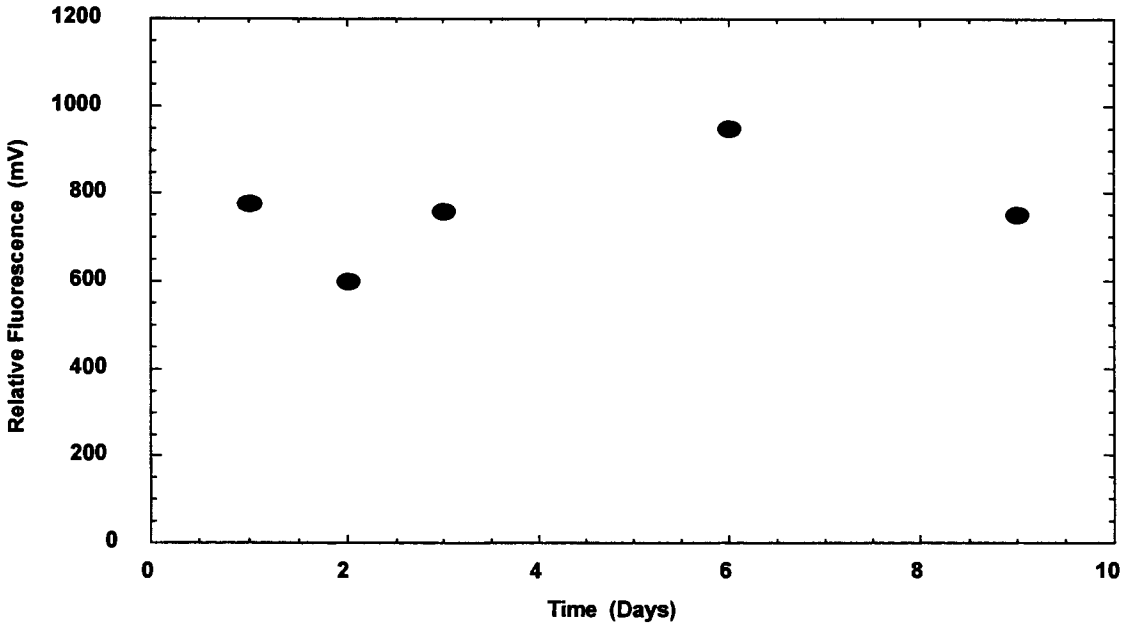

Figure 5. Biosensor lifetime graph

Enzyme Based Biosensor

A biosensor based on the haloalkane dehalogenase enzyme was also developed to take advantage of the very specific catalytic nature of the enzyme. Another consideration was the possible improvement in response time with enclosing membranes and inhibitory cell debris removed. As Figure 6 shows, the response to an identical addition of 1,2-DCA at the same conditions as in Figure 3, although significant, was both much lower and less rapid. The disadvantages to working with pure enzymes are that activity loss occurs very rapidly in the crude extract, and processing steps become more complicated and therefore more costly. Freeze-dried crude extracts stabilized by the addition of 2% bovine albumin before drying were tested in a 1 mM buffer measurement solution. One way to avoid the rapid loss in activity toward the desired analyte and improve handling and storage of the biocomponent would be freeze-drying.

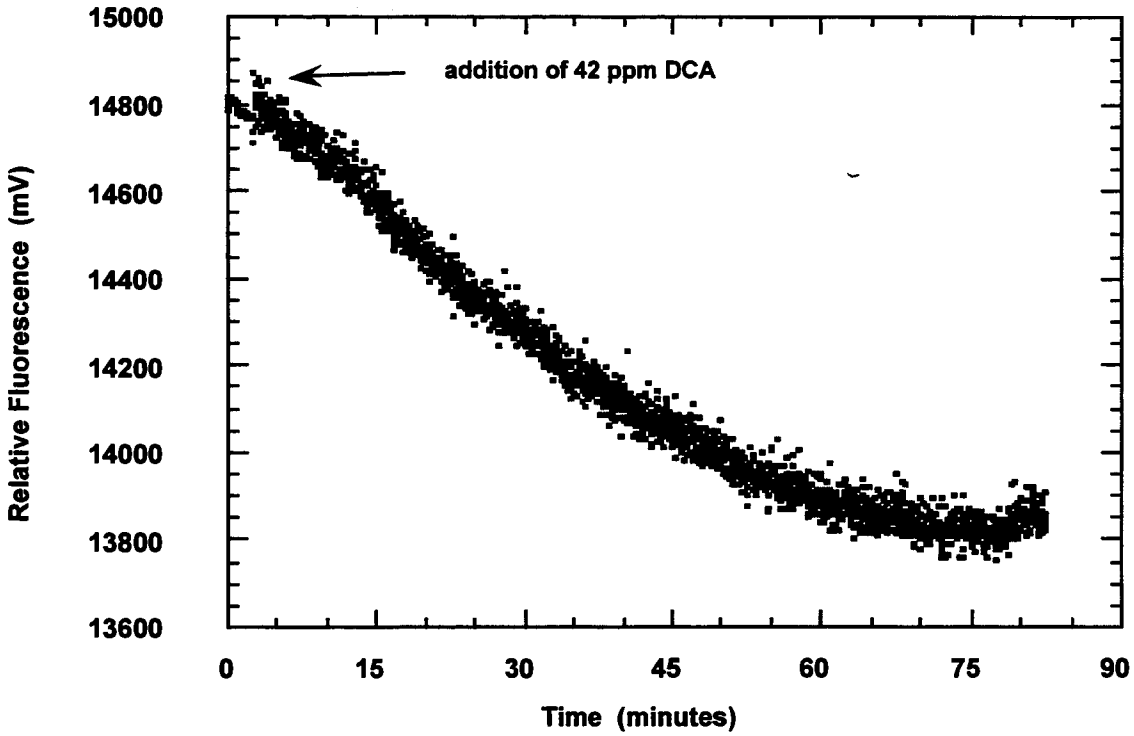

Figure 6. Immobilized enzyme biosensor response

CONCLUSIONS

Present Study

As can be seen from the results presented earlier the concept of creating a biosensor for recognition of 1,2-DCA has been validated. Biosensors made from whole cells, permeabilized whole cells, and freeze-dried enzymes were shown to be effective in recognizing relatively high doses of the analyte. The permeabilized whole cell sensor exhibited very fast response times with respect to groundwater migration rates. One problem that was observed with this system was the relatively long times (up to 60 minutes) that the biosensor needed to reach an equilibrium response before the analyte could be added. This delay makes the

current biosensor not applicable for use in bioreactors for process control but still does not hinder its usage for ground water monitoring.

The whole cell biosensor also showed excellent activity retention up to at least 9 days. Further studies have shown that over 50% of initial activity remains beyond 3 weeks. This activity loss can result from loss of viability or by diffusion out of the gel of the biocomponent or by loss of gel strength due to a deleterious sensing environment (low pH, high phosphate ion concentration). The calibration of the improved whole cell biosensor exhibited a linear response as would be expected by a mass-transport limited sensing device. The response was fairly reproducible across this range.

Future Work

The results that have been presented support expanding this research in order to further characterize this sensor system and test its usefulness in field situations. To date there are many biosensors that function well in laboratory settings but the ultimate goal of applying this technology to the field has been hard to achieve. The next step in this study will be to carry out experiments to characterize the biosensor response to changing pollutant levels in a soil column supplied with flowing ground water.

The whole cell sensor system shows promise for certain applications but has certain liabilities that must be addressed. Whole cell biosensors lack the specificity of pure enzyme sensors and any cross-sensitivity must be identified. The biosensor's response to environmental changes such as pH, buffer capacity, and temperature must also be characterized. The working lifetime of an alginate gel immobilized sensor under environmental conditions could be low as alginate gels are dissolved in the presence of phosphate ions. An improvement could be made by using hardening agents such as polyethyleneimine and glutaraldehyde after gel immobilization. This approach has been effective in other systems (Bajpai 1984). Alternatively, a different hydrogel such as hardened gelatins, agarose, or oxidized starch gels could be used.

Another substantial problem is the lack of environmentally relevant detection limits. Many common organic groundwater pollutants have an EPA mandated standard (MCL) for drinking water of 5 ppb. Several possibilities exist for improving the sensitivity of this system. Improvements could be made in the pH optode, the concentration of biocomponent immobilized to the sensor head, and the use of different immobilization techniques. Another improvement could be made by using a biocomponent with a higher activity towards the analyte of interest (van den Wijngaard 1992). As more environmentally relevant microbial species are discovered and characterized this could be a significant avenue for sensor improvements.

Although the basic concept for a freeze-dried enzyme biosensor was also validated, there are quite a few areas that could be improved as well as fully characterizing the sensor in much the same way that the whole cell biosensor needs to be (pH, buffer capacity, and temperature). The immobilization method used for this system needs to be optimized. Glutaraldehyde cross-linking is a very harsh immobilization method and another type of immobilization could improve the sensitivity of the sensor. Freeze-drying also causes large losses in activity if the stabilization formulation (excipient) is not chosen correctly. Although freeze-drying improves the long term storage capabilities of the biocomponent it is possible that immobilized crude extract would retain activity sufficiently long to offset the cost and difficulty of freeze-drying. Optimization of the excipients used to protect the enzymes during freeze-drying could possibly improve the activity retention to make freeze-drying feasible (Pikal 1990; Gibson 1992; Cleland 1993).

Other Possible Applications of This Type of System

There are many other pollutant / biocomponent combinations that could be used in this specific type (pH optode-based) of system. Further reading can be done in this area for a broader range of pollutants that can be hydrolytically dehalogenated (Keuning 1985; Slater 1994; Nagata 1997; Spain 1997).

ACKNOWLEDGMENTS

This work was supported in part by grants from Colorado State University's Agricultural Experiment Station and the Colorado Institute for Research in Biotechnology. We would also like to thank Dr. Dick B. Janssen for his generous donation of cultures of *Xanthobacter autotrophicus* GJ10.

REFERENCES

Bajpai, P., and Argyrios Margaritis (1984). "Improvement of Inulinase Stability of Calcium Alginate Immobilized *Kluyveromyces marxianus* Cells by Treatment with Hardening Agents."

Bousse, L. (1996). "Whole Cell Biosensors." Sensors and Actuators B **34**: 270-275.

Cleland, J. L., Michael F. Powell, and Steven Shire (1993). "The Development of Stable Protein Formulations : A Close Look at Protein Aggregation, Deamidation, and Oxidation." Critical Reviews in Therapeutic Drug Carrier Systems **10**(4): 307-377.

Dennison, M. J. and A. P. F. Turner (1995). "Biosensors for Environmental Monitoring." Biotechnology Advances **13**: 1-12.

Freeze, R. A. and J. A. Cherry (1979). Groundwater. Englewood Cliffs, Prentice-Hall, Inc.

Gaisford, W. C. and D. M. Rawson (1989). "Biosensors for Environmental Monitoring." Measurement and Control **22**: 183-186.

Gibson, T. D. and J. R. Woodward, Eds. (1992). Protein Stabilization in Biosensor Systems. Biosensors and Chemical Sensors - Optimizing Performance Through Polymeric Materials. Washington, D.C., ACS.

Hackel, V., J. Klein, R. Maegnet, and F. Wagner (1975). European Journal of Applied Microbiology **1**: 291.

Janssen, D. B., Alex Scheper, and Bernhard Witholt, Eds. (1984). Biodegradation of 2-Chloroethanol and 1,2-Dichloroethane by Pure Bacterial Cultures. Innovations in Biotechnology. Amsterdam, Elsevier Science Publishers B.V.

Janssen, D. B., Alex Scheper, Lubbert Dijkhuizen, and Bernhard Witholt (1985). "Degradation of Halogenated Aliphatic Compounds by *Xanthobacter autotrophicus* GJ10." Applied and Environmental Microbiology **49**(3): 673-677.

Karube, I., and Keijiro Nakanishi (1994). "Microbial Biosensors for Process and Environmental Control." IEEE Engineering in Medicine and Biology: 364-374.

Keuning, S., Dick B. Janssen, and Bernhard Witholt (1985). "Purification and Characterization of Hydrolytic Haloalkane Dehalogenase from *Xanthobacter autotrophicus* GJ10." Journal of Bacteriology **163**: 635-639.

Kierstan, M., and C. Bucke (1977). "The Immobilization of Microbial Cells, Subcellular Organelles, and Enzymes in Calcium Alginate Gels." Biotechnology and Bioengineering **19**: 387-397.

Marco, M.-P., and Damia Barcelo (1996). "Environmental Applications of Analytical Biosensors." Measurement Science and Technology **7**: 1547-1562.

McWhorter, D. C. and D. K. Sunada (1977). Ground-Water Hydrology and Hydraulics. Chelsea, Michigan, Water Resources Publications.

Müller, C. (1994). Faseroptische Sensoren zur Mehrkomponentenanalytik in der Biotechnologie. Institut fur Technische Chemie. Hannover, Universitat Hannover: 176.

Müller, C., Florian Schubert, and Thomas Scheper (1994). Multicomponent Fiberoptical Biosensor for use in Hemodialysis Monitoring. SPIE, Los Angeles, CA., SPIE.

Nagata, Y., Keisuke Miyauchi, Jiri Damborsky, Katka Manova, Alena Ansorgova, and Masamichi Takagi (1997). "Purification and Characterization of a Haloalkane Dehalogenase of a New Substrate Class from a g-Hexachlorocyclohexane-Degrading Bacterium, *Sphingomonas paucimobilis* UT26." Applied and Environmental Microbiology **63**(9): 3707-3710.

Peter, J., W. Hutter, W. Stoellnberger, and W. Hampel (1996). "Detection of Chlorinated and Brominated Hydrocarbons by an Ion Sensitive Whole Cell Biosensor." Biosensors and Bioelectronics **11**(12): 1215-1219.

Pikal, M. J. (1990). "Freeze-Drying of Proteins Part II : Formulation Selection." BioPharm **October**: 26-30.

Rawson, D. M. (1988). "Whole Cell Biosensors." International Industrial Biotechnology **8**(2): 18-22.

Rogers, K. a. G. C. L. (1996). "Environmental Biosensors : A Status Report." Environmental Science and Technology **30**(11): 486-491.

Rogers, K. R. (1995). "Biosensors for Environmental Applications." Biosensors and Bioelectronics **10**: 533-541.

Slater, J. H., Ed. (1994). Microbial Dehalogenation of Haloaliphatic Compounds. Biochemistry of Microbial Degradation. Dordrecht, Kluwer Academic Publishers.

Spain, J. (1997). "Synthetic Chemicals with Potential for Natural Attenuation." Bioremediation Journal **1**(1): 1-9.

van den Wijngaard, A. J., Koen W.H.J. van der Kamp, Jan van der Ploeg, Frens Pries, Bert Kazemier, and Dick B. Janssen (1992). "Degradation of 1,2-Dichloroethane by *Ancylobacter aquaticus* and Other Facultative Methylotrophs." Applied and Environmental Microbiolgy **58**(3): 976-983.

van den Wijngaard, A. J., Richele D. Wind, Dick B. Jannsen (1993). "Kinetics of Bacterial Growth on Chlorinated Aliphatic Compounds." Applied and Environmental Microbiology **59**(7): 2041-2048.

Zhujun, Z., Y. Zhang, M. Wangbai, R. Russel, and Z.M. Shakhsher (1982). "Poly(vinyl alcohol) as a Substrate for Indicator Immobilization for Fiber-Optic Chemical Sensors." Analytical Chemistry **54**: 821-823.

Modeling Root Uptake and Transport of Trichlorethylene

Jiang Hu[1], Muralidharan Narayanan[1], L. C. Davis[2], and L. E. Erickson[1]
Departments of [1]Chemical Engineering and [2]Biochemistry
Kansas State University
Manhattan, KS 66506

ABSTRACT

A model is developed to investigate the effect of vegetation on the fate of trichlorethylene (TCE) in the rhizosphere. Steady state is assumed and diffusion-advection equation is developed based on the knowledge of root structure. The TCE distribution along the root is investigated with different diffusion pathways present in the root. Experimental values are used to estimate the parameters which appear in the model.

INTRODUCTION

TCE is a major contaminant of soil and groundwater in the United States. It has been used as a degreaser by industry and military, and a solvent by the dry cleaning industry. Widespread use and indiscriminate disposal make TCE one of the most common pollutants listed by the U.S. Environmental Protection Agency (Newman et al., 1997).

Recent studies have shown that plants such as alfalfa enhance the bioremediation process of TCE in contaminated soils and groundwater. Plants help in stabilization and containment of contaminants during subsurface transport because roots act as additional sinks for water and TCE. Established vegetation can pump-and-treat contaminated water by economically using solar energy. Plants such as cottonwood, poplar, and alfalfa which are drought resistant and viable in contaminated soils extend their roots to draw up contaminated groundwater to the vadose zone. In this way they employ solar energy to pump contaminated subsurface groundwater (Narayanan et al., 1995). Vegetation plays a significant role in determining water-content profiles in actual plant-soil systems. Rapidly transpiring plants may be responsible for rapid depletion of soil water to create unsaturated zones. Consequently, the air-content profiles in vegetated soils are also closely related to the transpirational processes of established vegetation.

The purpose of this study is to predict the fate of TCE which enters the root near the water table and moves upward through the xylem into the unsaturated zone where the TCE concentration in soil is much lower because of gas phase diffusion which allows TCE to be dissipated into the atmosphere.

MODEL DEVELOPMENT

Root Structures

A stylized root cross section is illustrated in Figure 1. Cell walls near the soil interface between the cortex cells are porous, often with voids where several cells adjoin. Water and solutes move freely from soil solution to the interior of roots in the capillary spaces between cortex cells. At the endodermis, this movement is influenced by a low permeability barrier, the Casparian strip, that is formed around these specialized cells. The area outside the endodermis where free water and solute movement occurs is termed the apparent free space. This area also plays an important role in the movement of contaminants since it provides surface area for the adsorption of pollutants (Trapp and McFarlane, 1995).

Xylem is the principal tissue through which water and both organic and inorganic solutes are translocated in roots. Xylem acts as a long and continuous tube from root to leaf. Its vessels and tracheids are very narrow on the order of 5 to 50 μm in diameter. The xylem functions as an open conduit for the transport of water from the root the leaves. The water potential difference between the soil and the air is the driving force for water movement (Levitt, 1974).

Transport Processes

In this model, passive transport mechanisms based on diffusion and mass flow with the surrounding medium are considered. The microscopic movement of molecules results in mixing and a macroscopic compensation of concentration differences. This relation was formulated mathematically by Fick in 1855. Fick's first law of diffusion describes the net flux per unit area in an isotropic medium by a concentration gradient:

$$J = -D \cdot \frac{\partial C}{\partial x}$$

J is the net flux of substance per unit area ($kg \cdot s^{-1} \cdot m^{-2}$), D is the diffusion coefficient (m^2/s), and $\partial C/\partial x$ is the concentration gradient ($kg \cdot m^{-3} \cdot m^{-1}$). If ∂x is small ($\Delta x \rightarrow 0$), $\partial C/\partial x$ can be replaced by $\Delta C/\Delta x$. The net flux N of the substance (kg/s) is directly proportional to the area A (m^2):

$$N = J \cdot A = -A \cdot D \cdot \frac{\Delta C}{\Delta x}$$

The ratio between diffusion coefficient and pathway gives the conductance g (m/s). This is a measure of the velocity of exchange. The reciprocal of g is the resistance R (s/m):

$$\frac{D}{\Delta x} = \frac{1}{R} = g$$

The diffusion coefficient D for gases is around 10^{-5} to 10^{-4} (m^2/s), for liquids ca. 10^{-9} (m^2/s) and for solids ca. 10^{-14} (m^2/s). It can be seen that D primarily depends on the aggregate state and the diffusion within gases is rapid compared to liquids. If more than one resistance has to be considered, the total resistance depends on the values of the individual resistances and the geometry of the phases (Trapp and McFarlane, 1995).

Diffusion across phase boundaries requires the consideration of partitioning. If C_i and C_j are the concentrations in phases i and j, respectively, and K_{ij} is the partition coefficient. At equilibrium,

$$\frac{C_j}{C_i} = K_{ji}$$

The gradient $\Delta C_{ij}/\Delta x$ (in the case of non-equilibrium) is

$$\frac{\Delta C_{ij}}{\Delta x} = \frac{\left(C_i - \frac{C_j}{K_{ji}}\right)}{\Delta x}$$

Then the flux between phases i and j, N_{ij} (kg/s), is

$$N_{ij} = -A \cdot g \cdot \left(C_i - \frac{C_j}{K_{ji}}\right)$$

Net diffusion between the phases exists as long as C_i is not equal to C_j/K_{ji}.

The flux N (kg/s) due to advection of the medium may be described mathematically by the equation

$$N = Q \cdot C$$

where Q is the volumetric flow rate (m^3/s) due to advection and C is the concentration of chemical within flowing medium (kg/m^3).

The combination of a diffusive transport term with an advective transport term yields diffusion-advection equation. Diffusion and advection are universal processes. Therefore, their description is the basis for many transport models of chemicals in water, soil, and air. In plants, chemicals are passively transported by advection and diffusion.

Root Transport Model

Based on the knowledge of the root structure and transport processes described above, a model for the uptake and fate of contaminants in plant root is developed. The following assumptions are considered:

1) The convective flow is in the vertical direction, representing the movement of evapotranspiration.
2) There are no other transport processes except for passive processes such as diffusion and advection (in the transpiration stream). This means that any active transport, e.g., with carriers, is excluded.
3) Plants are well adapted and tolerant to the hazardous contaminants present in the soil and groundwater.
4) Roots are in cylindrical form as shown in Figure 2.
5) Transport is under steady state.
6) Contaminants present in root xylem are in form of dissolved contaminants.
7) There is no metabolism of contaminants in root xylem.

To model TCE transport in the root, the xylem is considered to be surrounded by an annular region of plant material between the xylem and soil. The basic equation for TCE diffusion in the radial direction in the annular region is:

$$\frac{1}{r}\cdot\frac{\partial}{\partial r}(rN)=0$$

where:

$$N=-D\cdot\frac{\partial C}{\partial r}$$

with boundary conditions:

$$C = C_{rw} \text{ at } r = R_1$$
$$C = C_w \text{ at } r = R_2$$

where R_1 is the radius at the xylem interface and R_2 is the radius at the soil interface. The solution of this equation for r=R1 gives:

$$N=\frac{D\cdot(C_{rw}-C_w)}{R_1\cdot\ln\frac{R_2}{R_1}}$$

For the xylem, we consider plug flow in a cylinder with diffusion of contaminant through the wall. The distance traveled z and residence time t are related by:

$$z=v\cdot t$$

where v is the velocity of the water in xylem. Thus,

$$V\cdot\frac{dC_{rw}}{dt}=-N\cdot A$$

where

$$V = \pi \cdot R_1^{\,2} \cdot L$$
$$A = 2 \cdot \pi \cdot R_1 \cdot L$$

L is the root length. Substitution of expressions for A, N, V gives:

$$\frac{dC_{rw}}{dt} = \frac{-2 \cdot D \cdot (C_{rw} - C_w)}{R_1^{\,2} \cdot \ln \frac{R_2}{R_1}}$$

For the initial condition of $C_{rw} = C_0$ at $t = 0$, integration yields:

$$\ln \frac{C_{rw} - C_w}{C_0 - C_w} = \frac{-2 \cdot D \cdot t}{R_1^{\,2} \cdot \ln \frac{R_2}{R_1}}$$

or

$$\frac{C_{rw} - C_w}{C_0 - C_w} = EXP\left(-\frac{t}{\tau}\right)$$

where

$$\tau = \frac{R_1^{\,2} \cdot \ln \frac{R_2}{R_1}}{2 \cdot D}$$

is a time constant.

The appropriate diffusivity to use in estimating the diffusion of TCE in roots has not been reported in the literature. One approach which is used is to treat the root as a porous solid in which the diffusivity of TCE in the fluid phase is reduced by dividing by a tortuosity factor which often ranges from 2 to 6 (Cussler, 1984). While the impermeable Casparian strip is a barrier for compounds which have low solubility within it, TCE might be expected to have a relatively high solubility and diffusivity in the relatively hydrophobic Casparian strip. Thus, the effective diffusivity to use where the roots are saturated with water is of the order of 10^{-8} to 10^{-6} cm^2/s. If some of the void space is filled with gas rather than liquid, the diffusivity would be larger.

DISCUSSION OF RESULTS

In Table 1, values are presented for several values of effective diffusivity, D, radius of the xylem region, R_1, and root radius, R_2. For small roots, it is clear that the value of the time constant is small and TCE in roots will approach equilibrium with TCE in soil. For larger values of R_1 and R_2, the approach to equilibrium is much slower. An examination of alfalfa roots shows that the diameter of the main root for mature plants varies from 2 mm near soil surface to 0.2 mm at 25 cm below the surface. The secondary roots range in diameter from 0.1 mm to 1 mm. Based on 10 L/m^2/day and 100 plants/m^2, water use is 100 mL/plant/day. The velocity of water in the xylem is estimated to range from about 0.01 cm/s to 0.2 cm/s based on transient experiments with deuterium as tracer and estimated velocities for roots of various sizes with up to 25% of the area assumed to be xylem and 100 mL/plant/day of water use. In Figures 3a-3f, 0.15 cm/s is used as the velocity to illustrate the variation of TCE concentration in the root with distance for a constant external TCE concentration in the soil and constant values of R_1 and R_2. The plots of relative concentration $(C_{rw}-C_w)/(C_0-C_w)$ in root xylem vs root length z are shown in Figures 3a-3f with different root radii. It is clear that the smaller the diffusion coefficient, the bigger the root resistance and the slower TCE in the root approaches to equilibrium with TCE in the soil.

Table 1. Effect of values of effective diffusivity , radius of xylem region, and root radius on the time constant for TCE diffusion.

Diffusion rate		10^{-6} cm^2/sec	10^{-7} cm^2/sec	10^{-8} cm^2/sec
R_1 (mm)	R_2 (mm)	τ (sec.)	τ (sec.)	τ (sec.)
0.01	0.1	1.15	11.5	115
0.09		4.27	42.7	427
0.05	0.5	28	280	2800
0.45		107	1070	10700
0.2	2.0	461	4610	46100
1.8		1707	17070	170700

CONCLUSIONS

From this study, we found that plant roots can enhance the bioremediation process of TCE by acting as a transport pathway in which TCE moves into plant roots with water and is transported to the vadose zone where it may diffuse into the soil and pass to the atmosphere. During this transport process, TCE in small roots approaches equilibrium with the TCE in the soil in a very short time, while TCE in bigger roots takes a longer time. The mature root which has developed a Casparian strip has a higher resistance to aqueous transport in the root wall; however this does not appear to prohibit the diffusion of TCE through the root wall.

ACKNOWLEDGEMENTS

This research was partially supported by the U.S. EPA under assistance agreements R-815709 and R-819653 to the Great Plains-Rocky Mountain Hazardous Substance Research Center for regions 7 and 8 under project 94-27. It has not been submitted to the EPA for peer review and, therefore, may not necessarily reflect views of the agency and no official endorsement should be inferred. The Center for Hazardous Substance Research also provided partial funding.

REFERENCES

1. Cussler, E. L. 1984, Diffusion: Mass Transfer in Fluid System, Cambridge University Press 172-193.

2. Levitt, J. 1974, Introduction to Plant Physiology, second edition the C.V.Mosby Company, 114-133.

3. Narayanan, Muralidharan, Davis, L. C. and Erickson, L. E. 1995, "Fate of Volatile Chlorinated Organic Compounds in a Laboratory Chamber with Alfalfa Plant", Environmental Science and Technology 29: 2437-2444.

4. Newman, L. A., Strand, S. E., Choe, N., Duffy, J., Ekuan, G., Ruszaj, M., Shurtleff, B. B., Wilmoth, J., Heilman, P., and Gordon, M. P. 1997, "Uptake and Biotransformation of Trichloroethylene by Hybrid Poplars", Environmental Science and Technology, 31: 1062-1067.

5. Trapp, S. and Craig Mc Farlane, 1995, J., Plant Contaminant, CRC Press 14-20 and 107-127.

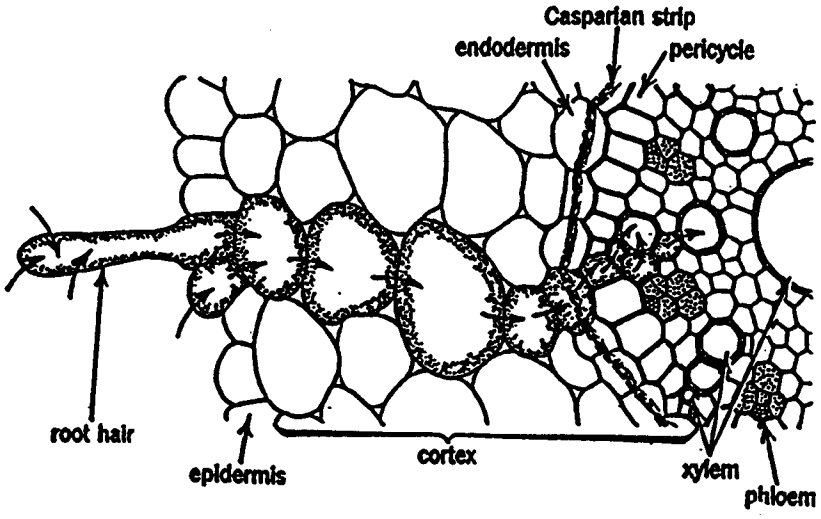

Figure 1. Wheat root cross section showing root anatomy and possible routes of water and solute movement. (From Trapp and McFarlane, 1995, Plant Contaminant. CRC Press, p. 19.)

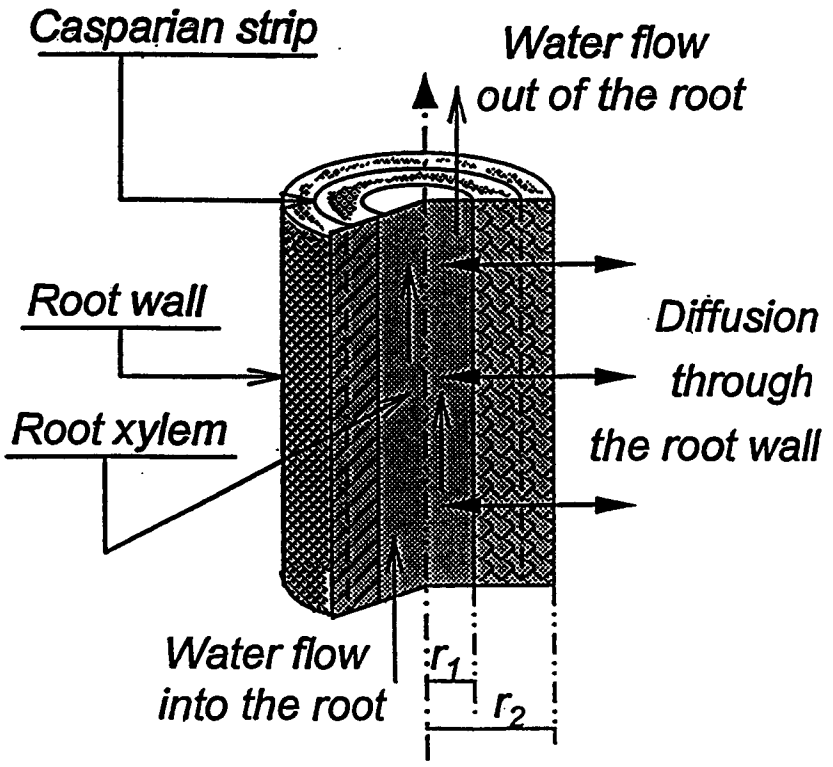

Figure 2. Schematic of root element structure.

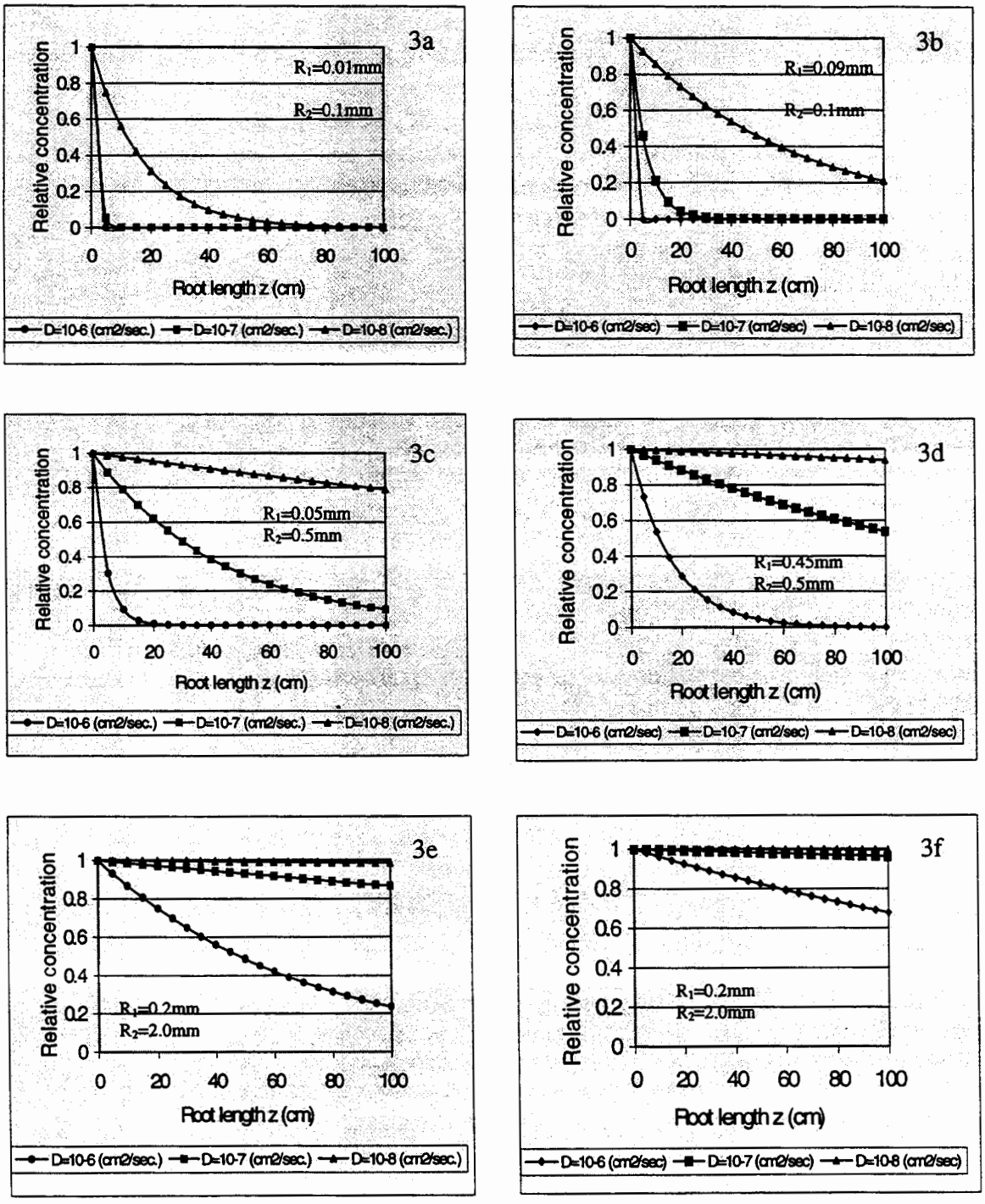

Figure 3. Relative concentration of TCE at the root surface as a function of root length and relative radial dimensional of xylem region (R_1) and root (R_2)

An Experimental Study of Trichloroethylene Fluxes into the Atmosphere

Qizhi Zhang[1], Lawrence C. Davis[2], Larry E. Erickson[1]
Departments of [1]Chemical Engineering and [2]Biochemistry
Kansas State University
Manhattan, KS 66506

ABSTRACT

Experiments were conducted with a six channel system to investigate the fate of non-aqueous phase liquid (NAPL) contaminants under vegetation and air sparging conditions. Trichloroethylene (TCE) was introduced into five experimental channels. Channels 1,2,5 and 6 were planted with alfalfa plants, and channel 4 was unplanted. Meanwhile, channels 1 and 6 were air sparged through gas dispersion stones installed along the channel bottoms.

Gas phase above the soil surface was monitored and flux rates of TCE entering the atmosphere were calculated based on the detected gas phase concentrations. The flux data of each channel and the time-integrated amount of TCE lost into the atmosphere are presented. The results indicate that both vegetation and air-sparging significantly increased TCE flux because of enhanced evapotranspiration and improved mass transfer from the NAPL phase into the aqueous phase.

Key words: flux, phytoremediation, air sparging, trichloroethylene , dichloroethylene

INTRODUCTION

Because of widespread contamination of groundwater and subsurface soils by volatile organic compounds (VOCs) and nonaqueous phase liquids (NAPLs), it is important to study the environmental fate and transport of these compounds in soils and groundwater and to explore appropriate remediation techniques. VOCs such as trichloroethylene (TCE), tetrachloroethylene (PCE), 1,1,1-trichloroethane (TCA) and chloroform (suspected teratogens) are resistant to biodegradation in aerobic subsurface environments, so they persist in polluted groundwater.

Researchers have found that vegetation may be used to actively promote microbial restoration of chemically contaminated soils and groundwater (Walton and Anderson, 1990; Ferro et al., 1994; Narayanan et al., 1995a; and Davis et al., 1993a). Plants can pump water from the saturated soil to the vadose zone. Within the vadose zone, there may be either degradation or volatilization of the contaminant (Narayanan et al., 1995a; and Narayanan et al., 1995b). The beneficial effects of vegetation have been reported in a number of studies (Davis et al., 1993a; Davis et al., 1993b; Erickson et al., 1994; Tracy et al., 1992; Schnoor et al., 1995; Shimp et al., 1993). As a result, phytoremediation, the use of vegetation for the in situ treatment of contaminated soils and groundwater, has become an emerging technology that promises effective and inexpensive cleanup of certain hazardous waste sites.

Plants remediate organic pollutants via three mechanisms: direct uptake of contaminants and subsequent accumulation of nonphytotoxic metabolites into plant tissue; release of exudates and enzymes that stimulate microbial activity and biochemical transformations; and enhancement of mineralization in the rhizosphere (Schnoor et al., 1995).

Air sparging (AS) is a relatively new technology that is being implemented at numerous sites around the country (Mercer and Cohen, 1990). In situ air sparging (IAS) systems operate in a manner similar to above-ground air strippers, with the soil acting as the packing. Air is injected and allowed to flow through the water column over the "packing". Air bubbles that contact dissolved/adsorbed phase contaminants in the aquifer cause volatilization of the VOCs. The volatile organics are then carried with the air flow (Johnson et al., 1993).

Volatilization is a predominant mass transfer process for compounds with high values of Henry's Law constant. The volatilization may be influenced by the composition of soils; for example, VOCs adsorb to soils with high organic content. This may reduce the potential and rate for volatilization of the VOCs (Reddy et al., 1995). At concentrations typical of a moderately polluted estuary (0.2-4μg/l) and under experimental conditions simulating winter, spring and summer, Wakeham et al. (1983) found that, in experimental marine ecosystems, volatilization appears to be the major removal process for all the investigated classes. For toluene, for example, half-lives of 16 days, 1.5 days and 13 days were found for spring, summer and winter, respectively. TCE and PCE showed similar half-lives, which ranged from 25 days to 15 days. Jensen and Rosenberg (1975), in experiments with both open and closed systems involving seawater, found that evaporative losses of PCE were greater than losses by degradation. Mass balances in previous studies (Zhang et al., 1996; Zhang et al., 1997) have demonstrated that, under alfalfa vegetation conditions, the disappearance of TCE due to biodegradation was insignificant during half year testing period. Volatilization of VOC contaminants like TCE from groundwater and subsequent transport to the atmosphere can provide a natural remediation pathway.

The purpose of the experimental work presented here was to obtain quantitative information on the loss of contaminant into the atmosphere under vegetation and air sparging conditions. Emphasis was placed on the evaluation of the influence that vegetation and air sparging have on the removal of contaminant. TCE was used in the experiments as a nonaqueous liquid residue in the saturated zone. The gas phase above the soil surface was monitored and gas phase flux rates of TCE and its breakdown product DCE were obtained.

EXPERIMENTAL METHODS

Physical Modeling

The aquifer model used in this study was a six channel system of which each channel was 0.10 m wide, 1.10 m long, and 0.60 m deep. It was constructed with steel bottoms, side panels, and sheet end panels. Channels 1,2,3,5, and 6 were planted with alfalfa plants, while channel 4

was unplanted. In addition, channels 1 and 6 were aerated at 2.14 L/m^2•day via alumina gas dispersion stones placed along the channel bottoms (see previous description in Zhang et al., 1997).

The whole system was continually illuminated with 12 cool white fluorescent lights (40W) at a height of 50 cm above the soil surface. The water table was kept at 35 cm deep measured from the bottom by holding the outflow tubing at a constant height. Distilled water was added into each channel at 1 L/day as inlet ground water. The plants, spaced at 10 cm intervals along the channels, were harvested monthly.

Sampling and Analysis

To investigate effects of vegetation and air sparging on the loss of contaminant into the atmosphere, 20 ml pure liquid TCE was injected into each flow stream inlet at the bottom of channels 1,2,3, 5 and 6. Six identical one-end-opened containers were placed along the top of each channel at six different positions to collect the soil gas above the surface (Figure 1). Gas samples were taken using 1 ml gas syringes through septa in the tops of the containers. The sample composition was then analyzed by a gas chromatograph equipped with a flame ionization detector.

The mass balance on each container can be written as:

$$V * \frac{dC}{dt} = F * A$$

where C is the contaminant concentration in the collecting container (mM); t is the accumulation time (minutes); A is the container cross sectional area (m^2); V is the container volume (m^3); and F is the flux of the contaminant entering the container from the channel soil surface (mmoles/m^{2}day). F is a function of time and equal to the actual flux from the channel soil surface at t=0.

Initially, in order to estimate the gradient of C versus t profile, the TCE accumulation process within each container was tracked over time. It was found that the concentration increased from zero linearly with time up to 40 minutes. To obtain accurate measurement above GC detection limits for TCE and dichloroethylene (DCE) and to ensure reasonable linearity of the concentration versus time profile, we chose 40 minutes as the time limit of linear accumulation. Then the gas samples were taken from containers at 40 minutes after container placement. Based on this linear accumulation assumption and the gas concentrations measured, at $0<t<40$ min., the actual channel flux can be obtained as follows:

$$N = F\big|_{t=0} = \frac{V}{A} * \frac{dC}{dt}\Big|_{t=0} = \frac{V}{A} * \frac{C-0}{t-0} = \frac{C*V}{A*t}$$

For TCE, we can write:

$$N_{TCE} = \frac{C_{TCE} * V}{A * t}$$

where N_{TCE} is the flux rate of TCE (mmoles/m^{2}day); C_{TCE} is TCE concentration (mM) measured in the gas containers; and t is the accumulation time, which was chosen as 40 minutes. A similar equation was used for DCE.

Furthermore, we assumed that each container gave the representative flux for the channel area between the center line of the container and that of the one closer to the inlet end. Accordingly, the gas TCE and DCE fluxes calculated using the above equation at six different sampling positions were converted into distance-weighted average fluxes for each channel, i.e.,

$$N_{TCE,avg.} = \frac{\sum_{1}^{6} (l_i - l_{i-1}) N_{TCE,i}}{L}$$

in which $N_{TCE,avg.}$ is the distance-weighted average flux of TCE; l_i is the distance from the ith gas collection container center to the inlet end (m) with i=1,2,...,6 from the inlet end to the outlet end; in order to include the entire area, we let l_0=0 and l_6=L; and L=1.10 m. An equivalent equation was written for DCE.

Finally, the distance-weighted averages were integrated over time, assuming that DCE resulted from equimolar transformation of TCE. Since we did not measure the flux data at the early period (about 40 days) after TCE injection, we assumed that the fluxes were zero when TCE was injected and that there existed linear flux-time relationships for the period between the original point and the first flux data points.

RESULTS AND DISCUSSION

The distance-weighted channel flux average data were plotted in Figures 2,3,4,5 and 6, which includes both individual fluxes of TCE and DCE and the total fluxes. Obviously, planted channels 1,2,5 and 6 had higher fluxes than the unplanted channel 4. The largest flux values (>5 mmoles/m^2 •day) appeared from the two air sparged channels where the gas flow enhanced the volatilization and consequently the flux. In addition, air sparging created turbulence and increased mixing in the saturated zone, which increased the contact between groundwater and the NAPL. The air sparging led to higher concentrations of TCE in the groundwater (Zhang et al., 1997). With higher groundwater TCE concentration and higher water upward flow rate due to evapotranspiration, two air sparged channels could have higher fluxes entering the atmosphere. As TCE was removed by both vertical fluxes and horizontal effluent flow out of the channels with time, values of fluxes decreased.

The results were integrated over time to obtain the estimated loss to the atmosphere from each channel. Figure 7 shows the losses of TCE (and DCE) into the atmosphere at different times of the test. After 183 days, there was no more TCE or DCE detected in the effluents from the system. From channel 4, which was neither planted nor air-sparged, 7% of injected TCE was lost into atmosphere. In comparison, as shown in Table 1, from channels 2 and 5, which were planted with alfalfa plants, the losses increased to 16% and 12%, respectively. The conjunction of vegetation with air sparging caused even higher losses, 17% from channel 1 and 21% from channel 6.

Table 1. Amount of TCE lost into the atmosphere within six months.

units	Ch1	Ch2	Ch4	Ch5	Ch6
mmoles	38.84	34.68	14.74	27.25	46.16
grams	5.11	4.56	1.94	3.58	6.07
%(of 29.2g)	17	16	7	12	21

CONCLUSIONS

The TCE fluxes into the atmosphere indicated that vegetation and air-sparging significantly increased TCE flux rates by enhancing upward water and air flow and by improving TCE mass transfer from the NAPL phase into the aqueous phase. Volatilization appeared to be the major removal process of TCE from groundwater.

ACKNOWLEDGMENTS

This research was partially supported by the U.S. EPA under assistance agreements R-815709 and R-819653 to the Great Plains-Rocky Mountain Hazardous Substance Research Center for regions 7 and 8 under project 94-27. It has not been submitted to the EPA for peer review and, therefore, may not necessarily reflect views of the agency, and no official endorsement should be inferred. The Center for Hazardous Substance Research also provided partial funding.

REFERENCES

Davis, L.C., L. E. Erickson, E. Lee, J.F. Shimp and J.C. Tracy, 1993a. Effects of plants on the bioremediation of contaminated soil and ground water. *Environ. Prog.*, **12**, p.67-75.

Davis, L.C., C. Chaffin, N. Muralidharan, V.P. Visser, W.G. Fateley, L. E. Erickson and R. M. Hammaker, 1993b. Monitoring the beneficial effects of plants in bioremediation of volatile organic compounds. *Proceedings of the 1993 Hazardous Substance Research Conference*, Engineering Extension Service, Kansas State University, Manhattan, KS. D. Tillison, L. E. Erickson, S.C. Grant and J. P. McDonald Ed., 236-247.

Erickson, L. E., L. C. Davis, S. K, Santharam, S. C. Kim, N. Muralidharan and C. W. Rice, 1994. Biodegradation in the rhizosphere: Analysis of the beneficial effects of vegetation. *87th Annual Meeting*, AWMA, Cincinnati, OH, June 19-24. Paper No.94-WA86.04.

Ferro, A. M., R. C. Sims and B. Bugbee, 1994. Hycrest crested wheatgrass accelerates the degradation of pentachlorophenol in soil. *J. Environ. Qual.*, **23**, 272-279.

Jensen, S. and R. Rosenberg, 1975. Degradability of some chlorinated aliphatic hydrocarbons in sea water and sterilized water. *Water Res.* **9**(7), 659-661.

Johnson, R.L., P.C. Johnson, D.B. McWhorter, R.E. Hinchee and I. Goodman, Fall 1993. An overview of air sparging. *Ground Water Monitoring Remediation*, Vol. XIII, No.4, 127-135.

Mercer, J.W., and Cohen, R. M., 1990. A review of immiscible fluids in the subsurface. *J. Contaminant Hydrology*, **6**,107-163.

Narayanan, M., L. C. Davis and L. E. Erickson, 1995a. Fate of volatile chlorinated organic compounds in a laboratory chamber with alfalfa plants. *Environ. Sci. Technol.*, **29**, 2437-2444.

Narayanan, M., L.C. Davis, J. C. Tracy, L. E. Erickson and R. M. Green, 1995b. Experimental and modeling studies of the fate of organic contaminants in the presence of alfalfa plants. *J. Hazardous Materials*, **41**, 229-249.

Reddy, K.R., K. Sinduja and J. Zhou, 1995. A review of in-situ air sparging for the remediation of VOC-contaminated saturated soils and groundwater. *Hazard. Waste & Hazard. Mater.*, **12** (2), 97-118.

Schnoor, J.L., L.A. Licht, S.C. McCutcheon, N.L. Wolfe and L. H. Carreira, 1995. Phytoremediation of organic and nutrient contaminants. Environ. Sci. & Technol., **29**(7), 318A-323A.

Shimp, J. F., J. C. Tracy, L. C. Davis, E. Lee, W. Huang, L. E. Erickson and , J. L. Schnoor, 1993. Beneficial effects of Plants in Remediation of soil and groundwater contaminated with organic materials. *CRC Critical Reviews in Environmental Science and Technology*, **23**, 41-77.

Tracy, J. C., L. E. Erickson, J. Shimp and L. C. Davis, 1992. Modeling the beneficial effects of vegetation in the management of landfill leachates. *Proceedings of the Air and Waste Management Association, 85th Annual Meeting*, paper 92-27.03.

Wakeham, S.G., Davis, A.C. and J.L. Karas, 1983. Mesocosm experiments to determine the fate and persistence of volatile organic compounds in coastal sea water. *Environ. Sci. Technol.* **17**, 611-617.

Walton, B. T. and T. A. Anderson, 1990. Microbial degradation of trichloroethylene in the rhizosphere: potential application to biological remediation of waste sites. *Appli. Environ. Microbiol.*, **56**, 1012-1016.

Zhang, Q., J. Hu, L. C. Davis and L. E. Erickson, 1997. Effect of air sparging on fate and transport of trichloroethylene in chambers with alfalfa plants. *Proceedings of the 12th Annual Conference on Hazardous Waste Research*, Kansas City, MO.

Zhang, Q., B. Goplen, S. Vanderhoof, L. C. Davis and L. E. Erickson, 1996. Fate and effect of trichloroethylene as nonaqueous phase liquid in chambers with alfalfa. *Proceedings of the 26th Annual Biochemical Engineering Conference,* L. E. Erickson Ed., 154-163.

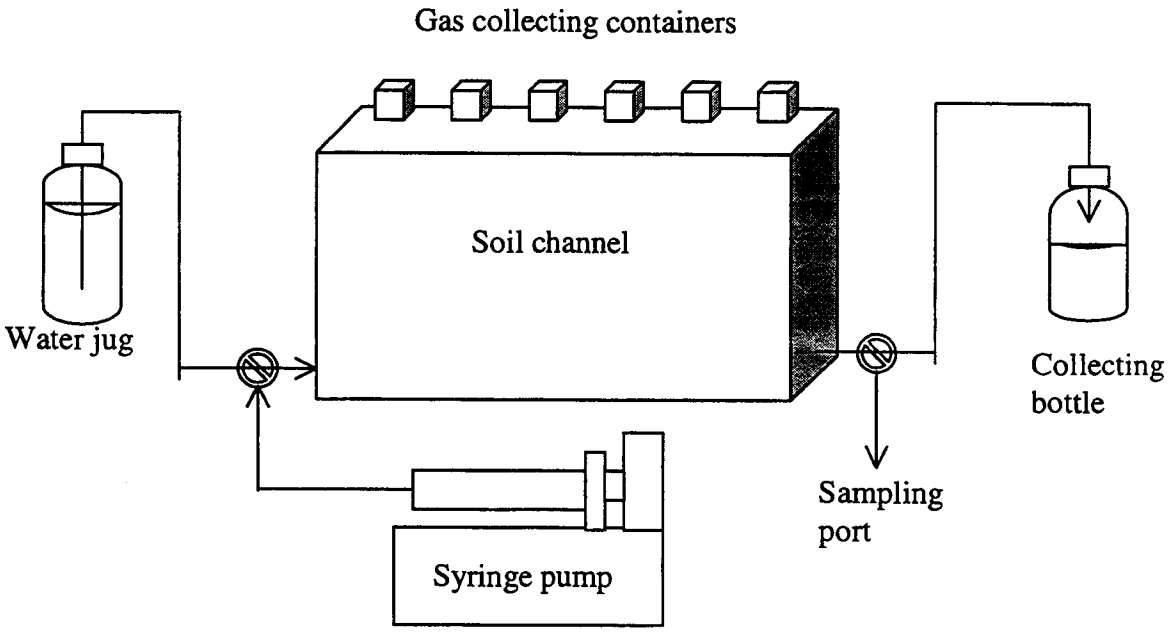

Figure 1. Diagram of the operating system.

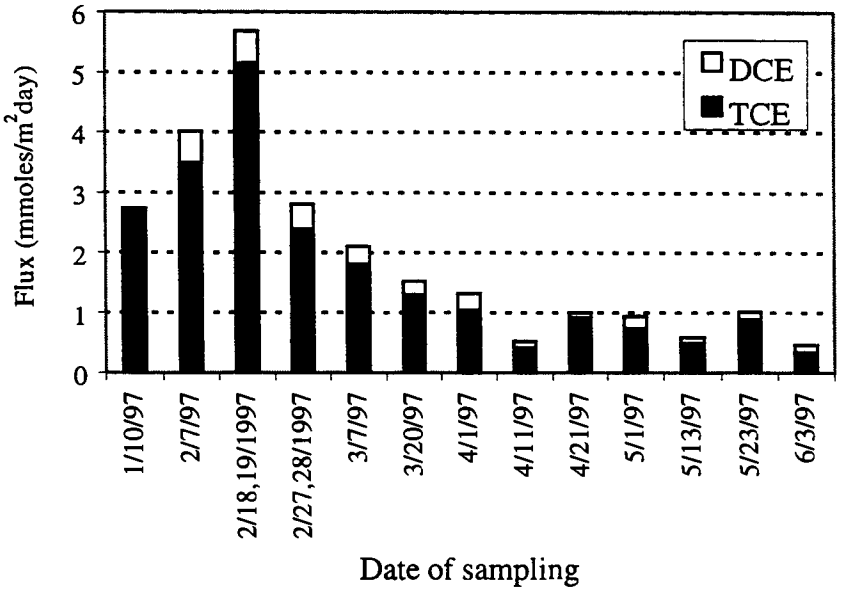

Figure 2. TCE and DCE flux rates from channel 1.

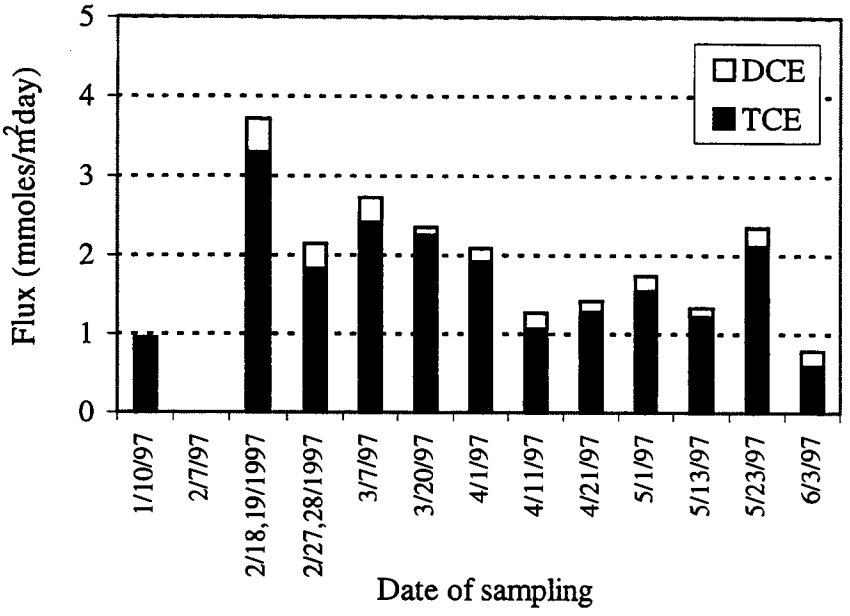

Figure 3. TCE and DCE flux rates from channel 2.

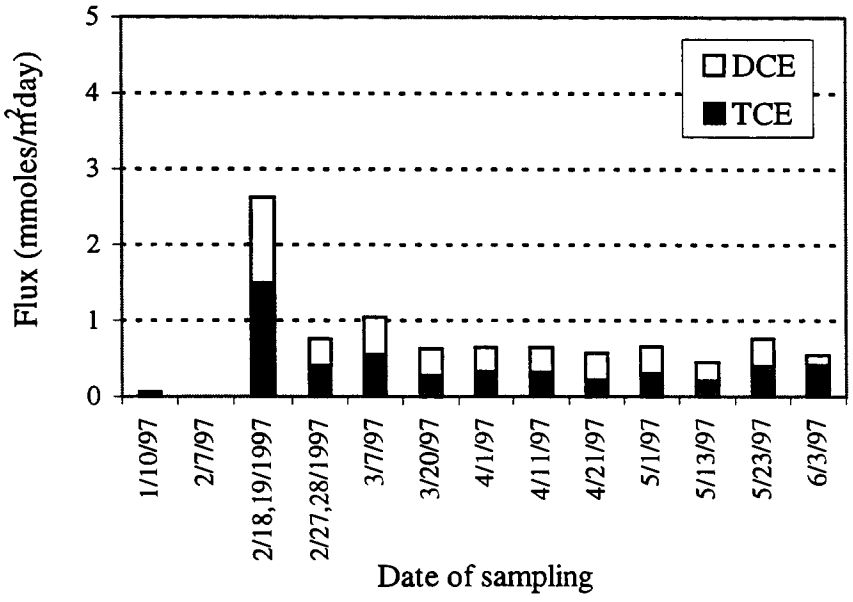

Figure 4. TCE and DCE flux rates from channel 4.

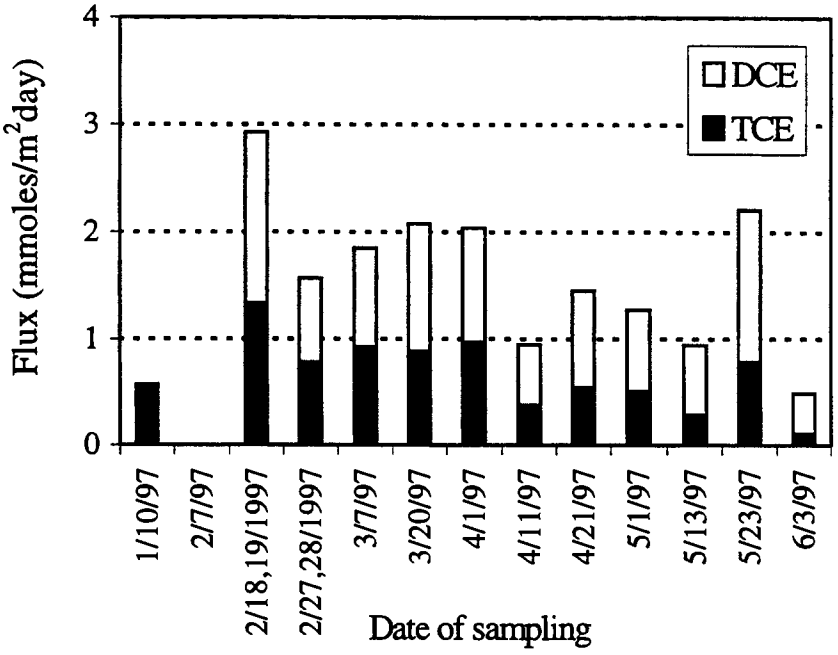

Figure 5. TCE and DCE flux rates from channel 5.

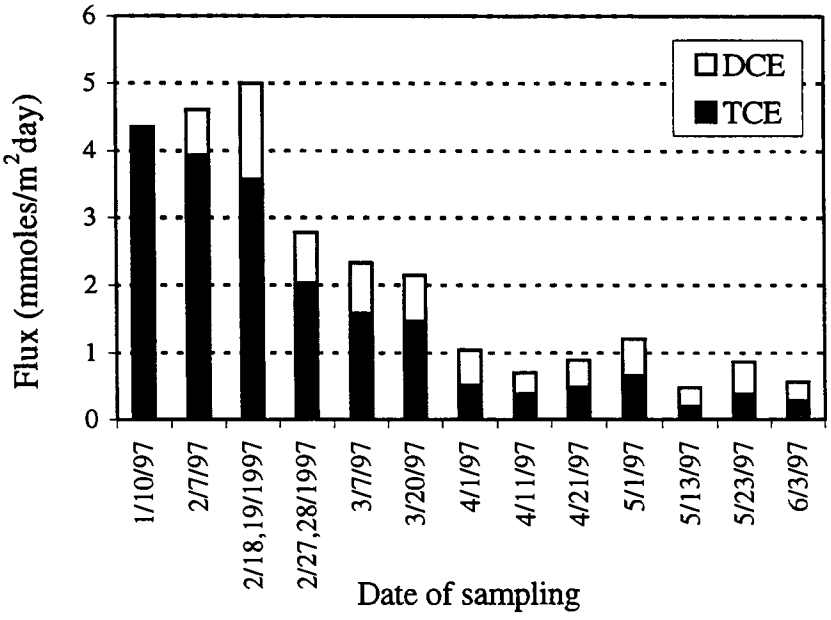

Figure 6. TCE and DCE flux rates from channel 6.

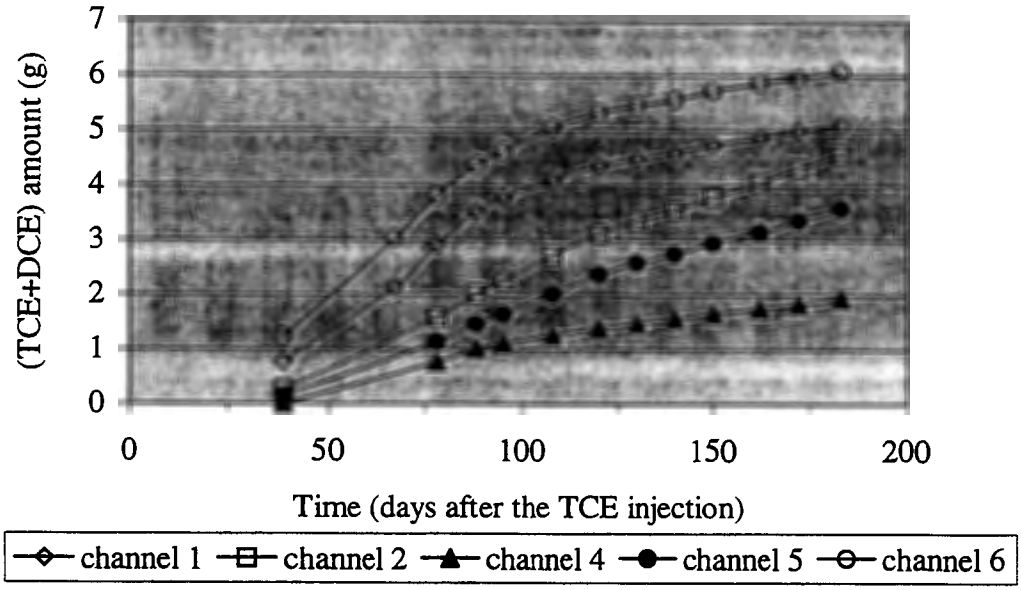

Figure 7. Amount of TCE+DCE lost to the atmosphere from five channels.

Toluene Contamination Enhances Populations of Toluene Degraders in the Rhizosphere

Xiaowei Wu and L. C. Davis
Department of Biochemistry
Kansas State University
Manhattan, KS 66506

ABSTRACT

A soil microcosm study was conducted to see the fate of released toluene degrader *Pseudomonas putida* F1 (P.pF1) in soil. Within two months, the populations of P.pF1 went down below detection limit (100 CFU/ g dry soil) in the presence or in the absence of plants, although they declined more slowly with plants present. With the treatment of diluted toluene solution (50 μg/ ml, 125 ml/ day), P.pF1 populations around poplars were brought up to level of 10^6 CFU/ g dry soil within three weeks. The microcosms planted with the biggest plants had the largest P.pF1 populations, although there was no significant difference observed between P.pF1 populations in planted and unplanted soils. The same toluene treatment of alfalfa microcosms was also able to increase the P.pF1 populations to above detection limit in soil microcosms inoculated with P.pF1 six months previously which had P.pF1 populations below detection limit for over four months. There was no significant difference in toluene concentrations in soil water of inoculated and uninoculated microcosms. There was no obvious inhibition of total heterotroph populations other than P.pF1 due to either the toxicity of toluene or the increasing population of P.pF1. Whether the population increase is due to the multiplication of a small number of P.pF1 which remained in soil after inoculation, or it is because the toluene treatment brought a viable but an unculturable population back to culturable state is not known.

Key words: *Pseudomonas putida* F1, microcosm, toluene

Microbial Transport in a Pilot-Scale Biological Treatment Zone

Daniel J. Adams[1], M. A. Malusis[2], K. F. Reardon[1], C. D. Shackelford[2]
Departments of [1]Chemical and Bioresource Engineering and [2]Civil Engineering
Colorado State University
Fort Collins, CO 80523-1370

and

Al W. Bourquin and Douglas C. Mosteller
Camp Dresser & McKee Inc.
Denver, CO 80202

ABSTRACT

Bioaugmentation may be an effective strategy for aquifer remediation in situations in which the desired metabolic capability is not present. A critical question for successful bioaugmentation is: will the added cells plug the aquifer downgradient of the addition point? To find the answer, a 50% scale model of the proposed bioaugmentation system was constructed and tested under approximate field conditions using soil and ground water from the site. Two strains of *Burkholderia cepacia* $PR1_{301c}$ (PR1) were tested: the original and an adhesion-deficient variant (ENV-435). Ground water flow in the system was characterized and microbial transport was measured by collecting cells from different sampling points. We found that most of the added PR1 did not move more than 2 inches, while most of the ENV-435 cells transported rapidly.

This work was supported in part by Grant MSS-9257305 to C. D. Shackelford from the National Science Foundation and by the City of Wichita.

A Model of the Effects of Acclimation on the Cardiorespiratory and Thermoregulatory Systems

D. Downey and R. C. Seagrave
Departments of Chemical Engineering and Biomedical Engineering
Iowa State University
Ames, IA 50011

ABSTRACT

This work involves the continuing development of a unique model that can be used to describe the complex interactions which occur to regulate temperature and blood flows in the human body. It is the first model, to our knowledge, which includes both the transport of oxygen and carbon dioxide (mass balances) along with energy balances interacting on this level. The scope of this research is, therefore, very wide.

This model was originally developed to describe the competitive interactions between muscles and skin in their need for blood flow during exercise. More recently, a detailed study of the control relations used to predict skin blood flow was undertaken. Also, the model was revised to describe the effects of water immersion and swimming.

The model has now been modified to account for the effects of acclimation on the distribution of temperature, blood flow, and oxygen/carbon dioxide concentration in the body. Acclimation can be defined as physiological changes induced by environmental changes. Exercise training effects have been studied in relation to acclimation since they often occur concurrently. Both acclimation and training effects are extremely important factors contributing to the functioning of the human body. Our original model now has three modified forms for the cases of acclimation of trained subjects, acclimation of untrained subjects, and training independent of acclimation. The results of these models compared to available experimental data are presented.

INTRODUCTION

Most previous models of the thermoregulatory system have consisted of at least three concentric cylinders with a layer of skin wrapped around a muscle layer which is, in turn, wrapped around the core. In this type of arrangement, an effective thermal conductivity is usually assumed to provide a combined description of both convection and conduction. This method is usually adequate to describe basic conduction, but it cannot properly account for the increases in blood flow that occur during exercise and/or heat stress.

Separate models of the circulatory system have been developed to describe blood flows that carry oxygen, carbon dioxide, and water, but they have either not included the changes in temperature which are also occurring or have over-simplified the situation. We are using a combination of these methods to develop this coupled model. The goal of our work is to describe the distribution of regional blood flows necessary to satisfy both oxygen requirements and thermoregulatory needs during exercise in varying environments. The specific focus of this paper is on how acclimation affects the functioning of these systems.

THE BASIC MODEL

This coupled model was first used to show the competitive blood flow interactions which occur during exercise (1). Excess blood flow to the muscles is required to carry the oxygen needed to produce work during exercise. Blood flow to the skin must consequently be increased to transfer the heat generated by this work to the surroundings through increased convective heat loss and evaporation. Therefore, a competition is often created between skin and muscles in their need for blood flow during extreme exercise. This competition is even more significant during exercise in the heat because when the ambient temperature is increased, skin blood flow must increase to increase skin temperature.

The model was developed using a consistent set of physical and physiological parameters for a standard man. Typical resting and constant values were chosen to satisfy the material and energy balances. The validity of these parameters was then tested in a sensitivity analysis. The modeling work was done on MATLAB using the Simulink modeling package on a DEC Station workstation. The equations were solved using a fifth order Runge-Kutta method available in Simulink.

Along with energy balances and mass balances for oxygen and carbon dioxide for each of the compartments, an oxygen/hemoglobin dissociation relationship was used to relate the concentration of oxygen in the air exiting the lungs to the concentration of oxygen in the blood exiting the lungs (1). This relationship also accounts for the Bohr Effect and changes in the core temperature. A corresponding dissociation relationship for carbon dioxide was used to relate the concentration of carbon dioxide in the air exiting the lungs to the concentration of carbon dioxide in the blood exiting the lungs. This relationship accounts for the Haldane Effect and temperature changes.

A respiratory quotient which is a function of exercise level is used to relate the metabolism of oxygen to carbon dioxide metabolism. The metabolism of oxygen is also related to energy metabolism by the calorific oxygen equivalent statement. This equation also has a dependence on the respiratory quotient, so all the material balances are coupled to each other and to the energy balances through metabolic terms as well as by blood flow.

Five major control relations are integrated into this system of equations to account for changes in volumetric flow rates. Control of evaporative heat loss is based on a linear model for sweat rate predictions (2). It is a function of both core and skin temperatures. Ventilation rate is regulated through a chemoreflex control model (3). It is in terms of arterial oxygen and carbon dioxide partial pressures.

To simulate repartitioning effects, blood flow to internal tissues is allowed to decrease to a set minimum value before cardiac output increases. Vasoconstriction of blood vessels in some tissues, such as splanchnic and renal, causes this redistribution of blood flow during exercise and/or heat stress. To determine muscle blood flow, we used a nonlinear control model which depends on the concentration of oxygen in the blood exiting the muscles. The gain in the muscle blood flow controller was set to achieve a known minimum concentration of oxygen in the blood exiting the muscles at a known maximum oxygen uptake. This sets the maximum muscle blood flow attainable.

The final control relationship, that for skin blood flow, was the most difficult to define. Because of the competition between skin and muscle for available blood flow, skin blood flow must be limited at some point. The control equation, which is a function of core temperature, was modified to develop an algorithm which includes changes with respect to ambient temperature and metabolism. This algorithm is consistent with the idea that at high ambient temperatures, skin blood

flow can increase by a greater amount at low levels of exercise, but at high exercise levels it cannot increase as much because muscle blood flow must also increase.

When the ambient temperature is significantly low and the subject is at rest, the core temperature starts to fall and another factor must be taken into account. Shivering is simulated to occur as an automatic increase in muscle metabolism when the core temperature falls below 36.6 degrees Celsius, which is considered to be the normal lower limit of the thermal comfort zone.

ADDITIONAL MODIFICATIONS

Several other interesting cases have been investigated using this model as a basis. First, since changing environmental conditions in the air was shown to have such an important effect, we decided to examine one completely different environment which is often encountered, when the skin is surrounded by water. This condition poses a problem for the body's thermoregulatory system because, when the skin is covered with water (as opposed to air), two important factors change. First, the heat transfer coefficient increases dramatically. This is mainly due to the increased thermal conductivity of water, which is much higher than that of air. Secondly, there is no evaporative heat loss under water. The first of these factors is much more significant, however, and the skin temperature rapidly approaches the water temperature. The case of swimming was also studied and it was found that core temperatures can still become compromisingly low even during exercise in water where more heat is being produced by the body. In addition, the heat transfer coefficient increases even more during swimming

In the case of exercise training, the model was revised to account for four major changes. First of all, there is not as much blood flow repartitioning from inactive tissues in trained subjects. Secondly, evaporative heat loss is increased. It is believed that this effect is due solely to an increased gain in evaporative heat loss dependent on core temperature. Third, skin blood flow can be decreased for moderate to heavy work in a warm environment. Finally, if the same exercise is performed after training, the metabolism level decreases.

ACCLIMATION

During acclimation to heat stress, numerous factors are changed in the human subject. Reductions in both heart rates and core temperatures have been found for a given work load in the heat. Peripheral blood flows, and probably also skin blood flows, decrease. Total blood volume increases and peripheral venous volume may increase as well. Skin temperatures decrease as evaporative cooling of the skin increases. The core to skin thermal conductance decreases while the core to skin temperature gradient increases. Some factors may remain unchanged during acclimation. Cardiac outputs and blood pressures have typically been observed to remain constant throughout the process.

In addition to acclimation to heat stress, acclimation can also occur in a cool or even cold environment. When a subject is first exposed to the cold, shivering thermogenesis occurs so excess heat is produced through a higher rate of shivering. When the exposure to cold is repeated, however, metabolic cold acclimation will include nonshivering thermogenesis whereby higher rates of basal heat production are maintained. In this case, there is an improved capacity to produce heat and heat is lost from the body surfaces faster. We have not accounted for this effect in our model yet.

Individual differences in subjects can produce varied responses to acclimation. Gender differences, for example, can produce different physiological responses to acclimation. Females

have a greater sweat gland density, but males can produce more sweat per gland. Gender studies have shown that, as the mechanisms for sweating differ, the average sweat rates also differ, and males and females have shown an even larger difference between their sweat rates after acclimation.

Generally, an improved sweating response is apparent during heat acclimation, which is probably arrived at by a reduction in the point of zero central drive. There is some evidence of an increase in gain, but this could be due to concurrent training. To attempt to separate these two effects, we have developed two models, one for acclimation of untrained subjects and the other for acclimation of trained subjects.

The model for acclimation of untrained subjects includes a skin blood flow algorithm modified for temperatures above 31 degrees Celsius for all levels of exercise. The core temperature set point for evaporative heat loss is also changed, but the gain remains the same. The model for acclimation of trained subjects combines factors which result from both training and acclimation. There is decreased blood flow repartitioning, consistent with the changes observed following training. An increased gain on evaporative heat loss is employed, as well as a revised core temperature set point which changes with acclimation. Finally, the skin blood flow algorithm is modified for moderate to heavy work in a warm environment.

RESULTS AND CONCLUSIONS

To develop both models for acclimation, experimental data taken from literature was compared to the temperatures predicted by the model. The control for skin blood flow and evaporative heat loss was set using data from unacclimated subjects taken on the first day and data from subjects believed to be completely acclimated on the tenth day. In Figure 1, the results are shown for a typical intermediate day during the process of acclimation. This example is from the model for trained subjects. The core temperature (dashed line) falls within the standard deviation for measured rectal temperature (X) and the skin temperature (solid line) also falls within the standard deviation for measured average skin temperature (*). The model prediction for muscle temperature is also shown (dotted line). The data points given here are means with upper and lower bounds representing the standard error (4).

It was previously mentioned that cardiac output does not usually change during acclimation. The resting cardiac output may decrease, however, with the decreased resting skin blood flows that often results from acclimation. Our original model would indicate that changing ambient temperatures at rest has little effect on skin blood flow. The modifications made for acclimation, however, would indicate that much more skin blood flow is necessary for unacclimated subjects at rest in the heat. This result is exemplified in Figure 2 which shows the model results compared to data (5). Here, the increased cardiac output, which is due almost entirely to increased skin blood flow in the model, is in good agreement with the data for unacclimated, but trained individuals. As acclimation time is increased, though, the model would indicate that cardiac output decreases more than the data show. This will be investigated further in the future development of the model.

The model agreement with experimental data is fairly good for the case of exercise in a cool environment. A typical example is shown in Figure 3 where the model core temperature (dashed line) is compared with measured rectal temperatures (X) and the model skin temperature (solid line) is compared with measured average skin temperatures (*). The measured values, from (6), are averages from five previously untrained subjects. The model muscle temperature is also shown (dotted line). The agreement with data for exercising in warmer ambient conditions is not as consistent. This is most likely due to the effect of varied humidity on the thermoregulatory system, as will be discussed in the Future Work section.

FUTURE WORK

A major factor which we have not yet taken into consideration is the effect of humidity on acclimation. It is clear that humidity is extremely important in how the body adjusts to an environment. In Figure 4, it can been seen that after acclimation to dry heat, both core and skin temperatures are overestimated by the current model, in this case the model for trained subjects. This would suggest that evaporative heat loss is underestimated and evaporation is actually more. When it is dry, more of the sweat which is produced can be evaporated and, thus, more heat is lost. After acclimation in humid conditions, however, core temperature is underestimated as this effect is reversed. Skin temperature is still overestimated in this case, but this is probably due to a slight overestimation of the skin blood flow. The symbols in this plot are consistent with those used in Figure 3. The experimental data are taken from (7) with data from four male subjects being averaged. The relative humidity is approximately 61 percent in the humid heat and 15 percent in the dry case.

The next step in the development of this model should be to incorporate water balances into the system of equations. After this is accomplished, it will be possible to account for important factors such as humidity and dehydration, which can have major effects on the functioning of the cardiorespiratory and thermoregulatory systems.

REFERENCES

(1) D. Downey. A coupled model of the cardiorespiratory and thermoregulatory systems. *M.S. Thesis*, Departments of Chemical Engineering and Biomedical Engineering, Iowa State University, Ames, Iowa.

(2) J. A. J. Stolwijk, B. Saltin, and A. P. Gagge. Physiological Factors Associated with Sweating During Exercise. *Aerospace Medicine*, 39:1101-1105, 1968.

(3) J. Duffin. A Mathematical Model of the Chemoreflex Control of Ventilation. *Respiration Physiology*, 15:277-301, 1972.

(4) D. Mitchell, L. C. Senay, C. H. Wyndham, A. J. vanRensburg, G. G. Rogers, and N. B. Strydom. Acclimatization in a hot, humid environment: energy exchange, body temperature, and sweating. *Journal of Applied Physiology*, 40(5):768-778, 1976.

(5) C. H. Wyndham, G. G. Rogers, L. C. Senay, and D. Mitchell. Acclimatization in a hot, humid environment: cardiovascular adjustments. *Journal of Applied Physiology*, 40(5):779-785, 1976.

(6) E. Schvartz, E. Saar, N. Meyerstein, and D. Benor. A comparison of three methods of acclimatization to dry heat. *Journal of Applied Physiology*, 34(2):214-219, 1973.

(7) A. J. Frye and E. Kamon. Sweating efficiency in acclimated men and women exercising in humid and dry heat. *Journal of Applied Physiology*, 54(4):972-977, 1983.

FIGURE 1

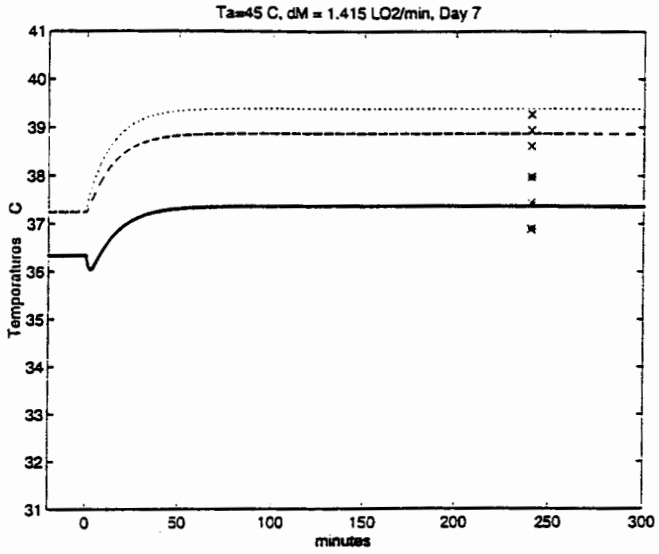

FIGURE 2: Ta = 45 °C, At Rest

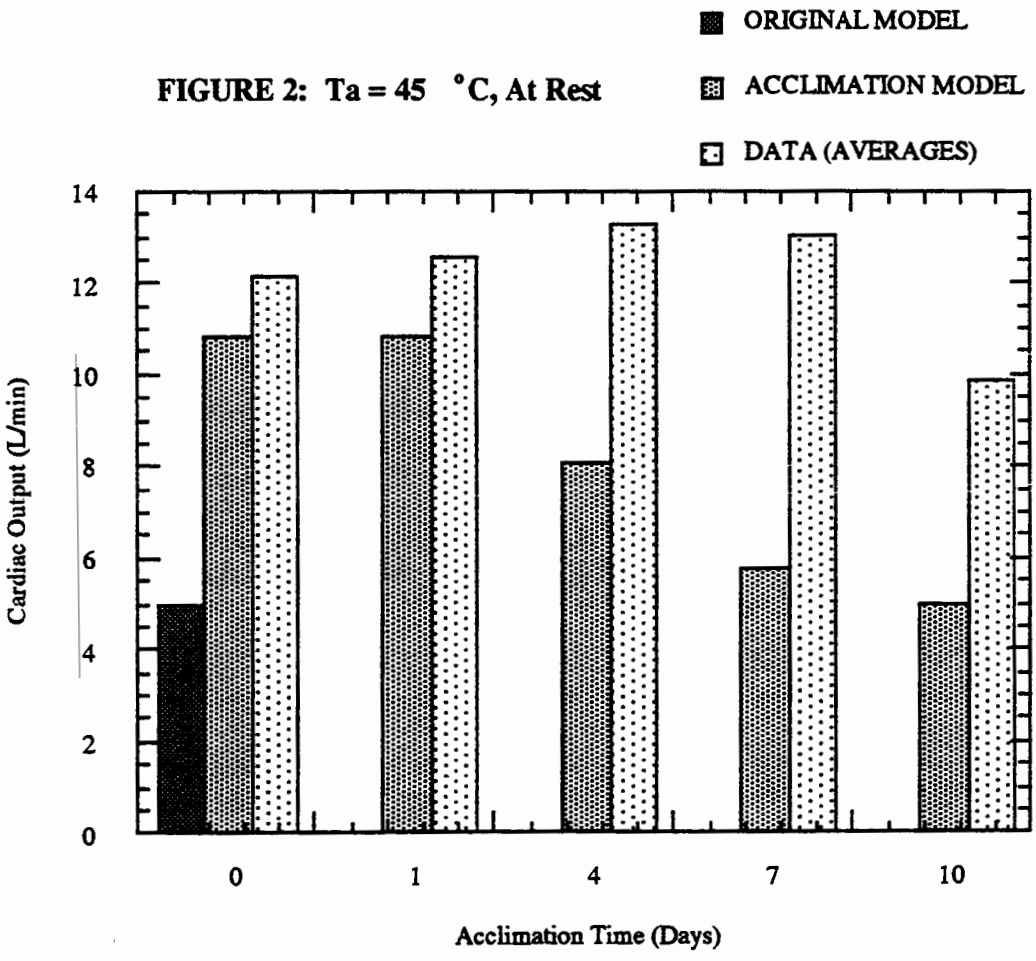

FIGURE 3

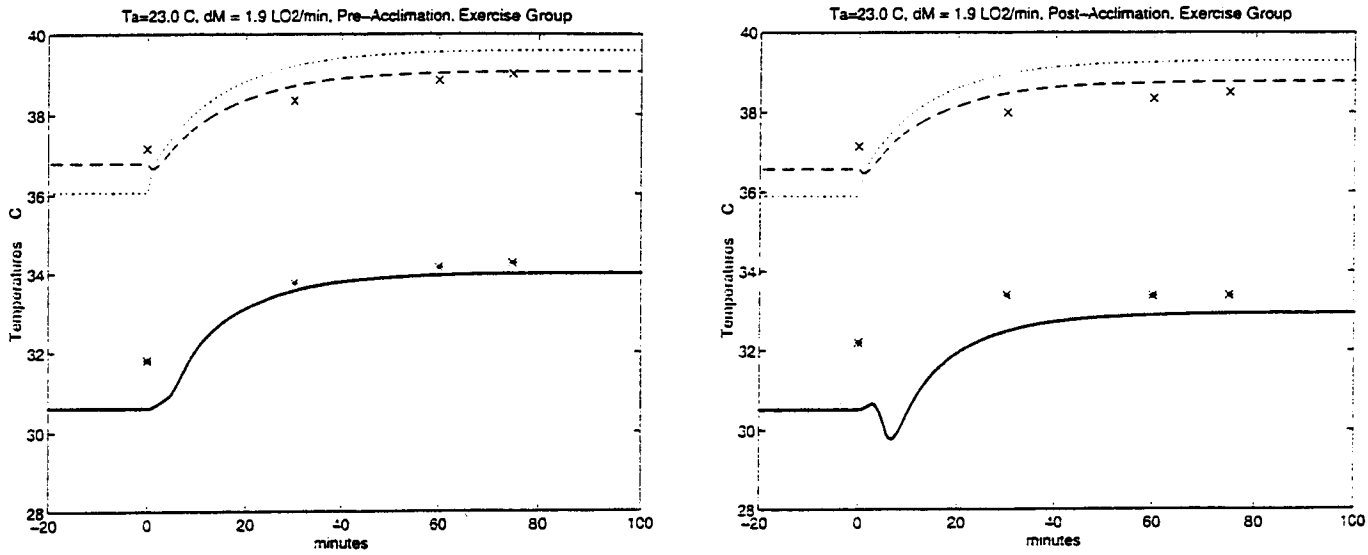

FIGURE 4

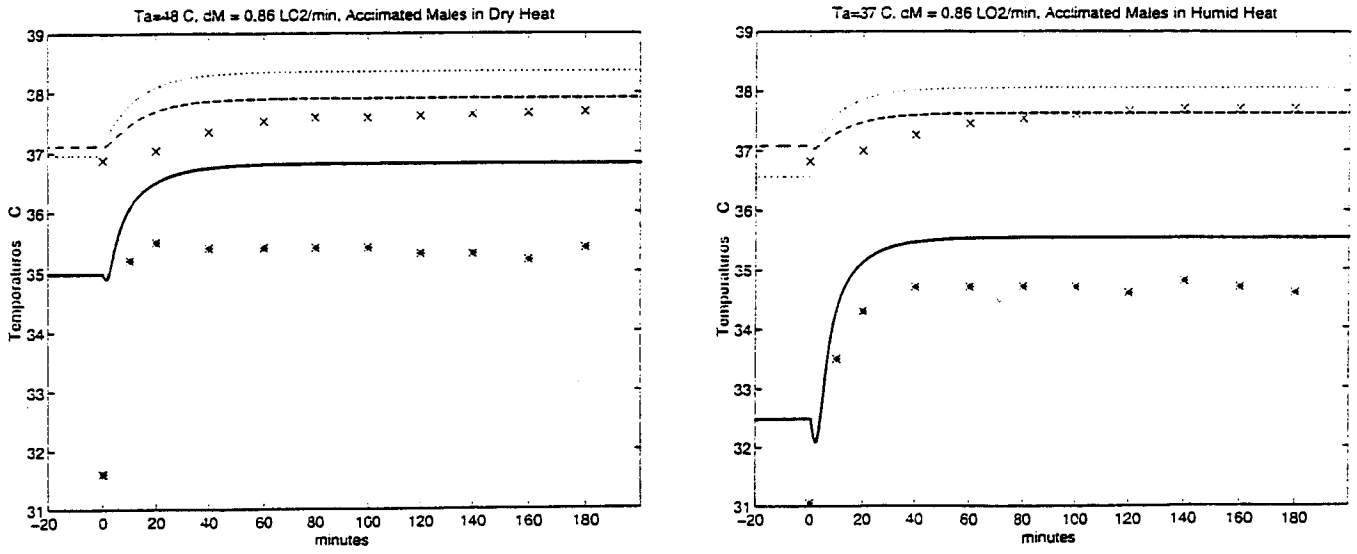

The Effects of Physiological Intermittent Pressures on Cartilage Regeneration

Scott E. Carver and Carole A. Heath
Department of Chemical Engineering
Iowa State University
Ames, IA 50011-2230

ABSTRACT

A bioreactor system has been developed which is designed to administer physiological levels of intermittent compressive force, through hydrostatic pressurization, to enhance matrix formation in long term perfusion culture. Isolated foal chondrocytes have been cultured in resorbable polymer meshes and grown in stainless steel reactors which allow semi-continuous feeding. Intermittent compressive forces have been applied to the cell/polymer constructs at different pressures (500 and 1000 psi) which may influence the three-dimensional structure of articular cartilage thought to give the tissue its weight bearing ability. Results indicate that physiological intermittent compressive forces enhance the chondrocytes ability to produce the extracellular matrix of articular cartilage. At both intermittent pressures, the concentration of sulfated glycosaminoglycan was found to be greater than concentrations in control samples. While collagen concentrations in the 500 psi and control samples were not significantly different, cultures at an intermittent pressure of 1000 psi enhanced the production of collagen. A correlation was found between the content of sulfated glycosaminoglycan and the compressive strength in pressurized samples. This correlation was not noted in control samples. These results imply that physiological intermittent compressive forces not only enhance the chondrocytes ability to produce their extracellular matrix but may help arrange that matrix to be more mechanically stable.

INTRODUCTION

The most prevalent form of arthritis, osteoarthritis, affects more than 30 million individuals of the United States alone.[1] This often debilitating disease involves the gradual degradation of articular cartilage due to traumatic injury or natural "wear & tear". If diagnosed early enough, the degradation can be arrested by injecting articular cartilage cells, chondrocytes, under a periosteal flap at the source of the injury.[2] However, if the defect becomes large the damaged tissue must be excised and replaced with an artificial prosthesis. These prostheses have limited lifespans and often cause more complications than they cure. An attractive alternative to an artificial prothesis is an engineered biological graft of articular cartilage developed *in vitro* to have the same biochemical and mechanical characteristics as tissue found *in vivo*.

Articular cartilage is both avascular and alymphatic. All nutrients required by the tissues cells are obtained from the synovial fluid encapsulated within the joint space. The only cell type found within articular cartilage is the chondrocyte which is responsible for the production and secretion of the organic components of the extracellular matrix. These organic components are collagen (namely types II, IX and XI) and proteoglycans which are composed of sulfated glycosaminoglycans. The fluid phase is made up of water and dissolved electrolytes which travel throughout the tissue via interstitial pores.

There are four key growth conditions needed in order to develop regenerated tissue *in vitro* which is comparable to native tissue. Chondrocytes require a three-dimensional culture environment in order to produce the correct phenotype of collagen.[3] If grown in two dimensions, as in a monolayer, chondrocytes dedifferentiate into fiboflasts and produce type I collagen which is present in fibrocartilage. Polymers of polyglycolic acid (PGA) formed into a non-woven mesh provide a suitable support structure which allow the chondrocytes to be cultured in three dimensions. PGA is biocompatible and resorbable and degrades into non-toxic components which are naturally removed. Chondrocytes *in vivo* are subjected to shear and compressive forces which they sense and respond to. Two types of pressure applications have been shown to enhance the production of the extracellular matrix by articular chondrocytes: intermittent pressures[4] and hydrostatic pressures applied at physiological levels.[5] In order to mimic an *in vivo* system, these two types of pressure applications must be combined. Long duration growth periods, from weeks to months, allow the chondrocytes to slowly create extracellular matrix. In order for long term cultures to be maintained, the constructs need to be supplied with fresh media periodically to maintain oxygen concentration levels. Semi-continuous perfusion of the *in vitro* environment helps fulfill nutrient requirements.

As of yet, these growth conditions have never been combined and it is the goal of this work to show that this combination will further enhance the chondrocytes to develop their respective matrix.

MATERIALS AND METHODS

A bioreaction system has been designed and constructed in which regenerated articular cartilage can be cultured under *in vivo* growth conditions (Fig. 1). Filtered house air flows through a series of Mac solenoid valves (Mid State Distributors; Des Moines, IA) which are electrically controlled with a programmable computer timer (Chrontrol; San Diego, CA). The supplied air is adjusted to a given pressure via a pressure regulator and is used to pressurize the contents of the high pressure reaction vessel (Fig. 2). Air is also used to open and close air-actuated valves (Omaha Valve and Fitting; Omaha, NE) located on each side of each reactor. When open, these valves allow media to be pumped into and out of the reaction space via a twelve channel media pump (Lab Research Products; Lincoln, NE). Twelve reactors are housed inside the incubation chamber which is maintained at 37 ^{0}C by a temperature control system. Inside each reactor is a three tiered support cage to which three PGA pads (Albany International; Mansfield, MA) are adhered with a medical adhesive.

Foal chondrocytes (College of Veterinary Medicine, Iowa State University; Ames, IA.) were dynamically seeded onto the PGA pads before the support cages were placed within the reactor at a concentration of 5 to 7.5 x 10^6 cells/pad. The reaction space was completely purged of air before the reactors were pressurized, leaving only water-based medium within the reactor. The contents of each reactor were pressurized with a reaction piston which is connected to a air piston located above each reactor. Two intermittent pressure were characterized (500 and 1000 psi) and the intermittent pressure regime was defined as 5 seconds pressurized and 15 seconds depressurized. This pressure regime was applied every four hours for 5 weeks and prior to pressurization each reactor was purged with fresh medium.

Six forms of quantitative and qualitative analysis were used to characterize regenerated samples. The H 33258 fluorometric assay was used to indirectly quantitate the total number of cells per construct by determining the total amount of DNA present.[6] The hydroxyproline assay was used to indirectly quantitate the total amount of collagen per sample by determining the total amount of this modified amino acid.[7] The sulfated glycosaminoglycan assay is a colorimetric assay allowing for the quantitation of the total proteoglycan present per sample.[8] The compressive modulus of each sample was quantitated from stress vs. strain data obtained with a Dynamic Mechanical Analyzer. Qualitative assessments of each regenerated sample were made using two forms of cellular microscopy. Light microscopy, in the phase contrast mode, was used to visualize s-GAG distributions, PGA density and cellular arrangement throughout the matrix. Transmission electron microscopy was used to assess collagen density and orientation of each regenerated sample.

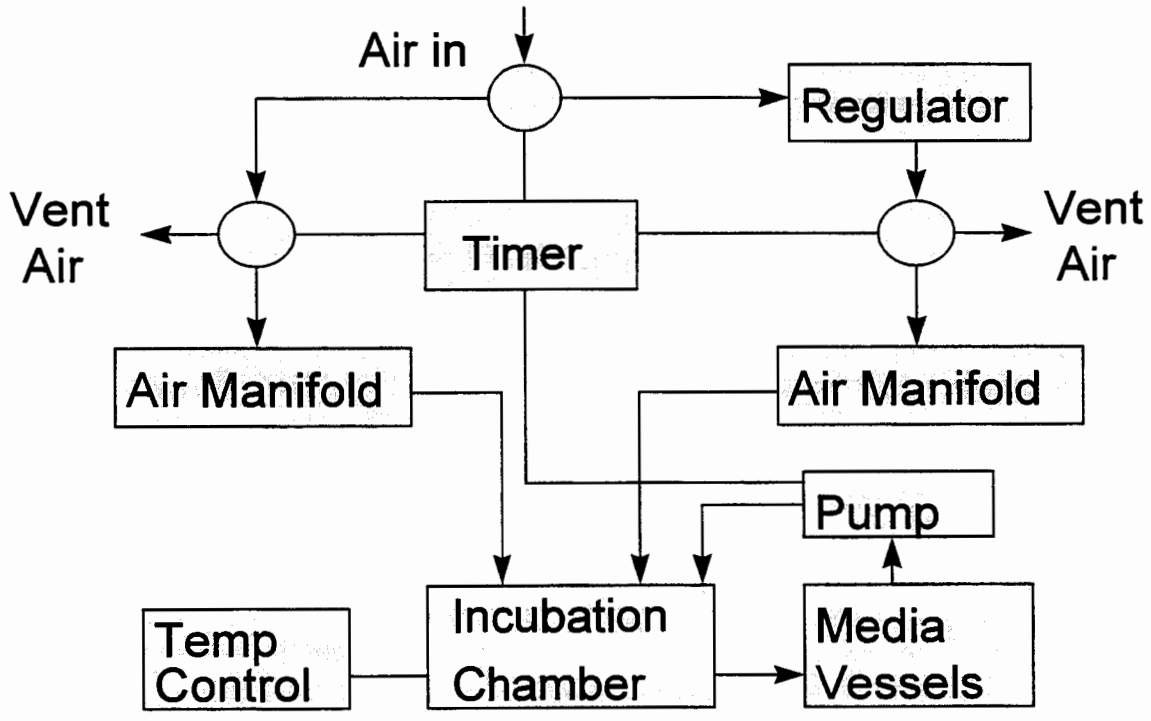

Figure 1: Flow diagram of the cartilage perfusion system

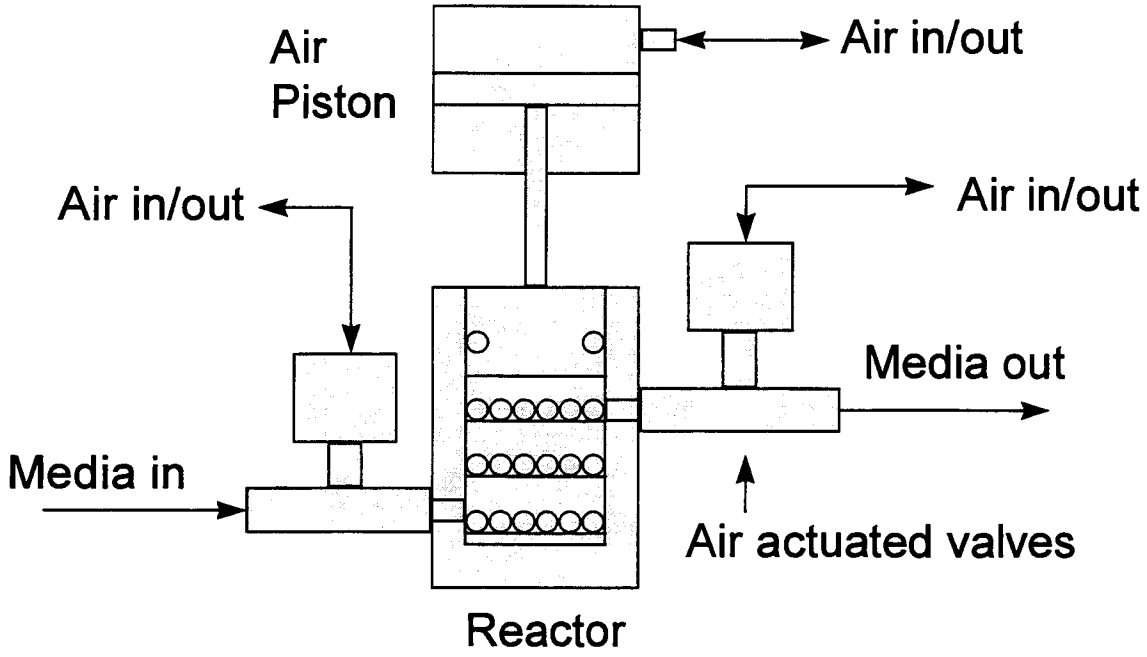

Figure 2: Schematic of the high pressure reaction vessel.

RESULTS AND DISCUSSION

Cell Concentration Profiles

Cell concentrations were determined for pressurized and control samples at 3, 4 and 5 weeks (Fig. 3). All cell concentrations were in the native regime at each week (1-6 x 10^7 cells/g tissue). As the weeks progress there seemed to be an apparent suppression in cell growth in pressurized samples. When chondrocytes are pressurized they are thought to concentrate on matrix production and not cellular replication.[4] However, since cell concentrations are based per gram tissue, these values may be artificially dropping as matrix production in pressurized samples increases, diluting the cell concentrations.

Collagen Concentration Profiles

Collagen concentrations were determined for pressurized and control samples at 3, 4 and 5 weeks (Fig. 4). All collagen concentrations are well below native values (125-220 mg/g tissue). This is due to the fact that all collagen present per sample was completely developed by the chondrocytes and, in order for native levels to be reached, longer growth periods may be needed. Collagen concentrations between 500 psi and control samples were found not to be significantly different. However, as the intermittent pressure was increased to 1000 psi, the collagen concentration increased implying that there is some minimum intermittent pressure (between 500 and 1000 psi) needed for the enhancement of collagen production.

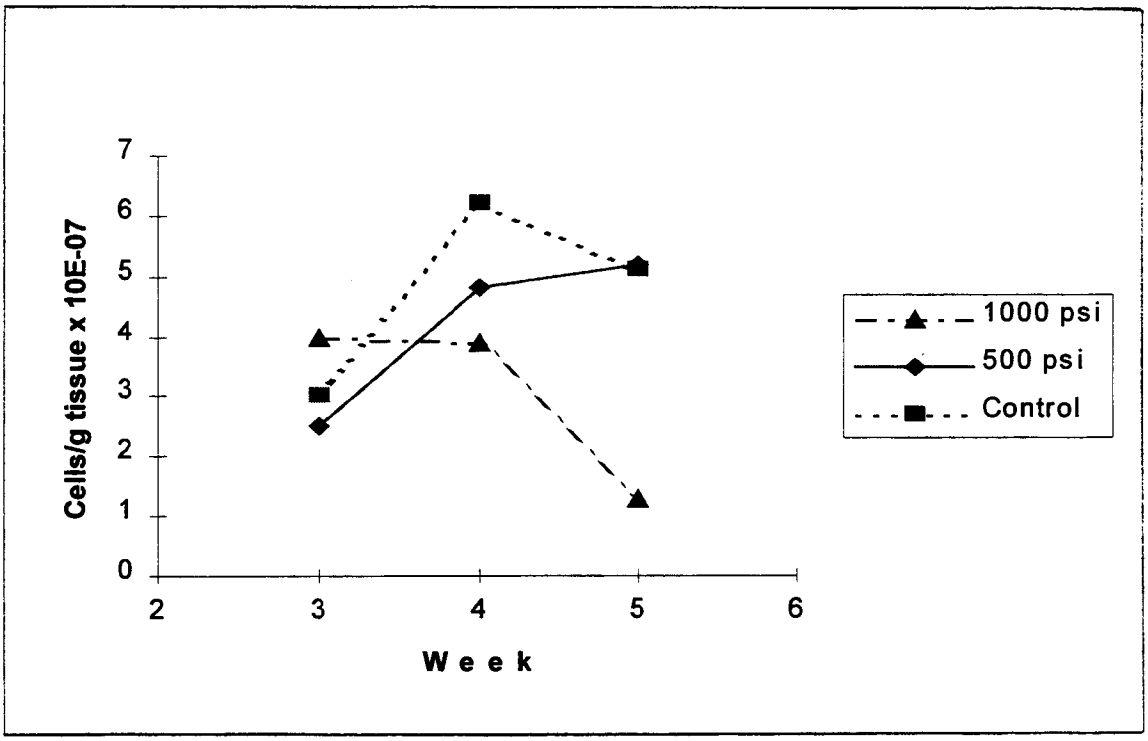

Figure 3: Cellular concentrations in intermittently pressurized and control samples.

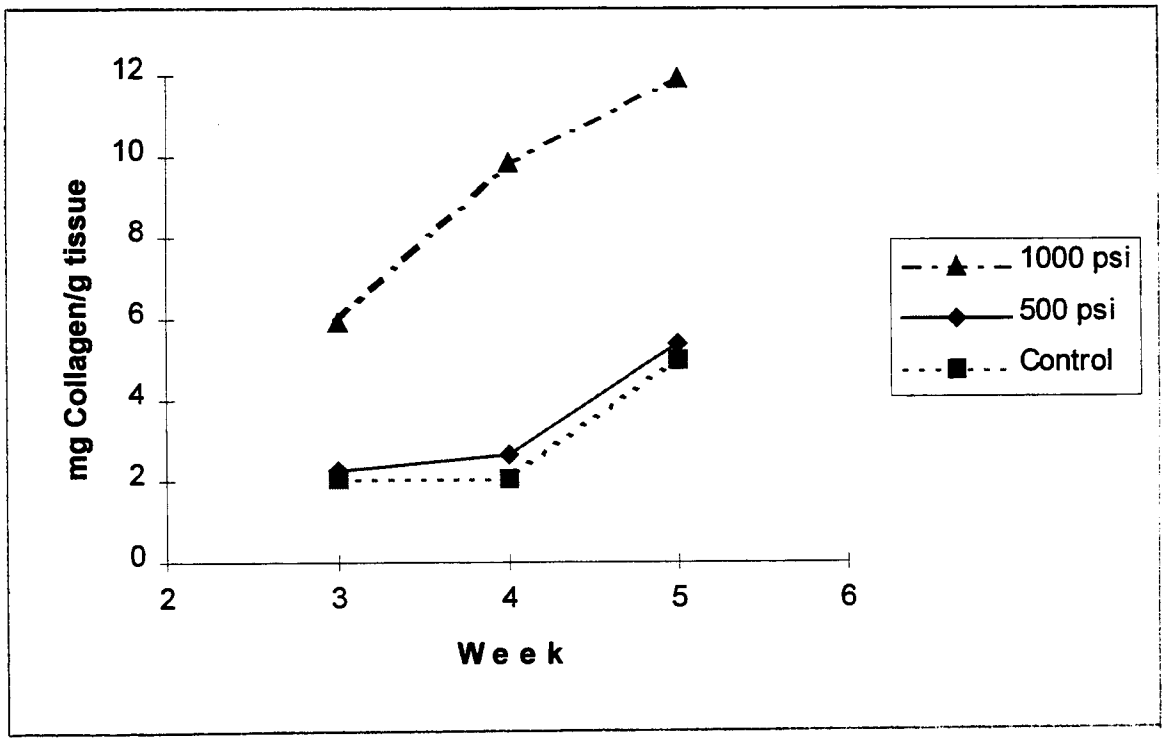

Figure 4: Collagen concentrations in intermittently pressurized and control samples.

Sulfated Glycosaminoglycan Concentration Profiles

Sulfated glycosaminoglycan (s-GAG) concentrations were determined for pressurized and control samples at 3, 4 and 5 weeks (Fig. 5). The control samples never reached the native regime, 40 to 100 mg s-GAG/g tissue. The 500 psi samples reached the native regime at 4 weeks where they remained, while the 1000 psi samples were at the high end of the native regime at 3 weeks and exceeded native levels. Intermittent pressures significantly enhanced the concentration of s-GAG between pressurized and control samples and as the level of pressure was increased, the concentration of s-GAG increased.

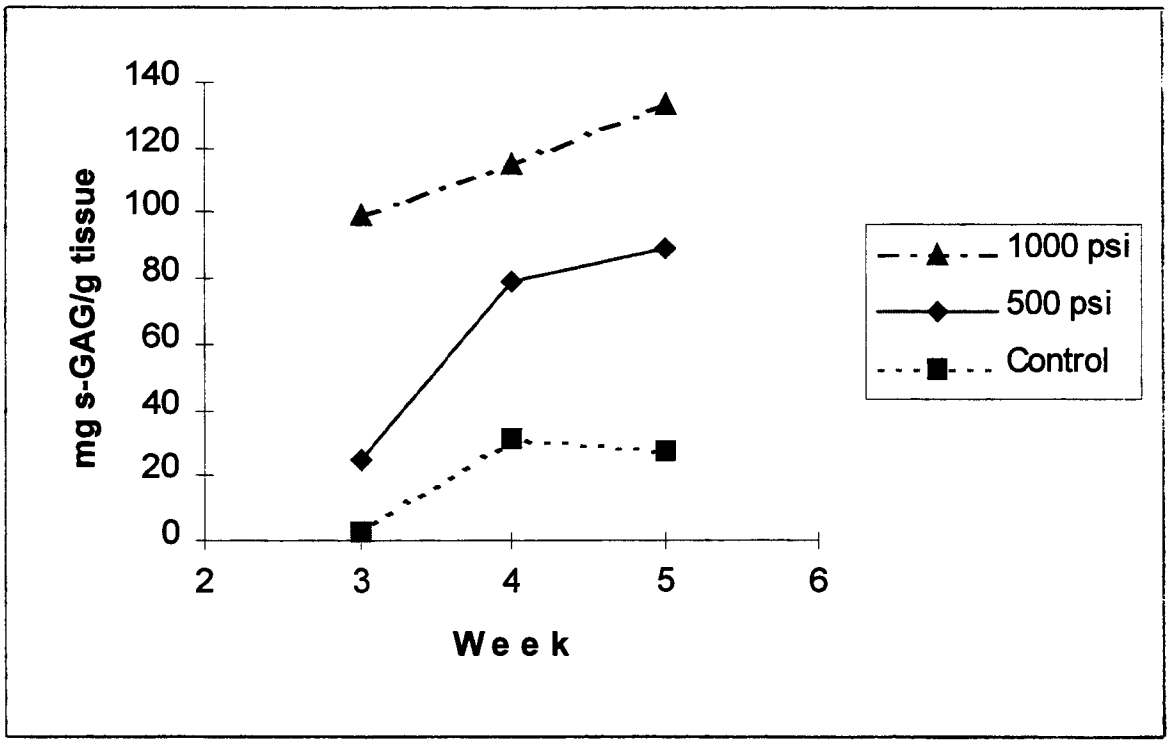

Figure 5: Sulfated glycosaminoglycan concentrations in intermittently pressurized and control samples.

s-GAG vs. Compressive Modulus Profiles

A correlation between s-GAG concentration and the compressive modulus in pressurized samples was found (Fig. 6 and 7). Since this correlation has never been noted in control samples, the intermittent pressures applied may be causing the s-GAG produced to aggregate. Regenerated samples consisting of s-GAG aggregates have a more cohesive matrix, causing the samples to be stronger and retain more water.

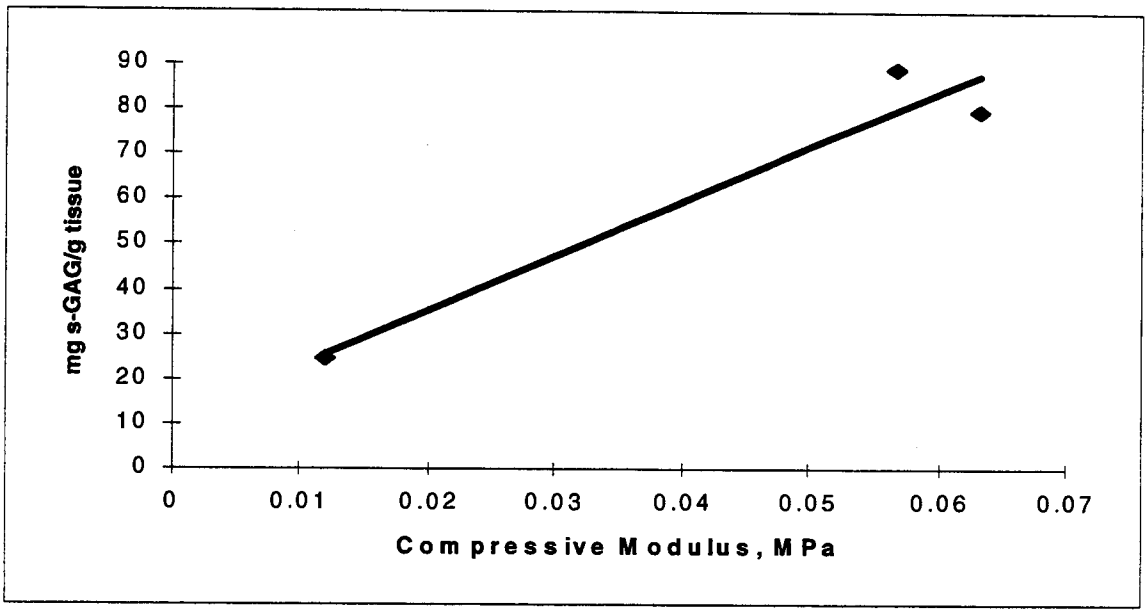

Figure 6: Sulfated glycosaminoglycan content vs. compressive modulus in 500 psi pressurized samples.

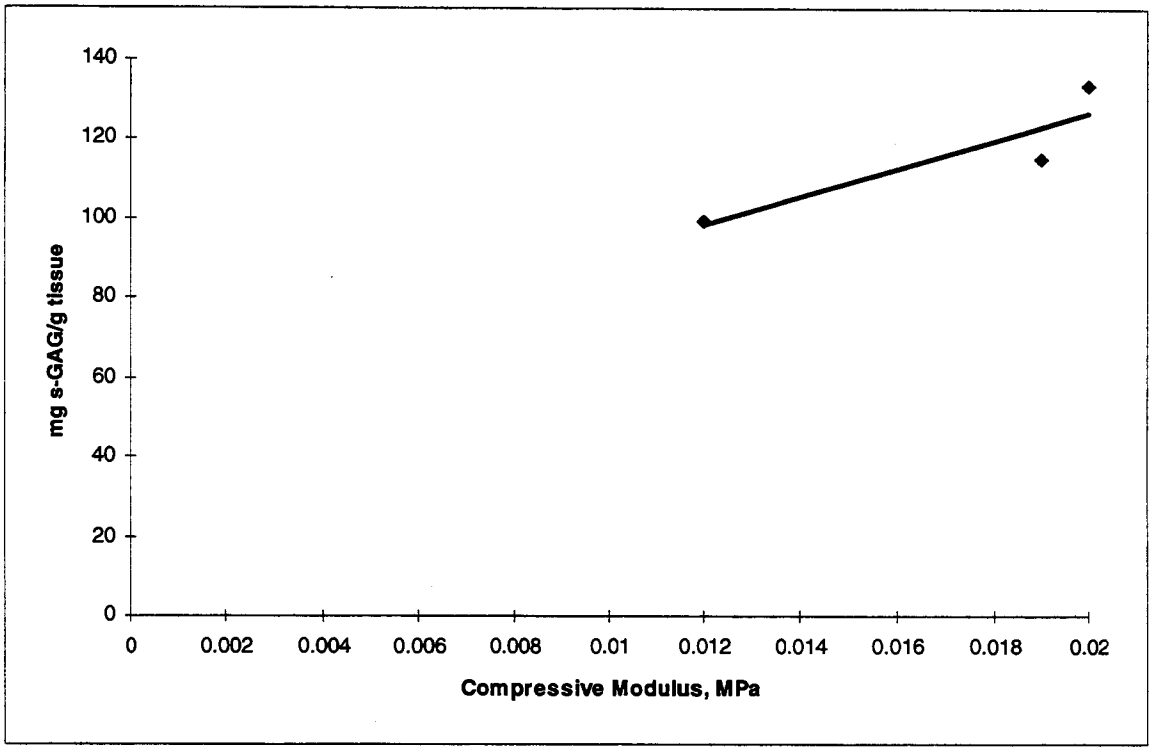

Figure 7: Sulfated glycosaminoglycan content vs. compressive modulus in 1000 psi pressurized samples.

Cellular Microscopy

Light and transmission electron micrographs of 500 psi and control samples are shown in Figure 8. At 3 weeks, pressurized samples show a faint staining of s-GAG in LM micrographs (Fig. 8a). Also, the chondrocytes are evenly distributed throughout the tissue and fragments of PGA remain. At 5 weeks, control samples appear similar to pressurized samples at 3 weeks (Fig. 8b). There is a faint staining of S-GAG in the sample and the cells are still evenly distributed throughout the tissue. However, there are no PGA fragments seen at 5 weeks. This is because the degradation time of PGA is on the order of 4 weeks. Pressurized samples at 5 weeks show a heavy staining of s-GAG and the cells appear flattened at the surface and rounded within the tissue (Fig. 8c). These LM micrographs suggest that intermittent pressure increases the production of s-GAG in regenerated samples and affects the morphology of the chondrocytes within that sample. At the ultrastructural level, few collagen fibrils are seen in the 3 week control sample (Fig. 8d). The pressurized sample at 3 weeks shows many more collagen fibrils than its control (Fig. 8e). As the weeks progress, the collagen density increases in pressurized samples and the fibrils begin to orientate themselves in certain non-random patterns (Fig. 8f). These TEM micrographs suggest that intermittent pressure enhances collagen production and helps orientate those fibrils in a distinct manner.

CONCLUSIONS

The intermittent pressure reaction system and its respective reactors have been shown to support cartilage regeneration. When these intermittent pressures are applied at the physiological level they increase extracellular matrix formation. Sulfated glycosaminoglycan concentrations tended to increase in regenerated samples as the level of intermittent pressure increased. Collagen concentration levels do not appear to be stimulated at the lower ends of physiological intermittent pressures; however, as intermittent pressures increase between 500 and 1000 psi, collagen synthesis increases. This suggests that there is some minimum intermittent pressure needed for the enhancement of collagen production. The chondrocytes ability to replicate also seems to be affected by intermittent pressurization. Pressurized samples tend to have lower cellular densities than control samples. Typically, when chondrocytes are pressurized they tend to focus on matrix production and not on cell replication causing a decrease in cell number per construct. However, since cellular density is based per gram tissue, an increase in matrix production could artificially drop cellular concenmtrations. The decreases in the cellular concentration profiles for the pressurized samples is most likely a coupling of these two effects. Finally, higher sulfated glycosaminoglycan concentrations result in a higher compressive modulus in pressurized samples. Since this correlation has never been seen in control samples this suggests that intermittent pressurization may be causing the s-GAG produced to aggregate. This would create a more cohesive matrix and help retain water within the sample giving the construct a greater ability to withstand mechanical loading.

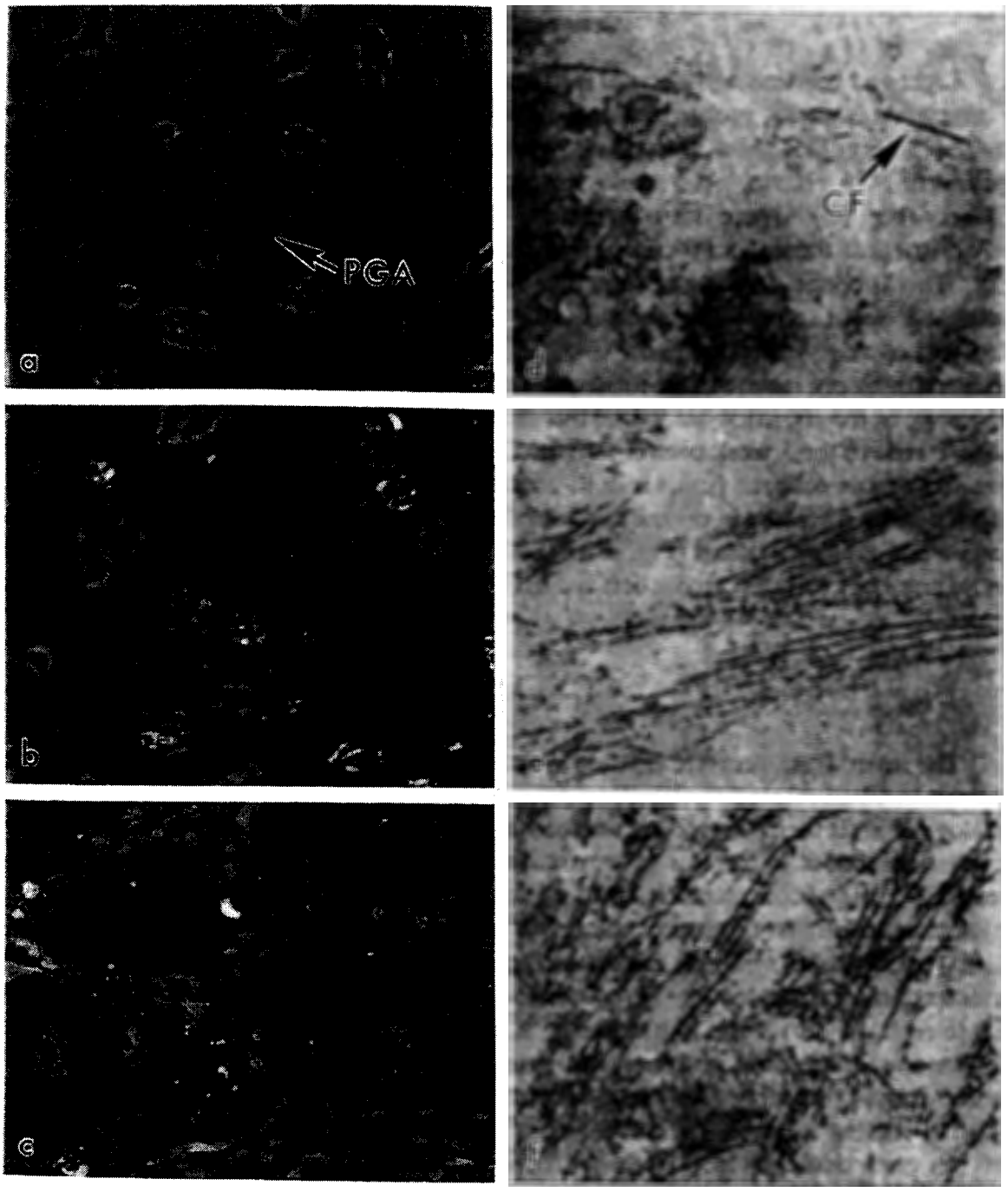

Figure 8: Light microscopy samples are stained with Safranin O and are photographed in the phase contrast mode at 400X. Transmission electron microscopy samples are stained with Lead Citrate/Uranyl Acetate and are photographed at 30,000X. All samples are from the 500 psi experiment. 8a.) LM 3 week pressurized sample. PGA=Polyglycolic acid. 8b.) LM 5 week control sample. 8c.) LM 5 week pressurized sample. 8d.) TEM 3 week control sample. CF=Collagen fibril. 8e.) TEM 3 week pressurized sample. 8f.) TEM 4 week pressurized sample.

ACKNOWLEDGEMENTS

This work was supported by funding from the National Science Foundation and the National Aeronautic and Space Administration.

REFERENCES

(1) V.C. Mow, A. Ratcliffe and R.A. Poole. Cartilage and Diarthroidial Joints as Paradigms for Hierarchical Materials and Structures. *Biomaterials*, 13:67-97, 1992.

(2) M. Brittberg, A. Lindahl, A. Nilsson, C. Ohlsson, O. Isaksson and L. Peterson. Treatment of Deep Cartilage Defects in the Knee with Autologous Chondrocyte Transplantation. *The New England Journal of Medicine*, 331:889-895, 1994.

(3) P.D. Benya and J.D. Shaffer. Dedifferentiated Chondrocytes Reexpress the Differentiated Collagen Phenotype When Cultured on Agarose Gels. *Cell*, 13:215-224, 1982.

(4) J.P. Veldhuijzen, A.H. Huisman, J.P.W. Vermeiden and B. Prahl-Anderson. The Growth of Cartilage Cells In Vitro and the Effect of Intermittent Compressive Force. A Histological Evaluation. *Connective Tissue Research*, 16:187-196, 1987.

(5) A.C. Hall, J.P.G. Urban and K.A. Gehl. The Effects of Hydrostatic Pressure on Matrix Synthesis in Articular Cartilage. *Journal of Orthopaedic Research*, 9:1-10, 1990.

(6) Y.J. Kim, R.L.Y. Sah, J.Y.H. Doong and A.J. Grodzinsky. Fluorometric Assay of DNA in Cartilage Explants Using Hoechst 33258. *Analytical Biochemistry*, 174: 168-176, 1988.

(7) J.F. Woessner. The Determination of Hydroxyproline in Tissue and Protein Samples Containing Small Proportions of this Imino Acid. *Archives of Biochemistry and Biophysics*, 93:440-447, 1961.

(8) R.W. Farndale, D.J. Buttle and A.J. Barrett. Improved Quantitation and Discrimination of Sulfated Glycosaminoglycans by Use of Dimethylmethylene Blue. *Biochimica et Biophysica Acta*, 883:173-177, 1986.

Design of a Bioartificial Nerve Graft for Regeneration in the Periphery

Gregory E. Rutkowski and Carole A. Heath
Department of Chemical Engineering
Iowa State University
Ames, IA 50011-2230

ABSTRACT

Nerve injuries complicate successful rehabilitation more than any other form of trauma because of loss of protective sensibility and tactile discrimination, denervation atrophy of muscles, and pain syndromes. While achieving full function and organ reinnervation after peripheral nerve injury is a challenge, a promising method of improving the rate and success of regeneration is the artificial nerve graft (ANG). An ANG under development in our laboratory consists of a porous resorbable tube containing cultured Schwann cells that help to direct and support nerve regeneration when used to bridge the gap between the ends of the severed nerve.

To aid in the design of the ANG, a simple reaction and diffusion model has been developed to describe the transport and uptake of nutrients by cells in the graft. Implementation of the model has required experimental determination of several key parameters including nutrient diffusivities as a function of polymer porosity with and without the presence of Schwann cells, nutrient consumption rates, and productivity of nerve growth factor, a potent stimulator of regeneration. We will present model predictions of ANG design based on these experimentally determined parameters.

Intracellular Calcium Changes in Endothelial Cells Exposed to Flow and Agonist Stimulation

L. Worthen and M. Nollert
Department of Chemical Engineering
University of Oklahoma
Norman, OK 73019

ABSTRACT

Fluorescence microscopy was used to study the intracellular calcium changes in primary cultures of human umbilical vein endothelial cells. A HEPES buffered saline solution was used with or without 10^{-7} M histamine, 10^{-8} M histamine, or 10^{-9} M histamine. The control experiments showed that flow does not affect the intracellular calcium levels. Cells exposed to histamine, an inflammatory mediator, in combination with flow, showed a sharp increase of at least 0.1 μM of free calcium concentration at the initiation of the flow. This increase was present at shear stress levels of 0.2 dynes/cm^2 up to 20 dynes/cm^2. Our conclusion is that the intracellular calcium changes are not affected by flow alone, but are affected by flow and the presence of inflammatory mediators.

HL-60 Cell-Cell Interactions Under Flow Mediated by Platelet Microparticles

S.B. Forlow and M.U. Nollert
School of Chemical Engineering and Materials Science
University of Oklahoma
Norman, OK 73019

ABSTRACT

One of the most important functions of the immune response system is the recruitment of leukocytes to areas of infection or tissue damage. The initial rolling interaction of leukocytes on the blood vessel wall is largely mediated by the selectin family of adhesion molecules. However, recent data has suggested another possibly important mechanism in the recruitment of cells to a site: enhanced or accelerated accumulation through leukocyte-leukocyte interactions. We have shown another mechanism that enables cell-cell interactions to occur and may contribute to further cell recruitment. The addition of platelet microparticles to HL-60 cells enables bound cells to interact with cells under flow. The interactions are clearly mediated by P-selectin expressed by the platelet microparticles and PSGL-1 on the HL-60 cells. As the concentration of platelet microparticles was increased cell-cell interactions occurred over a wider range of shear stresses. Increasing the concentration of microparticles in the system also increased the number and size of cell aggregates. The role of any type of cell-cell interactions is most likely physiologically relevant in enhancing accumulating of cells at a site when the selectin receptors on the endothelium are blocked by rolling or firmly attached cells.